博士論文

Measuring scattered P wave contributions to the transverse component seismograms and their frequency dependency for the characterisation of small-scale medium heterogeneities

[短波長不均質構造の特徴化のための
散乱P波のトランスバース成分への寄与と
その周波数依存性の測定]

Gugi Aucklandi Ganefianto

令和 5 年

Doctoral Thesis

Measuring scattered P wave contributions to the transverse component seismograms and their frequency dependency for the characterisation of small-scale medium heterogeneities

［短波長不均質構造の特徴化のための
散乱P波のトランスバース成分への寄与と
その周波数依存性の測定］

Gugi Aucklandi Ganefianto
(グギ･オークランディ･ガネフィアント)

Department of Geophysics
Graduate School of Science
Tohoku University

Thesis Committee Members:
Associate Professor Hisashi Nakahara (Chair, Supervisor)
Professor Takeshi Nishimura
Professor Toru Matsuzawa
Professor Ryota Hino
Associate Professor Kentaro Emoto (Kyushu University)

2023

Abstract

Heterogeneities in the subsurface structure have been extensively studied from the propagation of seismic waves, and these provided us with some valuable constrains on the detailed compositions of the Earth's medium. Deterministic approaches can be used to infer these heterogeneities, but they are limited to larger spatial scales. The scattering of seismic waves due to small-scale heterogeneities can provide stochastic measures of medium heterogeneity at smaller spatial scales. Stochastic descriptions of small-scale medium heterogeneities in the Earth often assume von Karman type random media, which are controlled by three key parameters: the root-mean-squared fractional fluctuation in seismic velocities ε, the correlation distance a, and the Hurst exponent κ. A range of parameter values have been estimated by studies applying the principles of seismic wave scattering. However, the number of estimated medium parameters, κ values in particular, is still lacking. Therefore, an easy-to-implement method for estimating κ values is desirable.

In this present study, we investigate a seismic scattering technique based on the transverse component P wave seismogram which is mainly composed of scattered energy off the small-scale heterogeneities. In this regard, scattering strength is represented by the parameter peak-ratio $\Re$, which is defined as the ratio of transverse component envelope peak amplitude over the 3-component sum envelope peak amplitude. The advantages of this peak-ratio approach are that it is computationally cheap, it requires only a single seismic station, and it is not dependent on local seismicity. Furthermore, the scarcity of

short-wavelength elements in the medium heterogeneity (and therefore κ) can be further characterised from the frequency dependency of the peak-ratio. We directly measure this frequency dependent behaviour by computing the frequency exponent m. The validity of the peak-ratio approach has been confirmed for ground surface stations. However, contributions from free-surface and topography on P wave seismogram are yet to be fully understood, especially with regard to borehole seismic stations. To alleviate this problem, we conduct numerical simulations of P wave propagation and analyse their synthetic seismograms to identify and understand the effects of free-surface and topography on the computation of peak-ratios and their frequency dependency. Then, we can make better judgment on the observations of these values from our real data applications.

The propagations of vertically incident plane P wave through 3D random heterogeneous media were simulated based on the Finite Difference Method (FDM) using the OpenSWPC code. Two types of surface condition were considered: One is a flat-free surface, and the other is according to the topography model of Mt. Fuji. To examine the free-surface effect, we set up station arrays on a flat free-surface that laterally cover the computation model and extending with respect to depth down to 10 km. To examine the topographic effect, we set up rings of stations at discrete radius of 2, 4, 6, 8, and 10 km from the summit of the topography model which is positioned at the model centre. Simulations are repeated using these ring arrays on a flat surface so that we can identify the effect of topography. When examining the effect of the free-surface, we found that destructive interference between the up-going incident and the down-going surface reflected phases may raise peak-ratios at borehole stations depending on their depths and the source wavelength hence frequency. At borehole depths around 2 km, the peak-ratio at 0.5-1 Hz is raised underestimating the frequency exponent, while at borehole depths around 250 m, the peak-ratio at 4-8 Hz is raised overestimating the frequency exponent. We also found that topography may increase peak-ratios but it may reduce their frequency exponents. And this effect is more effective at stations within 5 km from

the summit at higher elevations. Therefore, we judge that stations at similar elevations and borehole depths are exposed to similar levels of free-surface and topographic effects, hence, any variations with respect to peak-ratio and frequency exponent would reflect the medium heterogeneities at these stations.

Based on the above findings, we apply the peak-ratio method to the Hi-net stations spread across Japan and interpret the results. We use 390 stations at depths of 100-200 m and at elevations of less than 400 m. 99 deep earthquakes deeper than 300 km were used to focus on the P wave signals. We found that stations in young rock formations at geologically active regions show large peak-ratios, which indicates strong medium heterogeneities at those locations. Conversely, stations at old geologically inactive regions show small peak-ratios, which indicates weaker level of heterogeneity. This also explains the split with respect to peak-ratio between east and west Japan, since the volcanic front mostly run through east Japan. We also found that stations at sediments and plains show large frequency exponents especially compared to those near active volcanoes. This suggests that the power spectra of small-scale medium heterogeneities in sediments are rich in short-wavelength elements, while volcanoes may contain strong small-scale medium heterogeneities that are poor in short-wavelength components.

Using the same set of sources, we also consider 204 stations from the JMA volcanic seismometer network as a supporting case study. These JMA stations are located at 47 active volcanoes in Japan, which is substantial because there are no Hi-net stations this close to active volcanoes. We found that JMA stations show remarkably large peak-ratios but small frequency exponents. The contrast is especially conspicuous when compared to values from Hi-net data. This trend is similar to our observations of numerically simulated data, where stations closer to the summit of an active volcano show larger peak-ratios but smaller frequency exponents. Therefore, we interpret that peak-ratios and frequency exponents at stations at active volcanoes are significantly influenced by the topography of the volcano. Thus, when evaluating peak-ratio and its frequency dependency at these

stations, topography needs to be considered as a factor.

With this present study, we have successfully identified the significance of free-surface and topography on P wave seismogram especially in relation to scattering contributions to the transverse component. By mitigating these effects, we can better infer small-scale medium heterogeneity as construed by the estimations of peak-ratio and frequency exponent. Henceforth, relative estimations of the parameters of random velocity heterogeneity have now become possible. Moreover, numerical simulations that include precise topographic model and real station configuration will enable us to correct for the free-surface and topographic effects, hence allowing for the quantitative estimation of random medium parameters, κ value in particular. In this regard, we attempted to estimate the κ value at Mt. Fuji, thus showing the possibility of similar analysis to be done for other volcanoes. The present study has laid down the groundwork for the quantitative estimation of the random velocity heterogeneities in the Earth using transverse-component P-wave seismograms.

Acknowledgement

First and foremost, I would like to thank my supervisor, Associate Professor Hisashi Nakahara. I am thankful for his input, advice, and feedback, for sharing his wealth of knowledge and experience with me, and for all the conducive discussions we have had which are immeasurable in my growth these past years. Above all, I would like to thank him for his caring and patient guidance.

I would like to thank members of the solid earth physics laboratory for their valuable feedback. Many thanks especially to Professor Takeshi Nishimura for his overarching guidance and for kindly sharing his previous works for us to build upon. Many thanks also to Associate Professor Kentaro Emoto now at Kyushu University for his valuable support and expertise. I would like to express my gratitude to Associate Professor Tomofumi Kozono (now at the National Research Institute for Earth Science and Disaster Resilience, NIED) and Assistant Professor Masayuki Kano for their help. I would like to thank Professors Toru Matsuzawa, Satoshi Miura, Dapeng Zhao, Ryota Hino, Motoyuki Kido and other members of the Research Center for Prediction of Earthquakes and Volcanic Eruptions especially for their guidance in the weekly Wednesday seminars. To all other members of the laboratory and research centre whose names cannot all be listed, I am grateful for your support.

I greatly appreciate Professors Takuto Maeda, Shunsuke Takemura, and Takashi Furumura as the developers of the OpenSWPC for making their code available. I am also thankful to Dongdong Tian for writing the HinetPy code and for making it available to

us. Our data acquisition becomes a lot more straightforward because of it. I am thankful to NIED and the Japan Meteorological Agency (JMA) for the use of their seismograph networks. I am also thankful to the Incorporated Research Institutions for Seismology (IRIS) for their earthquake catalogue. I would like to thank the Earthquake and Volcano Information Center of the Earthquake Research Institute (EIC-ERI), the University of Tokyo for allowing me to use their supercomputer system. And I would like to thank the people involved in the ObsPy project, for without it, every instance of data acquisition, signal processing, and even the displaying of our results become that much harder. I am grateful to the Tohoku University, the Ministry of Education, Culture, Sports, Science and Technology Japan MEXT (No. 20540405), JST SPRING Grant (No. JPMJSP2114) for the numerous financial assistance throughout my years of study.

To Kojima-sensei, thank you for keeping me sane throughout my ordeals.

Finally, I am dedicating this to my parents, relatives, and everyone in my extended family, who supported me through a tumultuous period that also includes a global pandemic. You have always been my number one motivation in all of this.

Contents

Chapter 1

Introduction

Small-scale heterogeneities in the Earth can be represented by changes or fluctuations in seismic wave velocity fields. Often these are studied stochastically where velocity field fluctuations are represented by particular realisations of an ensemble of heterogeneous media. These media have the same statistical properties of random probability distribution describing their fluctuation. Averaging over the ensemble of such random media allows us to infer their physical quantities. Therefore, stochastic methods aim to characterise the randomness attribute of small-scale heterogeneity distribution.

In this chapter, we review the study of small-scale heterogeneities in the Earth. We start by defining the mathematical description of random media to stochastically represent the small-scale heterogeneity. Then, we shall give a rundown of previous approaches studying small-scale heterogeneities and the range of estimated parameters. In this study, we opt for a method based on the transverse component P waves. So we shall also review the development of this approach including its advantages and potential. We will end the chapter by laying out the objectives of this research.

1.1 Random Velocity Fluctuations in Heterogeneous Media

The Earth's seismic velocity structure consists of heterogeneities in wide spatial scales. Large-scale heterogeneities can be inferred deterministically using conventional seismic techniques such as tomography. On the other hand, we can describe small-scale velocity heterogeneities stochastically by superimposing random fluctuations onto a more deterministic background velocity structure, assuming minimum spatial variations in background velocities compared to the scale length typical for the random medium (Margerin, 2011). The realisations of such random media are described by their autocorrelation function (ACF) or its Fourier transform, the power spectral density function (PSDF). There are several types of ACF/PSDF. The often cited ones are the Gaussian type, the von Karman type, and the Exponential type which is a special case of von Karman type media. The key parameters in all are the root-mean-squared fractional fluctuation in velocity ε, and the correlation distance a (also known as the correlation length or the characteristic distance). In essence, ε (often given as a percentage) controls the amplitude of velocity heterogeneity within the medium, while a controls the size and dimension of patches of velocity heterogeneity. For the case of von Karman type media, the Hurst exponent κ is also important, as it reflects the scarcity of short-wavelength components of the heterogeneity in the random medium. Figure 1.1 shows examples of random media realisations with the different types of ACF/PSDF. All panels in Figure 1.1 depend on the same combination of correlation distance a and root-mean-squared fractional fluctuation in velocity ε, but it clearly shows that the details of the small-scale medium heterogeneity depend on the specifics of the chosen ACF/PSDF.

The Gaussian ACF is given by:

$$R(\mathbf{x}) = R(r) = \varepsilon^2 \mathrm{e}^{-r^2/a^2} \ , \tag{1.1}$$

where $\mathbf{x}$ is the position vector and $r \equiv |\mathbf{x}|$. Correspondingly, its PSDF for the 3D case is given by:

$$P(\boldsymbol{k}_m) = P(k_m) = \varepsilon^2 \sqrt{\pi^3} a^3 \mathrm{e}^{-k_m^2 a^2/4} \ , \tag{1.2}$$

where wavenumber of the fluctuation in the media k_m is the absolute value of the wavenumber vector $\boldsymbol{k}_m$.

The von Karman ACF is given by:

$$R(\mathbf{x}) = R(r) = \frac{\varepsilon^2 2^{1-\kappa}}{\Gamma(\kappa)} \left(\frac{r}{a}\right)^{\kappa} K_\kappa \left(\frac{r}{a}\right) \ , \tag{1.3}$$

$$\text{for} \quad \kappa = 0 \sim 1$$

where K_κ is the modified Bessel function of the second kind of order κ, and is one of the solutions to the modified Bessel differential equation (e.g., Abramowitz and Stegun (1972)). Γ is the gamma function (e.g., Snieder and van Wijk (2015)).

Correspondingly, the von Karman PSDF for the 3D case is given by:

$$P(\boldsymbol{k}_m) = P(k_m) = \frac{8\pi^{3/2} \varepsilon^2 a^3 \Gamma(\kappa + \frac{3}{2})}{\Gamma(\kappa) \left[1 + a^2 k_m^2\right]^{\kappa + \frac{3}{2}}} \ . \tag{1.4}$$

At large wavenumbers ($ak_m \gg 1$), Equation 1.4 obeys a power-law decay where it is $\propto (ak_m)^{-2\kappa - 3}$. Crucially, the roll-off of the power-law decay is controlled by the Hurst exponent κ. When κ is equal to 0.5, the medium is often referred to as the Exponential type.

For describing small-scale medium heterogeneities in the Earth, often a von Karman type medium is assumed. This is because, the heterogeneity in the Earth can be well explained by a power-law spectrum, and the von Karman PSDF similarly follows the power-law asymptotically at large wavenumbers (Saito et al., 2002; Suzaki, 2007; Sato, 2011; Sato et al., 2012; Sato, 2019). The Gaussian type media albeit mathematically

tractable, are limited for describing random media that are very poor in short-wavelength components because Gaussian type PSDF drops very quickly at large wavenumbers. In other words, Gaussian type media may be too smooth and inflexible to describe the rich short-wavelength heterogeneities in the Earth.

Figure 1.2 shows the ACF and PSDF for the Gaussian and the von Karman type media. At small wavenumbers, the von Karman PSDF is flat up to a corner of $k_c \sim 1/a$, where from then on, the power spectrum decreases according to $k_m^{-(2\kappa+3)}$ (Margerin, 2011). Thus, this power-law decay at large wavenumbers allows the PSDF of the von Karman type to be used to describe random media that are much richer in short-wavelength components compared to the Gaussian type, where the cap on the small-scale features is controlled by the κ value (Margerin, 2011; Sato et al., 2012).

It is important to reiterate the significance of the choice of κ value. As implied by Equation 1.4 and shown in Figure 1.2b, κ controls the roll-off of the power-law decay and acts as a limit on the small-scale features in the medium. As such, different κ values will produce different random medium realisations with different spectral characteristics, where small κ corresponds to random medium rich in short-wavelength elements, while large κ corresponds to random medium poor in short-wavelength elements (Figure 1.1).

Previous studies have estimated the key medium parameters of ε, a, and κ. It is possible to appraise these parameters deterministically. For example, Nakata and Beroza (2015) investigated the characteristics of medium heterogeneity at Long Beach, California by estimating the power spectra of high resolution 3D P wave velocity model obtained tomographically using a dense seismic array and ambient seismic wavefield. They found that the medium underneath the array can be described by a von Karman medium with $a = 0.1 - 0.51$ km, $\varepsilon = 10.7\%$, and $\kappa = 0.04$. In the mantle, Chevrot et al. (1998) constrained the spectrum of heterogeneity by combining the spectra of global and regional tomographic models. Their results suggest a κ range less than 0.5 and a in the order of

1000 km.

The power spectra of heterogeneity can be obtained from not only tomography results, but also from acoustic well logs. For example, Wu et al. (1994) estimated the power spectra of sonic logs from two deep boreholes (down to 4 and 6 km deep) as part of German Continental Deep Drilling Project (KTB). Additionally, Holliger (1996) analysed sonic logs from ten boreholes spread across six tectonic environments (across Europe and North America). The study found that the residual small-scale P wave velocity fluctuations of all sonic logs show similar spectral characteristics as described by their autocovariance functions modelled using the von Karman functions with κ of around 0.1, ε of around $4.8 - 6.7\%$, and a of around $0.14 - 0.16$ km. In Japan, a similar study was carried out where power spectra from five well logs of roughly 2 to 3 km in depth were obtained (Shiomi et al., 1997). κ value from a well log from a volcanic setting was estimated to be 0.225, while κ value from a well log from a sedimentary setting was estimated to be 0.045.

Such deterministic way of studying small-scale heterogeneities, however, is limited to longer spatial scales. This is because there is a resolution limit to the deterministic detection of heterogeneities. For example, only heterogeneity scale larger than the acoustic wavelength of the sonic log surveys can be discerned in from their power spectra. Other limiting factor is, for example, that conventional tomography is reliant on the ray-path coverage. Since observations are made with respect to specific phase arrivals with their distinct ray-paths, some regions may not be sampled or passed by the seismic rays depending on the source and receiver configuration. Moreover, high resolution data such as that of Nakata and Beroza (2015) is expensive in terms of equipment (as with the spatially dense array requirement) and computationally burdensome. For those using acoustic well log information, the cost of drilling is by no means cheap, yet analyses are restricted to 1D.

Therefore, estimations of small-scale random medium parameters are often done

stochastically, especially to overcome the resolution limit of the more deterministic approaches. Such stochastic studies are based on the scattering of seismic waves. Seismic scattering causes distortions and deflections of the wavefront caused by the small-scale random heterogeneous elements in the medium, as the wave travels through the heterogeneous region (Figure 1.3). Henceforth, the characteristics of the random fluctuations can be inferred by analysing the statistical fluctuations in the wavefield as a result of scattering (Margerin, 2011). In other words, we can infer small-scale heterogeneity by measuring the strength of seismic wave scattering caused by the heterogeneities themselves.

This can be done in several ways. For example, the phase fluctuation method makes use of the notion that the transmitted wavefront is distorted as a result of scattering (Figure 1.3). This introduces fluctuations in phase arrival times with respect to distance along the wavefront. Capon (1974) managed to detect these variations in the sub-arrays of LASA (Large Aperture Seismic Array, Montana) from P, PKP and PcP phases of events at distances between 28° to 168°. The study found that the fluctuations between sub-arrays can be modelled by random heterogeneities in the crust and upper mantle structure under LASA, with a of 12 km. Using LASA, Aki (1973) similarly identified variations in time delay and amplitude of teleseismic P waves, which were interpreted as being caused by scattering off random heterogeneities extending down to about 60 km in the crust under LASA, with a of about 10 km, and ε of 4%. Flatté and Wu (1988) analysed the arrival time and amplitude fluctuations using the NORSAR array in Norway to evaluate the power spectra of P wave velocity variations with respect to depth. They showed how the lithospheric and asthenospheric heterogeneities underneath the NORSAR array can be represented by two overlapping layers, where small-scale structures are abundant in the shallow layer while the deep layer is predominantly of larger-scale variations.

A more recent application can be found in Ma and Huang (2020). The teleseismic fluctuation wavefield method (TFWM) which looks at waveform correlation/coherence,

was implemented in the study. Using TFWM, Ma and Huang (2020) managed to constrain $\varepsilon^2 a$ in the lithosphere underneath the northern Tien Shan region. Subsequently, they evaluate the trade-off between ε and a using the Monte Carlo simulations to model the P wave coda envelope. Henceforth, Ma and Huang (2020) suggested a roughly 55-130 km thick random heterogeneous layer under the northern Tien Shan region, with a of about 0.4 km and ε of 6-9%, which they attributed to isolated melt pockets in the hot upwelling mantle substance.

Another approach looks at the effect of envelope broadening with respect to epicentral distance caused by the dominance of narrow angle (forward) scattering in the wavefield due to small-scale heterogeneities (Sato, 2011). Quantitatively, the envelope broadening phenomenon was attributed to narrow-angle scattering in the forward direction caused by the small-scale heterogeneity (Sato, 1989). Figure 1.3 illustrates this phenomenon, in which at a short travel distance we get an impulsive large amplitude seismic signal, whereas with large travel distance the likelihood of more scattering occurrences increases, hence more energy is arriving later than the direct wave, resulting in an amplitude decay and long duration signal hence the broadening of seismogram envelope.

In this regard, Obara and Sato (1995) inferred that multiple forward scatterings of seismic waves due to random heterogeneities caused the broadening of seismogram envelopes around the direct S waves of intermediate depth and deep seismic events in the lithospheric slab. This envelope broadening was analysed to infer regional differences in small-scale heterogeneities, particularly with respect to the volcanic front at the the Kanto-Tokai region, Japan. The study of seismogram envelope in von Karman random media has also indicated that the envelope broadening effect is regulated by the roll-off of the von Karman type PSDF (Saito et al., 2002). Based on seismogram envelope simulation using the Markov Approximation, Saito et al. (2005) indicated that the fore-arc region of the northeastern section of Honshu Island can be represented by a von Karman medium with κ of 0.8. The study of Takahashi et al. (2009) provides distributions

of κ values in the northeastern region of Japan by computing the delay time to the peak value of high frequency S wave records of local earthquakes following the envelope broadening effect modelled by Markov Approximation. For the first 20 km depth, κ values estimated in the lithosphere of northeast Japan range from $0.28 \sim 0.68$.

Often, seismic scattering hence heterogeneity can also be described by the scattering coefficient g_0, or the scattering parameter Q_s^{-1}. g_0 represents a measure of medium heterogeneity as scattering power per unit volume, and it is proportional to the Q_s^{-1}, in which $Q_s^{-1} = g_0 V/\omega$, where V is the seismic wave velocity and ω is the angular frequency. Both of these parameters are useful for conceptualising the scattering medium by way of the mean free path ℓ, which is the reciprocal of g_0, and represents the typical scale length over which a scattering event would have likely occurred, in other words, the typical propagation distance before an instance of scattering (Figure 1.3). Hence, ℓ can help us perceive the distribution of medium heterogeneities controlling the scattering occurrences.

Carcolé and Sato (2010) assumes an isotropic scattering model to analyse S wave signals and the following coda using the multiple lapse time window analysis (MLTWA) in order to map the distributions of Q_s^{-1} over Japan (among other parameters). Ogiso (2018) mapped g_0 over southwestern Japan at multiple depth ranges in a more advanced way. For each earthquake in their dataset, g_0 was simultaneously estimated along with the intrinsic attenuation factor Q_i^{-1} (e.g., the loss of seismic energy through heat conversion, etc.) through a seismogram envelope fitting method which includes the coda window. The model envelope was obtained based on the source radiation energy, the Green's function of the envelope, and the site amplification term (Sens-Schönfelder and Wegler, 2006; Eulenfeld and Wegler, 2016). The estimated parameters are then mapped onto a 3D space using sensitivity kernels obtained via Monte Carlo simulations (Takeuchi, 2016). Przybilla et al. (2009) evaluated the scattering coefficient using the NORSAR array. Based on the Born Approximation and through conducting the Monte Carlo simulations,

they evaluated combinations of ε^2/a, and from the frequency dependence of scattering, they estimated that heterogeneity in the crust in the region surrounding the array has a κ value of 0.2.

Table 1.1 summarises the ranges of random medium parameters estimated by studies of small-scale heterogeneities in the lithosphere and the upper crust. We differentiate these ranges into those found in weak heterogeneous regions (i.e., ordinary crust and lithosphere) and those found in active or strong heterogeneous regions (e.g., active volcanoes and volcanic regions). Typically, strong heterogeneous regions contain larger ε and smaller a values.

Table 1.1 neatly summarises the ranges of estimated parameters, though there are studies that show values outside of the ranges given. For example, Wang and Shearer (2017) suggested a two-layer model for Southern California in which very strong scattering was introduced in the shallow layer with ε of 40%. Conspicuously small a values ($a \approx$ 0.001 km) can be found in the Michigan Basin based on modellings using cross-well seismic data (da Silva et al., 2018).

In Calvet and Margerin (2013), von Karman models with κ of 1 to 5 were used, although, κ values within the range of 0.1–1.0 are more typical. Still, the number of estimated κ values is more limited, as it is the parameter most often assumed, usually by the Exponential type random media (i.e., $\kappa = 0.5$). Therefore, a method for estimating κ that is straightforward and easy to implement is certainly beneficial.

1.2 Review of Studies Based on the Transverse Component of P Waves

In this section, we focus on the study of small-scale heterogeneity based on the transverse component of P waves. Bearing in mind that P waves are compressional waves with particle motion polarised along the propagation direction, it is useful to consider the

following thought experiment in order to understand the connection between P wave scattering, seismogram envelope and small-scale heterogeneity.

Imagine a vertically incident P wave ray coming from below. In a fictitious condition of homogeneous Earth, this wave would have travelled unobstructed up to the surface. Hence, the sensors at a seismic station on the surface would only detect signals in the vertical direction following the polarisation nature of P waves. This is true for layered structures as well. However, in the real Earth, small-scale heterogeneities can scatter the directions of the incoming P wave rays, which will introduce particle motion in the horizontal directions. Similarly, when the incident ray is coming in at an oblique angle, the initial particle motion induced by the P wave is restricted in the vertical and radial directions. The occurrences of scattering then partition P wave energies into the transverse direction (Figure 1.3). Thus, the transverse component signal of P wave records contain information on small-scale medium heterogeneity.

This transverse component excitation was formulated in Sato (2006) and Sato and Korn (2008) based on the Markov Approximation, which is an extension of radiative transfer theory that incorporates aspects of parabolic approximation for slowly varying structure (Sato, 2019). It is useful to adopt the parabolic approximation when examining the time window around the peak value of the wavelet at large wavenumbers, where the assumption of forward narrow-angle scattering is particularly accurate (Sato, 2019). Using Markov Approximation, Sato (2006) successfully synthesised the seismogram envelope of plane vector-wave in 3D infinite random media, and reproduced the broadening effect in P wave envelope. Sato (2006) also modelled the amplitude excitation in the P wave transverse envelope, and established the link between P wave scattering strength and random heterogeneity. Sato (2006) concluded that the analysis of teleseismic P wave envelope can be a good stochastic approach for measuring small-scale medium heterogeneity, following the partitioning of P wave energy into the transverse component.

Following Sato (2006)'s conclusion, Kubanza et al. (2007) presented a real data ap-

plication of the measurement of scattering strength from the transverse component of P waves. They proposed computing the ratio of of maximum P wave amplitude in the transverse component seismogram envelope over the maximum in the three-component sum envelope. This peak-ratio is then used to parameterise scattering strength. It can be linked to the randomness quantity of small-scale heterogeneity at a seismic station, that is, peak-ratio is approximately equal to $1.81\varepsilon^2 h/a$, where h is the medium thickness, and a Gaussian type function is assumed. Kubanza et al. (2007) used deep teleseismic earthquakes deeper than 300 km from the western Pacific region to evaluate seismic scattering at the worldwide IRIS-GSN seismometer network. They found that stations located at active tectonic regions such as those near to the plate margins show larger peak-ratios, whereas stations located on stable continents show smaller peak-ratios. They attributed this observation to the abundance of heterogeneous elements in an active settings and likewise, the deficiency of such heterogeneity at stable continents.

On a more regional scope, Nishimura (2012) used about 90 deep earthquakes deeper than 300 km to measure seismic scattering strength in Japan. Nishimura (2012) utilised the extensive Hi-net seismometers (High Sensitivity Seismograph Network), which covers Japan at a dense station spacing of 15 to 20 km. The study found that stations along the volcanic front, and in the vicinity of active quaternary volcanoes and/or active faults, show large peak-ratio values. Conversely, stations that are far from the volcanic front, from any quaternary volcanoes, or from active faults, show relatively small ratios albeit larger still than those inferred in Kubanza et al. (2007) for the stable continents.

A not too dissimilar concept was also applied in Cafferky and Schmandt (2015), where the transverse component is used to gauge scattering significance, based on the same understanding that it would not receive any P energy had it not been for scattering off the three-dimensional heterogeneity. The spectral ratio of transverse over vertical components was computed across the United States using the USArray to measure scattering contribution at each station in relation to relative body wave attenuation parameter. It

was found that larger ratio (stronger scattering) tends to correlate with higher relative body wave attenuation parameter, suggesting major scattering contributions to seismic attenuation.

Thus, peak-ratio can be a useful metric for quantifying seismic scattering strength due to small-scale medium heterogeneity. Its one considerable disadvantage is with regard to ambiguity in separating the heterogeneity and the thickness of the medium. But there can be several significant advantages to this approach. The bulk of the computational load in the determination of peak-ratio is in the calculation of seismogram envelopes which uses common seismic processing steps. As such, the computing performance cost of the method is relatively low. The peak-ratio method can also reduce the effect of intrinsic absorption. The technique can also be applied using only a single seismic station hence an array of stations can provide us with a spatial distribution of scattering strength measurements. Furthermore, it has the benefit of not requiring local seismicity as sources. Henceforth, the same set of teleseismic sources can be used to systematically evaluate seismic scattering over a wide region and study scopes that depend on the coverage of the seismic array.

Additionally, when evaluated across multiple frequency bands, it has been noted that there is a general increase in peak-ratio with increasing frequency (e.g., Figure 7 of Kubanza et al. (2007); Figure 2 of Nishimura (2012)). This frequency dependent behaviour can be further utilised for characterising the scarcity in short-wavelength elements of small-scale heterogeneity of the von Karman type, in other words, for estimating κ. A strong link with frequency was found in media rich in short-wavelength components (small κ). On the contrary, media poor in short-wavelength components (large κ) correspond to weaker frequency dependency (Saito et al., 2002). Extending the works by Saito et al. (2002), Suzaki (2007) studied the vector-wave envelope synthesis in von Karman media and proposed a relation between the frequency dependency of peak-ratio and κ, in which peak-ratio follows the power law with respect to frequency, and its exponent is

controlled only by κ. Suzaki (2007) applied this method to IRIS stations classified into active and stable groups. This shows how the κ value at individual seismic stations can be evaluated straightforwardly by utilising the frequency dependency of peak-ratio, provided that evaluations are made at multiple frequency bands. Therefore, the peak-ratio approach can provide an easy-to-implement alternative for estimating κ values.

The approach outlined in Suzaki (2007) is appealing because it comes with all the benefits of the peak-ratio method (low computing cost, single station requirement, not dependent on local seismicity). Yet, it is still imperfect. So far, the theory has been mostly concerned with an infinite medium case. But in the real world situation, our means of acquisition (seismometer) are located on a nominal half-space. In this regard, Emoto et al. (2010, 2012) synthesised vector wave envelopes at stations on the free-surface and validated the use of ground surface stations. But the influence of the free-surface on borehole stations is yet to be fully comprehended. In addition, the impact of topography has not been fully addressed. Thus, there is still a lack of understanding with regard to free-surface and topographic effects on peak-ratios and their frequency dependency. Therefore, we need to validate the use of borehole stations and volcanic stations with regard to the peak-ratio approach.

1.3 Purpose of This Research

Therefore, this research aims to evaluate the characterisation of small-scale medium heterogeneities in the Earth through the study of peak-ratio and its frequency dependency in light of free-surface and topographic effects. Both numerically synthesised data and recorded data from real seismic station networks are to be used.

The theory behind the use of peak-ratio to describe small-scale medium heterogeneities is the numerical synthesis of seismogram envelopes using Markov Approximation. So we introduce them in Chapter 2 before we present the procedures on how to

measure peak-ratio and its frequency dependency at a seismic station. Most importantly, in Chapter 2, we identify the free-surface and topographic effects by performing numerical simulations of seismic wave propagation, particularly, we found that stations at similar depths and installation heights would experience similar level of free-surface and topographic effects. Based on the results, we amend the original procedures to mitigate the effects of free-surface and topography.

In Chapter 3, real data analysis will be carried out. Peak-ratios and their frequency dependencies will be calculated at borehole seismic stations spread across Japan. Free-surface and topographic effects are mitigated here by carefully choosing stations of similar elevations and borehole depths, following the implications from the numerical simulations. Therefore, lateral variations in terms of peak-ratio and its frequency dependency can be used to interpret the small-scale medium heterogeneities underneath these stations.

In Chapter 4 we will focus on the analysis of peak-ratios and their frequency dependency at stations located at active volcanoes. This is an important case study because we expect volcanoes to be strongly heterogeneous. But also because a dominant topographic presence is to be expected in the vicinity of the seismic stations.

In Chapter 5 we will bridge the above individual chapters to discuss the evidence for free-surface and topographic effects in both real and simulated data. By categorising real world stations according to their borehole depths, installation heights, and proximity to a strong topographic presence (active volcano), we show how the same characteristics identified in the simulated dataset can be observed in real case scenarios. Thus, our mitigation approach will be justified. We will also discuss how in the future, peak-ratio and its frequency dependency can be better approximated to reflect the small-scale medium heterogeneities.

Finally, we will provide the conclusions of this study in Chapter 6.

Table 1.1 Ranges of estimated random medium parameters from studies of small-scale heterogeneities in the lithosphere and upper crust at weak heterogeneous regions (ordinary crust) and strong heterogeneous regions (e.g., volcanoes).

Medium Parameter	Range (weak heterogeneity)	Range (strong heterogeneity)
a	0.1–25 km	0.05–10 km
ε	1–10%	6–20%
κ	0.04–0.8	0.05–0.5

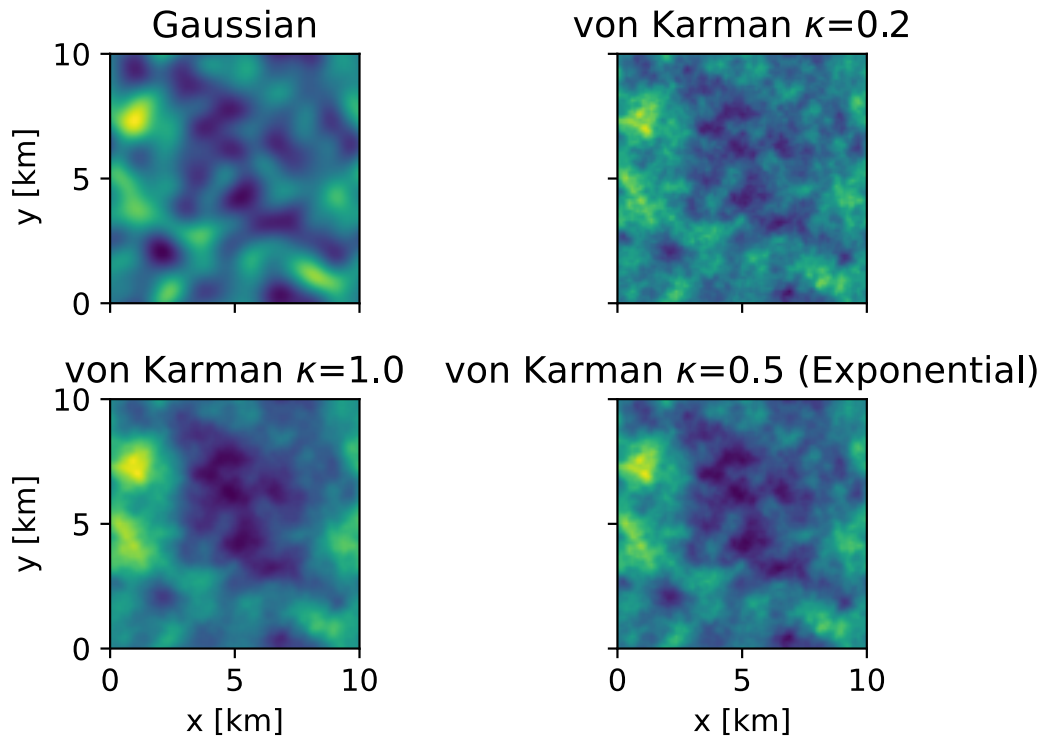

Figure 1.1 The rendering of random media realisations, with equal correlation distance a of 1 km and root-mean-squared fractional fluctuation in velocity ε of 10%. Different panels signify the differing realisations of the media according to their specific autocorrelation functions: Gaussian type, von Karman type with a small κ value ($\kappa = 0.2$), von Karman type with a large κ value ($\kappa = 1.0$), and Exponential type (von Karman type with κ=0.5).

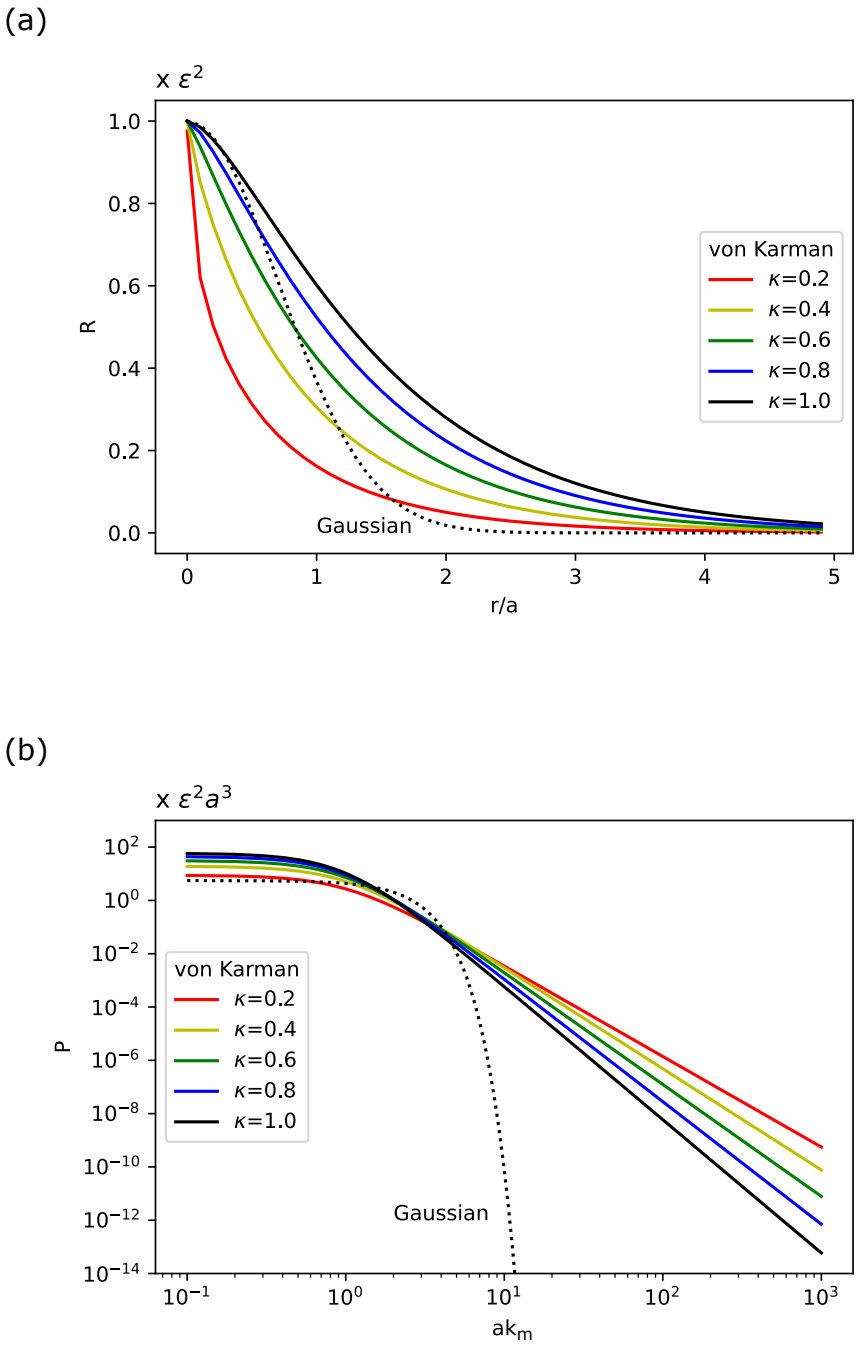

Figure 1.2 Plots of (a) the autocorrelation function (ACF), and (b) the power spectral density function (PSDF), of the Gaussian type and the von Karman type random media.

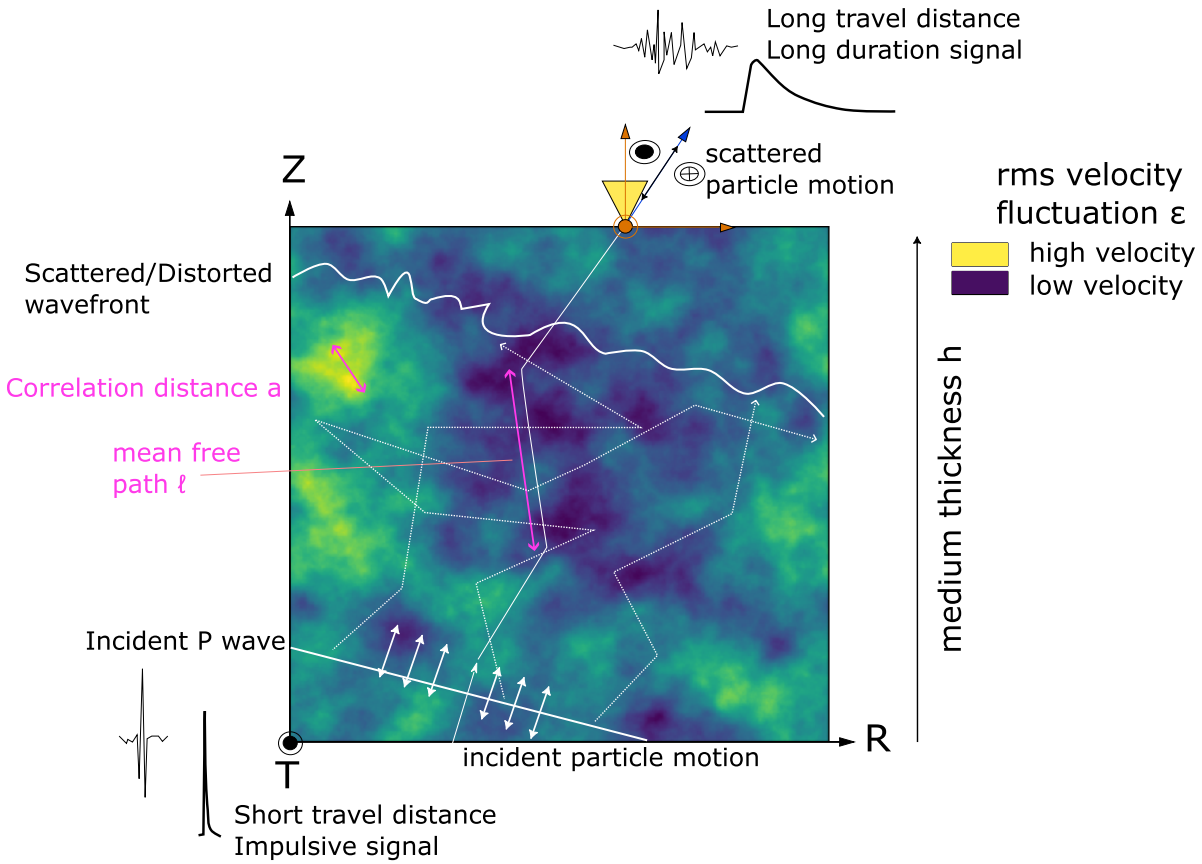

Figure 1.3 The fundamentals of seismic wave scattering. An incident wave is travelling through a random medium whose heterogeneous elements scatter the propagating wave. The typical scale length of heterogeneity is given by the correlation distance a. The typical distance between scattering events is given by the mean free path ℓ. The amplitude of velocity perturbations in the random medium is controlled by the root-mean-squared fractional fluctuation in velocity ε. As a result, the transmitted wave is distorted. For an incident P wave coming in at an oblique angle, the initial particle motion is contained within the vertical (Z) and radial (R) directions before scattering partitions energies into the transverse (T) direction. At a short travel distance, seismic signal is impulsive with a large amplitude. At long travel distance, there is a decay in amplitude, and we have a long duration signal and the broadening of the seismogram envelope.

Chapter 2

Numerical Simulations for Examining the Effects of Free-Surface and Topography on Peak-Ratio and its Frequency Dependency

The main purpose of this chapter is to devise a strategy for mitigating free-surface and topographic effects when analysing peak-ratios and their frequency dependency. In order to do that we need to first understand how free-surface and topography can influence the computation of peak-ratio $\Re$ and frequency exponent m. We shall investigate this by conducting numerical simulations that incorporates such features. Henceforth, from the results of the numerical simulations, we can understand how to mitigate these free-surface and topographic effects in real data analysis.

Before we get to the above, first we ought to review the connection between small-scale medium heterogeneity and the peak-ratio as well as its frequency dependency. This can be explained through Markov Approximation. In this regard, we will start by describing how seismogram envelopes of scattered waves travelling through random media can be

synthesised using the Markov Approximation. The resulting transverse component excitation is the basis for computing peak-ratio as a measure of seismic scattering strength. Subsequently, following the frequency dependent behaviour of numerically synthesised envelopes, we will explain how this aspect can be linked to the Hurst exponent of the von Karman type media κ through the computation of frequency exponent m. In this chapter, we will also lay out the procedural steps for obtaining equivalent seismogram envelope from the seismogram data in order to compute the peak-ratio. Correspondingly, we will also show how to quantify the frequency dependent behaviour of peak-ratio by estimating the frequency exponent m.

2.1 Peak-Ratio and its Frequency Dependency Expected from the Markov Approximation

The envelope of the seismogram of scattered waves by the small-scale random heterogeneities described in Section 1.1 can be synthesised using the Markov Approximation. The Markov Approximation was first introduced into seismology by Sato (1989). Since then, the envelope synthesis technique has been comprehensively expanded for example in Sato (2006) and Sato and Korn (2008), and summarised in Emoto (2018). Here we shall run through the method of the Markov Approximation to obtain synthesised vector wave envelope.

The Markov Approximation assumes multiple forward narrow-angle scattering. So first, it is useful to consider scattering from a single localised velocity fluctuation by the Born Approximation (e.g., in Shearer and Earle (2004); Sato et al. (2012); Emoto (2018)). From the Born approximation, we can calculate the scattering coefficient which describes the scattering power per unit volume. The PSDF term governs the contribution of the wavenumber to the scattering coefficient (Emoto, 2018). And this contribution of the PSDF term to scattering coefficient can be determined separately for the P-to-P, S-to-S,

P-to-S, and S-to-P scatterings.

From the Born Approximation, we can also determine the dominant scattering angle θ for the different types of scattering (P-to-P, etc.). θ is defined as the angle between the incident ray's propagation direction and the propagation direction of the scattered ray. According to the Born Approximation, the dominant angle is dependent on the ak value, where k is the wavenumber of the seismic wave. For the case of wavelength longer than the correlation distance ($ak < 1$), Born Approximation shows that for all scattering types, scattering is more or less isotropic. On the other hand, for the case of wavelength shorter than the correlation distance ($ak \gg 1$) forward narrow-angle scattering is dominant, in other words, θ is small. Furthermore, P-to-S or S-to-P conversions are negligible for the case of $ak \gg 1$, thus allowing for the separate examination of P wave scatterings. Please refer to Figure 2 of Emoto (2018) for the visual description of the Born Approximation.

This scattering regime dominated by forward narrow-angle scatterings is the focus of the Markov Approximation. Under this scattering condition, at each instance throughout the wave propagation, the slice of the medium perpendicular to the main direction of propagation can be seen as a collection of many local scatterers which independently redirect the ray in a randomly manner (Margerin, 2011). Therefore, the realignment of ray directions after some travel distance depends solely on the heterogeneities within that travel distance (Sato, 1989; Sato and Korn, 2008).

This does not mean however, that the Markov Approximation is not applicable for the case where the wavelength is longer than the correlation distance of the heterogeneity. When there are scatterings at large angles, they can be considered as contributing towards the apparent or intrinsic energy losses (Sato, 1989; Margerin, 2011). Additionally, when the propagation distance is larger than the transport mean free path — which is true for teleseismic events and other events at large hypocentral distances — the wave is deemed to have lost information on its original propagation direction (Margerin, 2011).

Consider a plane P wave travelling vertically (z-direction) in a random heterogeneous

medium. For the case of dominant forward narrow-angle scattering, the scalar potential of the plane wave is:

$$\phi(\mathbf{x}_\perp, z, t) = \frac{1}{2\pi}\int_{-\infty}^{\infty} d\omega \mathrm{e}^{ik_0 z - i\omega t}\frac{1}{ik_0}U(\mathbf{x}_\perp, z, \omega)\ . \tag{2.1}$$

The wavenumber k_0 is equal to ω/V_0, and x or y is in the direction of the transverse component. U follows the parabolic wave equation given as:

$$2ik_0\partial_z U + \Delta_\perp U - 2k_0^2\xi U = 0\ . \tag{2.2}$$

Here, $\Delta_\perp \equiv \partial_x^2 + \partial_y^2$. In Equation 2.2, we may neglect the second derivative with respect to z because the variation of U along the z direction is small. We can calculate the mean-squared (MS) seismogram envelope by introducing the two-frequency mutual coherence function (TFMCF):

$$\Gamma_2(\mathbf{x}'_\perp, \mathbf{x}''_\perp, z, \omega', \omega'') \equiv \langle U(\mathbf{x}'_\perp, z, \omega')\ \ U^*(\mathbf{x}''_\perp, z, \omega'')\rangle\ . \tag{2.3}$$

Equation 2.3 correlates U between two points in the transverse direction $(\mathbf{x}'_\perp, \mathbf{x}''_\perp)$ at a distance z and different angular frequencies (ω', ω''), where U^* is the complex conjugate of U. From Equations 2.2 and 2.3 we can obtain the master equation for the TFMCF:

$$2i\partial_z\Gamma_2 + \left(\frac{\Delta'_\perp}{k'_0} - \frac{\Delta''_\perp}{k''_0}\right)\Gamma_2 - 2\left\langle\left[k'_0\xi(\mathbf{x}'_\perp, z) - k''_0\xi(\mathbf{x}''_\perp, z)\right]U(\mathbf{x}'_\perp, z, \omega')U^*(\mathbf{x}''_\perp, z, \omega'')\right\rangle = 0 \tag{2.4}$$

where $k'_0 = \omega'/V_0$ and $k''_0 = \omega''/V_0$. Neglecting backward scattering and assuming that variation in Γ_2 in the z-direction is small similar to that of U, we introduce $A(r_\perp) \equiv \int_{-\infty}^{\infty} R(\mathbf{x}_\perp, z)dz$. Here, $r_\perp \equiv \sqrt{x^2+y^2}$ is the transverse distance, and R refers to the

autocorrelation function (ACF) of the random heterogeneity (e.g., Equations 1.1, 1.3). We can then rewrite Equation 2.4 as:

$$2i\partial_z\Gamma_2 - \frac{k_d}{{k_c}^2}\Delta_{\perp d}\,\Gamma_2 + 2i{k_c}^2\left[A(0) - A(\mathbf{x}_{\perp d})\right]\Gamma_2 + \frac{1}{2}i{k_d}^2\left[A(0) + A(\mathbf{x}_{\perp d})\right]\Gamma_2 = 0 \quad (2.5)$$

where $k_c \equiv \frac{\omega_c}{V_0} \equiv \frac{(\omega'+\omega'')}{2V_0}$; $k_d \equiv \frac{\omega_d}{V_0} \equiv \frac{(\omega'-\omega'')}{V_0}$; $\mathbf{x}_{\perp c} \equiv \frac{(\mathbf{x}'_\perp+\mathbf{x}''_\perp)}{2}$; $\mathbf{x}_{\perp d} \equiv \mathbf{x}'_\perp - \mathbf{x}''_\perp$ and $\omega_d \ll \omega_c$. Finally, using the factorisation $\Gamma_2 = {}_0\Gamma_2 \mathrm{e}^{-A(0)k_d^2 z/2}$, we get the final master equation for ${}_0\Gamma_2$:

$$\partial_z\ {}_0\Gamma_2 + i\frac{k_d}{2k_c^2}\Delta_{\perp d}\ {}_0\Gamma_2 + k_c^2[A(0) - A(r_{\perp d})]\ {}_0\Gamma_2 = 0 \quad (2.6)$$

where assuming that the randomness is isotropic, $r_{\perp d} \equiv |\mathbf{x}_{\perp d}|$. MS envelope is obtained in Markov Approximation by solving Equation 2.6 and performing the inverse Fourier transform. For the x component, this can be defined as:

$$\widehat{I}_{x0}(z,t,\omega_c) = \frac{1}{2\pi}\int_{-\infty}^{\infty} d\omega_d \mathrm{e}^{-i\omega_d(t-z/V_0)}\left[-\frac{\partial^2_{x_d}}{k_c^2}\ {}_0\Gamma_2(\mathbf{x}_{\perp d}, z, \omega_c, \omega_d)\right]_{\mathbf{x}_{\perp d}=0}. \quad (2.7)$$

Assuming that the randomness is isotropic, Equation 2.7 can be slightly modified to express the y component MS envelope as:

$$\widehat{I}_{y0}(z,t,\omega_c) = \frac{1}{2\pi}\int_{-\infty}^{\infty} d\omega_d \mathrm{e}^{-i\omega_d(t-z/V_0)}\left[-\frac{\partial^2_{y_d}}{k_c^2}\ {}_0\Gamma_2(\mathbf{x}_{\perp d}, z, \omega_c, \omega_d)\right]_{\mathbf{x}_{\perp d}=0}. \quad (2.8)$$

Correspondingly, the z component MS envelope is given as:

$$\widehat{I}_{z0}(z,t,\omega_c) = \frac{1}{2\pi}\int_{-\infty}^{\infty} d\omega_d \mathrm{e}^{-i\omega_d(t-z/V_0)}\left[\left(1+\frac{\Delta_\perp}{k_c^2}\right)\ {}_0\Gamma_2(\mathbf{x}_{\perp d}, z, \omega_c, \omega_d)\right]_{\mathbf{x}_{\perp d}=0}. \quad (2.9)$$

The reference intensity $\widehat{I}_0^R$ represents the three-component sum envelope. Thus, it is the total of all three components $\widehat{I}_0^R = \widehat{I}_{x0} + \widehat{I}_{y0} + \widehat{I}_{z0}$. Defined explicitly, it can be shown as:

$$\widehat{I}_0^R(z,t,\omega_c) = \frac{1}{2\pi}\int_{-\infty}^{\infty} d\omega_d \mathrm{e}^{-i\omega_d(t-z/V_0)}\ {}_0\Gamma_2(\mathbf{x}_{\perp d}, z, \omega_c, \omega_d)_{\mathbf{x}_{\perp d}=0}\ . \tag{2.10}$$

The validity of the Markov Approximation has been confirmed for example by comparing MS envelopes to those obtained using the finite difference method (FDM) simulation (e.g., Emoto et al. (2012)). Since the initial incident P wave is in the vertical direction, the transverse component MS envelope virtually reflects the scattering effect from the random heterogeneities in the medium. Thus, this theoretical P wave envelope synthesis well explains the origin of transverse component amplitude as a consequence of seismic wave scattering. Therefore conversely, this partitioning of energy into the transverse component offers a stochastic measure of small-scale medium heterogeneity (Sato, 2006). The original study of Sato (2006) considered a Gaussian type ACF, but the connection between scattering strength and transverse component excitation is clear. Kubanza et al. (2007) took this understanding and applied it to the real data by analysing observed MS envelopes at global seismic stations, more specifically the peak amplitudes of the P wave envelopes.

In this regard, the observed vertical, radial, and transverse component MS envelopes can be denoted as $\widehat{I}_Z$, $\widehat{I}_R$, and $\widehat{I}_T$, respectively. The proposed method is particularly interested in the transverse and the three-component sum envelopes' peak values, which we can express as $\left[\widehat{I}_T\right]^{peak}$ and $\left[\widehat{I}_Z + \widehat{I}_R + \widehat{I}_T\right]^{peak}$, respectively. The ratio of the former over the latter is defined as the peak-ratio $\Re$, that is:

$$\Re \equiv \frac{\left[\widehat{I}_T\right]^{peak}}{\left[\widehat{I}_Z + \widehat{I}_R + \widehat{I}_T\right]^{peak}} \ . \tag{2.11}$$

Under the description and notation given in Sato (2006) we have $\widehat{I}_T = \widehat{I}_{x0}$ or $\widehat{I}_{y0}$, $\widehat{I}_R = \widehat{I}_{y0}$ or $\widehat{I}_{x0}$, and $\widehat{I}_Z = \widehat{I}_{z0}$ with 3D infinite medium Gaussian type ACF and a plane wave case. Under this condition, peak-ratio approximates the randomness quantity of the medium as:

$$\Re \approx 1.81\frac{\varepsilon^2 h}{a} \ . \tag{2.12}$$

As explained in Section 1.1, the correlation distance a characterises the scale of medium heterogeneity. In simple terms, it controls the spatial distribution of individual patches of velocity heterogeneity. The root-mean-squared fractional fluctuation in velocity ε (normally given in percent) controls the amplitude of velocity heterogeneity contrast within the medium. The thickness of the heterogeneous medium is given by h. Thus, peak-ratio can also be used to describe the intensity of small-scale heterogeneity underneath the seismic station.

Peak-ratio computations both on a global scale (Kubanza et al., 2007) and on a regional scale (Nishimura, 2012) indicate an overall increase in peak-ratio with increasing frequency band. Furthermore, following Suzaki (2007) and Saito et al. (2002), we can link this frequency dependent behaviour of peak-ratio to the κ value of the von Karman type medium. Thus, the roll-off in the von Karman PSDF can be typified from the frequency dependency of peak-ratio. And by doing so, we can characterise the small-scale random heterogeneity particularly in terms of the abundance of the short-wavelength elements in the medium.

Here we show the derivation for measuring the frequency dependent behaviour of peak-ratio $\Re$. Particularly, we propose using the parameter called the frequency exponent

m. As we shall see, we can use this frequency exponent for characterising small-scale medium heterogeneity following its inverse relationship with κ. Therefore, there is an inherent link between $\Re$, m, and κ. In the following, we shall describe this connection in a more explicit manner. According to Suzaki (2007), peak-ratio follows the power law with respect to frequency in which

$$\Re = \beta(\varepsilon, a, h, \kappa) f_c^{\frac{4}{p(\kappa)}-2} \ . \tag{2.13}$$

In Equation 2.13, β corresponds to a constant of proportionality, and f_c is the central frequency. The parameter p is a function of κ defined in Saito et al. (2002). In the synthesis of MS envelope through von Karman type random media using Markov Approximation, p value controls the width/duration of seismogram envelope (Saito et al., 2002, 2005). Following the master equation, at a long distance r from the source, the MS envelope synthesis depends on the term $[A(0) - A(r_{\perp d})]$ where $r_{\perp d}$ is the distance on the transverse plane tangent to a sphere of radius r. According to Saito et al. (2002), this term is dependent on $B(r_{\perp d}/a, \kappa)$ which is defined as:

$$B(x,\kappa) \equiv \frac{2^{-\kappa+3/2}\sqrt{\pi}}{\Gamma(\kappa)} \left[\lim_{x\to 0}\left(x^{\kappa+1/2}K_{\kappa+1/2}(x)\right) - x^{\kappa+1/2}K_{\kappa+1/2}(x)\right] \ , \tag{2.14}$$

where K_κ is the modified Bessel function of the second kind of order κ (e.g., Abramowitz and Stegun (1972)), and Γ is the gamma function (e.g., Snieder and van Wijk (2015)). At small separation of $r_{\perp d}$ smaller than a, that is $x \ll 1$, we may approximate

$$B(x,\kappa) \approx C(\kappa)x^{p(\kappa)} \qquad\qquad x \ll 1 \ . \tag{2.15}$$

Here the parameter $p(\kappa)$ first appears as the exponent of transverse distance over the correlation distance ($x \equiv r_{\perp d}/a$), along with the parameter $C(\kappa)$. Both of these parameters can be estimated numerically by discretely varying κ in Equation 2.14 (Saito

et al., 2002).

Taking the log of both sides of Equation 2.13, we can write:

$$\log(\Re) = m \log(f_c) + \mathscr{A} \tag{2.16}$$

where $\mathscr{A}$ is a constant. In Equation 2.16 the parameter m emerges as the gradient of the log of $\Re$ with respect to frequency. Hence, we define the frequency exponent m which directly measures the frequency dependency of peak-ratio. Accordingly, following Equation 2.13 and 2.16, m is related to κ via the p value as:

$$m(\kappa) = \frac{4}{p(\kappa)} - 2 \ . \tag{2.17}$$

In Table 2.1 we present the estimates of p value given a discrete set of κ values. These numbers were obtained from the numerical evaluation of Saito et al. (2002). Following Equation 2.17, m can be calculated using the p value. And so, we also present these m estimates in Table 2.1. The corresponding plot of p value versus κ using the data from Table 2.1 is shown in Figure 2.1. The interpolated plot allows us to evaluate arbitrary data points that are not given in Table 2.1. Similarly, Figure 2.2 shows the associated plot of frequency exponent m versus κ. Thus, Figure 2.2 illustrates the inverse relationship between the frequency dependency of peak-ratio as represented by the frequency exponent, and the roll-off of the power spectra of von Karman type media as given by the κ value. In other words, we can theoretically convert m into κ. Therefore, the frequency exponent can potentially be a useful proxy for evaluating the roll-off of the power spectra of von Karman type random media, thus assisting the characterisation of small-scale medium heterogeneity at the evaluated seismic station. In this regard, large frequency exponent m values correspond to small κ values and therefore random media rich in short-wavelength components, whereas small frequency exponent m values correspond to large κ values and therefore random media poor in short-wavelength components.

2.2 Data Analysis Procedures for Estimating Peak-Ratio and its Frequency Dependency

Following Equation 2.11, we can calculate peak-ratio by obtaining the MS envelopes. To do so, we can follow the data analysis procedures outlined in Kubanza et al. (2007). They are:

1. *Bandpass filter* instrument response corrected seismic signals into separate frequency bands.
2. *Rotate* the vertical-NS-EW (ZNE) components into the vertical-radial-transverse (ZRT) directions.
3. Compute the *signal-to-noise ratio (S/N)* and discard any source-receiver pairs with ratio of less than ten.
4. *Square* the seismogram traces of the remaining pairs.
5. *Normalise* the squared seismograms.
6. *Stack* normalised seismograms to obtain the MS envelopes.

Each of these steps shall be explained further in the following.

Filtering

In seismogram data processing, filtering is commonly performed in terms of octave, where one octave is the doubling of frequency (Havskov and Ottemöler, 2010). For example, Kubanza et al. (2007) implemented the frequency bands of 0.5-1, 1-2, and 2-4 Hz. While Nishimura (2012) and Ganefianto et al. (2021) used the 0.5-1, 1-2, 2-4, and 4-8 Hz bands. In accordance to the previous studies, here we use the Butterworth bandpass filter to classify our data into four separate frequency bands: 0.5-1, 1-2, 2-4, 4-8 Hz.

Following Kanasewich (1981) and Havskov and Ottemöler (2010) a Butterworth low-pass filter amplitude response can be expressed by:

$$B_L(f) = \frac{1}{\sqrt{1 + (f/f_0)^{2n}}} \ . \tag{2.18}$$

The cut-off frequency is given as f_0, and n is the order of the Butterworth filter. Furthermore, Kanasewich (1981) stated that a Butterworth highpass filter is equivalent to the subtraction of the lowpass filter from one, giving:

$$B_H(f) = \frac{1}{\sqrt{1 + (f_0/f)^{2n}}} \ . \tag{2.19}$$

A bandpass is therefore the combination of both lowpass and highpass filters (Kanasewich, 1981). Filtered data in each frequency band is to be treated individually. In other words, the rest of the procedures shall be applied to each frequency band separately.

Rotating Seismogram Components

As per Equation 2.11, it is imperative that our signals correspond to the vertical, radial, and transverse components. Particularly for the real dataset, data were typically acquired in terms of vertical, north-south and east-west components instead. Therefore, we need to rotate our seismogram data from the available north-south and east-west components into the radial and transverse components.

The component rotation is defined according to the coordinates of the station and the source. The radial and transverse amplitudes can be computed from the NS and EW amplitudes using:

$$\text{Radial} = -\text{NS}\ \cos(\varphi) - \text{EW}\ \sin(\varphi) \ , \tag{2.20}$$

$$\text{Transverse} = \text{NS}\ \sin(\varphi) - \text{EW}\ \cos(\varphi) \ . \tag{2.21}$$

The back-azimuth φ is the angle between North and the direction from the station towards the source (Havskov and Ottemöler, 2010). Figure 2.3 shows a diagram defining the transverse and radial directions, as well as φ used to rotate the seismogram data.

Signal-to-Noise Ratio

Often, acquired seismic data can be noisy. We discard noisy data by calculating the S/N of the (rotated) seismograms. To calculate S/N, first we need to specify the signal and noise time-windows. With regard to real dataset, we can define these time-windows in relation to the expected P arrival according to the ak135 earth-model (Kennett et al., 1995). For example, we set the signal time-window to be a 20 s window commencing from the expected P arrival. Correspondingly, the noise time-window is set to be a 15 s window prior to the expected P arrival. The ak135 earth-model is commonly used because it has been shown to demonstrate significantly better fit compared to other earth-models such as iasp91 and sp6 models, for a broad range of phases (Kennett et al., 1995). And it has been widely used, for example, as the global reference model in the 3D teleseismic tomography studies of the Murray Basin, southeast Australia (Rawlinson et al., 2006).

For each seismogram, S/N is computed by taking the square of the amplitude data and integrating it over the time-windows. The ratio of the results for the signal window over the noise window is the S/N or:

$$S/N = \frac{\int_0^{T_{signal}} u(t)^2 dt}{\int_0^{T_{noise}} u(t)^2 dt} \ . \tag{2.22}$$

The time-windows for the signal and the noise are denoted as T_{signal} and T_{noise}, respectively, and $u(t)$ is the trace data. Any source-receiver pairs with S/N$<$10 in any of the three components are to be removed from the analysis.

Squaring Seismograms

So far, the steps involved are mainly concerned with preparation and data quality assessment. Now in this step, the aim is to actually obtain the squared seismogram envelope for each component and for individual source-receiver pairs. The squared envelope is given in Kubanza et al. (2007) as:

$$e_j(t) = u_j(t)^2 + \mathscr{H}\left[u_j(t)\right]^2 \tag{2.23}$$

where $u_j(t)$ is the trace signal of the j component in which j corresponds to the vertical, radial, or the transverse component. $\mathscr{H}$ denotes the Hilbert transform. Following Sato et al. (2012), $u(t)$ can be written in Fourier integral as,

$$u(t) = \frac{1}{2\pi}\int_{-\infty}^{\infty} \hat{u}(\omega)\ \mathrm{e}^{-i\omega t} d\omega \tag{2.24}$$

from which the Hilbert transform can then be expressed as,

$$\mathscr{H}[u(t)] = \frac{1}{2\pi}\int_{-\infty}^{\infty} \hat{u}(\omega)\ \mathrm{e}^{-i\omega(t+|\pi/(2\omega)|)} d\omega\ . \tag{2.25}$$

Figure 2.4 illustrates the process of obtaining the seismogram envelope. The example is given for a simulated seismogram at a depth of 6600 m from a flat surface, using a vertically incident plane P wave source. Shown is for one of the horizontal components at a frequency band of 4-8 Hz. Notice that there is a phase difference of $\pm\pi/2$ between the original trace (black line in Figure 2.4) and the Hilbert transformed trace (blue dotted line in Figure 2.4). The envelope of the seismogram is given by $\sqrt{u(t)^2 + \mathscr{H}[u(t)]^2}$ (green line in Figure 2.4). Thus as per Equation 2.23, the square of this envelope trace is the final output of this step, giving us the squared seismogram envelope, which we illustrate in the bottom panel of Figure 2.4.

Normalisation

Especially when analysing real data, we are dealing with earthquake records of varying hypocentral distances and magnitudes. Therefore, their squared seismogram envelopes need to be normalised. The normalised squared seismogram envelope is given in Kubanza et al. (2007) as:

$$E_j(t) = \frac{e_j(t)}{\bar{E}_0} \tag{2.26}$$

where j is the vertical, radial, or the transverse component. $\bar{E}_0$ is the normalisation factor defined in Kubanza et al. (2007) as:

$$\bar{E}_0 = \frac{1}{T}\left[\int_0^T e_{\text{vertical}}(t')dt' + \int_0^T e_{\text{radial}}(t')dt' + \int_0^T e_{\text{transverse}}(t')dt'\right] \tag{2.27}$$

where T is the normalisation time-window. The chosen time-window should include the key characteristics of the envelope described in Kubanza et al. (2007). Namely, it should be long enough to show the equi-partition of energy into all three components in the later coda as a consequence of scattering. On the other hand, it should exclude direct S wave arrival.

Stacking

Stacking is the final step in the procedures to obtain the MS envelopes. Specifically, the aim is to get a set of three representative seismogram envelopes corresponding to the three components. When analysing real dataset, the three envelopes will be associated with a single seismic station. In this regard, only receivers which hold data from more than ten sources are kept in the process. For each component, the squared seismogram envelopes at these stations are lined up with respect to their expected P arrival time. Their amplitudes are then stacked or averaged according to time in order to get the mean of the squared envelopes. Thus, the MS envelope for each component is obtained at a

particular station.

In a simulated situation, we can stack stations at similar distances from the same source. Hence, their arrival times are also at a similar lapse-time (i.e., we do not need to line up the traces as is the case when analysing real dataset). Accordingly, the MS envelopes of the three orthogonal components may not correspond to a single station, but rather, they may represent envelopes at a particular distance.

The stacking process is illustrated in Figure 2.5. The example is shown using simulated data from 58 stations at an equal depth of 6600 m from a flat surface, at a frequency band of 4-8 Hz. In Figure 2.5, the thick black line in the vertical z component corresponds to $\widehat{I}_Z$. The vertically incident source used in this particular example means that either thick black lines from the two horizontal components can interchangeably correspond to $\widehat{I}_T$ and $\widehat{I}_R$. Henceforth, from these MS envelopes we can compute the peak-ratio using Equation 2.11.

With regard to the frequency exponent calculation in data analysis, the peak-ratios evaluated under multiple frequency bands are to be used. More specifically, frequency exponent can be estimated by plotting the log of peak-ratio $\Re$ versus the log of central frequency f_c, from which, Equation 2.16 can be found via least-squares fitting.

For example, for the frequency bands evaluated in this study, f_c corresponds to 0.75, 1.5, 3.0, and 6.0 Hz for the 0.5-1, 1-2, 2-4, and 4-8 Hz band, respectively. The peak-ratio axis should then correspond to the $\Re$ values evaluated at each respective frequency band. Following Equation 2.16, the gradient of the best-fit line through the resulting plot is therefore, the estimated frequency exponent m. More practical examples of frequency exponent calculation will be given in subsequent chapters.

2.3 Seismic Wave Propagation Simulation for Numerical Evaluation of Peak-Ratio and its Frequency Dependency

In previous sections of this chapter, we have laid out how small-scale medium heterogeneities can be described through the calculation of peak-ratio and its frequency dependency. However, their implementation hitherto assumes an infinite random medium. And even though Emoto et al. (2010, 2012) have confirmed the validity of the approach for stations on the ground surface, the significance of the free-surface with regard to borehole stations is yet to be investigated. Furthermore, the effect of surface topography on peak-ratio and its frequency dependency is still poorly understood.

Therefore, in order to understand better the ramifications surrounding the presence of free-surface and topography on the computation of peak-ratio and its frequency dependency, we perform 3D simulations of seismic wave propagation. For its implementation, we apply the finite difference method (FDM). Specifically, we use the staggered-grid 3D FDM implementation proposed by Maeda et al. (2017) named OpenSWPC.

It is necessary to first introduce the methodology and theory behind the applied FDM approach. Later, we shall present numerical simulation outputs with regard to cases addressing the free-surface effect, and cases addressing the topographic effect.

2.3.1 3D Staggered-Grid Finite Difference Method

FDM is a widely used numerical modelling approach to simulate the propagation of seismic waves. Frankel and Clayton (1986) numerically studied seismic scattering including the excitation of coda waves by implementing 2D FDM simulations of wave propagation in random heterogeneous media. Furthermore, MS envelopes derived using the FDM simulation have been shown to be in agreement to those derived using the Markov ap-

proximation, for the case of vertically incidence plane wave through layered random elastic media with Gaussian ACF (Emoto et al., 2012). In other words, FDM simulation has been used to confirm the validity of Markov approximation.

Applications of 3D staggered-grid FDM simulation have also been shown to be fruitful for studying the seismic wave field under various local and regional settings. Nakamura et al. (2012) demonstrated the importance of appropriate boundary conditions for an accurate synthesis of seismic waveforms by incorporating ocean-bottom topography and a seawater layer in their FDM simulation of suboceanic earthquake. Ripperger et al. (2003) studied the influence of the free-surface topography of a volcano on the seismic wave field using the Merapi volcano topographical model. Takemura et al. (2015a) distinguished between high-frequency scatterings that were formed due to the irregular surface topography and those formed due to the small-scale velocity heterogeneity of the subsurface.

In the staggered-grid FDM simulation, seismic wave propagation in viscoelastic media can be modelled by solving the equation of motion of continuum mechanics. The equation can be expressed in terms of velocity and stress components as:

$$\rho \frac{\partial v_i}{\partial t} = \sum_{j=1}^{N_D} \frac{\partial \sigma_{ij}}{\partial x_j} + f_i \ , \tag{2.28}$$

where N_D is model dimension, in other words, for a three-dimensional case, $N_D = 3$; v_i is the particle velocity of the elastic motion in the i^{th} component; σ_{ij} is the $(i,j)^{th}$ component of the stress tensor; f_i is the i^{th} component of the body force; and ρ is density.

In the scheme proposed in Maeda et al. (2017), the generalised Zener body is adopted to model the viscoelastic body. A Zener body is a serial connection of a spring, and a parallel connected spring and dashpot. A generalised Zener body is the parallel connection of L number of Zener bodies with different relaxation times of stress τ_σ, and of strain τ_ϵ.

Solving Equation 2.28 requires us to define the constitutive equation which relates the

stress to the particle velocity. The constitutive equations given in Maeda et al. (2017) are:

$$\frac{\partial \sigma_{ii}}{\partial t} = \left[(\lambda_R + 2\mu_R)\left(1+\tau^P\right) - 2\mu_R\left(1+\tau^S\right)\right] \times \sum_{k=1}^{3} \frac{\partial v_k}{\partial x_k} + 2\mu_R\left(1+\tau^S\right)\frac{\partial v_i}{\partial x_i} + \sum_{\ell=1}^{L} r_{ii\ell} \ ,$$

$$\frac{\partial \sigma_{ij}}{\partial t} = \mu_R\left(1+\tau^S\right)\left(\frac{\partial v_i}{\partial x_j} + \frac{\partial v_j}{\partial x_i}\right) + \sum_{\ell=1}^{L} r_{ij\ell} \quad \text{for } i \neq j \ , \tag{2.29}$$

where $\pi_R \equiv \lambda_R + 2\mu_R$ and μ_R are the relaxed moduli, while τ^P and τ^S are the relaxation times for P and S waves, respectively. The memory variable $r_{ij\ell}$ (Robertsson et al., 1994; Maeda et al., 2013) is then introduced. The memory variable equation is shown in Maeda et al. (2013) in a time-marching system as:

$$\frac{\partial r_{ij\ell}}{\partial t} = -\frac{1}{\tau_{\sigma\ell}}\left\{r_{ij\ell} + \left[(\lambda_R + 2\mu_R)\tau^P - 2\mu_R\tau^S\right] \times \partial_k v_k \delta_{ij} + \mu_R\tau^S(\partial_i v_j + \partial_j v_i)\right\} \tag{2.30}$$

The equation of motion (Equation 2.28) and the constitutive equation with memory variable (Equation 2.29 and 2.30) are to be solved numerically based on a staggered-grid FDM with second-order accuracy in time and fourth-order accuracy in space. In the unit cell containing the discretised-wavefield variables, the centre consists of the normal-stress components, and the sides consists of the shear-stress components and the particle velocity (Nakamura et al., 2012). The first-order Crank-Nicholson method (Robertsson et al., 1994) is used to explicitly solve the constitutive equation with memory variable. The explicit solution, for example, can be found in Maeda et al. (2013), where numerical simulation forward in time is performed using explicit discretization formula.

2.3.2 The Effect of Free-Surface Interaction on the Estimation of Peak-Ratio and its Frequency Dependency

In this section, the aim is to understand how the inclusion of a flat free-surface may influence the estimation of peak-ratio and its frequency dependency. This is important especially when borehole stations are used. The simulation setting can be described in terms of the computational model/grid parameters, the source condition, and the receivers array configuration.

First, for our model grid, we set up $512 \times 512 \times 512$ grid points, separated by 0.05 km, for a total model extent of 25.6 km in length, width, and depth each. Small-scale random heterogeneities are imposed onto the simulation model according to the von Karman type random media, with background P and S wave velocities of 5 km/s and 2 km/s, respectively, correlation distance a of 0.5 km, and root-mean-squared fractional fluctuation in seismic velocity ε of 5% (Yoshimoto et al., 1997; Yamanaka and Yamada, 2006; Takemura et al., 2015a). We perform our simulations using three different κ values: $\kappa = 0.1$, $\kappa = 0.3$, and $\kappa = 0.6$. The model's top boundary condition is defined by a flat free-surface. For the side boundary condition, an appropriate absorbing boundary condition is required to minimise artificial reflections from the computational model side boundaries. We use the Perfectly Matched Layer (PML) boundary setting of the OpenSWPC code (Maeda et al., 2017).

With regard to the source, we introduce a vertically incident plane P wave of the Kupper wavelet near the bottom of the simulation model. Because of this vertical incidence, the transverse direction can be defined as either of the horizontal components. To simulate the different frequencies, we can change the wavelength of the P wave source. We set wavelengths of 8, 4, 2, and 1 km which correspond to the maximum frequencies of 1.2, 2.4, 4.8, and 9.6 Hz, with regard to the OpenSWPC simulation output, respectively. Bandpass-filtered seismograms from these simulation runs thus represent synthetic dataset at the 0.5-1, 1-2, 2-4, and 4-8 Hz frequency bands, respectively.

We set up two receivers arrays, one covering the whole extent of the computational model, and one that is focused near the centre of the computational model as shown in Figure 2.6. For the former, we define a 7×7 array, spaced at every 4 km. For the latter, we define a 3×3 array, spaced at every 2 km. This configuration also helps minimise the effect of artificial reflection from the model side boundaries. Both arrays are then duplicated with respect to depth, down to the depth of 10 km. In Figure 2.6a, the lateral extent of the model is being covered by the 7×7 array, while another 3×3 array surrounds the centre of the model. Figure 2.6b illustrates the extension of these arrays with respect to depth (shown are for the 7×7 array). Especially, in relation to the vertically incident plane P wave initiated near the bottom of the random heterogeneous model.

By using this configuration, we can approximate the ensemble averaging process. Ideally, to obtain a synthetic envelope using numerical simulation, one would want to stack over an ensemble of many random medium realisations. In other words, ideally one would stack synthesised envelopes obtained through the many different realisations of heterogeneities with the same random medium parameters, for example, by using numerous random number seeds. However, such a way would require a significant number of simulation runs and would be very time consuming. Since the randomness of the heterogeneity is assumed to be isotropic, and because we are primarily interested in evaluating the effect of the free-surface on borehole stations, in other words, we are primarily concerned with station depth, we stack synthesised envelopes obtained at stations with the same depth. Thus, this gives us synthetic MS envelopes at different depths.

There are two main characteristics of the simulation results. One is that as the incident wave travels up-wards through the random heterogeneous medium, the wavefront is being distorted due to scattering off the small-scale heterogeneities (Figure 2.7). Secondly, after the initial wave hits the free-surface, we see the reflected wave propagating down-ward. This development of down-going surface reflected phase is a significant mechanism, as it turns out to have a strong impact on MS envelope amplitude.

More specifically, the down-going surface reflected wave may interfere with the up-going incident wave. Moreover, we observe that at specific depths of a quarter of the wavelength, the up-going and down-going waves are out of phase hence interfere destructively (Figure 2.7). As a consequence, this diminishes the amplitude of the vertical component MS envelope, hence inflating the overall peak-ratio.

Some P-to-S conversions are visible in the shallow depths following the free-surface interaction (Figure 2.7 panel number 5). But this conversion seems to matter very little to the transverse component contribution, aided by the fact that the colouring gives no information with regard to the amplitude.

The observation of wave interference especially the destructive interference between the up-going incident and down-going surface reflected waves is an important finding not least because it is difficult to incorporate such mechanism into envelope modelling. In the following we will describe with more specifics, how this mechanism may affect the estimation of peak-ratios and their frequency dependency.

Figure 2.8 gives an example of how the free-surface effect may influence the peak-ratio estimation at a specific station depth. At a station depth of 6600 m, the stacked MS envelopes show two main pulses representing the initial up-going incident wave and the down-going surface reflected wave at a later lapse-time. In such kind of situation, the impact from the free-surface is virtually non-existent as the two phases are clearly separate. For this particular example, peak-ratio is estimated to be approximately 0.05 which is also roughly equal to 1.81 times $\varepsilon^2 h/a$ of the simulation model ($\varepsilon = 5\%$, $a = 0.5$ km, $h \approx 5$ km). Similarly, we see minimal impact from the free-surface for stations located on the ground surface because the two phases are completely in-phase rather than out of phase hence no destructive interference.

However at station depth of 300 m, which is close to a quarter of the wavelength used for the frequency band shown in this particular example (4-8 Hz), the impact from the free-surface is significant. At this depth, the up-going incident phase and the down-

going surface reflected phase are out of phase and interfere destructively. As a result, the vertical MS envelope shows a diminished amplitude and contribution to the three-component sum MS envelope is dominated by fluctuations in the horizontal components (Figure 2.8). The resulting peak-ratio estimate is 0.5 which is ten times larger than the case for a deep station depth. We can expect similar effects at different depths depending on the frequency band.

The overarching result of this free-surface effect is how the frequency exponent might be affected due to the contamination of peak-ratio (raised/inflated/overestimated value) at a specific frequency band. The affected peak-ratio thus depends on the depth of the station in connection to the dominant frequency (wavelength) of the source. Figure 2.9 shows the principle cases of this free-surface effect on the estimation of frequency component. For example, as we mentioned, at very deep station depth, the free-surface effect is virtually non-existent, hence, the plot of $\log \Re$ versus $\log f_c$ can be approximated by a straight line (Figure 2.9a, station depth equals to 9.8 km). Furthermore, for this example, the simulation was performed using $\kappa = 0.1$. According to Suzaki (2007) relation, this corresponds to an m value of 1.36 (Table 2.1), which is not too far from the estimated value according to the simulation at depth ($m = 1.23$, Figure 2.9a). At much shallower depths, however, we are seeing the significance of the free-surface effect. At station depth of 2 km, the interference effect occurs at the low frequency band, thus inflating the peak-ratio estimate for that frequency. Hence, the overall frequency exponent is underestimated as a whole at $m = 0.53$ (Figure 2.9b). Estimation of frequency exponent without using the affected low frequency band peak-ratio returns an m value of 1.50, which is much closer to the estimate at depth and that according to Suzaki (2007) relation. At station depth of 1.0 km, it is the peak-ratio at the mid frequency band that is contaminated (Figure 2.9c). Estimated frequency exponent using peak-ratios from all frequency bands is 1.54, whereas if we discard the contaminated peak-ratio value, the estimated frequency exponent is 1.87. Though the impact at this depth is more sub-

dued, the contaminated peak-ratio means that the fit of the frequency trend-line is not so good. On the other hand, at station depth of 0.2 km, the peak-ratio estimate at the high frequency band is raised due to the free-surface effect. Hence, the overall frequency exponent is overestimated at $m = 2.89$ (Figure 2.9d). Removing the contaminated high frequency band peak-ratio from the frequency exponent calculation gives $m = 1.70$, which is much closer to the estimate at depth and that according to Suzaki (2007) relation.

In Figure 2.10 we show the overall implication of the free-surface effect on the frequency exponent with respect to depth. Because of the vertically incident source, each horizontal component can be taken as the transverse component, hence peak-ratio as well as the frequency exponent can be computed twice for every κ for each point in depth, in other words, six data points of m per depth in Figure 2.10. According to our simulation results, regardless of the κ value used in the simulation, there is a large fluctuation in frequency exponent at shallow depths as a result of the free-surface effect. More specifically, at depths greater than 5 km, m values are relatively stable with respect to depth as there is no effect from the free-surface. In other words, at these depths, frequency exponent reflects the random medium heterogeneities more rigorously. On the other hand, frequency exponents at depths of less than 1 km are overestimated in comparison, because of the contamination by the free-surface with regard to peak-ratio at high frequency. In a similar manner, frequency exponents at depths around 2 km are underestimated because of the contamination by the free-surface with regard to peak-ratio at low frequency.

An important observation is that with increasing κ there is an overall decrease in frequency exponent (Figure 2.10). The extent of this decrease, however, is not as strong as what is predicted by Suzaki (2007), even though the relation seems to reasonably match the numerical results for $\kappa = 0.1$ especially at deep depths. Therefore, we need to be careful when using Suzaki (2007) relation for converting m into κ, especially at small m values.

However, assuming a constant depth, relative differences in frequency exponent do

reflect changes in κ value. In other words, it is clear that there is an inverse relationship between frequency exponent and κ. Indeed quantitatively speaking, there is a strong fluctuation with respect to depth due to the free-surface effect. But at any given depth, frequency exponent typically decreases with increasing κ. Therefore, two stations with similar depths experience a similar extent of the free-surface effect. Hence, any remaining variation in terms of frequency exponent reflects the different characteristics of heterogeneities in the random medium at those stations. Henceforth, to mitigate the free-surface effect in interpreting peak-ratios and their frequency dependency at borehole stations, it is better to compare stations at similar depths (strictly speaking, station depth in relation to the seismic wavelength).

2.3.3 The Effect of Topography on the Estimation of Peak-Ratio and its Frequency Dependency

Through FDM numerical simulation, we would also like to examine the impact of irregular surface topography on scattering. Such understanding is especially important when analysing peak-ratio and its frequency dependency at stations located in areas dominated by strong topographic irregularities, for example, at (active) volcanoes. And so, in this section, we investigate the effect of volcano topography on the estimation of peak-ratio and its frequency dependency using simulated data.

The crux of model parameter settings is brought over from the previously described simulations examining the effect of the free-surface (Section 2.3.2). Specifically, we use the same source specification of vertically incident plane P wave of the Kupper wavelet at varying wavelengths, initiated near the bottom of the simulation model. The computational model size is also the same at $512 \times 512 \times 512$ grids spaced at every 0.05 km. The PML absorbing boundary condition is also applied. Random velocity fluctuation corresponding to a von Karman type medium is imposed, with κ of 0.8, ε of 10% and a of 4 km (Saito et al., 2005).

The numerical simulations can be differentiated according to the following main classifications. The first is the frequency band of the simulation which we control by changing the wavelength of the source. This is similar to the previous set of simulations where we have 0.5-1, 1-2, 2-4, and 4-8 Hz frequency bands. The second classification is whether we incorporate a topographic model for our surface condition, or to set a flat free-surface condition. For the former, the volcano topography of Mount Fuji (elevation 3,776 m National Catalogue of the Active Volcanoes in Japan (2013)) is used. Specifically, we make use of the ground surface (top layer) structure of the Japan Integrated Velocity Structure Model (JIVSM) which follows the ETOPO1 topography model. Therefore, we explicitly arrange for two sets of simulations where the only difference between them is their surface conditions (one is a flat surface while the other is a volcano topography). By doing so, we can attribute variations in the resulting peak-ratio and frequency exponent computations to the inclusion of volcano topography. In this regard, the summit is placed at the centre of the simulation model. Hence we assume that the radial component is in the outward direction from the model centre, because of the vertically incident simulation source.

With regard to array configuration, we set up stations at discrete radius of 2, 4, 6, 8, and 10 km from the model centre and thus the summit. Figure 2.11a shows this array configuration for the case of simulation type with topography, though the same array positioning is also used for the case with a flat surface. Figure 2.11b illustrates the array configuration in relation to the vertically incident plane P wave source initiated near the bottom of the random heterogeneous model for both flat surface and topography cases.

Figure 2.12 shows some snapshots of numerical simulation result with topography. In this regard, topography may act like extra scatterers that deflect the vertically incident wave into the horizontal components. Thus, the topography of the summit area is the most significant feature of this simulation, as its steep gradient can easily trap the incoming waves and generate strong horizontal motions. This topographically induced scattering is the strong contribution of transverse component motion to the three-

component sum MS envelope even at lower frequencies. Figure 2.13 shows an example of MS envelopes at a station 2 km away from the model centre/summit. With the inclusion of topography, large transverse (and radial) MS envelopes are developed, demonstrating that a significant portion of the three-component sum MS envelope is made up by the horizontal motions. On the contrary, for a flat surface case, the three-component sum MS envelope is dominated by the vertical motion.

We can observe that the contrast in topography is more significant at stations nearer to the summit (radius $<$ 5 km horizontally from the summit), as the ground surface is flattening far away from the summit (radius $>$ 5 km horizontally from the summit). In other words, we can expect the significance of the topographic effect to be more prevalent at these near summit stations compared to the far-away stations. Therefore, we differentiate stations into near and far-away stations. At each of these stations, we calculate its peak-ratios for the case with and without topography and plot them on a linear graph. Thus, the point should adhere to the 1:1 line where topographic effect is weak. In Figure 2.14 we show these comparisons of peak-ratio estimates at individual stations between the (simulation) case with volcano topography ($\Re_{topo}$) and the (simulation) case with a flat surface ($\Re_{flat}$). The panels in Figure 2.14 are classified according to frequency band and whether the stations belong to the near or far-away group. We see that $\Re_{topo}$ is larger overall when compared to $\Re_{flat}$ especially for the near stations at the low frequencies. Critically however, such implication is less conspicuous in the far-away stations for the same frequencies as shown by their correlation coefficient. Accordingly, the adherence to the 1:1 line is much more exact for the far-away stations at the low frequencies. This is because the spread of the scatter-plots increases with frequency. This could be because stronger scattering off the medium heterogeneities at high frequencies introduces stronger fluctuation in the data and masks the contribution of topographic scattering.

To assess the topographic effect further, we estimated the deviation from the 1:1 line

by calculating the average difference in peak-ratio ($\overline{\Re_{flat}} - \overline{\Re_{topo}}$). The negative values implies that topography increases the peak-ratio estimates. Crucially though, we see a greater contrast between the near stations group and the far-away stations group in the low frequencies particularly in the 1-2 Hz band (average difference of -0.14 in the near stations as opposed to -0.02 for the far-away stations). In other words, topographic effect seems to be more effective in increasing peak-ratio in this low frequency band. This could be connected to the general increase in scattering with frequency which could conceal the significance of topographic scattering, and the characteristic scale of topography in relation to the seismic wavelength, which can affect the effectiveness of topographic scatterings.

In summary, the inclusion of topography may increase peak-ratio and this is more significant at the near stations. Our simulation also shows that such impact seems to be more effective in the low frequencies. As a result of these observations, frequency exponent is reduced by the inclusion of topography, and the effect is more significant at stations near the summit compared to those far away from the summit.

Figure 2.15 shows the comparison in frequency exponents obtained from the two sets of numerical simulations with contrasting surface conditions. For stations far away from the summit where topographic effect is expected to be less prominent, the contrast in frequency exponents between the flat simulation case and the simulation case with topography is less significant. This is shown by the relatively weak scatter and a reasonably strong positive correlation with a correlation coefficient of 0.79, in other words, the plot follows the 1:1 line relatively closely. On the other hand, at stations close to the summit, we can see stronger scatter in the plots hence weaker correlation coefficient. It also includes clusters above the 1:1 line indicating that the inclusion of topography may lower frequency exponent estimation. Similarly, to estimate the deviation from the 1:1 line, we calculate the average difference in frequency exponents ($\overline{m_{flat}} - \overline{m_{topo}}$). The result shows positive 0.2 for the close stations group. In other words, frequency exponents estimated

from the simulations with topography are smaller on average compared to those obtained from the simulations with a flat surface condition, particularly at stations where there is a more imposing topographic contrast. This indicates that topography may reduce frequency exponent estimates.

2.4 The Effects of Changing Random Medium Parameters

In this section we shall look at how changing the random medium parameters of ε, a, and κ can affect peak-ratio and frequency exponent estimations, particularly using simulation settings used for investigating the topographic effect.

2.4.1 The Effects of Changing ε and a on Peak-Ratio

Here we show a range of random medium parameters used in the simulations addressing the topographic effect. They can be useful for clarifying the significance of medium parameters and topography. For both simulation cases with a flat surface and topography, first we look at how changing ε affects the distributions of peak-ratios from the numerically simulated data, by fixing all other simulation settings. Then, we do the same for a.

First, a range of ε values ($\varepsilon = 5\%, 10\%, 20\%$) are tried while keeping a equals to 4 km and with $\kappa = 0.8$. Peak-ratios are computed from the synthesised data at individual stations. We show the distributions of these peak-ratios in Figure 2.16. The main key feature to be observed from Figure 2.16 is that with increasing ε, peak-ratios ostensibly increase as well. We move from a range of $0.04 - 0.10$ in terms of average peak-ratios across all frequency bands for the case of $\varepsilon = 5\%$, to a range of $0.13 - 0.26$ for the case of $\varepsilon = 10\%$ and $0.34 - 0.43$ for the case of $\varepsilon = 20\%$. This feature can be explained by the relationship between peak-ratio and ε, where according to Equation 2.12, peak-ratio

is proportional to ε^2 assuming an infinite random medium.

The peak-ratios estimated from these simulations seem to well overestimate values calculated using Equation 2.12. Simulated values were obtained with a von Karman type distribution, but Equation 2.12 assumes a Gaussian type random fluctuation which lack in small-scale heterogeneities of the short-wavelength components. It is also worth mentioning that the simulation cases with topography surface condition are also mostly showing larger values compared to their counterparts with the flat free-surface condition. This suggests additional or stronger transverse component excitation as a result of topography.

Similarly, we tried a range of a values while keeping ε equals to 10% and with $\kappa = 0.8$. Figure 2.17 shows the distributions of estimated peak-ratios at $a = 0.5$ km, $a = 4$ km and $a = 8$ km. Increasing a from 4 to 8 km does not seem to introduce much changes to the resulting distributions. The range in terms of average peak-ratios across all frequency bands stays at $0.13 - 0.26$. Decreasing the a value to 0.5 km does seem to be more impactful. Specifically, it increases peak-ratio estimates at large frequencies (e.g., increasing averages from about $0.18 - 0.23$ to about 0.27 at 2-4 Hz, and from about $0.21 - 0.24$ to about $0.34 - 0.37$ at 4-8 Hz). This may be explained by Equation 2.12 where peak-ratio is inversely proportional to a. At low frequencies, however, estimated peak-ratios are very small, especially in the 0.5-1 Hz frequency band. This seems to be linked instead to the generally low scattering coefficient with regard to the small a value but with a relatively long wavelength. Similarly, the simulation cases with topography surface condition generally show larger values compared to their counterparts with the flat free-surface condition.

2.4.2 The Effect of the Hurst Exponent κ on the Frequency Dependency of Peak-Ratio

With regard to the use of the von Karman type random media, their κ values has been linked to the frequency dependency of peak-ratio which we measured in terms of the frequency exponent m. Thus, the role of κ is tested particularly with regard to their influence on peak-ratios and their frequency dependency, by comparing simulation results using $\kappa = 0.6$ and $\kappa = 0.8$. a and ε were fixed at 0.5 km and 10%, respectively.

Figure 2.18 shows the distributions of estimated peak-ratios using $\kappa = 0.6$ and $\kappa = 0.8$ at the four frequency bands. Overall, changing the κ value does not seem to change the peak-ratio distributions much. Averages of the distributions generally increase from $0.02 - 0.03$ at 0.5-1 Hz, to $0.09 - 0.13$ at 1-2 Hz, to $0.24 - 0.27$ at 2-4 Hz, to $0.34 - 0.37$ at 4-8 Hz. However, the impact of κ value can be seen when comparing their distributions of frequency exponent m values (Figure 2.19). Results from larger κ value show smaller distributions of frequency exponents. Increasing the κ value reduces the frequency exponent on average for both simulation cases with a flat free-surface and topography surface conditions. This inverse relationship between frequency exponent and κ is expected by previous studies. It is also worth mentioning that in both κ cases, inclusion of topography reduces the average values of frequency exponent (Figure 2.19), suggesting that topographic effect may reduce the frequency dependency of peak-ratio.

The frequency exponents estimated from these simulations, however, seem to well overestimate values according to Suzaki (2007) relation (Figure 2.19). We speculate that there is some limitation with regard to Suzaki (2007) findings on the effect of small-scale heterogeneity on seismogram envelope synthesis especially at large κ values, prompting us to be careful when using the relation to convert κ into m and vice-versa, as we have already pointed out.

The observed topographic effect should compel us to consider the level of topographic irregularities surrounding the seismic stations when examining their peak-ratios and the

frequency dependency. This may not be entirely straightforward to appraise. Instead, we suggest looking at station elevation as a proxy. Stations installed at higher elevations would most likely be located on mountainous areas where there is a strong presence of topography. Therefore, we can expect the topographic effect to be stronger at these stations. Thus, to mitigate the topographic effect in interpreting peak-ratios and their frequency dependency, it is better to use stations of similar installation heights or elevations.

2.5 Summary

The peak-ratio $\Re$ as a measure of seismic scattering strength shows a frequency dependent behaviour for von Karman type random media. For measuring this frequency dependency of peak-ratio, we propose computing the frequency exponent m, which has been linked to the κ value of the von Karman type PSDF. Specifically, m is shown to be inversely related to κ, where large m corresponds to a strong frequency dependency with medium heterogeneity rich in short-wavelength elements.

3D numerical simulations of seismic wave propagation based on the finite difference method were performed to understand better the influences of the free-surface and topography on the calculation of peak-ratio and frequency exponent. We have identified the following free-surface and topographic effects:

- Numerical simulation results with a flat free-surface boundary condition shows how the interference between the up-going incident wave and the down-going surface reflected wave may raise peak-ratio estimate at a specific frequency and depth, hence affecting the frequency exponent calculation at that depth, too.

- Numerical simulation results using a volcano topography as the surface boundary condition shows how a strong presence of topographic irregularities (near to the

summit of the active volcano) may increase peak-ratio while slightly reducing the frequency exponent.

We suggest that limiting examination to stations with similar installation depths and elevations can help mitigate the free-surface and topographic effects when analysing peak-ratio and its frequency dependency. That is because under such criteria, the stations would experience similar levels of free-surface and topography effects.

Table 2.1 The p value and the frequency exponent m estimates for a given κ value of the von Karman type power spectral density function. The p values were obtained from the numerical evaluation of Saito et al. (2002). The estimated m values follow from Equation 2.17 which is derived from the numerical expression of peak-ratio frequency dependency found in Suzaki (2007).

κ	p	m
0.1	1.19	1.36
0.2	1.38	0.90
0.3	1.56	0.56
0.4	1.71	0.34
0.5	1.83	0.19
0.6	1.91	0.09
0.7	1.95	0.05
0.8	1.98	0.02
0.9	1.99	0.01
1.0	1.99	0.01

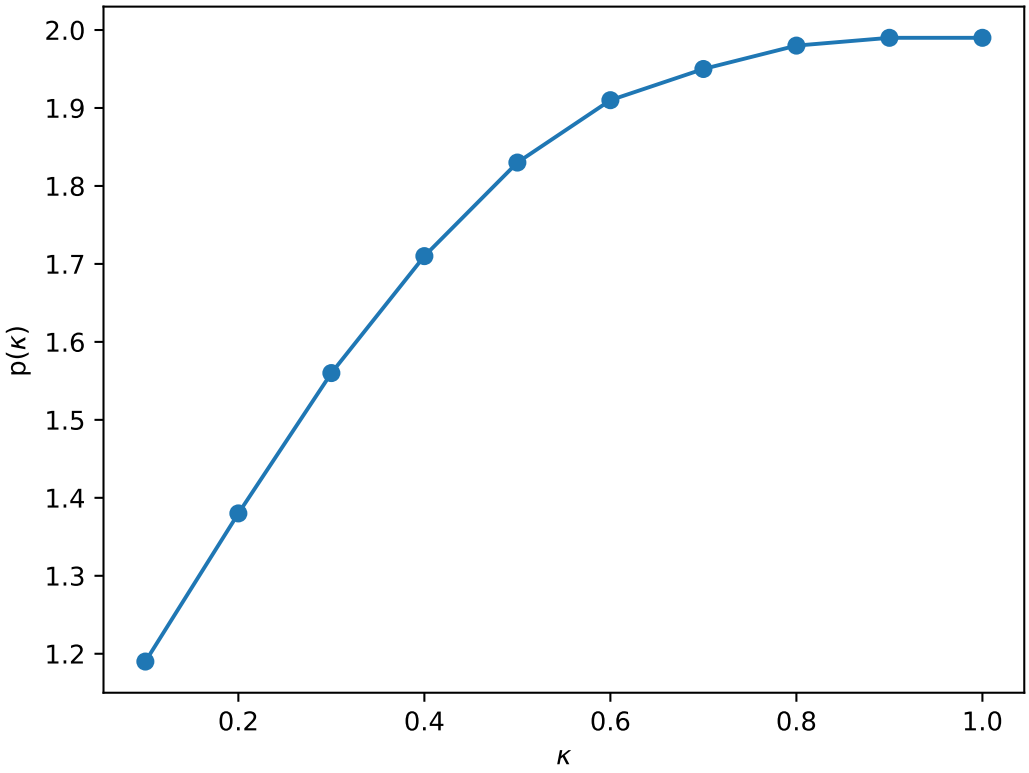

Figure 2.1 The relationship between the p value and the κ value of the von Karman type power spectral density function, reproduced using values given in Saito et al. (2002). The same values are presented in Table 2.1.

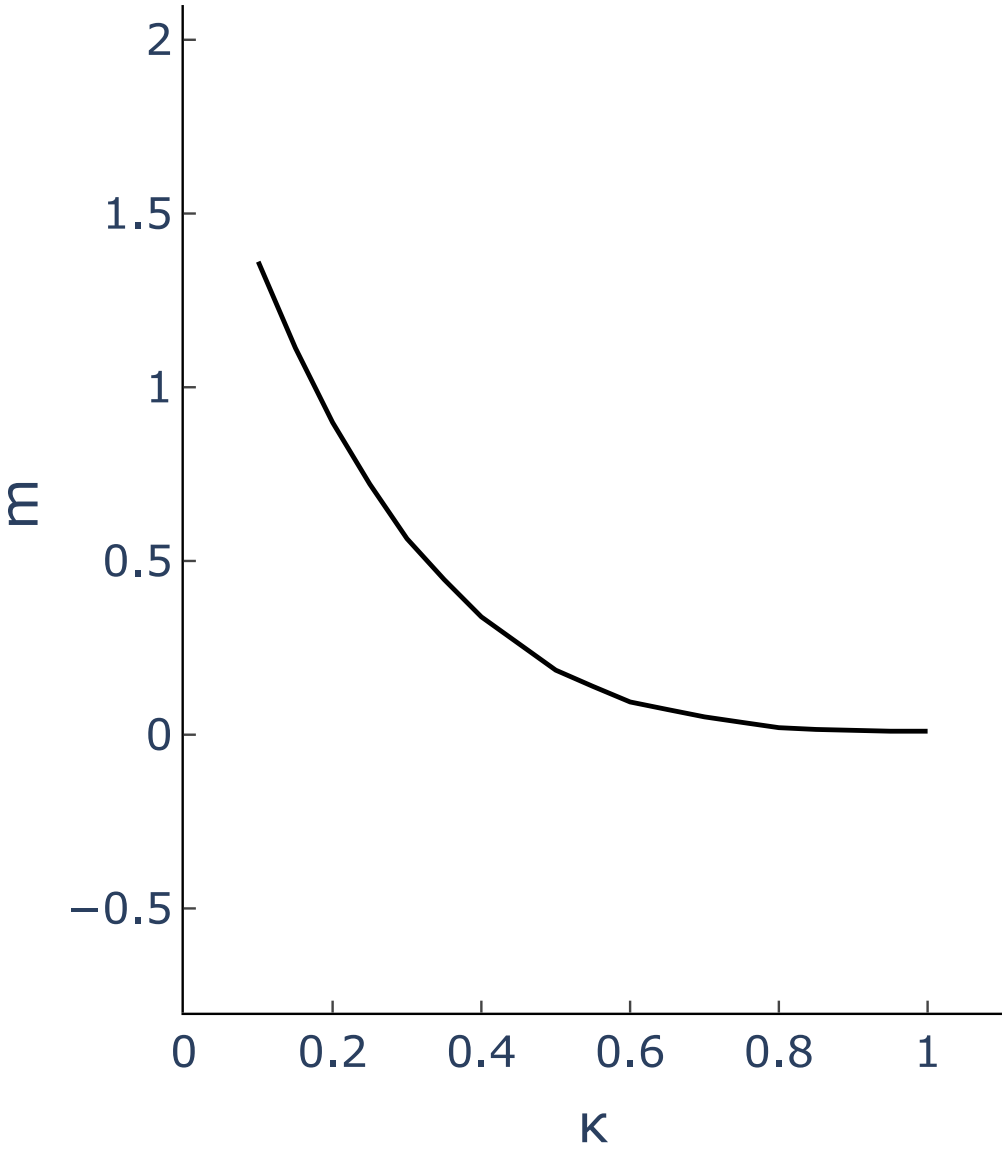

Figure 2.2 The relationship between the frequency exponent m and the κ value of the von Karman type power spectral density function. Refer to Table 2.1 for the values used to produce the plot.

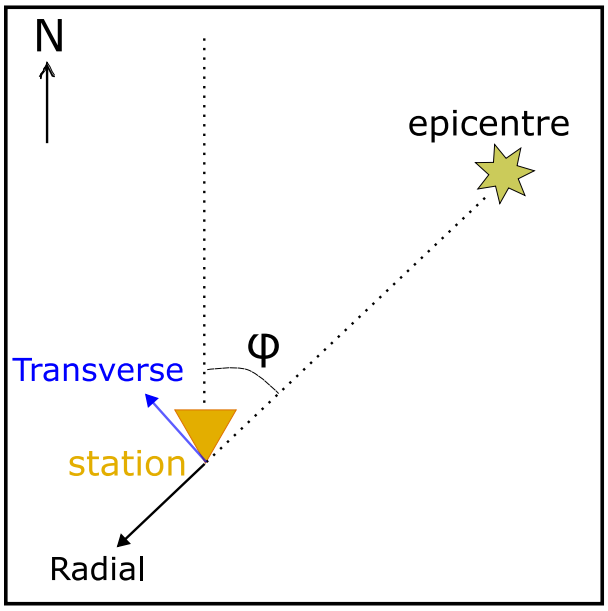

Figure 2.3 Definitions for the radial and transverse directions and the back-azimuth φ used to rotate seismograms from the typical NS and EW components.

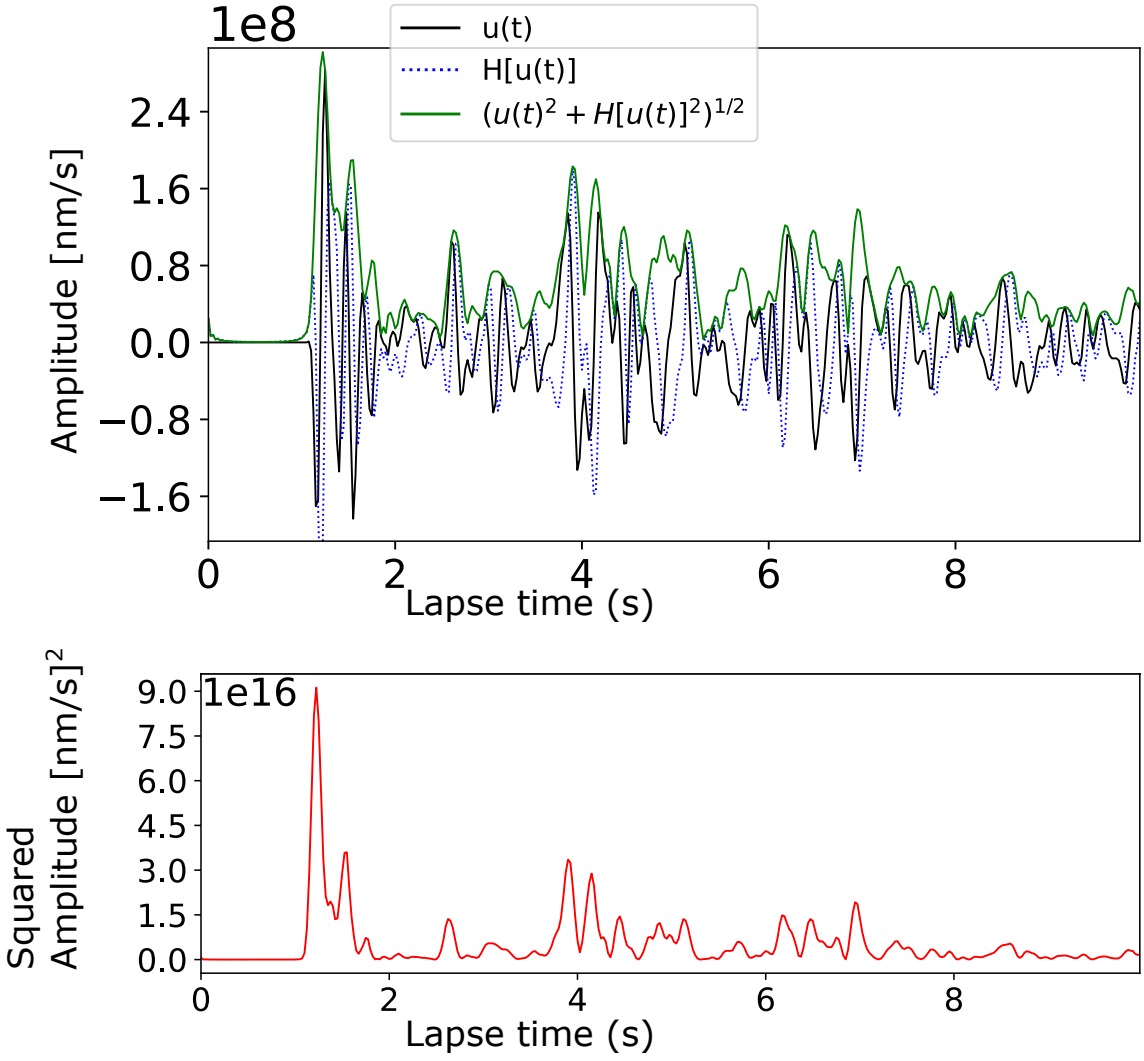

Figure 2.4 Visualising the computation of seismogram envelope. In the *top* panel, black line is the original trace signal $u(t)$, and blue dotted line is its Hilbert transform $\mathscr{H}[u(t)]$. The envelope tangent to successive peaks of the oscillating signal is shown in green, and is given by $\sqrt{u(t)^2 + \mathscr{H}[u(t)]^2}$. For the quantification of seismic scattering strength, we use the square of this green trace, which is shown in the *bottom* panel. Example is from one of the horizontal components of a simulated seismogram from a station at 6600 m depth from a flat surface using a vertically incident P wave source at a frequency band of 4-8 Hz.

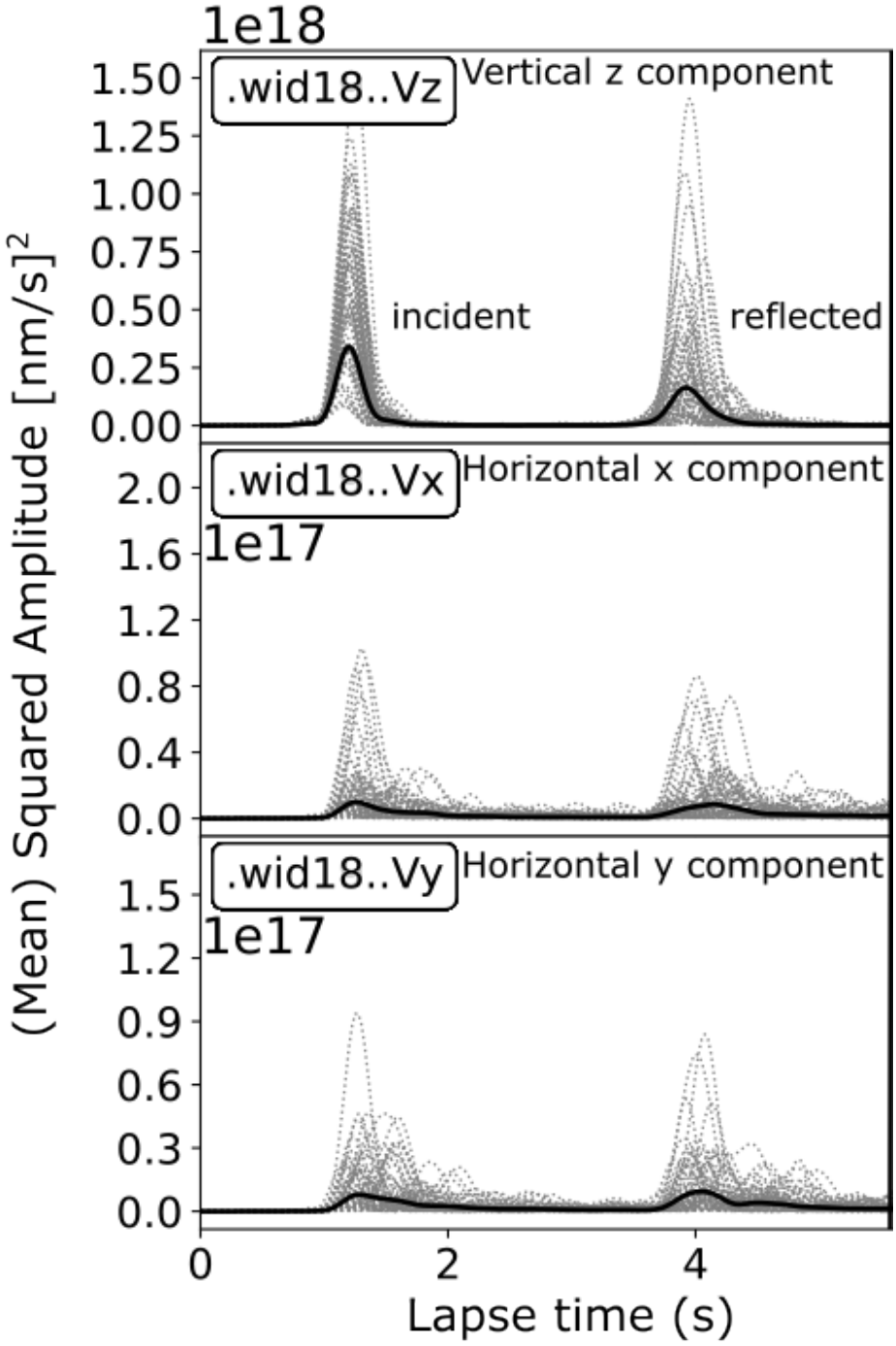

Figure 2.5 Demonstrating the stacking process. This example shows simulated data from 58 stations at an equal depth of 6600 m using a vertically incident plane P wave source at the 4-8 Hz frequency band. Dotted traces are individual squared seismograms at the different stations. The thick black line is the MS envelope, obtained by stacking the individual dotted traces. The two pulses correspond to the incident and the surface reflected wave signals, which we will clarify in the later section. If real dataset were to be used, the dotted lines would correspond to the different earthquake signals.

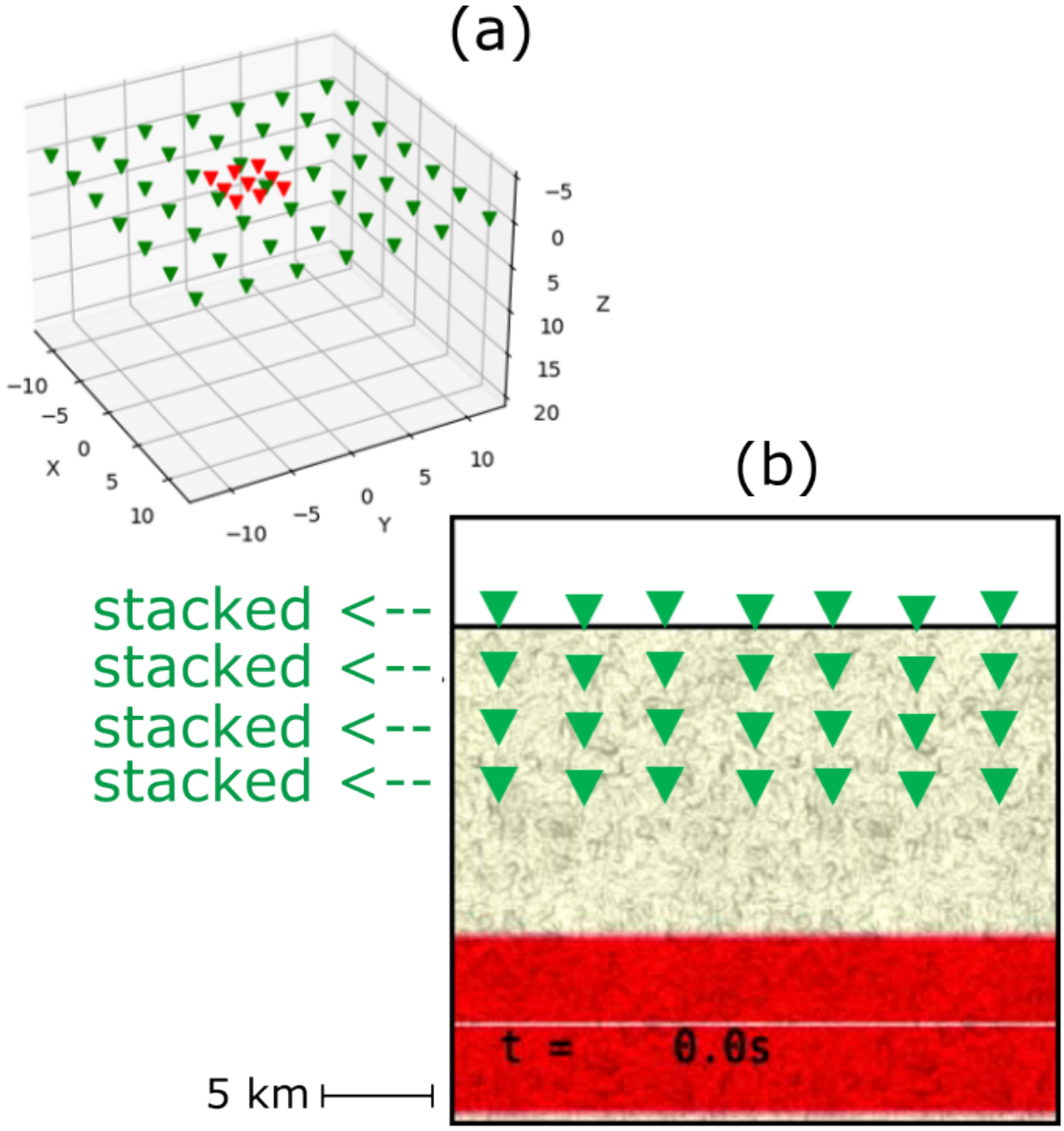

Figure 2.6 Virtual stations (arrays) configuration for the simulation with a flat free-surface condition. (a) The lateral configuration of stations showing the 7×7 array (green triangles) covering the extent of the simulation model and the 3×3 array (red triangles) situated near the model centre. (b) A schematic showing the extension of the arrays with depth, in relation to the initial incident plane P wave near the bottom of the model travelling vertically through the random heterogeneous medium. Stations at equal depths are to be stacked, giving synthetic seismogram envelopes at multiple depth levels.

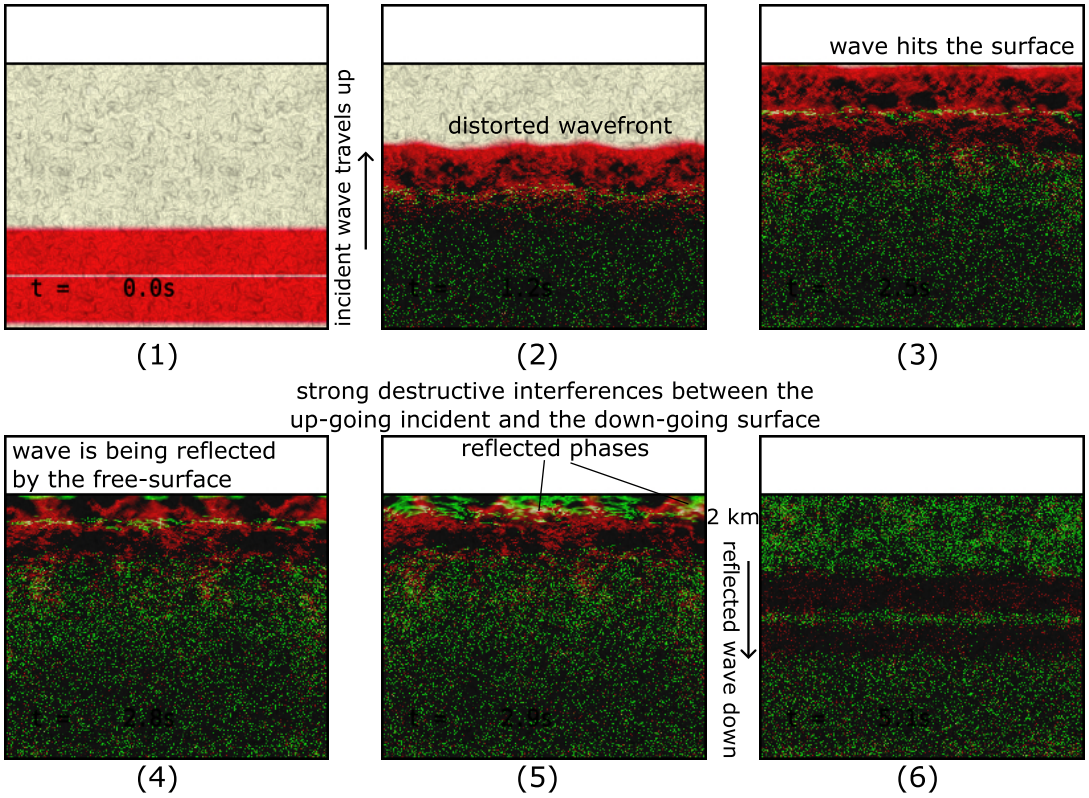

Figure 2.7 Vertical cross-sections showing key snapshots of numerical simulation results with a flat free-surface. P wave amplitude is shown in red while green represents the S wave amplitude. (1) The initial condition where a plane P wave with a source wavelength of 8 km is initiated; (2) Incident wave is travelling vertically upward, wavefront is distorted due to scattering by the random heterogeneities as it propagates; (3) Incident wave hits the flat free-surface; (4) Free-surface interaction generates a down-going surface reflected phase; (5) Interference between the up-going and down-going phases where at depths around a quarter of the source wavelength (2 km), strong destructive interference may occur; (6) Wave is fully reflected and propagates downward.

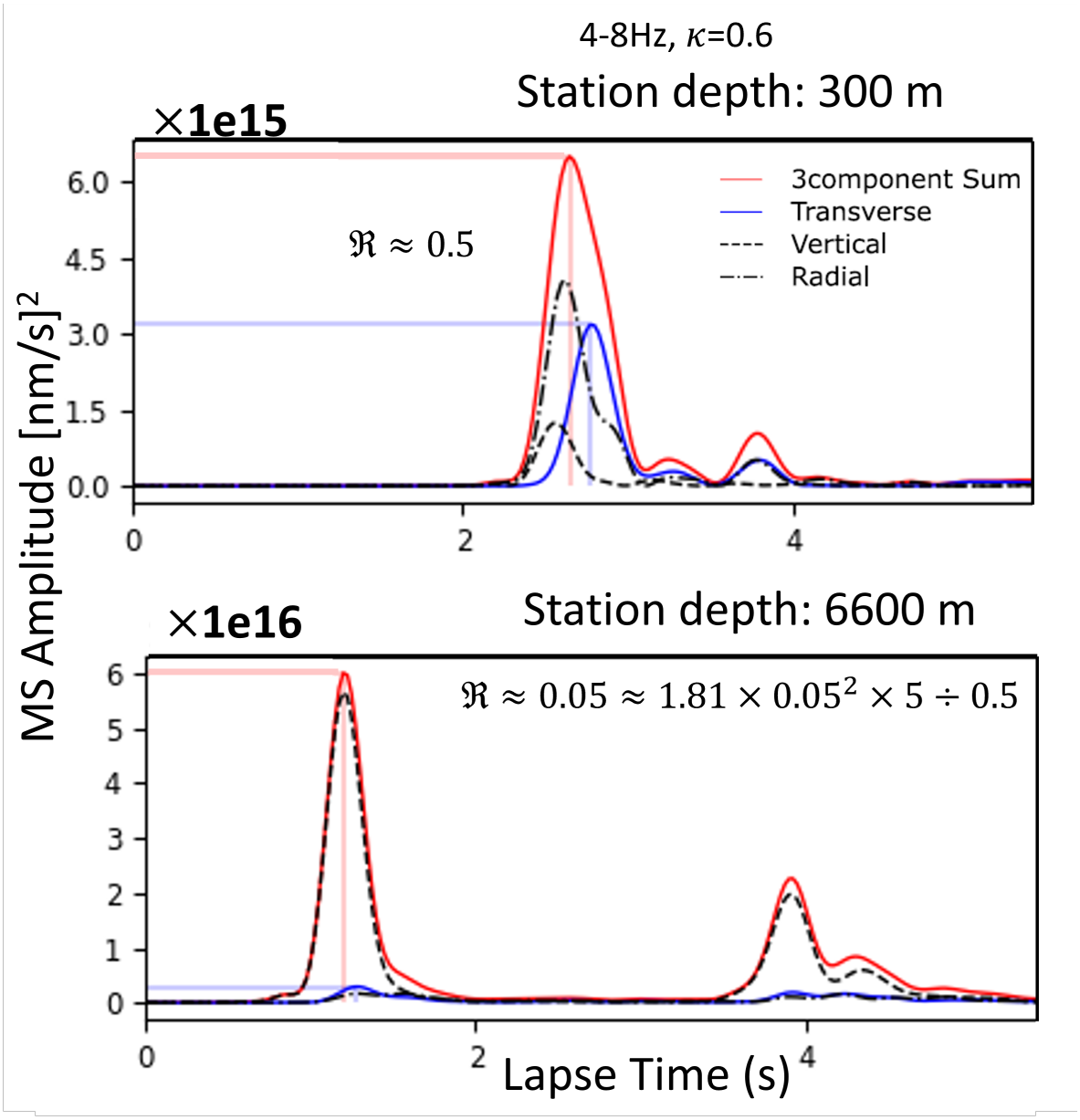

Figure 2.8 Stacked mean-squared (MS) envelopes synthesised from numerical simulation with a flat free-surface condition. Examples are from the frequency band of 4-8 Hz, using κ of 0.6. (*top*) Stacked envelopes at station depth of 300 m. Note the small amplitude of the vertical envelope as a result of the destructive interference between the up-going incident and the down-going surface reflected phases. (*bottom*) Stacked envelopes at station depth of 6600 m, where the up-going incident and down-going surface reflected phases are clearly separate.

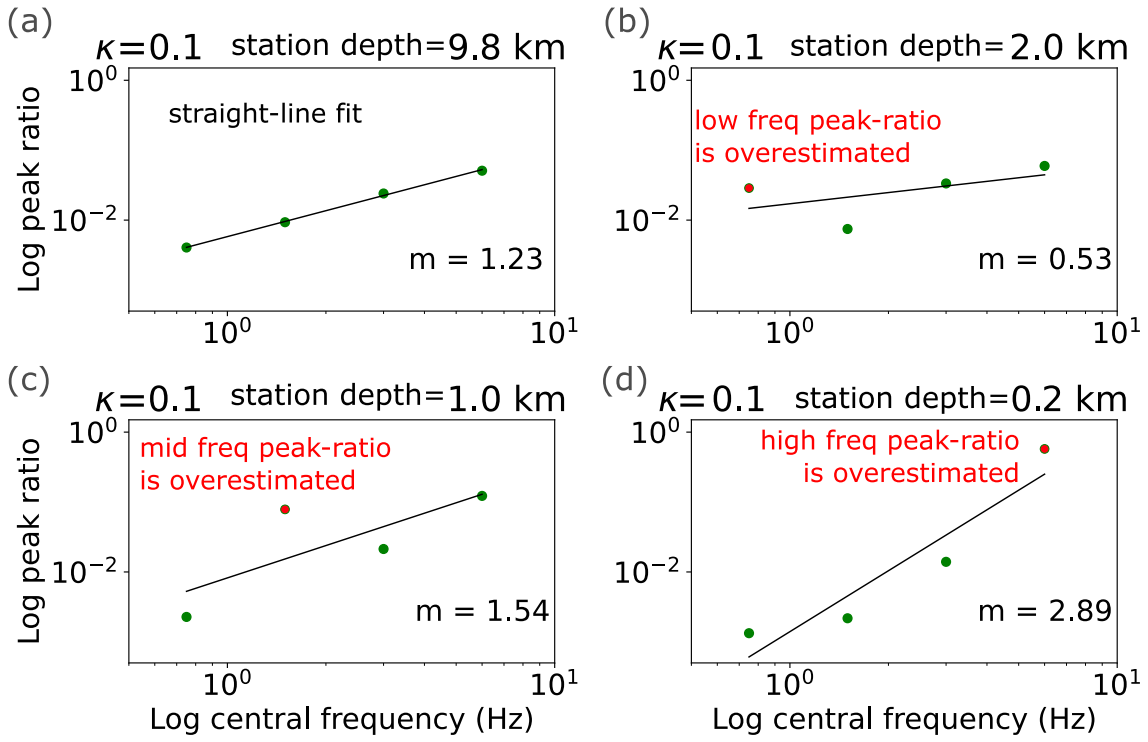

Figure 2.9 The free-surface effect causes peak-ratio $\Re$ at specific frequency band to be raised at depths around a quarter of the source wavelength hence affecting the frequency exponent m estimation. (a) At very deep station depths, the free-surface effect is virtually non-existent hence a straight-line fit is appropriate. (b) At station depths of around 2000 m, peak-ratio at the lowest frequency band is raised, underestimating the overall frequency exponent. (c) At station depths of around 1000 m, peak-ratio at the mid frequency band is raised. (d) At station depths of around 200 m, peak-ratio at the highest frequency band is raised, overestimating the overall frequency exponent.

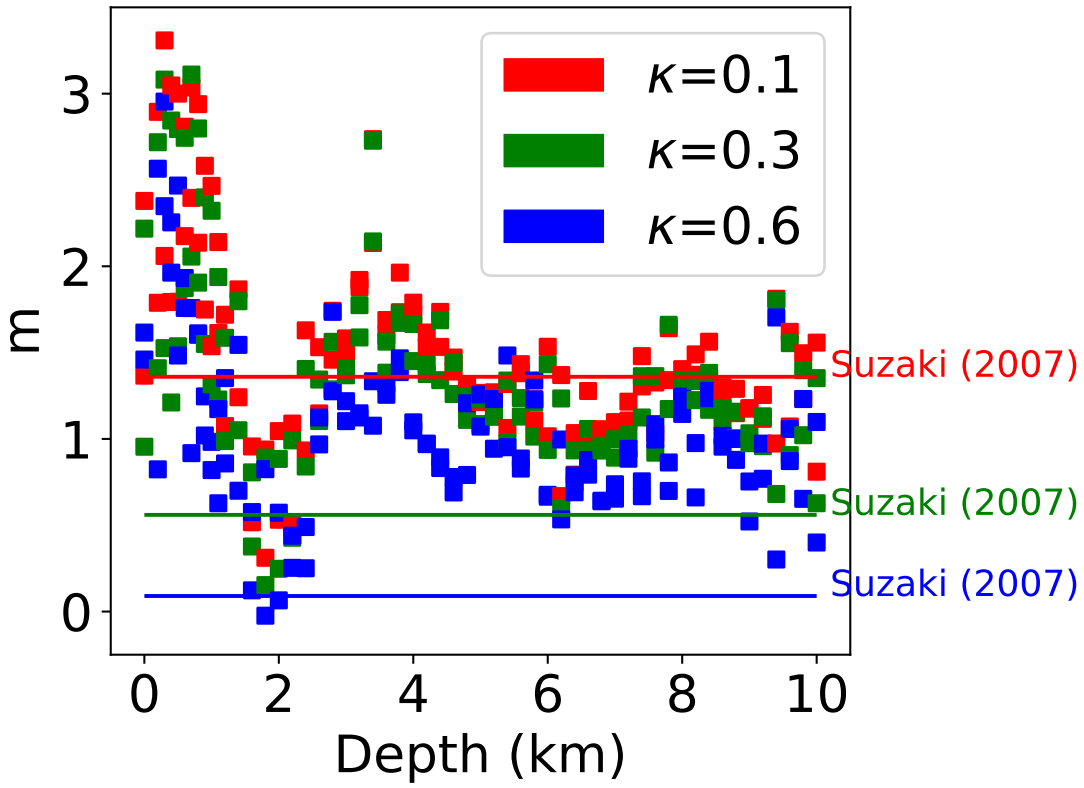

Figure 2.10 Numerical simulation results of frequency exponent m with respect to station depth. With increasing κ, numerically estimated frequency exponent is overall decreasing (red, green, blue square plots), but Suzaki (2007) relation does not seem to well predict their relationship especially for larger κ values (red, green, blue lines). There is a large fluctuation in frequency exponent at shallow depths due to the free-surface effect. At depths >5 km, frequency exponent is relatively stable with respect to depth since the free-surface effect is virtually non-existent at these depths.

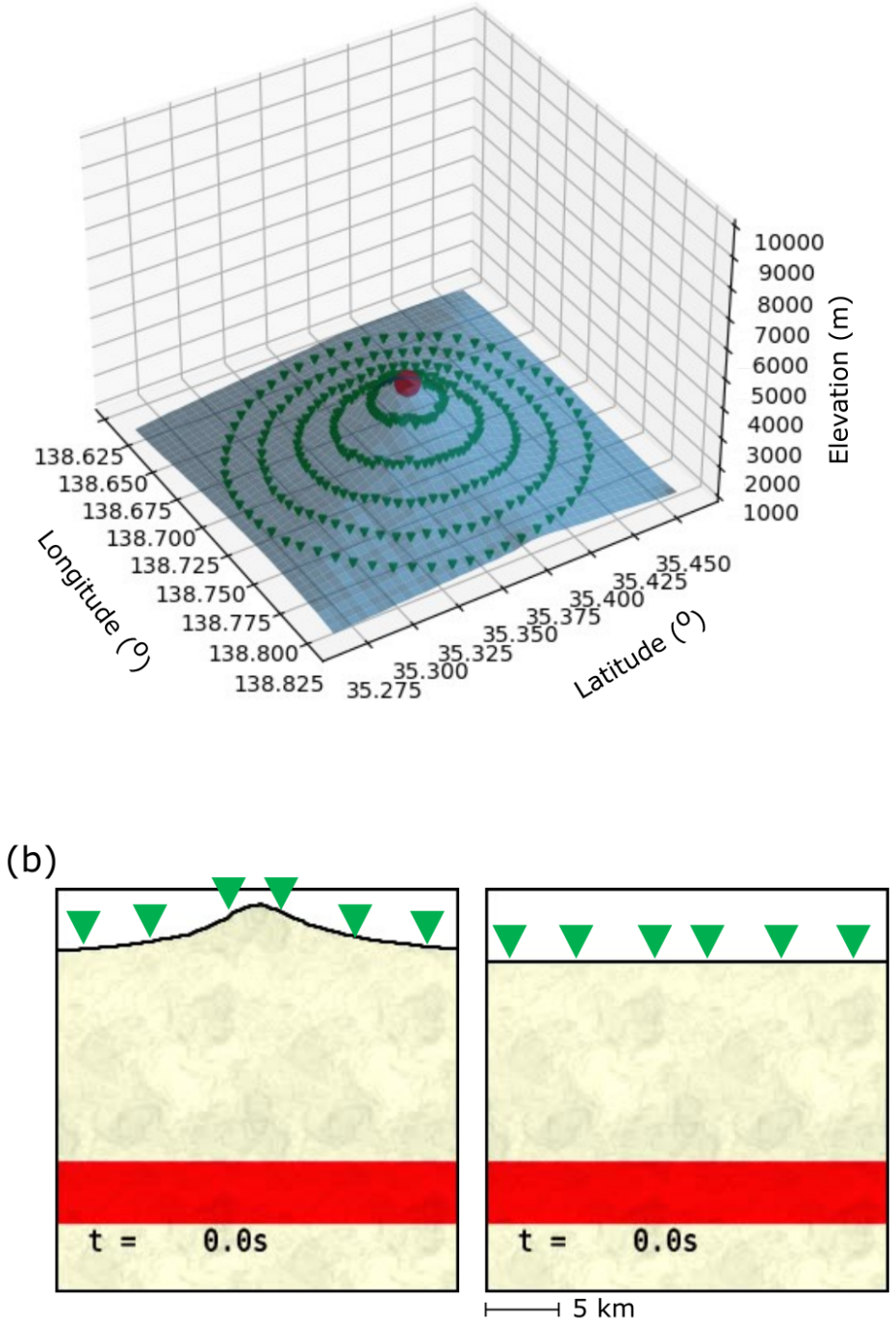

Figure 2.11 Virtual stations arrays configuration in the simulations for examining the effect of topography on peak-ratio ($\Re$) and its frequency dependency (m). (a) Arrays are set at discrete radius (2, 4, 6, 8, and 10 km) from the model centre which is the summit of the volcano. The model for the real volcano topography is from the JIVSM model of Mt. Fuji. (b) A schematic showing the contrast in surface conditions. In both instances, the same station configuration as Figure 2.11a is defined. Furthermore, we use the same random medium heterogeneity and vertically incident plane P wave from near the bottom of the model. Therefore, any variation in $\Re$ and m can be attributed to the contrast in the surface conditions of the simulations.

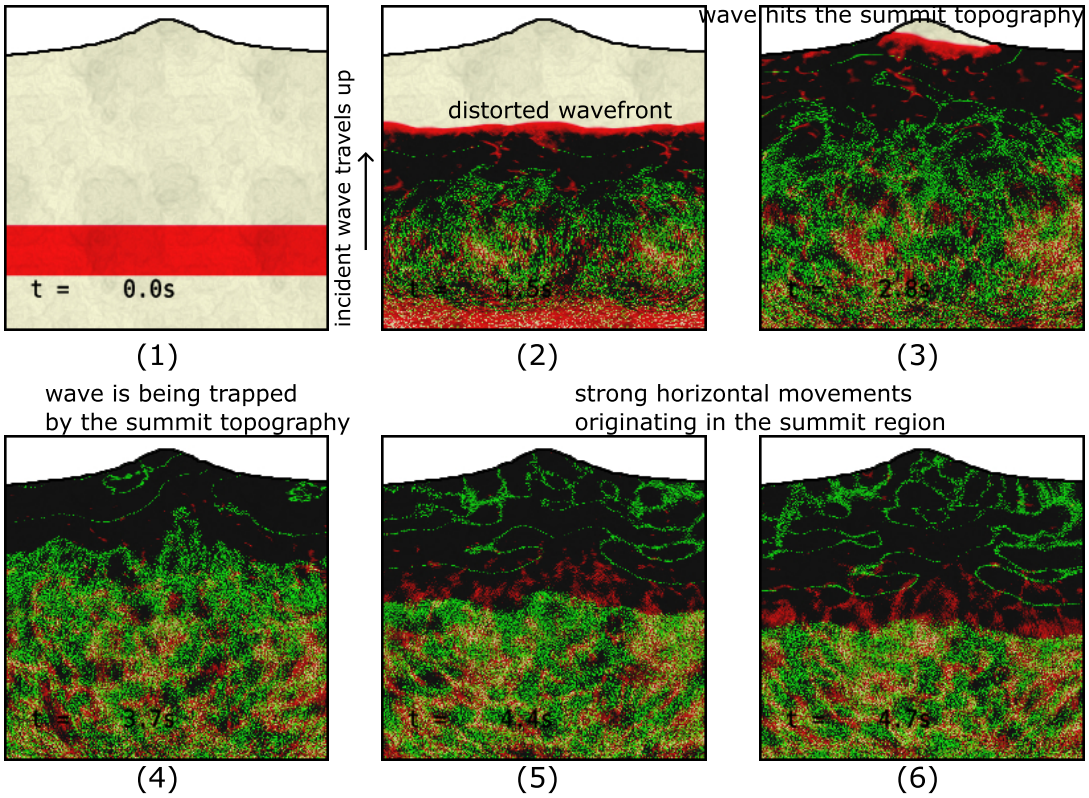

Figure 2.12 Vertical cross-sections showing key snapshots of numerical simulation results with a volcano topography as the surface condition. P wave amplitude is shown in red while green represents the S wave amplitude. (1) The initial condition where a plane P wave is initiated; (2) Incident wave is travelling vertically upward, wavefront is distorted due to scattering by the random heterogeneities as it propagates; (3) Incident wave arrives at the summit region; (4, 5, 6) The concave summit area reflects and traps wave, introducing strong horizontal motions.

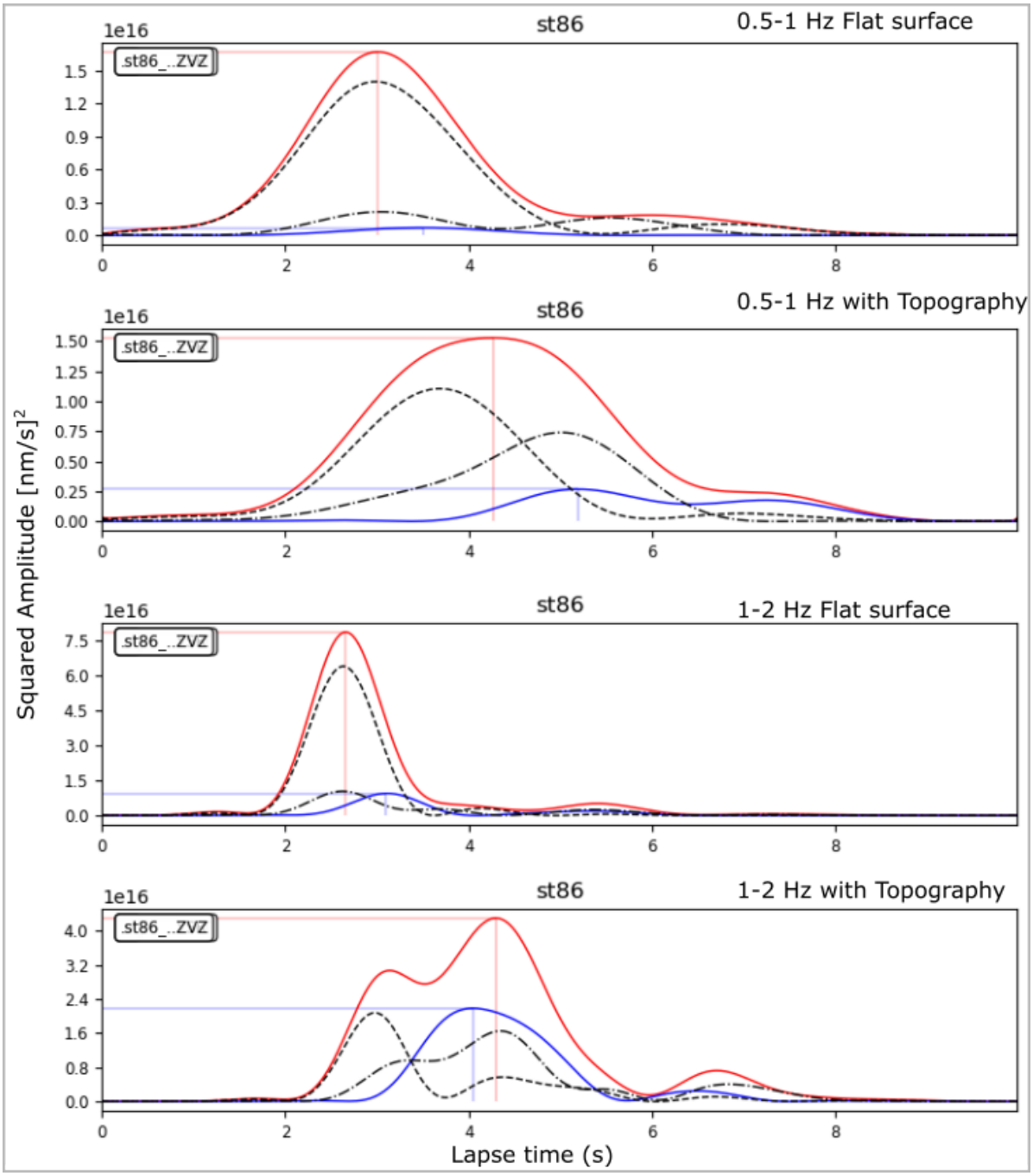

Figure 2.13 Comparisons of mean-squared (MS) envelopes synthesised under two surface conditions: Flat free-surface, and topography according to Mt. Fuji JIVSM model. Shown are for the 0.5-1 and 1-2 Hz high frequency bands at a station 2 km away from the model centre/summit. Red are 3-component sum MS envelopes. Blue are transverse MS envelopes. Dash and dash-dot lines are for vertical and radial MS envelopes, respectively. In the case with topography, the transverse envelope significantly contributes to the 3-component sum envelope compared to the flat free-surface case.

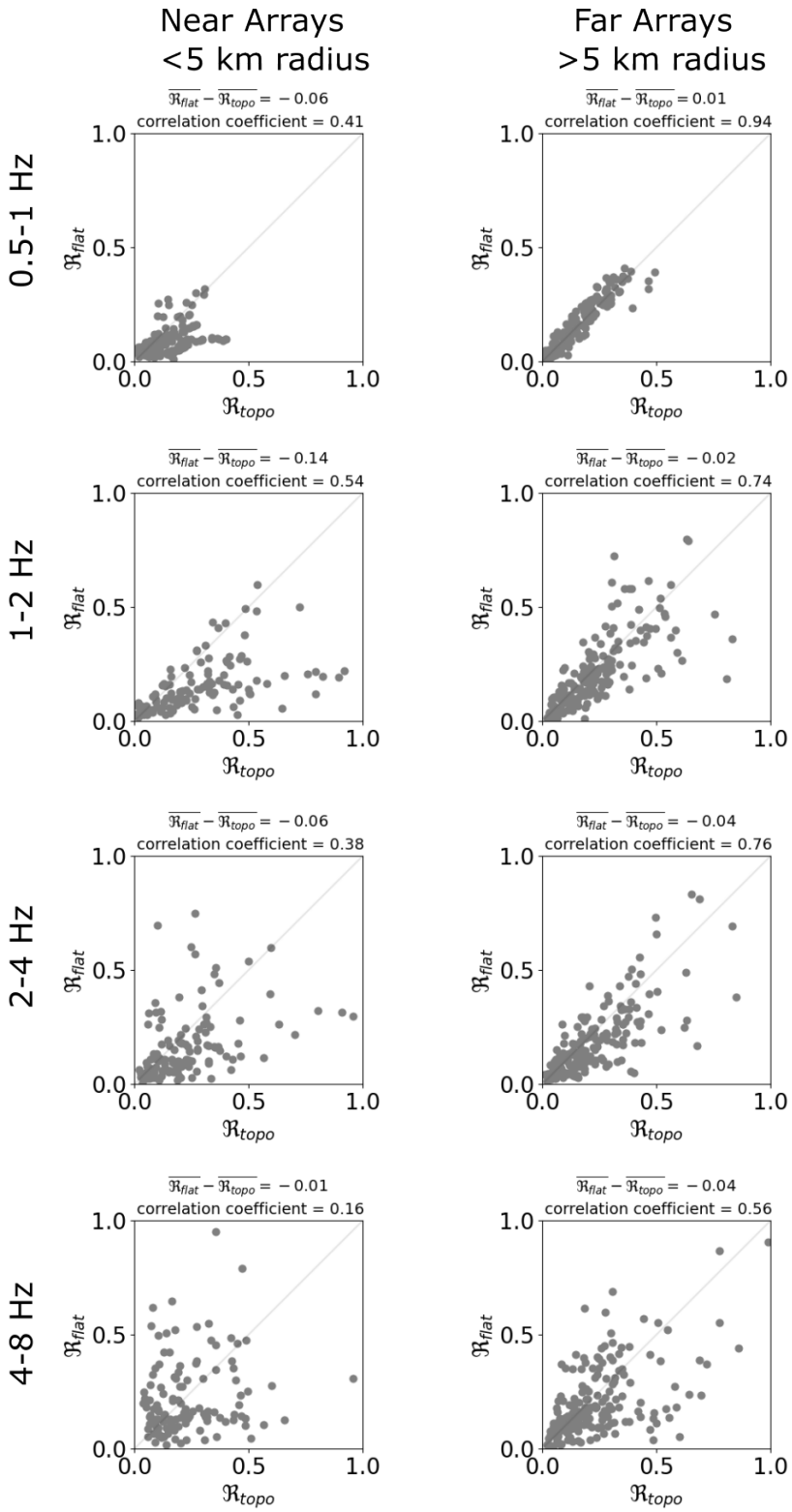

Figure 2.14 Comparisons of peak-ratio $\Re$ at the virtual stations, between numerical simulations with a flat surface ($\Re_{flat}$) and those using Mt. Fuji JIVSM topography ($\Re_{topo}$). Topography raises peak-ratio estimation which is more effective at the near stations (<5 km radius from the summit) and in the low frequencies especially 1-2 Hz.

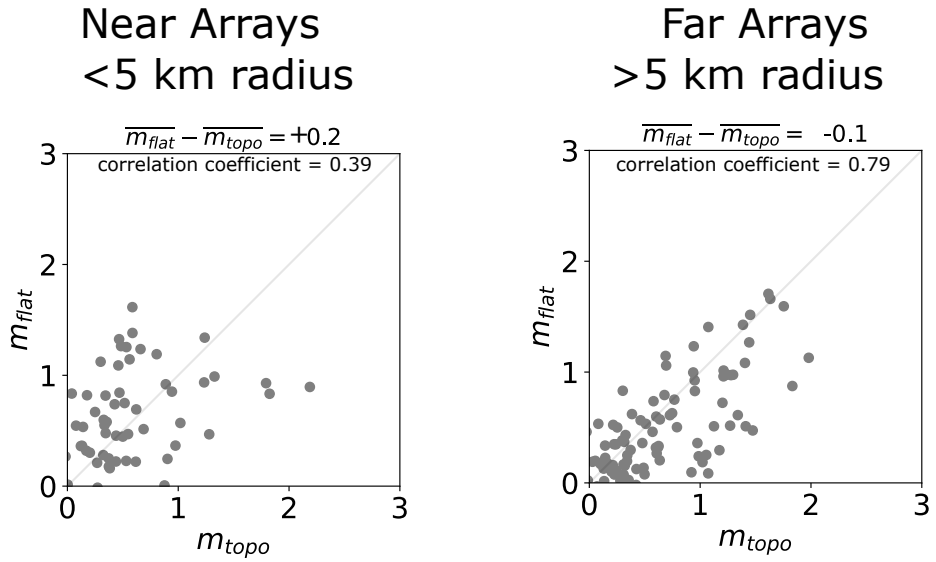

Figure 2.15 Comparisons of frequency exponent m obtained from numerical simulations with a flat surface (m_{flat}) and those using Mt. Fuji JIVSM topography model as the surface condition (m_{topo}). (*left*) For stations close to the summit at a radius of less than 5 km. (*right*) Stations far away from the summit at a radius of more than 5 km. The deviation from the 1:1 line, as a result of the topographic effect, is more significant at the near summit stations.

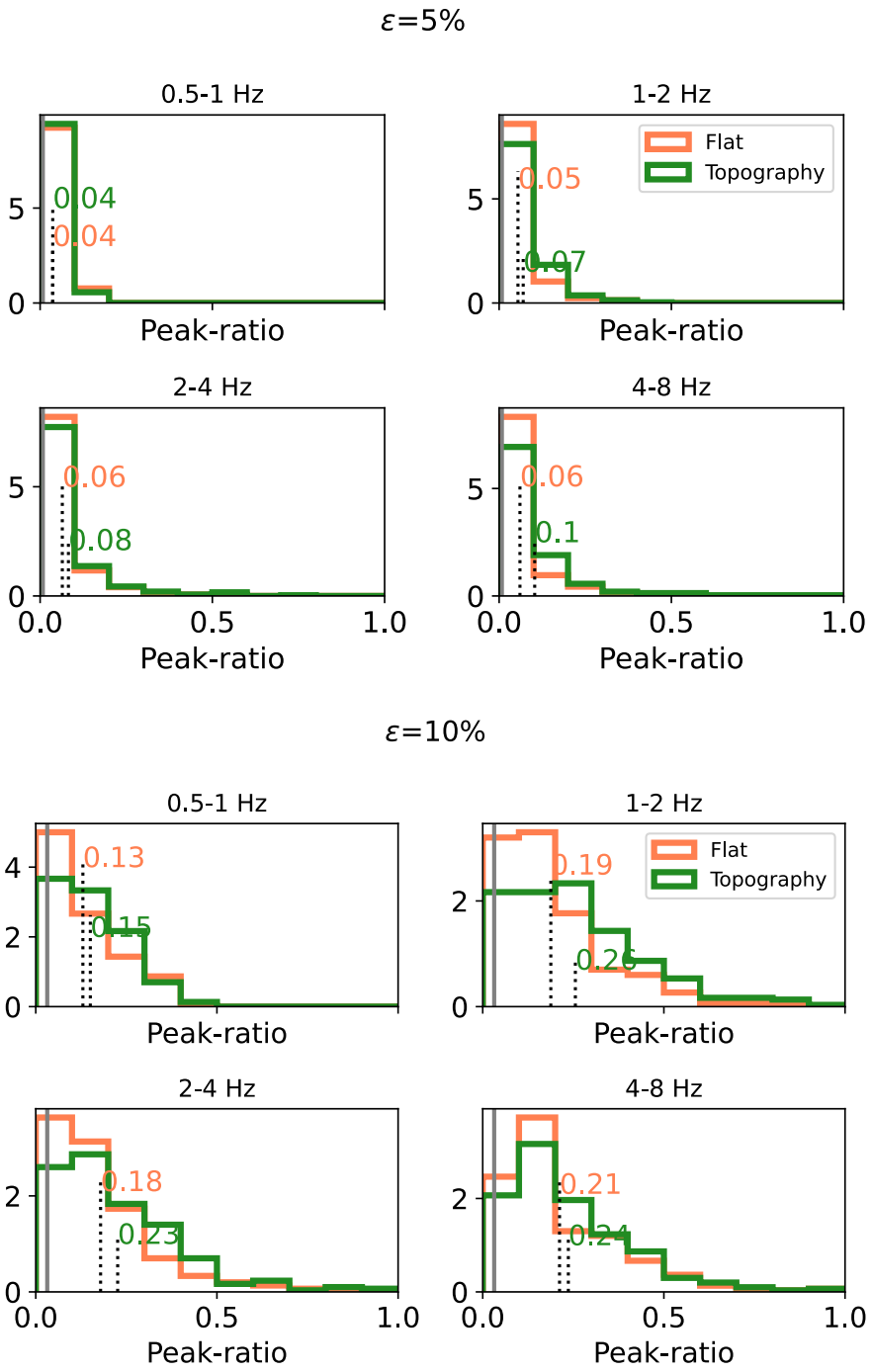

Figure 2.16 Normalised histograms of peak-ratio $\Re$ at four frequency bands (0.5-1, 1-2, 2-4, and 4-8 Hz) obtained using synthesised data at a range of root-mean-squared fractional fluctuation in velocity ε values. Correlation distance a is fixed at 4 km. Light red and green are for simulations with a flat free-surface and volcano topography according to Mt. Fuji JIVSM model as their surface conditions, respectively. Dotted lines mark the means of the distributions. Solid lines mark the estimated peak-ratio according to Equation 2.12 assuming $h = 7$ km. For $\varepsilon = 5\%$ (top) and $\varepsilon = 10\%$ (bottom).

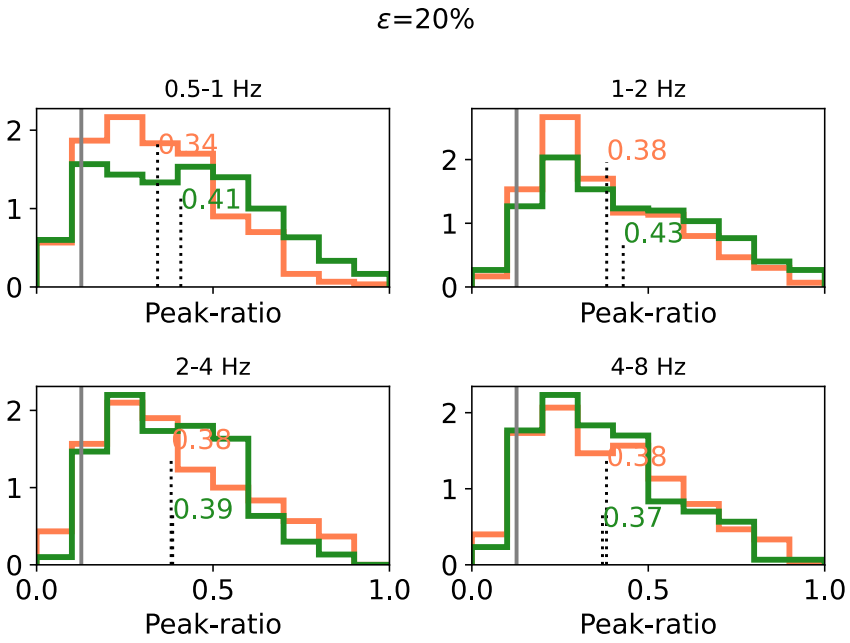

Figure 2.16 (*continued*) For $\varepsilon = 20\%$.

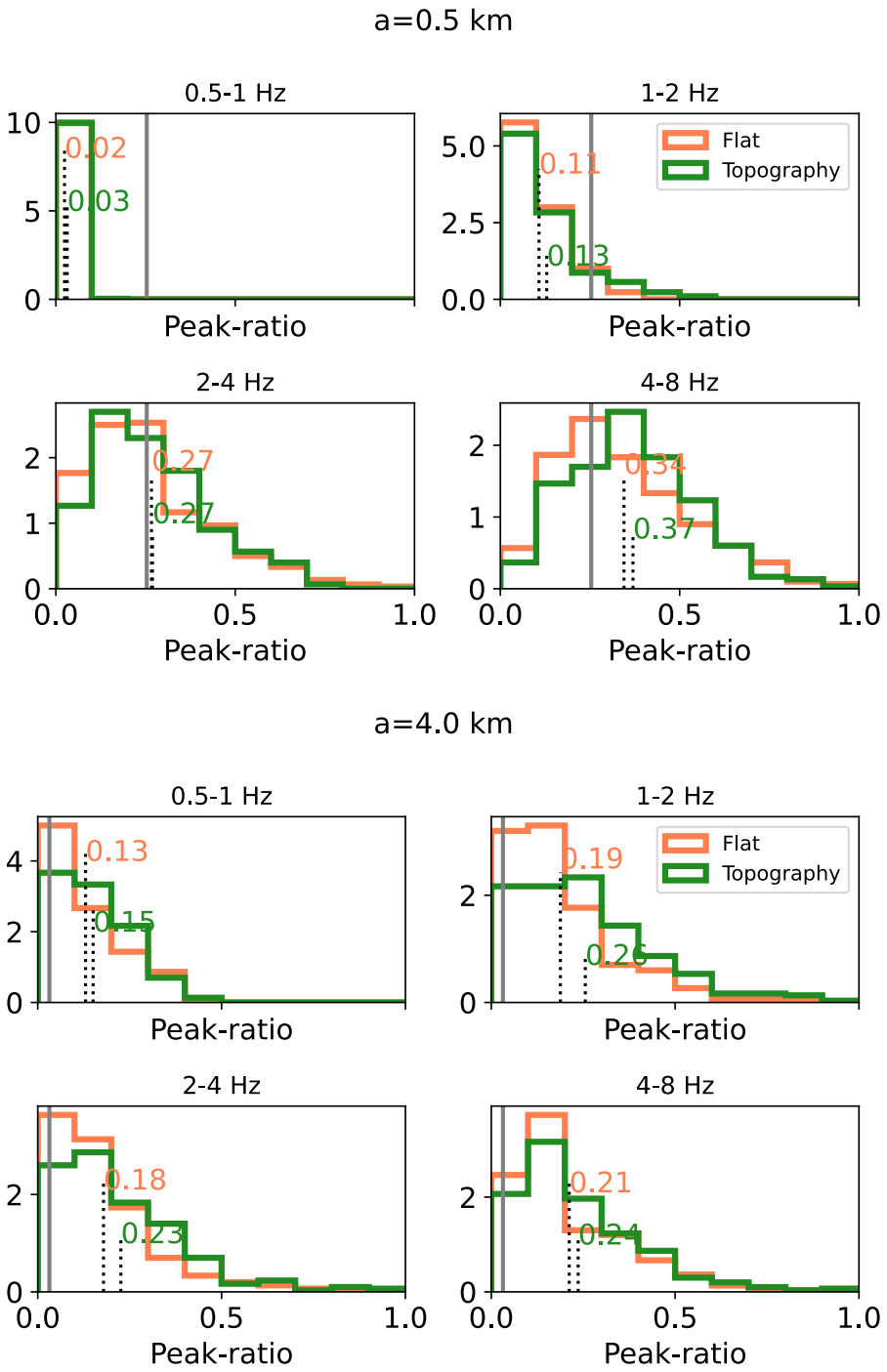

Figure 2.17 Normalised histograms of peak-ratio $\Re$ at four frequency bands (0.5-1, 1-2, 2-4, and 4-8 Hz) obtained using synthesised data at a range of correlation distance a values. The root-mean-squared fractional fluctuation in velocity ε is fixed at 10%. Orange and green are for simulations with a flat free-surface and volcano topography according to Mt. Fuji JIVSM model as their surface conditions, respectively. Dotted lines mark the means of the distributions. Solid lines mark the estimated peak-ratio according to Equation 2.12 assuming $h = 7$ km. For $a = 0.5$ km (top) and $a = 4$ km (bottom).

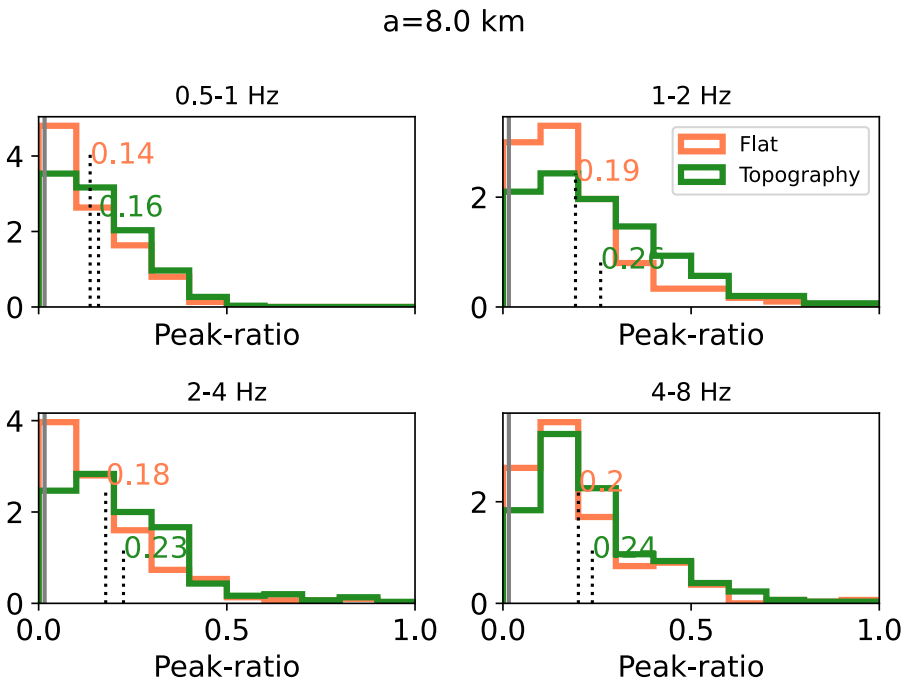

Figure 2.17 (*continued*) For $a = 8$ km.

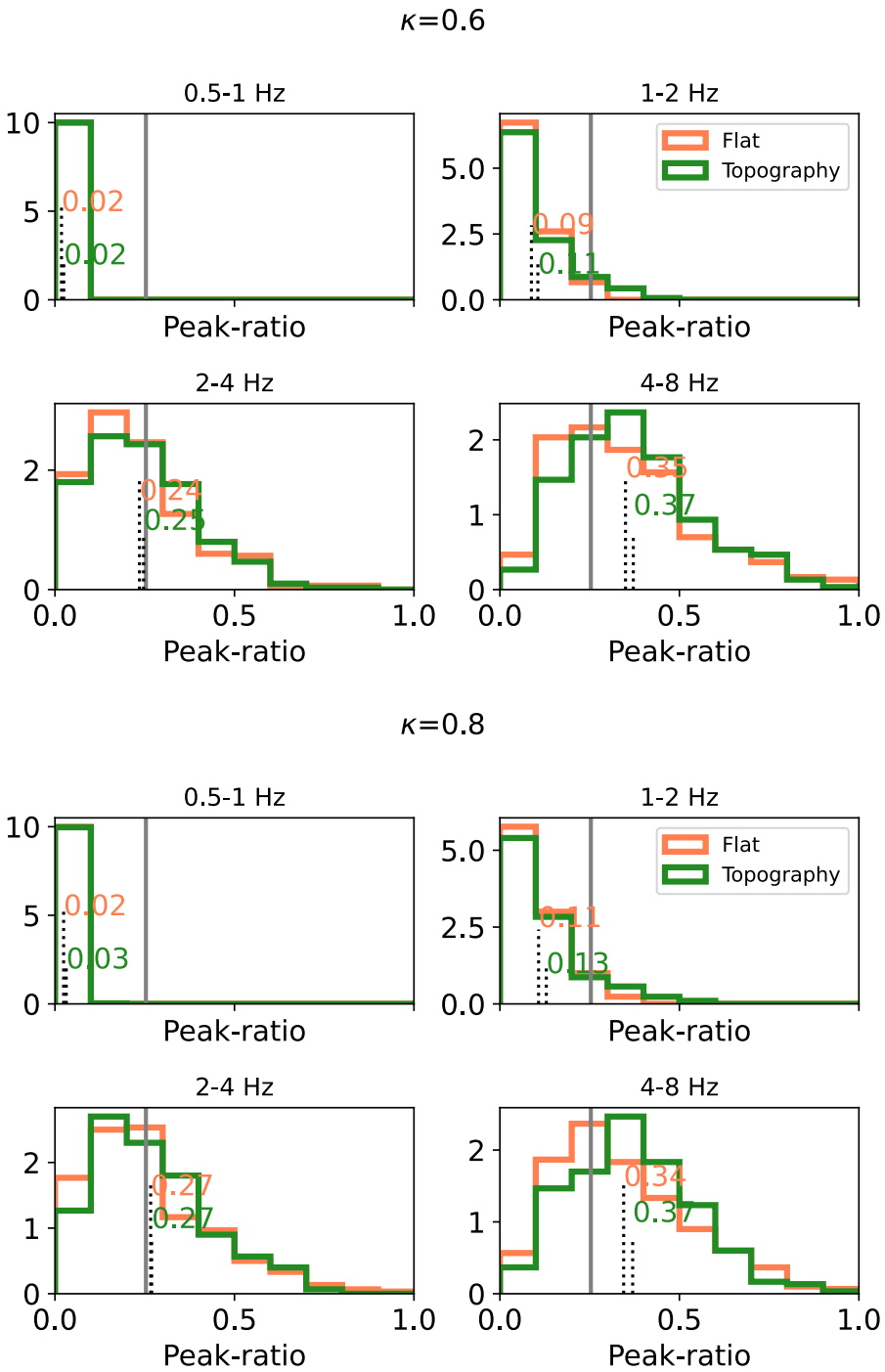

Figure 2.18 Normalised histograms of peak-ratio $\Re$ at four frequency bands (0.5-1, 1-2, 2-4, and 4-8 Hz) obtained from synthesised data using $\kappa = 0.6$ and $\kappa = 0.8$. The root-mean-squared fractional fluctuation in velocity ε and correlation distance a are fixed at 10% and 0.5 km, respectively. Orange and green are for simulations with a flat free-surface and volcano topography according to Mt. Fuji JIVSM model as their surface conditions, respectively. Dotted lines mark the means of the distributions. Solid lines mark the estimated peak-ratio according to Equation 2.12 assuming $h = 7$ km.

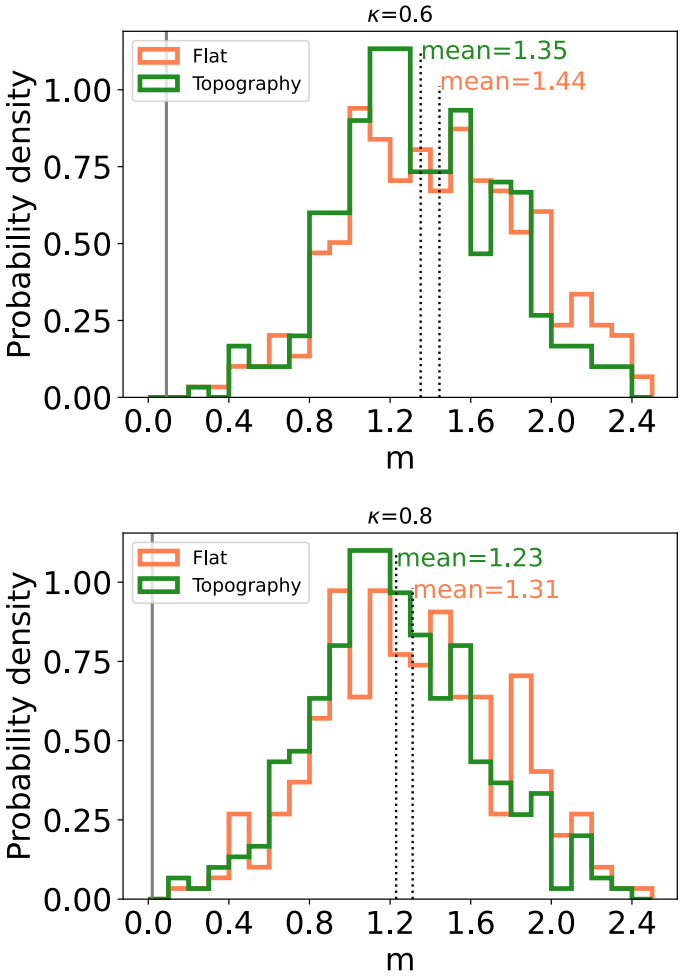

Figure 2.19 Normalised histograms of frequency exponent m obtained from synthesised data using $\kappa = 0.6$ and $\kappa = 0.8$. The root-mean-squared fractional fluctuation in velocity ε and correlation distance a are fixed at 10% and 0.5 km, respectively. Orange and green are for simulations with a flat free-surface and volcano topography according to Mt. Fuji JIVSM model as their surface conditions, respectively. Dotted lines mark the means of the distributions. Grey solid lines mark the estimated frequency exponent according to Suzaki (2007) relation (Table 2.1).

Chapter 3

Peak-Ratios and their Frequency Dependency at Hi-net Stations

In this chapter, we aim to first revisit the study of Nishimura (2012) by presenting the spatial distribution of peak-ratio in Japan using Hi-net stations after mitigating the effects of the free-surface and topography. In particular, we reexamine whether features pointed out in the previous study can be similarly identified even after the mitigating attempt. More specifically, whether there is a tendency to show larger peak-ratios for parts of Japan that are more geologically active (e.g., close to active volcanoes), thus interpreting the source of seismic scattering as coming from the strong heterogeneities at active areas. Additionally, we expect an overall increase in peak-ratio with respect to frequency. In this regard, we shall quantify the frequency dependency of peak-ratio in Japan by calculating the frequency exponent m, and present their distribution over Japan. Interpretations for the distribution of frequency dependency of peak-ratio shall also be discussed in a similar manner.

3.1 Data

To measure peak-ratio values in Japan, we make use of the Hi-net seismometer network, managed by NIED (National Research Institute for Earth Science and Disaster Resilience, 2019). In total, we consider 803 Hi-net stations for our peak-ratio analysis of Japan. More specifically, we consider 112 stations from the Hokkaido region, 117 from the Tohoku region, 328 from the Kanto-Chubu region, 168 from the Kinki-Chugoku-Shikoku region, and 78 from the Kyushu region. Figure 3.1 shows the coverage of Hi-net stations over the islands, with station spacing of roughly between 15 to 20 km. This dense and wide station coverage allows for the examination of lateral distribution of peak-ratios and their frequency dependency. To reduce anthropogenic noise sources, Hi-net stations are installed at the bottom of boreholes. Most of these boreholes are at depths of 100-300 m. Some reach a few kilometres particularly those located near large cities to minimise anthropogenic noises.

Following the implications from the numerical simulations, to mitigate the free-surface and topographic effects, we compare only Hi-net stations of similar depths and installation heights. In this regard, we focus on Hi-net stations between the depths of 100-200 m, and at elevations of less than 400 m. The remaining number of stations is 390. Many of the removed stations are from the Kanto plains due to the deep station installation (the area is within the Tokyo metropolitan area), and from the Chubu region due to the high station elevation (the region consists of tall mountains). Otherwise, we still have a decent station coverage over the remaining regions.

We consider data from 99 seismic events that occurred between 2010 and 2019. Using the same set of events for all Hi-net stations allows for a more systematic survey of seismic scattering across Japan. To avoid contamination by the depth phases, and in accordance to the previous studies (Kubanza et al., 2007; Nishimura, 2012), we take only deep earthquakes with a minimum depth of 300 km. Using only deep earthquakes also ensures that the hypocentral distances are so far away that the direct S wave phase is excluded

in the analysis time window. In other words, we can mainly focus on the P wave arrivals for the time-window in our analysis. We chose data from moderate earthquakes with a magnitude range of 5.0-6.5. We did not consider smaller microearthquakes because they are less likely to provide sufficient signal quality especially for the range of hypocentral distances that we take. We also did not consider larger magnitude earthquakes to keep the P wave source time function as simple as possible. Epicentral distances range from 0° to 60°, with the back-azimuths mostly distributed in the NE-NW and the SE-SW directions. Figure 3.2 shows the distribution of these events.

Events were selected from the Incorporated Research Institutions for Seismology (IRIS) catalogue. The earthquake metadata were downloaded through the available FDSN (International Federation of Digital Seismograph Networks) web service using the ObsPy Python package (Krischer et al., 2015; Megies et al., 2011). The continuous waveform data are provided by the National Research Institute for Earth Science and Disaster Resilience (NIED). We utilise the HinetPy Python package (Tian, 2020) to access and obtain the waveform data.

3.2 Results

3.2.1 MS Envelopes

Before we calculate the peak-ratio, we need to first obtain the MS envelopes at individual Hi-net stations. We follow the same data processing steps that were laid out in Kubanza et al. (2007) and described in Section 2.2. These are: (1) Seismogram filtering into several frequency bands; (2) Rotating the vertical-north-east (ZNE) seismograms into the vertical-radial-transverse (ZRT) components; (3) Select data according to the signal-to-noise ratio (S/N); (4) Squaring of the seismograms; (5) Normalisation of the squared seismograms and finally; (6) Stacking of seismic traces at individual stations.

First we prepare the seismograms. Seismogram traces were filtered using the But-

terworth bandpass filter into four separate frequency bands: 0.5-1, 1-2, 2-4, and 4-8 Hz. For each source-receiver pair, signals are rotated from the vertical, north-south, east-west (ZNE) components into the vertical, radial and transverse (ZRT) components. The back-azimuths of the source and receiver coordinates were used to rotate the seismogram components.

Next, we want to make sure that at the end of the time window, the coda level is still several times higher than the noise level before the P wave onset (Kubanza et al., 2007). To do so, we computed S/N and discard source-receiver pairs with S/N of less than 10 in any of the three components. For this, we used a signal time-window of 20 s after the expected P wave onset, and a noise time-window of 15 s prior to the expected P wave onset. For simplicity, the P wave onset is determined assuming the ak135 1D earth-model (Kennett et al., 1995). The ak135 model has been shown to be a good fit for a broad range of phases, and is widely used as the global reference model for 3D tomography studies (e.g., Rawlinson et al. (2006)).

Of the remaining dataset, squared envelope seismograms were calculated and then normalised according to Equation 2.23 and 2.26, respectively. For the normalisation time-window T, we use $T = 45$ s, commencing 10 s prior to the expected P wave onset. We deem this time-window to be long enough to show the equi-partition of energy into all three components in the later coda as a consequence of scattering, as described in Kubanza et al. (2007). But it is not so long to include direct S wave arrival considering the hypocentres of the sources used.

Finally, for each Hi-net station that contains usable signals from more than 10 earthquakes, we stack the available normalised seismogram envelopes per component. Thus, we obtain $\langle E_j(t) \rangle$ which is the j-th component MS envelope.

Figure 3.3 shows an example of MS envelopes at station KANH from eastern Tohoku area at the four frequency bands of 0.5-1, 1-2, 2-4, and 4-8 Hz. Shown are the transverse, vertical, radial, and the three-component sum MS envelopes. The typical MS envelopes

have several characteristics that can be explained by the oblique incidence of arriving P wave travelling through the random heterogeneous medium underneath the station (Kubanza et al., 2007). These characteristics can be recognised in Figure 3.3 as follows. The first 5 s or so commencing from the P wave onset, the vertical component envelope is by far the one with the largest amplitude compared to the transverse and radial components. This is the case at all frequency bands. On the other hand, transverse component envelope is usually smaller than the radial component, especially in the lower frequency bands. Thus, the transverse envelope typically has the smallest amplitude. There is also a delay between the time when peak amplitude is reached for the vertical envelope and the time when peak amplitude is reached for the transverse envelope.

The above observations can be explained as follows. Direct P arrival is dominant in the early part of the seismogram. Therefore, the large vertical component was anticipated. Direct P is also expected for the radial component but not the transverse component. Hence, the amplitude of the transverse component envelope is small. Furthermore, the transverse component mainly consists of scattered arrivals that come after the direct wave. Hence, there is a delay in reaching the transverse envelope peak, although this is also the case for normal incidence.

From the MS envelopes, the peak-ratio $\Re$ is calculated by dividing the peak amplitude of the transverse component envelope over the peak amplitude of the three-component sum envelope (Equation 2.11). For the example given in Figure 3.3, the peak-ratio values at the 0.5-1, 1-2, 2-4, and 4-8 Hz frequency bands are 0.03, 0.06, 0.11, and 0.25, respectively. Evidently, we see an increase in peak-ratio with increasing frequency. In fact, this trend is almost ubiquitous across all Hi-net stations. This observational trend was also present in Kubanza et al. (2007) and Nishimura (2012). Thus, a frequency dependent behaviour in peak-ratio is clearly indicated.

3.2.2 Peak-Ratio Distribution Across Japan

We estimated peak-ratios at a number of Hi-net stations with similar depths and installation heights across Japan. The ranges of peak-ratios found in our results are 3.22×10^{-5} to 0.64 at the frequency band of 0.5-1 Hz, 1.73×10^{-6} to 0.72 at 1-2 Hz, 1.07×10^{-5} to 0.78 at 2-4 Hz, and 0.03 to 0.85 at 4-8 Hz. The mean values across the frequency bands of 0.5-1, 1-2, 2-4, and 4-8 Hz are 0.15, 0.14, 0.17, and 0.23, with standard-deviations of 0.10, 0.08, 0.10, and 0.13, respectively.

The spatial distribution of peak-ratios across Japan can be viewed using the coordinates of Hi-net stations. That is because Hi-net stations are densely distributed, albeit that there is a lack of stations coverage in the Kanto and Chubu regions in this case. This gap in station coverage is due to differences in common borehole depths and elevations as mentioned previously. In Figure 3.4, we show the distributions of peak-ratios at individual Hi-net stations across the four frequency bands (0.5-1, 1-2, 2-4, and 4-8 Hz). The spatial distributions of peak-ratios across all frequencies are very much alike, even though we see that overall, peak-ratios are increasing with frequency.

A particularly key observation made in Nishimura (2012) is how Japan can be split into eastern and western portions based on their peak-ratios i.e according to the strength of seismic wave scattering. This observation can also be made in Figure 3.4. More specifically, eastern Japan shows large peak-ratios while western Japan shows small peak-ratios. According to Nishimura (2012), the boundary between the east and west half can be located in the Chubu region, though it is difficult to confirm this in Figure 3.4 due to the lack of stations in the region. Moreover, we can still see some regional trends in peak-ratio. For example, even though western Japan generally shows small peak-ratios, we can still find large peak-ratios on Kyushu. Conversely, even though eastern Japan shows larger peak-ratios overall, we can still find small peak-ratios in the Iwate Prefecture of eastern Tohoku region.

To examine whether earthquake specification and therefore, near source heterogeneity

is significantly driving the peak-ratio estimation, we calculated peak-ratios from the unstacked envelopes from each available earthquake. We then plot the peak-ratio values with respect to the epicentral distance, incident angle, and back-azimuth of the event. In Figure 3.5, we show an example of the results at station KANH from eastern Tohoku area. Because values are obtained using unstacked data, the spread is wide regardless of epicentral distance, incident angle, or back-azimuth. However, we see clusterings around the estimated peak-ratio value at station KANH from using the stacked MS envelopes (Figure 3.3). Because there is no clear trend in relation to the location of the source, we surmise that peak-ratios at seismic stations are more reflective of scattering heterogeneities in the rather shallow near station region. This notion where scattering effect is much weaker at depth is also supported by previous works (e.g., Flatté and Wu (1988); Wang and Shearer (2017)).

The uncertainty of our results was evaluated using the delete-1 Jack-knife test. To perform the delete-1 Jack-knife test, we remove a recording from one earthquake at a time at individual seismic stations. Hence, we obtain n estimates of peak-ratio values where n is the number of available events. The mean and standard-deviation of this set of n estimates can then be calculated. And we present the error as the coefficient of variation (obtained by dividing the standard-deviation by the mean) in percentages.

The maximum error in the frequency band of 0.5-1, 1-2, 2-4, and 4-8 Hz, are 14.7%, 16.2%, 10.8%, and 19.0%, respectively. However, the typical errors within each frequency band are significantly smaller than the maximum (Figure 3.6). On average, the error in the frequency band of 0.5-1, 1-2, 2-4, and 4-8 Hz are 3.3%, 2.7%, 2.4%, and 3.5%. Therefore, the error in our peak-ratio computation is considerably less than 5%.

3.2.3 Distribution of Frequency Exponent Across Japan

As shown in Figure 3.4 peak-ratio is generally increasing with frequency. We directly measure this frequency dependency of peak-ratio at Hi-net stations by calculating the

frequency exponent m. Large frequency exponent corresponds to a strong frequency dependency at the particular station and vice-versa. Two examples of estimated frequency exponents at two contrasting stations are shown in Figure 3.7. The first is from station MKIH from the Kagawa prefecture in the northeastern Shikoku (Figure 3.7 top). At this station strong peak-ratio frequency dependency can be seen, which is illustrated by the steep line of best fit with a large frequency exponent value ($m = 0.52$). Conversely, the frequency exponent value at the second example, station KMIH from eastern Tohoku (Figure 3.7 bottom), is small ($m = 0.16$), with a shallower line-of-best-fit. This signifies a rather weak frequency dependency of peak-ratio at this particular station.

In Figure 3.8, we present the corresponding spatial distribution of frequency exponents at Hi-net stations. Only Hi-net stations that have four peak-ratio values across each of the four frequency bands are shown. The range of frequency exponents found in our analysis is rather wide at 0.01 to 1.71, but most estimates fall within the range of 0.01 to 0.80. The average frequency exponent is 0.33 with a standard-deviation of 0.23. With regard to the spatial distribution of frequency exponents, we see no clear split between east and west Japan unlike what we saw with the peak-ratio estimation. Instead, we see strong frequency dependency at some more localised areas. For example, to the East, we can find strong frequency dependency ($m > 0.375$) at the Sendai plain and central Tohoku region, as well as north Hokkaido. And to the West, we can see similar strong frequency dependency in the Chugoku and Shikoku regions, especially in the region along the Seto inland sea.

With regard to the frequency exponent computation, we measure the fit of the straight line to the observed peak-ratio data. We do so by calculating the *root-mean-square-error* (rmse) which can be obtained from the formula:

$$\text{rmse} \equiv \sqrt{\frac{\sum_{i=1}^{N}(\text{res}_i)^2}{N}} \ . \tag{3.1}$$

Here, $N = 4$ corresponds to the four frequency bands used in this study. And res_i

corresponds to the residual between the observed peak-ratio data and the modelled peak-ratio value given by the line of best fit, in the i^{th} frequency band. In this regard, the range of root-mean-square-errors found in our Hi-net analysis goes from 0.002 to 0.198. However, typical values are less than 0.070, with an average of 0.042 (Figure 3.9).

3.3 Discussions

In order to interpret the distribution of peak-ratios and their frequency dependency in Japan, we categorised Hi-net stations according to geological activity, and the age of the geological formation. To make the categorisation according to the level of geological activity, we combine several types of data. More specifically, we use information on geomorphological classification in Japan from Wakamatsu et al. (2005), the locations of active volcanoes in Japan from the National Catalogue of the Active Volcanoes in Japan (2013), and the map of active fault traces in Japan from the Digital Active Fault Map of Japan (2002). As for the categorisation according to the geological age, we refer to the map of geologic age in Wakamatsu et al. (2005).

3.3.1 Interpretation of Peak-Ratios and their Frequency Dependency in Japan in Relation to Geological Activity

According to Kubanza et al. (2007) and Nishimura (2012), peak-ratio values can be attributed to the level of geological activity in the region surrounding the seismic station. Particularly, high peak-ratios can be found in geologically active regions and vice-versa. Therefore, the large peak-ratios in east Japan (Figure 3.4) may be attributed to the presence of active volcanoes in the area, given by the fact that the volcanic front is running along this part of Japan. Conversely, the lower peak-ratios in west Japan (Figure 3.4) may be attributed to the scarcity of active volcanoes in the Kinki, Chugoku, and Shikoku regions. For the same reason, the island of Kyushu displays large peak-ratios

for a region in the West because of the presence of active volcanism on the island. And similarly, the Iwate region of east Tohoku shows small peak-ratios for a region in the East because of its unique geological settings compared to the surrounding areas (older formation, not passed by the volcanic front).

Thus, to examine the above interpretation more systematically, we classify Hi-net stations into several categories: (i) active fault group; (ii) active volcano group; (iii) plains and sediments group (iv) active volcano plus active fault group; and (v) non-active group. This classification is the same one used in Nishimura (2012). The five groups are exclusive from one another. The active fault group (Category i) consists of stations within 20 km from at least one active fault trace, as inferred from the Digital Active Fault Map of Japan (2002). The active volcano group (Category ii) consists of stations within 20 km from at least one active volcano whose coordinates are documented in National Catalogue of the Active Volcanoes in Japan (2013). If a station is within 20 km from at least one active fault and one active volcano, then that station is categorised into the active volcano plus active fault group (Category iv). The plains and sediments group (Category iii) consists of stations that fall into areas classified as *terrace covered with volcanic ash soil*, *natural levee*, *back marsh*, *abandoned river channel*, *delta and coastal lowland*, *marine sand and gravel bars*, *sand dune*, *reclaimed land*, and *filled land* in Wakamatsu et al. (2005). Finally, if a station belongs to neither of these groups (that is, it is more than 20 km removed from an active volcano and an active fault, and is not located on a plain), that station is categorised into the non-active group (Category v).

In Figure 3.10 we show the distributions of peak-ratio with regard to the above categorisation at the four frequency bands. It shows that categories that include active volcanoes (Category ii and iv) can be mostly found in the east Japan. Peak-ratios at these groups are typically quite high, especially compared to those found in the non-active regions (Category v). Furthermore, stations in Iwate Prefecture — which show small peak-ratios even though they are located in the east side — are mainly classified

as non-active (Category v). Thus our results support the interpretation that connects high peak-ratio values in east Japan with presences of active volcanoes.

This interpretation, linking peak-ratio thus scattering strength to tectonic setting or volcanic activity is aligned with other studies in the region. For example, the split between eastern and western Japan in relation to the strength of seismic scattering was also documented in Carcolé and Sato (2010), where the distribution of S wave scattering loss parameter Q_s^{-1} in Japan was calculated using data from the same Hi-net network based on the MLTWA method. Carcolé and Sato (2010) similarly shows that there is a strong scattering attenuation in the East, and a much weaker scattering attenuation in the West. Likewise, they attributed the strong seismic scattering in the East to the location of the volcanic front. Ogiso (2018) also estimated the scattering coefficient g_0 in the southwestern Japan using a Monte-Carlo simulation based envelope fitting approach, and mapped the results onto a 3D space tomographically using sensitivity kernels. Similarly, strong seismic scattering was found on the island of Kyushu where volcanic activity is much more prominent compared to other areas in the study.

Similar contrast can also be observed when comparing reported values of ε and a from areas in the East and West. For example, Yoshimoto et al. (1997) analysed seismogram envelopes from the Nikko region, which is located in the eastern half, in the vicinity of the volcanic arcs. The reported ε estimate is in the range of 5-8%, whereas a estimate is in the range of 0.3-0.8 km. This kind of numbers is affirmative of strong scattering heterogeneities. On the contrary, estimated statistical parameters for western Japan may show longer correlation distance and weaker rms fractional fluctuation in velocity. This has been shown by the results of finite difference simulations. For example, Emoto et al. (2017) estimated the best-fit combination of $\varepsilon = 5\%$ and $a = 3.1$ km for southwestern Japan. Additionally, Kobayashi et al. (2015) indicated that an ε value of 3% and an a value of 1 km are able to model the crustal heterogeneity in the Chugoku region of western Japan.

For a more quantitative examination with regard to the above categorisation of peak-ratios, we perform the t-value test or simply t-test. This test is a statistical tool to evaluate whether two sample means are statistically different from one another (e.g., Brase and Brase (2013)). In relation to this, we put together the mean plus-and-minus 95% confidence interval, standard-deviation, and number of stations with regard to our peak-ratio estimates, classified according to the various categories in Table 3.1. From the table, we see that the non-active regions (Category v) consistently exhibits the smallest peak-ratios across all frequency bands (0.13-0.21). The largest peak-ratios can be found in Category iv (0.24-0.34), except in the 2-4 Hz frequency band where it is second from largest (the largest being Category iii). Furthermore, according to the t-test results, the differences in peak-ratios between Category v and Category iv are statistically significant with at least 95% confidence level in all frequency bands. This further reinforces the contrast in peak-ratios between active and non-active regions found in Japan obtained from the Hi-net stations data.

In Figure 3.11 we present the distributions of frequency exponent with regard to the same aforementioned categorisation. The large frequency exponents in the Sendai plain (central Tohoku) and north Hokkaido can be attributed to stations belonging to Category iii and v. Whereas to the West, large frequency exponents in the Shikoku and Chugoku regions can be attributed to stations belonging to Category i and v. An interesting observation is how active regions in east Japan that are close to active volcanoes (Category ii and iv) are showing smaller frequency exponents compared to others. This suggests that even though we see strong seismic scattering at active volcanoes (as inferred from the peak-ratios), the strong small-scale heterogeneities that cause the scattering can be rather depleted in short-wavelength elements.

In Table 3.1 we similarly present the mean plus-and-minus 95% confidence interval, standard-deviation, and number of stations with regard to the frequency exponent estimates, classified into the different categories. The largest frequency exponent ($m = 0.40$)

can be found in the plains and sediments (Category iii), whereas the smallest estimates ($m < 0.30$) can be found near the active volcanoes (Category ii and iv). t-test results show that the differences between Category iii and ii, and between Category iii and iv are statistically significant at at least 95% confidence level. This indicates a contrast in the power spectra between sediments and active volcanoes. Small-scale medium heterogeneities in the plains and sediments are richer in short-wavelength components (smaller κ), while small-scale medium heterogeneities at active volcanoes are poorer in short-wavelength components (larger κ).

In fact, this interpretation is consistent with information obtained from acoustic well log observations in Japan. Using data from five wells with depths ranging from roughly 1 to 3 kilometres, Shiomi et al. (1997) showed that for the first few kilometres, spectral decays obtained for wells located at an active volcano group (Kuju volcano group, Kyushu) are stronger (larger κ) compared to those found in wells at sedimentary rock formations (Kanto plain). Furthermore, spectral characteristics of heterogeneity obtained from inversion of S wave peak-delay times in the southern Aegean (Ranjan et al., 2019) showed strong seismic scattering and small κ in the shallow depths (<20 km) across the Peloponnese region. They attributed this trait to upper crustal layers made out of sedimentary rocks and a concoction of oceanic and continental crust materials scrapped off from the subduction of the oceanic lithosphere and thrust upon the continental lithosphere (accretionary sedimentary wedge). A similar remark can be made for the sediments and plains in our results, where we can find the largest frequency exponent estimates (hence small κ) in addition to the moderately large peak-ratio. Therefore, we surmise that large frequency exponents in our results may represent shallow formations that mostly consisted of sedimentary rocks which may incorporate rich small-scale medium heterogeneities in short-wavelength elements and thus a clear scattering frequency dependency.

3.3.2 Interpretation of Peak-Ratios and their Frequency Dependency in Japan in Relation to the Age of the Geological Formation

We saw Hi-net stations in the East mostly consist of large peak-ratios (Figure 3.4) and in the previous section we attributed this to the tectonic activity in the region particularly to the distribution of active volcanoes along the volcanic front. Some areas however are showing small peak-ratios which we can categorise as non active areas. In particular, the Iwate Prefecture whose geology is mostly consisted of older geological units shows this characteristic. And so, in addition to comparing the results of peak-ratio and its frequency dependency to the distributions of active faults, active volcanoes, and sediments, we also made comparisons with respect to geological age. In this regard, Hi-net stations are classified according to map of geologic age found in Wakamatsu et al. (2005), thus grouping them according to the age of the geological formation where the station is installed in.

According to the map of geologic age by Wakamatsu et al. (2005), older rock formations (Pre-Tertiary) can be mostly found in the Iwate Prefecture, and in western Japan apart from Kyushu (i.e., precisely where small peak-ratios can be identified). In fact, in Figure 3.12 we show the distributions of peak-ratio categorised according to the geological age at the four frequency bands. We can clearly see that small peak-ratios are mostly distributed in rocks dated as Pre-Tertiary.

In accordance to this, in Table 3.2 we compile the peak-ratio mean plus-and-minus 95% confidence interval, standard-deviation, and number of stations, classified according to geological age. The Pre-Tertiary age group always show the lowest peak-ratio estimates across all frequency bands (0.10-0.15). Whereas the largest peak-ratios (0.20-0.33) can be found in the Quaternary group which mostly consists of volcanic rocks (Wakamatsu et al., 2005), except in the 0.5-1 Hz frequency band where it is the second largest (the

largest being the Pleistocene group).

The t-test results corroborate the age discrimination of peak-ratios. At all frequency bands, the peak-ratio differences between the Pre-Tertiary group and the much younger formations (Holocene, Pleistocene, and Quaternary) are statistically significant at least at the 95% confidence level. In addition, peak-ratio in the Quaternary group also shows statistical significance at a minimum of 95% confidence level, when compared to the Tertiary and the Pre-Tertiary groups. This suggests that the distribution of peak-ratio estimates in Japan can be well explained by the age of the geological formation. In which, younger rocks seem to contain stronger inhomogeneities which would introduce stronger seismic scattering hence larger peak-ratios compared to much older rocks.

Thus, geological age is a good descriptor for interpreting peak-ratio distribution in Japan, if not better than level of geological activities (active volcanoes, faults, sediments). But our results from these two classification approaches are supportive of rather than contradictive to each other. This is because younger rocks are more likely to be found in a geologically active region such as near an active volcano. And conversely, older rocks are more likely to be found in a stable, less geologically active region. Therefore, the strong small-scale heterogeneities found in younger rocks may come as a result of more recent geological activities such as fluid intrusions, hydrothermal activities, magmatism, or volcanic activities.

Correspondingly, in Table 3.2 we present the frequency exponent mean plus-and-minus 95% confidence interval, standard-deviation, and number of stations, categorised according to the geological age. The largest and smallest frequency exponent estimates can be found in the Quaternary group and Tertiary group, respectively. However, we find no statistical significance with regard to the frequency exponent when comparing any of the stations groups. In the previous section, we suggested that large frequency exponents may correspond to the distribution of sedimentary rocks. In this regard, the same stations categorised as sediments and plains previously are classified into the

Pleistocene and Holocene age groups here. However, these two geological age groups also include many stations from all other geological activity categories. In other words, geological age cannot differentiate sedimentary formations which was shown to represent the large frequency exponents in our results. Therefore, the age of geological formation together with geological activity can help explain the distribution of peak-ratios in Japan, but only the latter is useful for describing their frequency dependency.

3.4 Summary

We computed the peak-ratio $\Re$ to estimate the scattering strength in Japan using the Hi-net seismometer network. Peak-ratio is observed to be increasing with frequency. So we also directly measure the frequency dependency of peak-ratios at Hi-net stations by computing the frequency exponent m. The effects of the free-surface and topography were mitigated by analysing only Hi-net stations of similar depths and elevations. The spatial distributions of peak-ratio and frequency exponent over Japan can be viewed using the Hi-net stations coordinates themselves. This owes to the network's dense and wide coverage over Japan. The following results can be presented:

- Through performing the delete-1 Jack-knife test, the uncertainty in the peak-ratio computation was estimated to be less than 5% overall. Whereas the fit of the straight line with regard to the frequency exponent computation was obtained by calculating the root-mean-square-error.

- The distributions of peak-ratios were examined by considering the level of geological activity in the surrounding regions and the age of the geological formation where the station is installed in. We interpret that large peak-ratios may indicate strong heterogeneities in young rocks at geologically active regions, and vice-versa. This may also explain the split in peak-ratio between east and west Japan across all frequency bands. Large peak-ratios in east Japan can be attributed to the location

of the volcanic front, and the small peak-ratios in most of western Japan can be attributed to the lack of active volcanoes in the region.

- The distribution of frequency exponent was examined in a similar manner to peak-ratio. There is no clear distinction with respect to geological age. But large frequency exponents can be observed at sediments and plains, especially compared to the small frequency exponents near to active volcanoes, suggesting a contrast in their power spectra. We interpret this as sediments having small-scale heterogeneities richer in short-wavelength components.

- Analyses of peak-ratio and frequency exponent indicate that strong medium heterogeneities at active volcanoes might have induced strong seismic scatterings, but the small-scale heterogeneities themselves might have been particularly poor in short-wavelength components.

Table 3.1 Peak-ratio $\Re$ and frequency exponent m mean plus-and-minus 95% confidence interval for all used Hi-net data, and at stations categorised as: (i) active fault; (ii) active volcano; (iii) plains and sediments; (iv) active volcano plus active fault; and (v) non-active group. Also given are the standard-deviation (S.D.) and the number of available stations (N).

	$\Re$			m		
		S.D.	N		S.D.	N
All data						
0.5-1 Hz	0.148 ± 0.010	0.10	376			
1-2 Hz	0.143 ± 0.008	0.08	382	0.332 ± 0.026	0.23	301
2-4 Hz	0.172 ± 0.011	0.10	382			
4-8 Hz	0.233 ± 0.014	0.13	377			
Category i (active fault)						
0.5-1 Hz	0.150 ± 0.017	0.10	145			
1-2 Hz	0.148 ± 0.014	0.09	146	0.328 ± 0.043	0.23	115
2-4 Hz	0.170 ± 0.017	0.10	146			
4-8 Hz	0.228 ± 0.022	0.13	145			
Category ii (active volcano)						
0.5-1 Hz	0.164 ± 0.030	0.06	18			
1-2 Hz	0.168 ± 0.021	0.04	18	0.283 ± 0.057	0.10	15
2-4 Hz	0.175 ± 0.045	0.09	18			
4-8 Hz	0.280 ± 0.061	0.12	18			
Category iii (plains & sediments)						
0.5-1 Hz	0.174 ± 0.038	0.10	31			
1-2 Hz	0.151 ± 0.033	0.09	33	0.396 ± 0.090	0.22	26
2-4 Hz	0.256 ± 0.046	0.13	33			

Table 3.1 continued from previous page

4-8 Hz	0.268 ± 0.037	0.10	33			
Category iv (active volcano + active fault)						
0.5-1 Hz	0.237 ± 0.048	0.10	20			
1-2 Hz	0.169 ± 0.030	0.06	20	0.252 ± 0.084	0.16	17
2-4 Hz	0.220 ± 0.041	0.09	20			
4-8 Hz	0.343 ± 0.057	0.12	20			
Category v (non-active)						
0.5-1 Hz	0.129 ± 0.014	0.09	162			
1-2 Hz	0.132 ± 0.011	0.07	165	0.340 ± 0.041	0.24	128
2-4 Hz	0.152 ± 0.014	0.09	165			
4-8 Hz	0.212 ± 0.021	0.13	161			

Table 3.2 Peak-ratio $\Re$ and frequency exponent m mean plus-and-minus 95% confidence interval for all used Hi-net data, and at stations categorised according to geological age. Also given are the standard-deviation (S.D.) and the number of available stations (N).

	$\Re$			m		
		S.D.	N		S.D.	N
All data						
0.5-1 Hz	0.148 ± 0.010	0.10	374			
1-2 Hz	0.144 ± 0.008	0.08	380	0.332 ± 0.026	0.23	299
2-4 Hz	0.173 ± 0.011	0.10	380			
4-8 Hz	0.233 ± 0.014	0.13	375			
Holocene						
0.5-1 Hz	0.155 ± 0.022	0.10	83			
1-2 Hz	0.145 ± 0.017	0.08	84	0.338 ± 0.052	0.21	65
2-4 Hz	0.187 ± 0.024	0.11	84			
4-8 Hz	0.233 ± 0.025	0.11	83			
Pleistocene						
0.5-1 Hz	0.205 ± 0.025	0.10	70			
1-2 Hz	0.158 ± 0.019	0.08	73	0.333 ± 0.046	0.18	58
2-4 Hz	0.239 ± 0.027	0.11	73			
4-8 Hz	0.311 ± 0.032	0.13	72			
Quaternary						
0.5-1 Hz	0.200 ± 0.050	0.12	25			
1-2 Hz	0.213 ± 0.051	0.12	25	0.345 ± 0.130	0.28	20
2-4 Hz	0.252 ± 0.068	0.16	25			
4-8 Hz	0.329 ± 0.068	0.16	25			

Table 3.2 continued from previous page

Tertiary						
0.5-1 Hz	0.142 ± 0.018	0.08	88			
1-2 Hz	0.138 ± 0.015	0.07	89	0.312 ± 0.058	0.25	75
2-4 Hz	0.142 ± 0.016	0.07	89			
4-8 Hz	0.239 ± 0.024	0.11	87			
Pre-Tertiary						
0.5-1 Hz	0.099 ± 0.013	0.07	108			
1-2 Hz	0.122 ± 0.011	0.05	109	0.340 ± 0.052	0.24	81
2-4 Hz	0.125 ± 0.010	0.05	109			
4-8 Hz	0.153 ± 0.018	0.09	108			

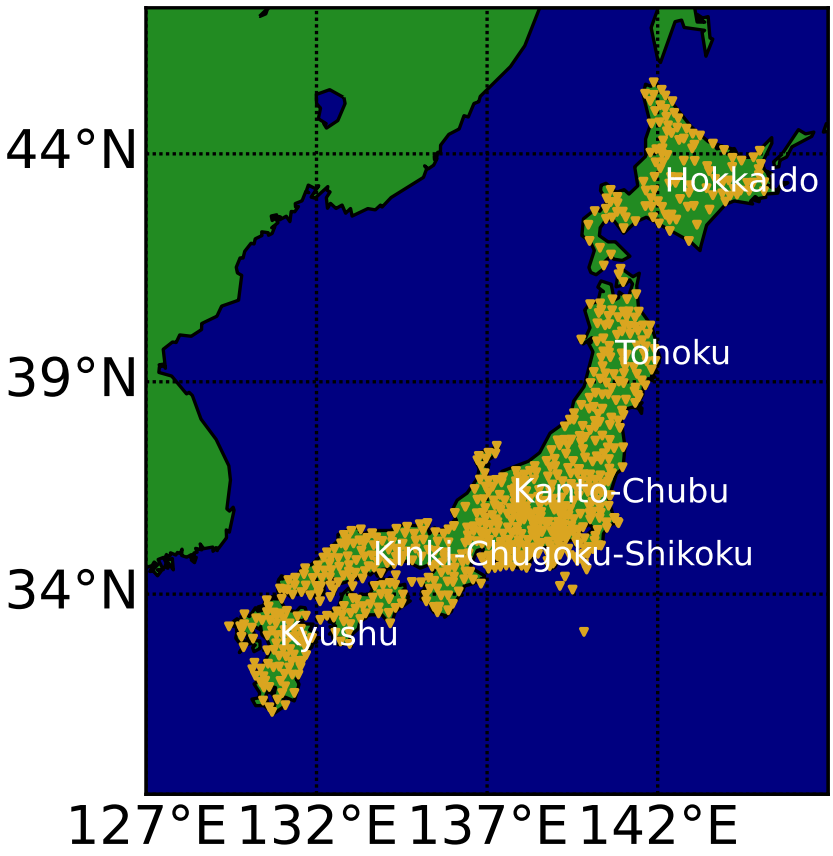

Figure 3.1 The coverage of Hi-net stations in Japan (yellow). There are 803 Hi-net stations with station spacing of 15-20 km. Most stations are located at depths of 100-300 m.

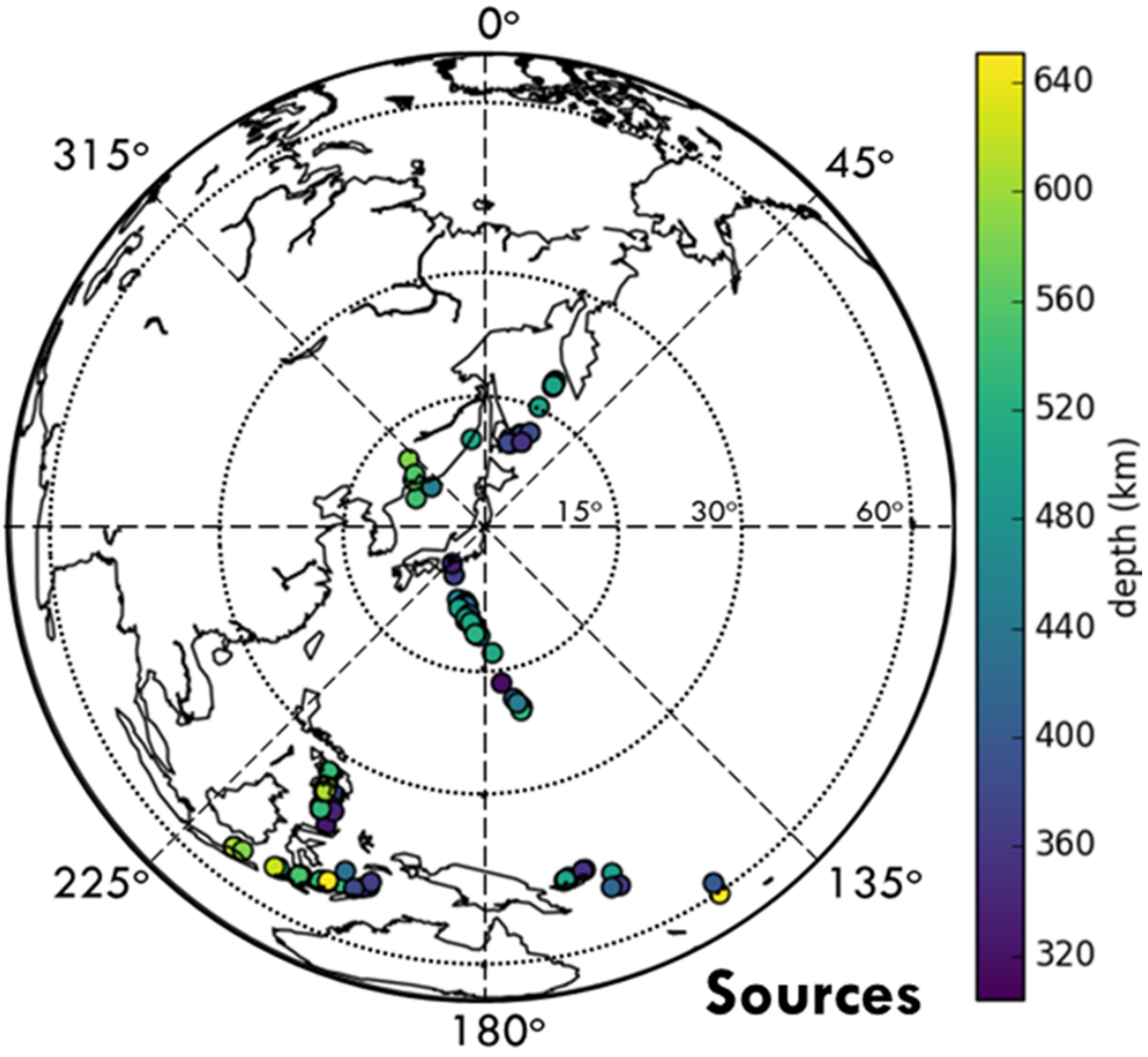

Figure 3.2 99 deep earthquakes (>300 km) used to estimate the peak-ratio values in Japan.

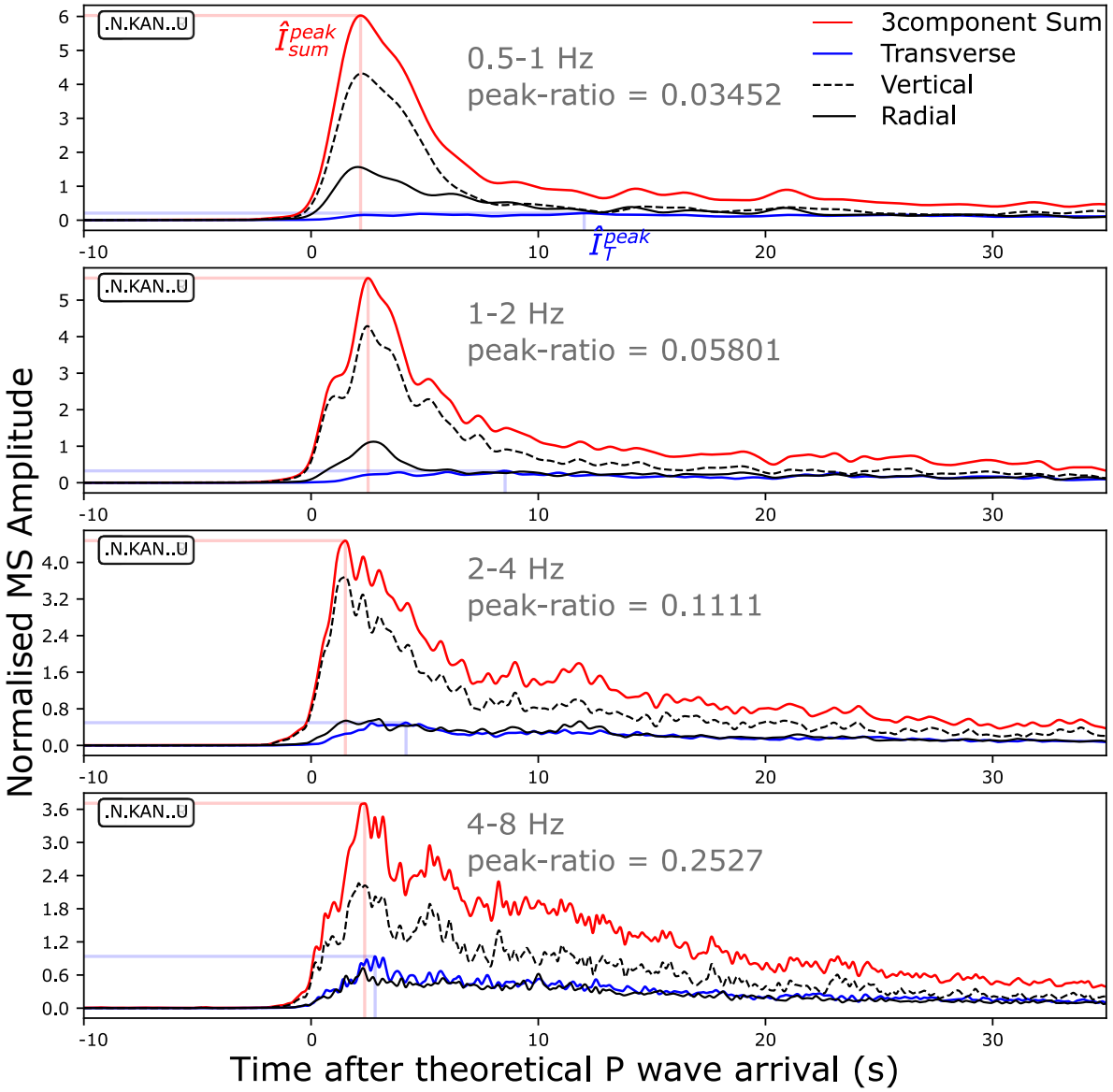

Figure 3.3 Mean squared (MS) envelope example computed at the four frequency bands of 0.5-1, 1-2, 2-4, and 4-8 Hz for station KANH from east Tohoku. Blue traces signify the transverse component envelopes, whilst red traces signify the three-component sum envelopes. Dashed-black and black lines are the vertical and radial component envelopes, respectively. The translucent lines mark the peaks of the transverse and the three-component sum envelopes, and they are denoted here as $\hat{I}^{peak}_{T}$ and $\hat{I}^{peak}_{sum}$, respectively. The peak-ratio $\Re$ is obtained by dividing the former over the latter (i.e., $\Re = \hat{I}^{peak}_{T} / \hat{I}^{peak}_{sum}$). Time is given relative to the theoretical P wave onset according to the ak135 model.

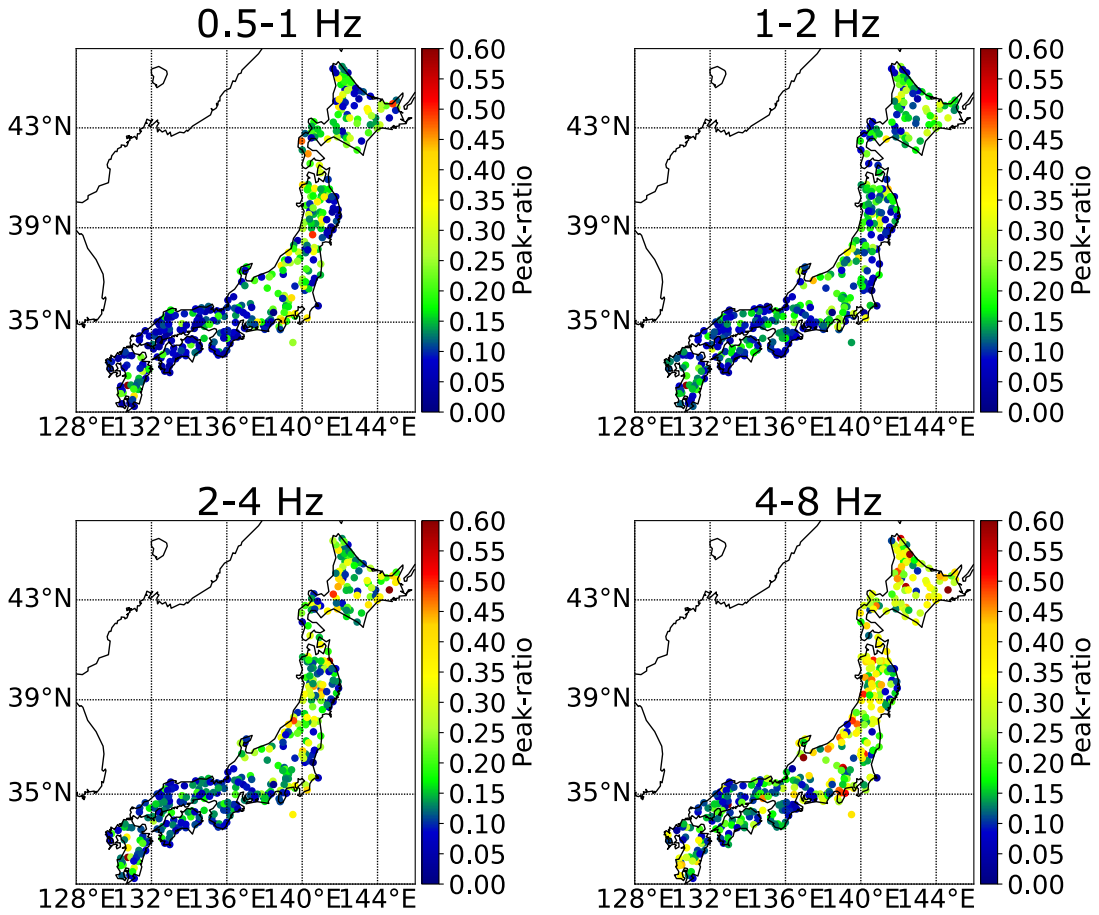

Figure 3.4 Lateral distributions of peak-ratios $\Re$ calculated at the Hi-net stations at four frequency bands: 0.5-1, 1-2, 2-4, and 4-8 Hz. Only stations at similar borehole depths (100-200 m) and installation heights (<400 m) are compared to mitigate the effects of the free-surface and topography. Overall, peak-ratio is increasing with frequency band.

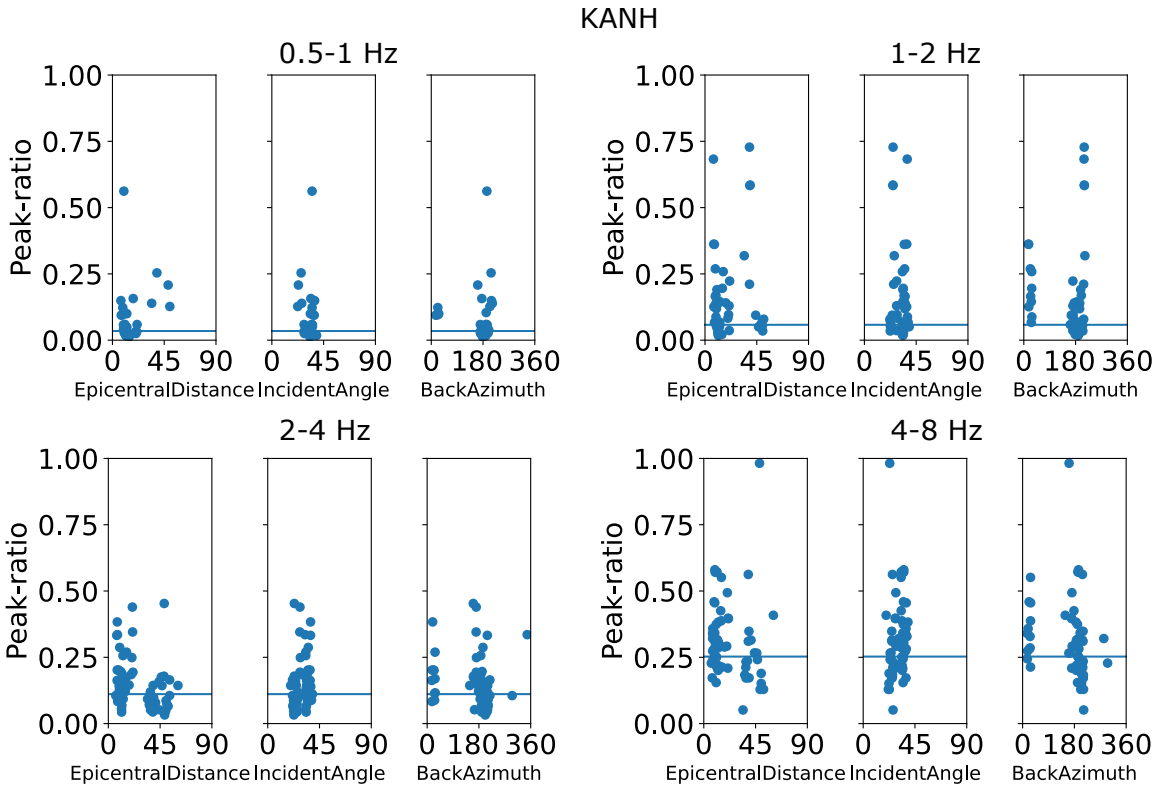

Figure 3.5 Unstacked peak-ratio $\Re$ calculated per event data at station KANH versus the epicentral distance, incident angle, and back azimuth of the event. Horizontal lines mark the estimated peak-ratio value at station KANH from the stacked MS envelopes (Figure 3.3). Units of the horizontal axes are in degrees.

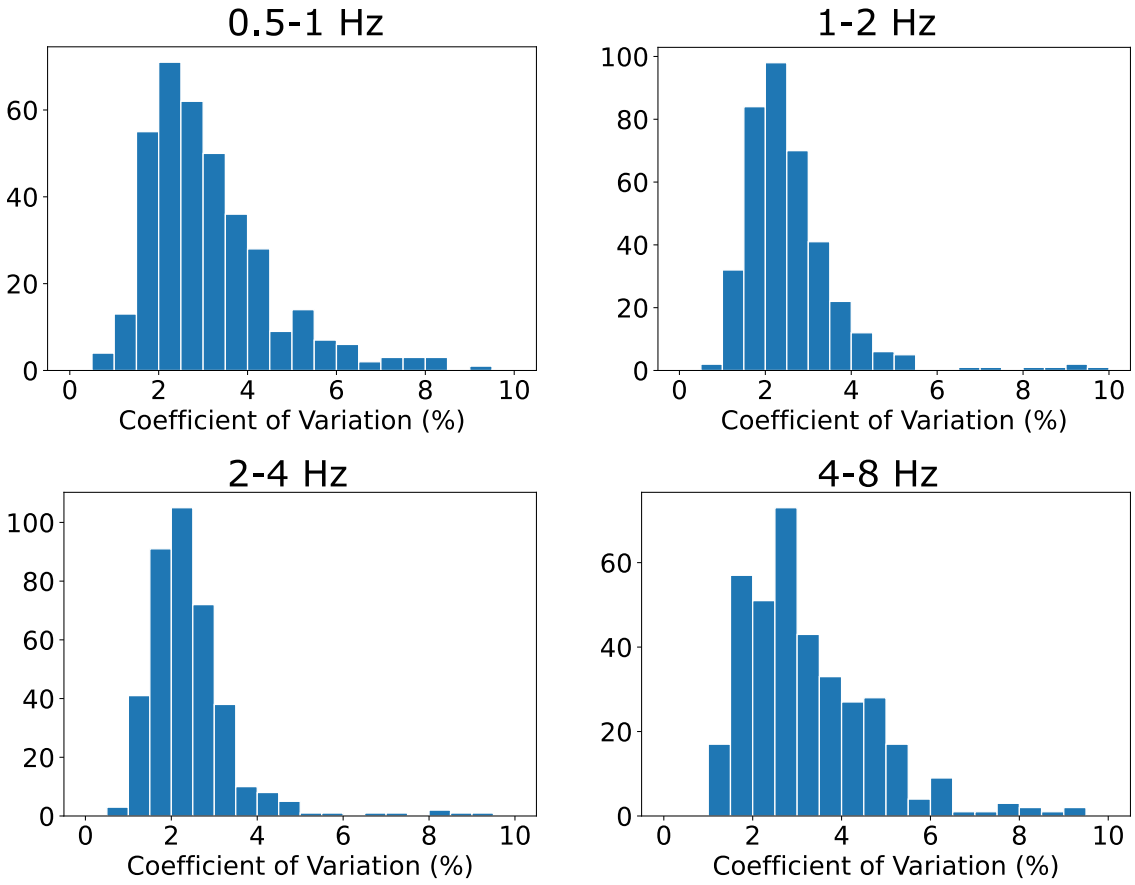

Figure 3.6 Histograms of the coefficient of variations of peak-ratio at Hi-net stations, representing the uncertainty in the peak-ratio computation at four frequency bands: 0.5-1, 1-2, 2-4, and 4-8 Hz. The typical error across all frequency bands is less than 5%.

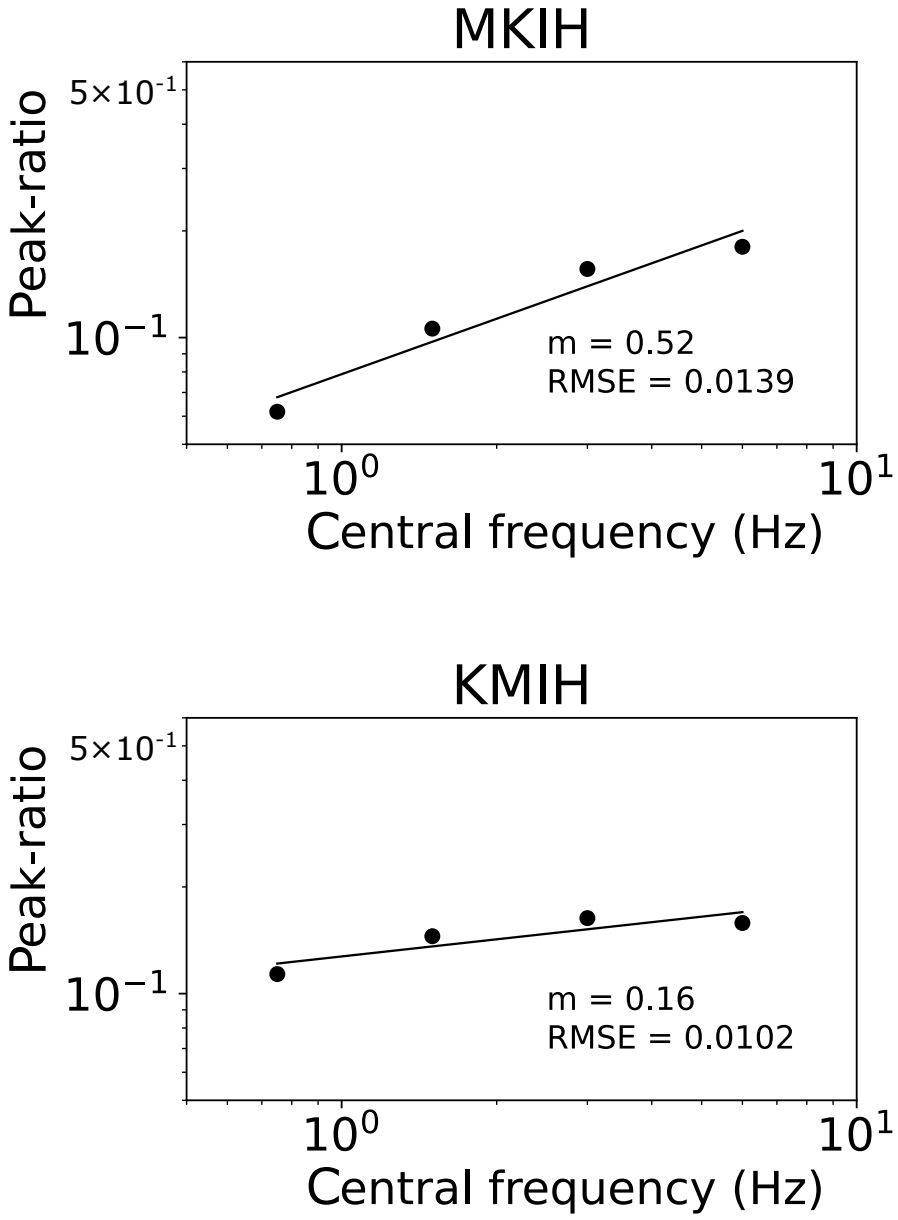

Figure 3.7 Frequency dependency of peak-ratio, quantified by the frequency exponent m. (*top*) Station MKIH from the Kagawa Prefecture of northeastern Shikoku, showing a strong frequency dependency with a large frequency exponent of $m = 0.52$. (*bottom*) Station KMIH from eastern Tohoku region, showing a weak frequency dependency with a low frequency exponent of $m = 0.16$.

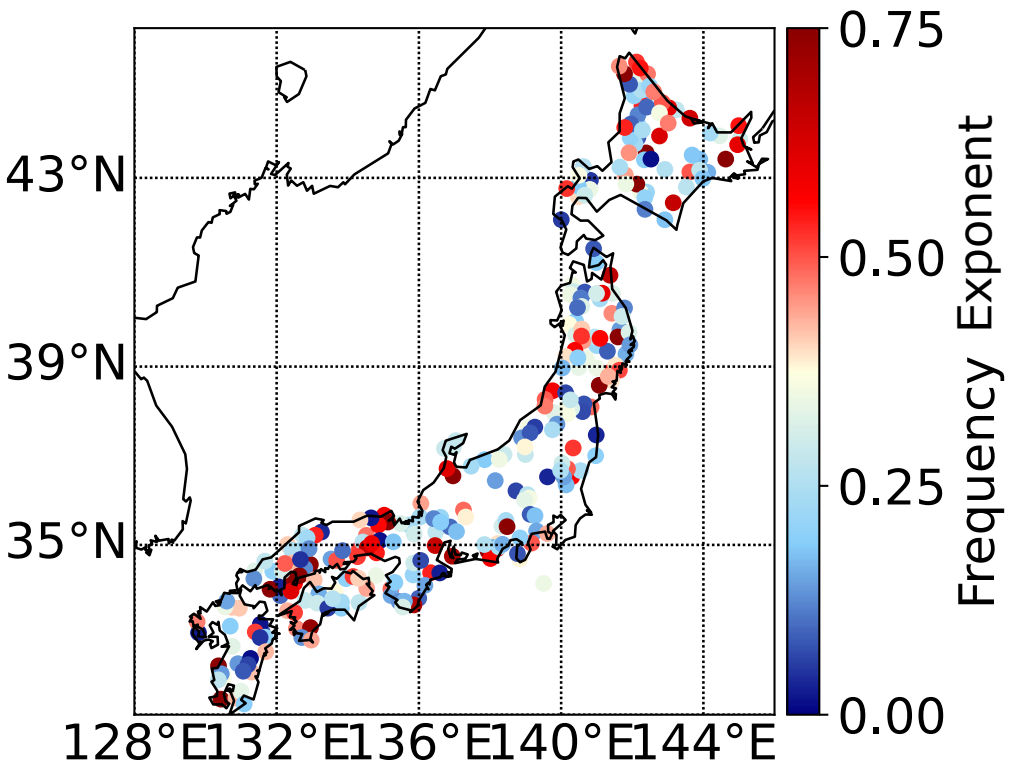

Figure 3.8 Lateral distribution of peak-ratio frequency dependency at Hi-net stations as directly measured by the frequency exponent m. Only stations at similar borehole depths (100-200 m) and installation heights (<400 m) are compared to mitigate the effects of the free-surface and topography.

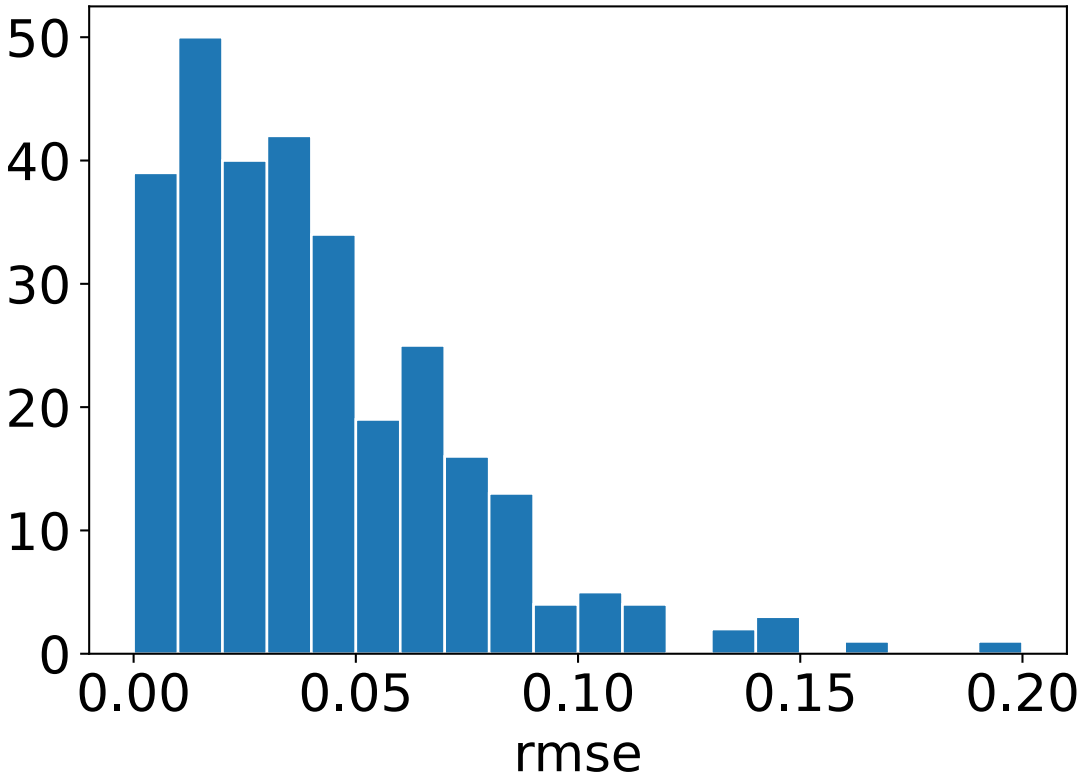

Figure 3.9 Histogram of root-mean-square-errors (rmse) which represents the error in the computation of frequency exponent m at Hi-net stations. The typical error is less than 0.07.

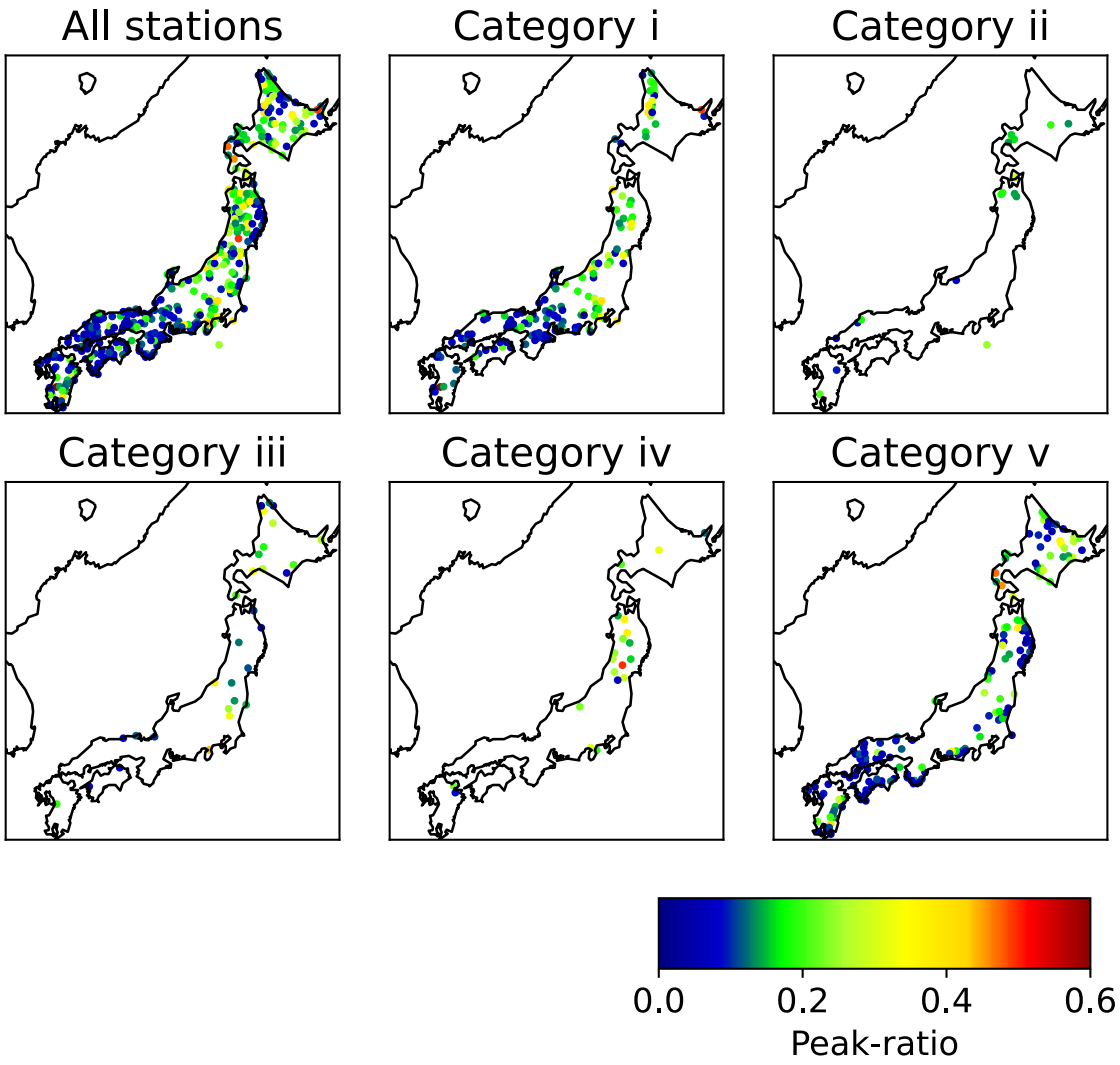

Figure 3.10 Distributions of peak-ratio $\Re$ in Japan, classified into: (i) active fault; (ii) active volcano; (iii) plains and sediments; (iv) active volcano plus active fault; and (v) non-active group. For the frequency band of 0.5-1 Hz.

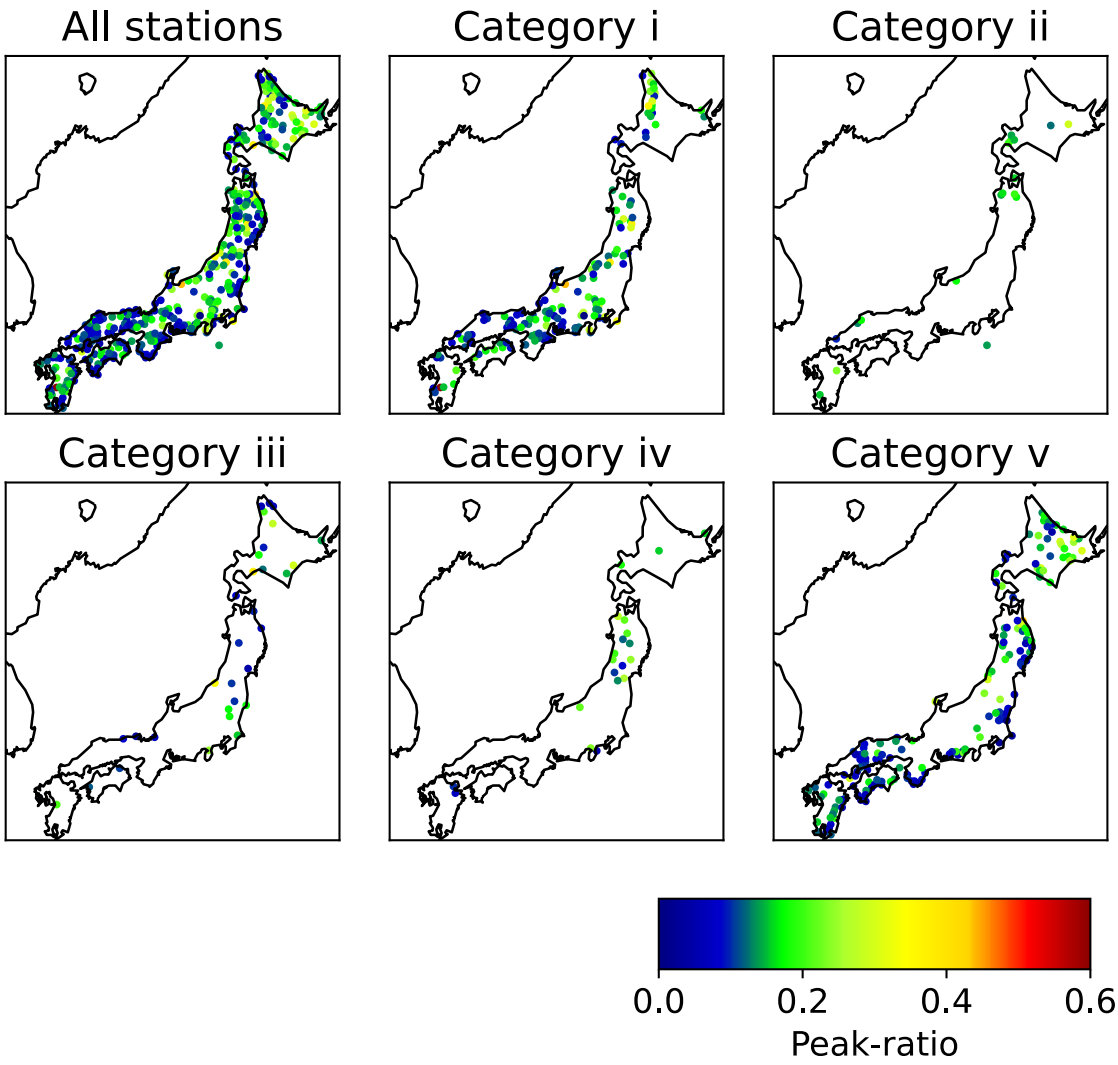

Figure 3.10 (*continued*) For the frequency band of 1-2 Hz.

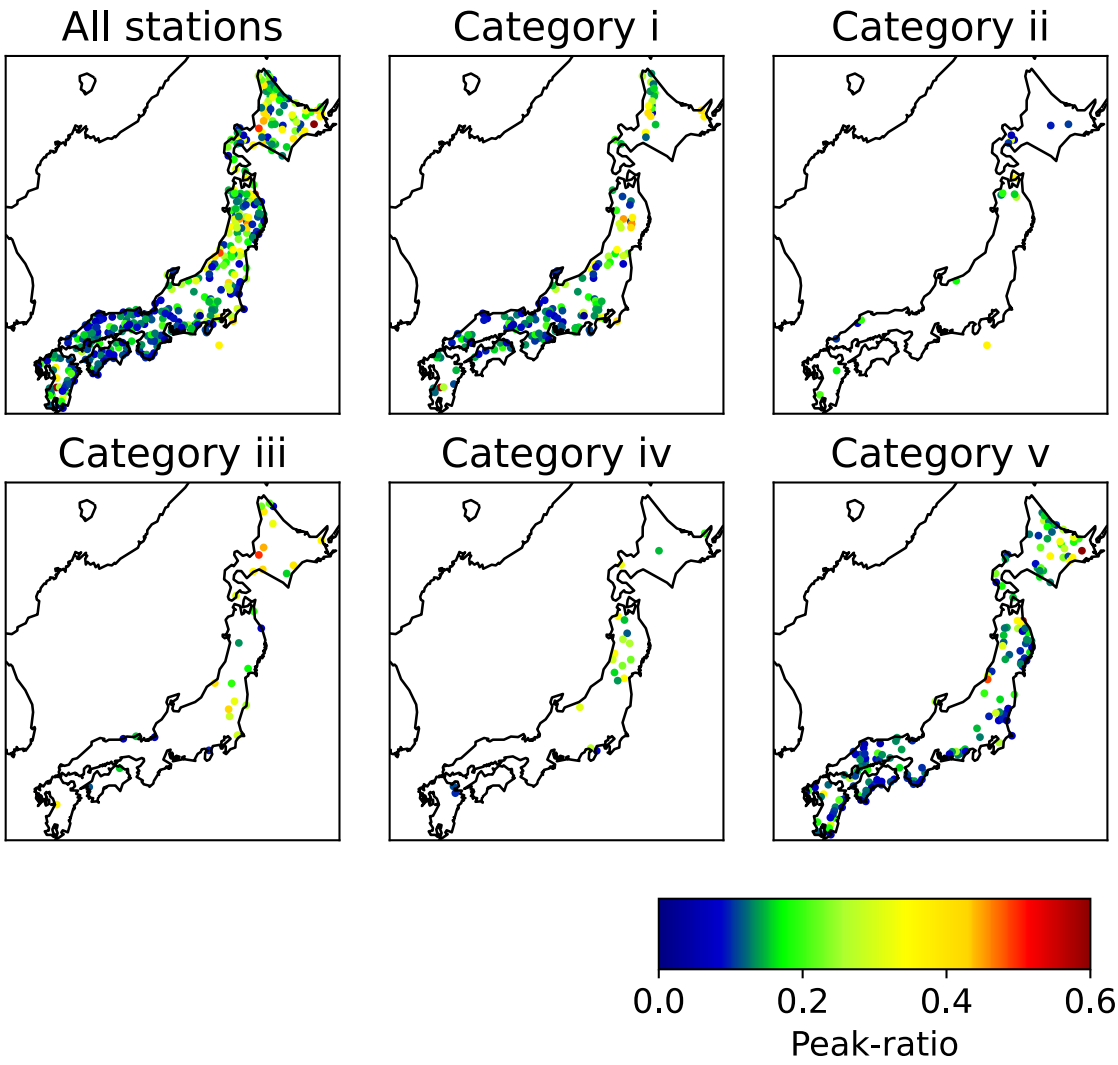

Figure 3.10 (*continued*) For the frequency band of 2-4 Hz.

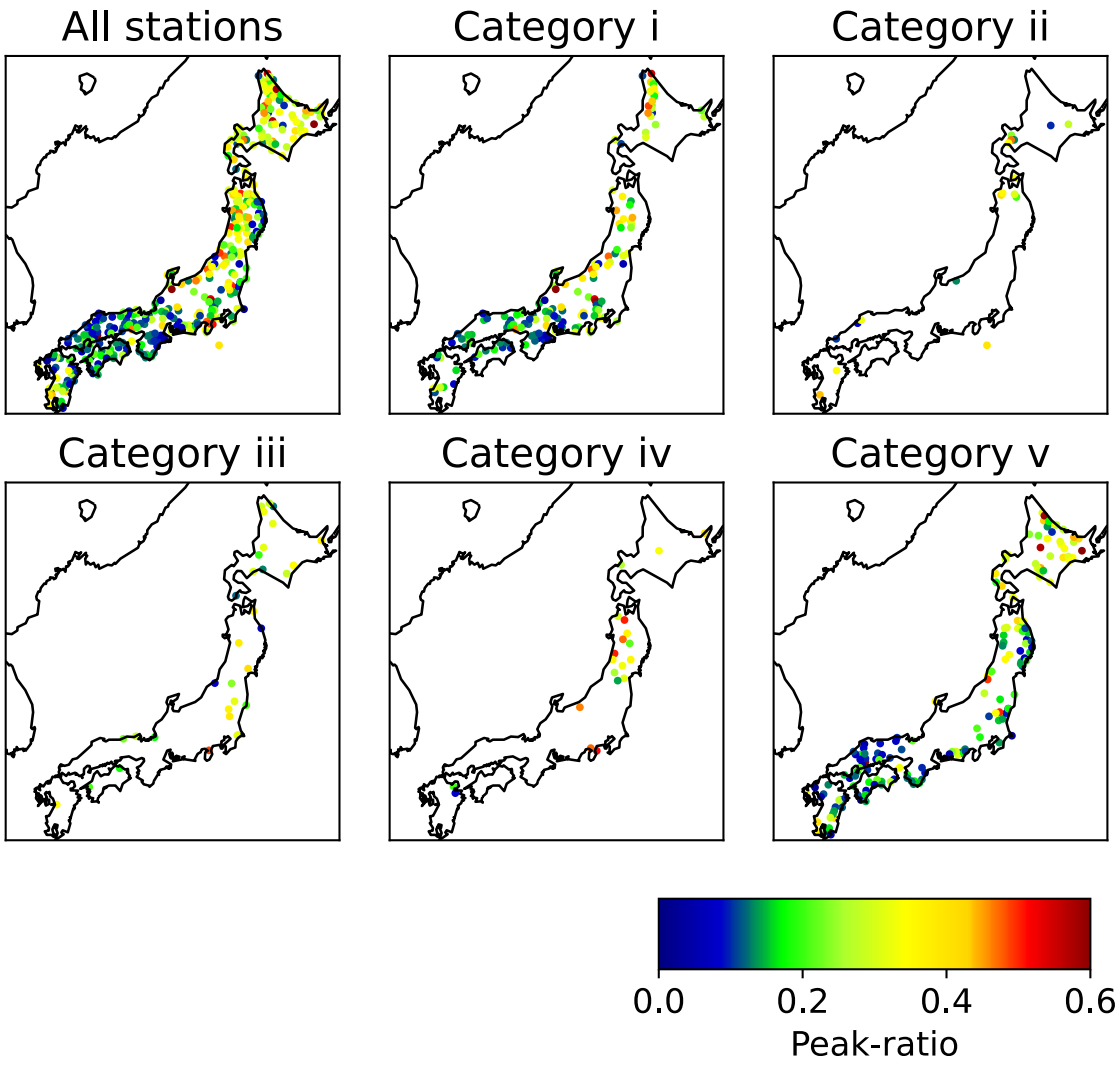

Figure 3.10 (*continued*) For the frequency band of 4-8 Hz.

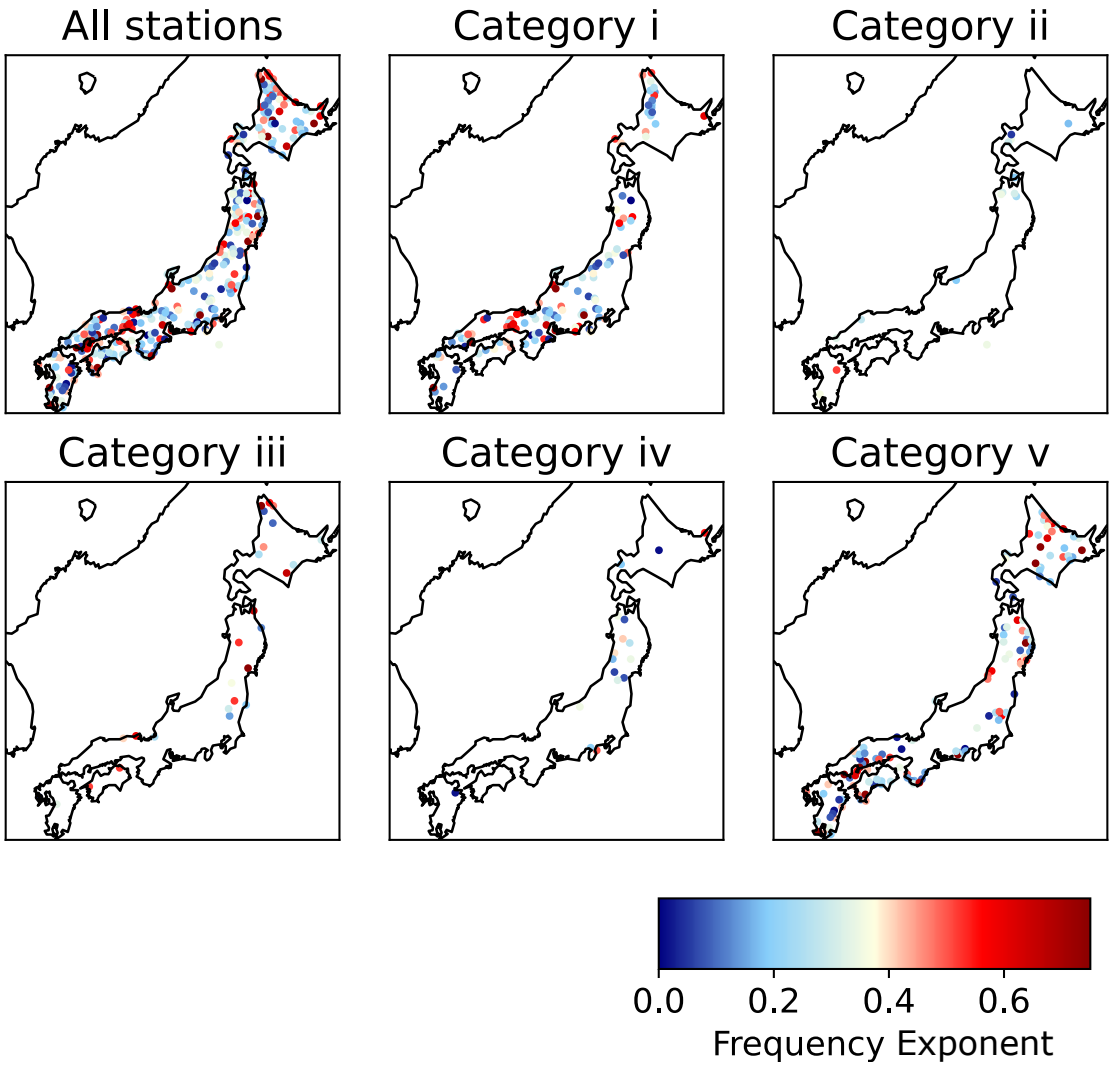

Figure 3.11 Distributions of frequency exponent m in Japan, classified into: (i) active fault; (ii) active volcano; (iii) plains and sediments; (iv) active volcano plus active fault; and (v) non-active group.

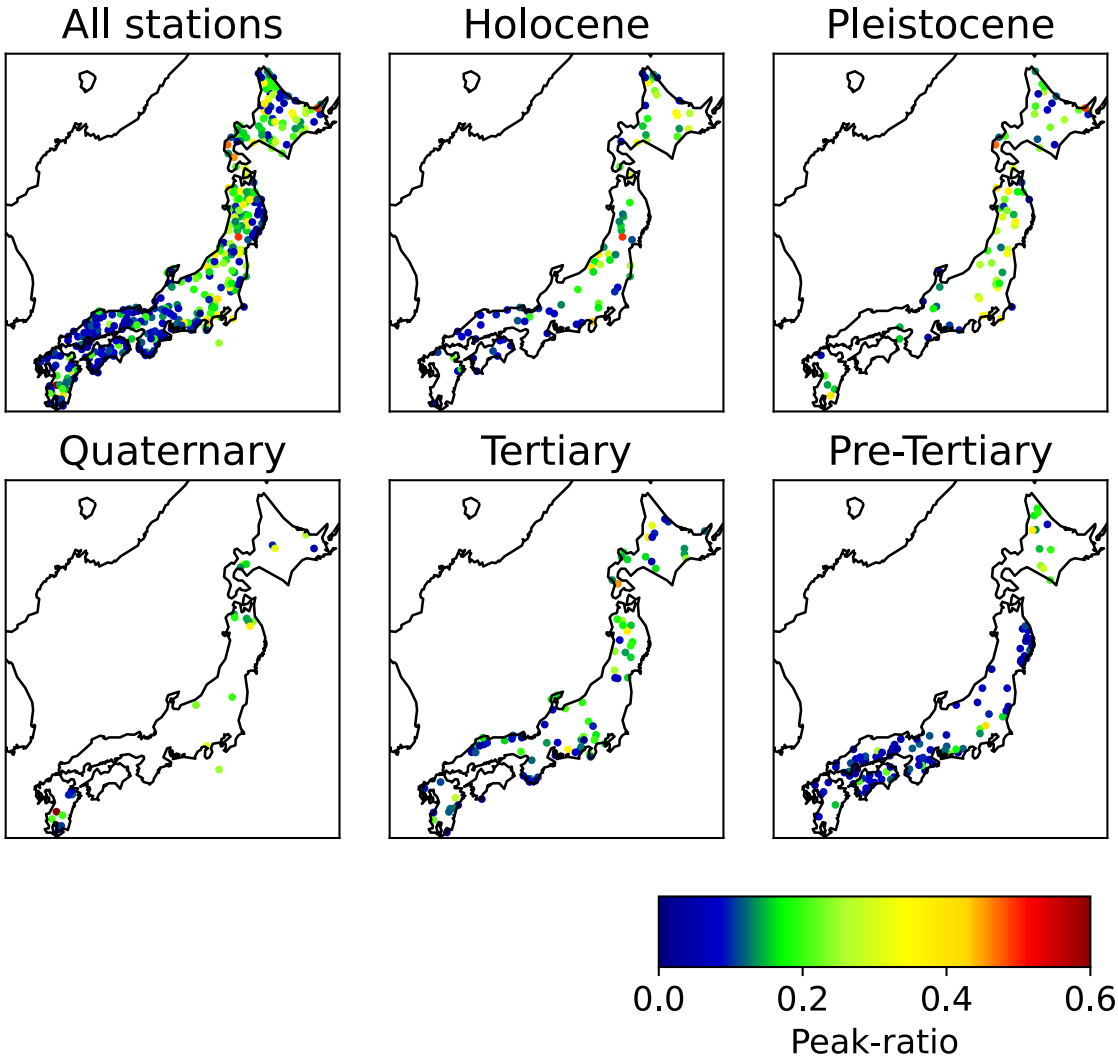

Figure 3.12 Distributions of peak-ratio $\Re$ in Japan categorised according to the age of geological formation. For the frequency band of 0.5-1 Hz.

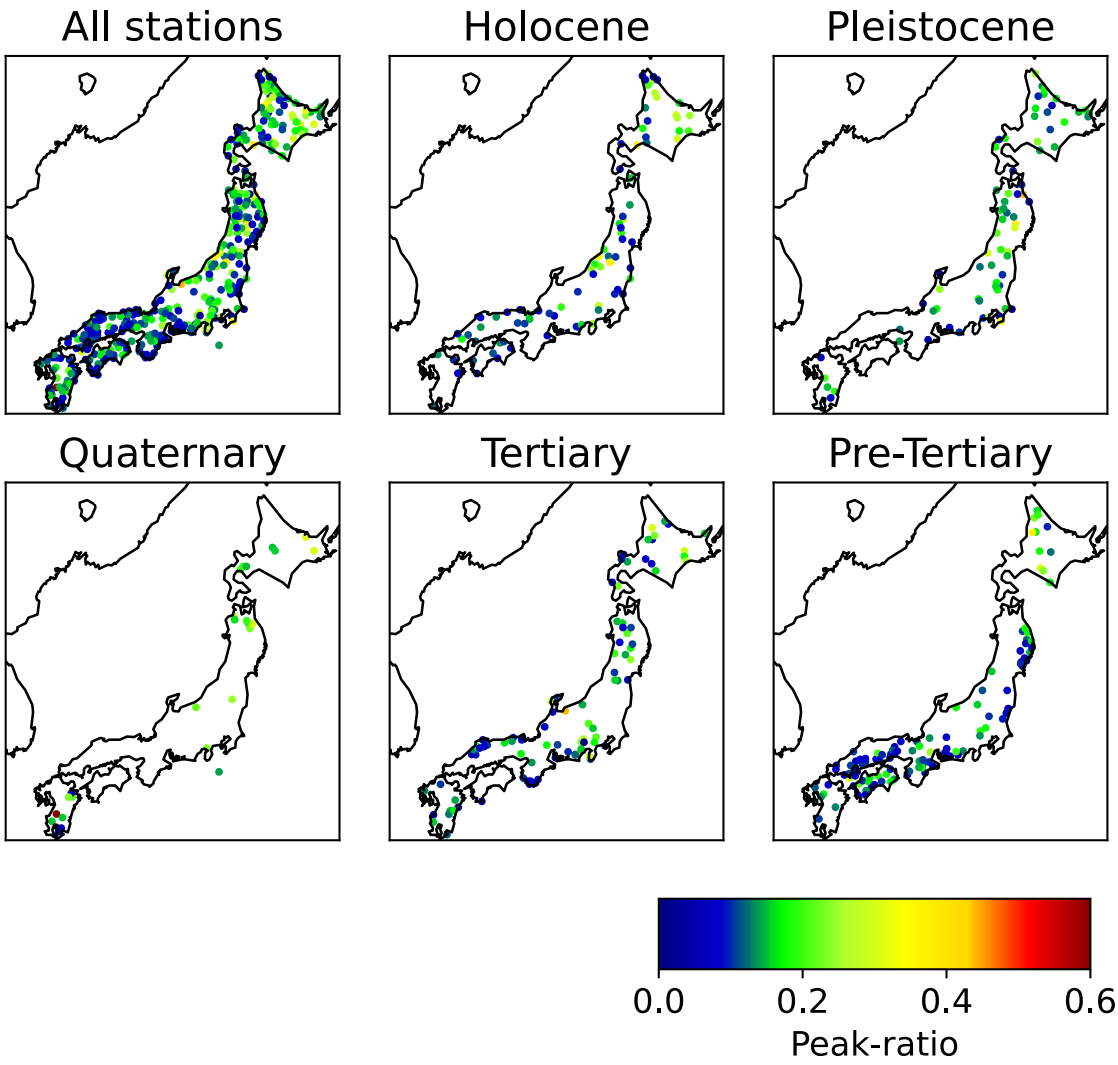

Figure 3.12 (*continued*) For the frequency band of 1-2 Hz.

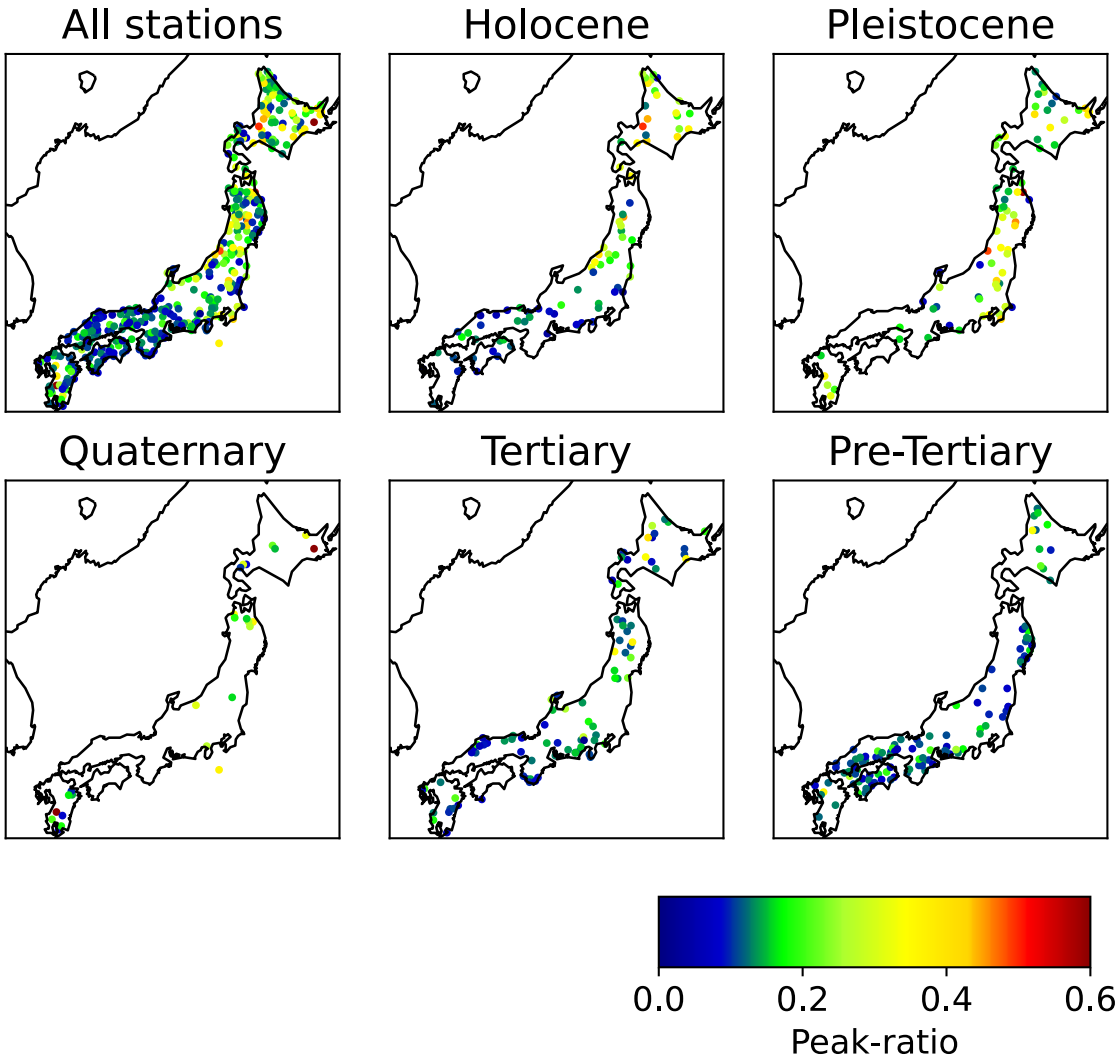

Figure 3.12 (*continued*) For the frequency band of 2-4 Hz.

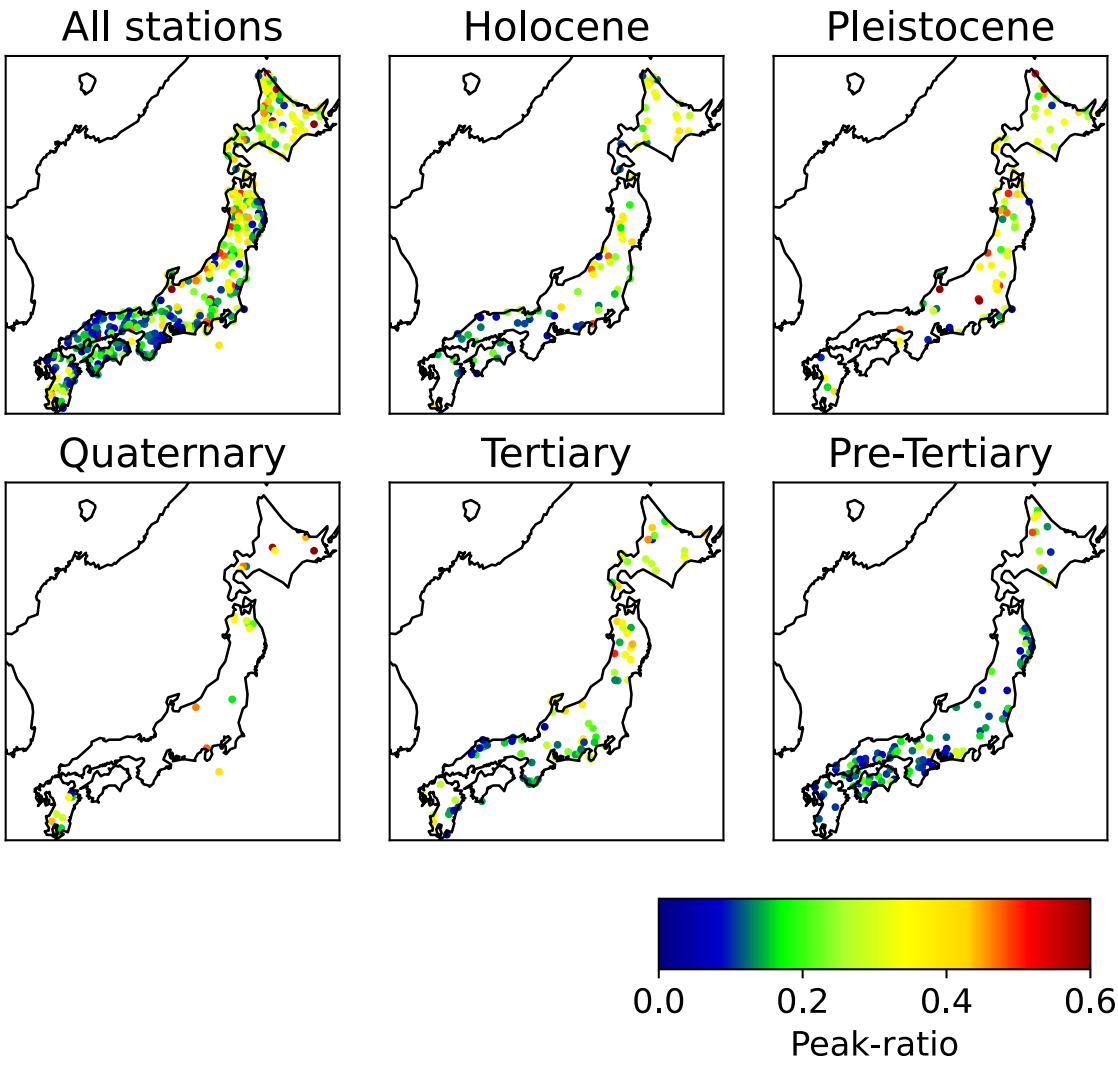

Figure 3.12 (*continued*) For the frequency band of 4-8 Hz.

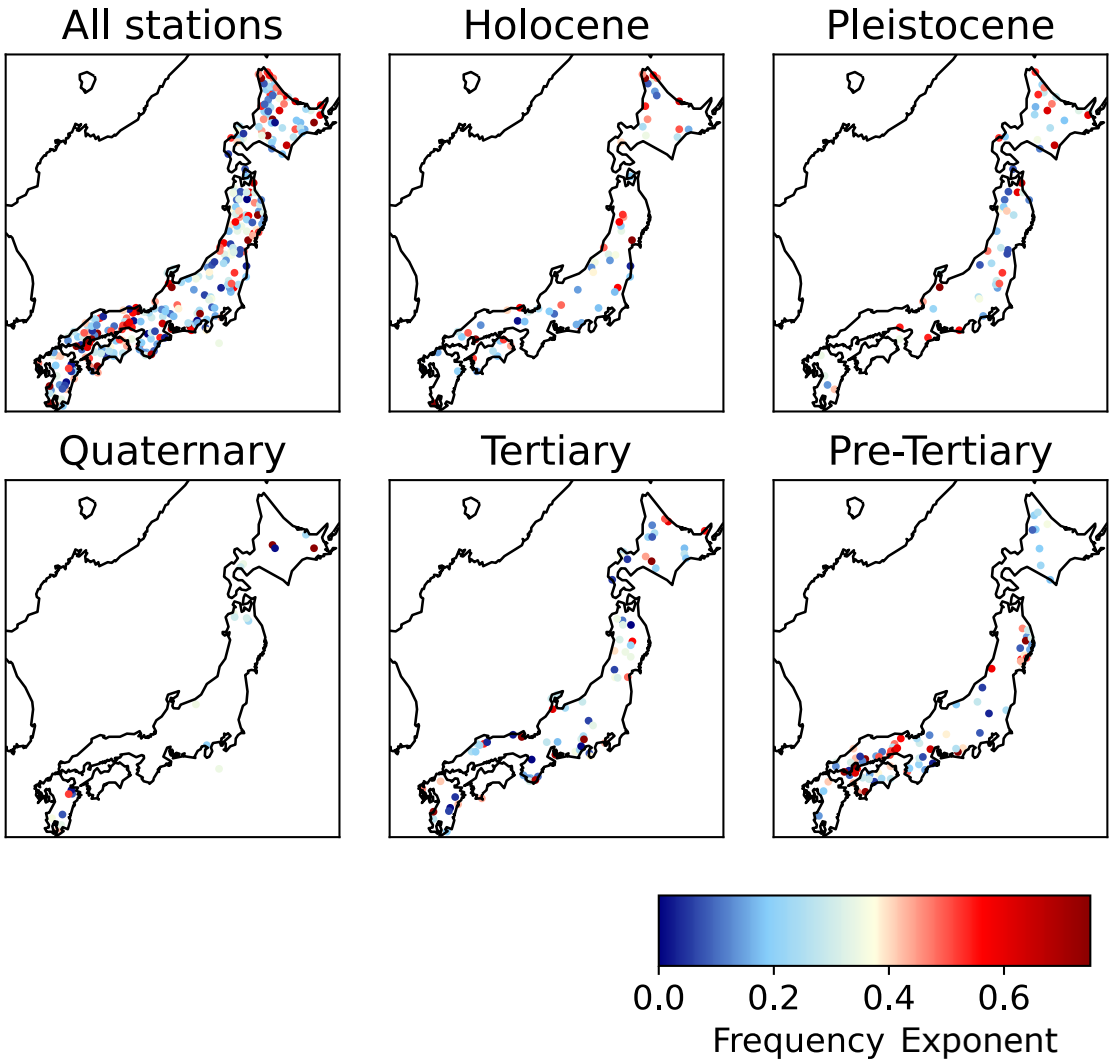

Figure 3.13 Distributions of frequency exponent m in Japan categorised according to the age of geological formation.

Chapter 4

Peak-Ratios and their Frequency Dependency at JMA Stations in Active Volcanoes in Japan

In Chapter 3, we examined the peak-ratios $\Re$ and their frequency dependency at Hi-net stations, and showed that large peak-ratios in Japan are intricately linked to the strong heterogeneities in young rock formations at geologically active regions particularly surrounding active volcanoes. Additionally, the characteristic (roll-off) of the power spectra of the random heterogeneous medium can be inferred from the frequency dependency of peak-ratio, particularly through the computation of the frequency exponent m. But due to the complexities of volcano topographies, topographic effect — as described using numerical simulations in Chapter 2 — can be expected to be influential at active volcanoes.

Given all of the above, however, analysis of peak-ratio and its frequency dependency at the volcano edifices themselves is still missing. Hi-net stations are not positioned on these active volcanoes, therefore we need to turn to other available networks. Particularly, we use the seismometer network deployed at active volcanoes that are operated by the Japan

Meteorological Agency (JMA). Therefore, the scope of this chapter is to categorically examine peak-ratios and their frequency dependency at active volcanoes. We shall discuss peak-ratio and frequency exponent at active volcanoes across Japan while recognising the significance of topography. This chapter should offer a complementary case study to the experiments at Hi-net stations, especially with regard to seismic scattering measurements in Japan.

4.1 Data

According to the National Catalogue of the Active Volcanoes in Japan (2013) published by JMA, there are 111 active volcanoes spread across Japan (Figure 4.1). Out of the 111 volcanic centres, 50 are deemed by the Coordinating Committee for Prediction of Volcanic Eruption to be requiring enhanced monitoring and observation systems for the purpose of volcanic disaster prevention. Following this verdict, JMA maintains and operates permanent observation equipments including seismometers.

We make use of these JMA seismometers to categorically examine the peak-ratios at quaternary active volcanoes in Japan. As the fundamental purpose of these JMA stations is to monitor the activity of these active volcanoes, these stations are installed within 10 km of the active craters at each volcano. The inset in Figure 4.1 shows an example of the JMA seismometer network configuration at a volcano. In this particular example, we show the configuration at the Sakurajima Volcano in southern Kyushu. Similar array configuration can be found at other active volcanoes as well. Altogether, we consider a total of 204 JMA stations for our analysis of peak-ratio and its frequency dependency at active volcanoes in Japan.

Using these JMA stations, we collected seismogram data from 99 seismic events that occurred between 2010 and 2019. These earthquakes are the same set of events that we used in our Hi-net data analysis as elaborated in Chapter 3. Accordingly, the distribution

of these events can be seen in Figure 3.2. With the peak-ratio approach, we can use the same set of events across the entire network. Henceforth, that allows for a systematic survey of seismic scattering at volcanoes across Japan.

4.2 Results

4.2.1 MS Envelopes

To evaluate peak-ratios and their frequency dependency at JMA stations, firstly, we obtained the MS envelopes at individual stations following the procedures developed in Kubanza et al. (2007) which we elaborated in Section 2.2. We use the same bandpass filters to separate our analysis into four frequency bands: 0.5-1, 1-2, 2-4, and 4-8 Hz. Data are rotated into the vertical-radial-transverse (ZRT) components using the back-azimuths information. By calculating the signal-to-noise ratio (S/N), good quality data with S/N of larger than 10 are chosen.

Of the remaining pairs, we computed the squared envelopes which are to be normalised so that we can compare signals from various hypocentral distances and magnitudes. For the normalisation time-window (Equation 2.27), we consider $T = 45$ s, starting 10 s prior to the expected direct P arrival according to the ak135 earth-model. We deem this time-window to be long enough to show the equipartition of P wave energy into all three components in the later coda as a consequence of scattering (Kubanza et al., 2007), but it is not long enough to include the direct S wave arrivals. If the station shows recordings from more than 10 events, we stack the available normalised seismograms to retrieve the MS envelopes for that station, for the different components, and for the multiple frequency bands.

Figure 4.2 shows an example of MS envelopes at station KOMA which is used to monitor the Hokkaido-Komagatake Volcano. Shown are the transverse, vertical, radial, and the three-component sum MS envelopes at the frequency bands of 0.5-1, 1-2, 2-4, and

4-8 Hz. There is a couple of differences in terms of MS envelope characteristics to those typically found at the Hi-net stations. For once, the transverse envelope is already quite conspicuous even in the lower frequencies. Moreover, vertical motion is not necessarily the dominant movement in the early part of the envelope. As a consequence, the three-component sum envelope may no longer coincide mostly with the peak of the vertical envelope. Hence, the three-component sum envelope peak may actually arrive after the peak of the transverse component envelope.

The above characteristics may have been caused by strong topographic irregularities at active volcanoes. Numerical simulations have shown that the inclusion of topography may increase peak-ratio at the low frequencies (Section 2.3.3), thus signifying a developed transverse component MS envelope. Topographic scattering is also very localised (Takemura et al., 2015a) which means that its signals can arrive rather early in the time-window, hence the less dominant vertical motion.

Accordingly, peak-ratio $\Re$ can be obtained from the MS envelopes by dividing the peak amplitude of the transverse component envelope over the peak amplitude of the three-component sum envelope (Equation 2.11). For the example given in Figure 4.2, peak-ratios at the 0.5-1, 1-2, 2-4, and 4-8 Hz frequency bands are 0.31, 0.36, 0.37, and 0.44, respectively. Even at the low frequencies, these values are already quite significant, especially in comparison to the previously observed peak-ratios (Figure 3.4). But at the same time, their frequency dependent behaviour is not as pronounced. Numerical simulations have indicated this same effect as a result of topography (Section 2.3.3). These aspects shall be thoroughly discussed in Chapter 5.

4.2.2 Peak-Ratios at Active Volcanoes in Japan

From the 204 JMA stations in the dataset, we obtained peak-ratios at 134, 140, 136, and 109 stations for the frequency bands of 0.5-1, 1-2, 2-4, and 4-8 Hz, respectively. Some stations were discarded due to poor signal quality as per the procedures. The ranges of

peak-ratio values found at JMA stations are from 0.08 to 0.63 at the frequency band of 0.5-1 Hz, 0.10 to 0.66 at 1-2 Hz, 0.08 to 0.70 at 2-4 Hz, and 0.12 to 0.65 at 4-8 Hz. The mean values across the frequency bands of 0.5-1, 1-2, 2-4, and 4-8 Hz are 0.33, 0.35, 0.36, and 0.39, with standard-deviations of 0.12, 0.13, 0.13, and 0.12, respectively.

With regard to the spatial distribution of peak-ratios, we have a lack of results from the western half of Japan, especially from the Kinki, Chugoku, and Shikoku regions. Because JMA stations are found on active volcanoes, their scarcity in those regions explains the lack of results. For the same reason, stations are mostly found to the East along the volcanic arc, clustered around each individual volcanoes. Therefore, in Figure 4.3 we show the distribution of peak-ratio at the four frequency bands across four regions in Japan. Here we present values averaged for each volcano. We use the same colour scheme as the one used in Chapter 3 which itself mimics the colours used in Nishimura (2012).

Admittedly, variations in peak-ratio exist across the multiple stations located at individual volcanoes. But variations in (averaged) peak-ratio across multiple volcanoes are still significant. To illustrate this, we compare the standard-deviation of averaged peak-ratio values across all volcanoes, to the mean of the standard-deviations of peak-ratios computed at each volcano. The former represents the variation in peak-ratio at active volcanoes in Japan as shown by Figure 4.3, while the latter represents the typical variation in peak-ratio at each volcano. Respectively, these values are 0.09 and 0.06 for the 0.5-1 Hz frequency band, 0.08 and 0.06 for the 1-2 Hz frequency band, 0.08 and 0.07 for the 2-4 Hz frequency band, and 0.08 and 0.04 for the 4-8 Hz frequency band. Note that both values are smaller than the standard-deviation computed using all stations at all volcanoes combined (Table 4.1).

When assessing these peak-ratios, ultimately we ought to consider each volcano's unique settings, not the least their topography. But Figure 4.3 ostensibly shows that active volcanoes in Hokkaido indicate larger peak-ratios overall. For example, in the mid

frequency range of 2-4 Hz, we can observe peak-ratios of around 0.40 in Hokkaido. For comparison, in the Tohoku region we observe smaller peak-ratios in the range of roughly $0.2 - 0.3$. Nevertheless, the overall peak-ratio values at active volcanoes consistently score considerably high on the scale. This is true at all frequency bands. For example, we do not often see ratios less than 0.2 even in the lower frequencies. Unsurprisingly these values are closer to those found in east Japan than those found in west Japan, and to those found in young active regions in Japan. This suggests strong seismic scattering overall at active volcanoes.

JMA stations can be further differentiated into ground surface stations and borehole stations. We categorise JMA stations as borehole stations if they are installed at a depth of greater than 45 m from the ground level. Data shows that most borehole JMA stations are actually installed at depths of around 100 m. In Figure 4.4 we show histograms of peak-ratios at JMA ground surface and borehole stations at the four frequency bands. Histograms are normalised as the probability density functions, thus distributions of peak-ratios at JMA ground surface stations and JMA borehole stations can be directly compared. Figure 4.4 shows that at all frequency bands, the ground surface stations display larger peak-ratios than the borehole stations.

We evaluate the uncertainty in peak-ratio computation at the JMA stations by doing the delete-1 Jack-knife test. Uncertainties are presented in terms of the coefficient of variation as percentages. For the frequency bands of 0.5-1, 1-2, 2-4, and 4-8 Hz, the maximum errors are 11.7%, 14.2%, 15.5%, and 17.2%, respectively. However, typically errors are much smaller than the maximum, as can be ascertained in Figure 4.5. The average errors at the 0.5-1, 1-2, 2-4, and 4-8 Hz frequency bands are 3.9%, 3.3%, 3.5%, and 4.0%, respectively. In other words, the uncertainty in JMA station peak-ratios is typically less than 5%.

4.2.3 Frequency Exponents at Active Volcanoes in Japan

We directly measure the frequency dependency of peak-ratio at JMA stations by calculating their frequency exponent m. The range of m values found using the JMA stations data is from 0.01 to 0.67, with an average of 0.20 and a standard-deviation of 0.15 (Table 4.1). Additionally, there is no clear difference in frequency exponent between JMA ground surface and borehole stations, where they show average frequency exponents of 0.19 and 0.21, with standard-deviations of 0.16 and 0.14, respectively (Table 4.1). We conducted the t-value test, comparing the frequency exponents at ground surface and borehole JMA stations. The result shows that there is no statistical significance in their difference at a confidence level of less than 50%.

Figure 4.6 shows the frequency exponents at active volcanoes in Japan where values are similarly averaged according to the specific volcanoes. Similarly, variations in frequency exponent at each volcano exist, though variations across volcanoes are significant. The standard-deviation of averaged frequency exponents across all volcanoes is 0.15, while the mean of the standard-deviations of frequency exponents at each volcano is 0.05. Frequency exponents at some stations are not calculated primarily because these stations do not have four peak-ratio values across each of the four frequency bands. Hence a few volcanoes are missing with regard to frequency exponent. Also, the same colour scale to the one used in Chapter 3 is used.

The volcano with the largest frequency exponent is Chokaisan, with an estimated m value of 0.67. Chokaisan is a wide, gentle and somewhat symmetric volcano that is isolated in the back-arc portion of the Tohoku region. Conversely, the volcano with the smallest frequency exponent is Kuchinoerabujima, with an estimated m of 0.02. Kuchinoerabujima is an island volcano to the south of Kyushu. It is important to point out that contrary to the peak-ratio observations, frequency exponents at active volcanoes consistently score low on the scale. For example, we do not generally see volcanoes with large or even moderate m values greater than 0.2 (Figure 4.6). This suggests that the

frequency dependent behaviour of peak-ratio at active volcanoes are rather weak.

We estimated the fit of the line with regard to the frequency exponent computation at JMA stations by calculating the root-mean-square-error. We found that the range of errors goes from 0.003 to 0.150. But most errors are less than 0.090 with an average of 0.058 (Figure 4.7).

4.3 Discussions

So far, results of peak-ratio computation and its frequency dependency using JMA volcanic seismometer network have presented the following key observations. One is that peak-ratios at active volcanoes are predominantly of high values. In contrast however, in terms of their frequency dependency, frequency exponents at active volcanoes are predominantly small. Peak-ratios at active volcanoes were computed using JMA ground surface stations and JMA borehole stations. Our results indicated that the former is showing larger values than the latter. In this discussion section, we would like to provide some explanations to these observations.

4.3.1 Topographic Effect on Peak-Ratios and Their Frequency Dependency at Active Volcanoes

Our results indicated that peak-ratios at active volcanoes are dominated by large values across all frequency bands (Figure 4.3). At active volcanoes, topography is a significant influencing factor. Numerical simulation results indicated that topography is more influential at the near summit stations compared to those further away (Section 2.3.3).

And so, we plot peak-ratios at JMA stations with respect to distance to the summit or volcanic centre according to the National Catalogue of the Active Volcanoes in Japan (2013). There seems to be a correlation between peak-ratio and distance from summit, where there is a tendency for peak-ratio to decrease with increasing distance from the

summit (Figure 4.8). Even though there are small peak-ratios at stations near to the summit, the largest ratios are found at short distances within 5 km from the summit. Furthermore, the trend of decreasing peak-ratio with distance from the summit is becoming much clearer when we include values from Hi-net stations (immediately) surrounding the volcano (e.g., Nishimura (2012)). Topography is becoming less rough with distance from the volcanic centre, hence its effect is becoming less forceful. That is, we expect less topographically sourced scatterings the further we are from the volcanic centre.

This result also compels us to examine peak-ratios at JMA stations with respect to those at Hi-net stations as presented in Chapter 3. It is imperative to see such examination because topographic contrast is clearly more of a factor in that case. Therefore it can provide a more compelling case of topographic effect in peak-ratio estimation. We shall explore this further in the general discussions.

Contrary to the peak-ratio observation, our results indicated that peak-ratio frequency dependency at active volcanoes are dominated by small frequency exponents (Figure 4.6). So far, we have reasons to consider the topographic effect as a significant factor in this observation. Yet, with regard to the frequency exponent comparison of JMA stations, it is difficult to differentiate these stations according to the significance of topography because all of them are located on active volcanoes. This is especially true in contrast to, for example, when we compare stations at active volcanoes to those at a region much further away.

Instead, here we try to present cases where the contrast in topography can be visibly recognised. In this regard, we choose two volcanoes by comparing their topography according to the JIVSM ground surface model. These are the Taisetsuzan Volcano and the Chokaisan Volcano (Figure 4.9). Taisetsuzan is an inland volcano located in Hokkaido with an elevation of 2291 m (National Catalogue of the Active Volcanoes in Japan, 2013). It is part of a mountain chain composed of many stratovolcanoes and lava domes, as a

result, it has a complex rugged topography. In contrast, Chokaisan is an isolated volcano containing smooth highly eroded and gently sloping features located in the back arc of the Tohoku region with an elevation of 2236 m (National Catalogue of the Active Volcanoes in Japan, 2013). The topography of Chokaisan is not as rough compared to Taisetsuzan (Figure 4.9). As such, we may say that topographic irregularities are stronger and more significant at Taisetsuzan compared to at Chokaisan, hence similarly, we may expect stronger topographic effect at Taisetsuzan.

We plot the averaged peak-ratios against the central frequency f_c (different frequency bands) in Figure 4.9. Clearly, it shows stronger frequency dependent behaviour at Chokaisan compared to at Taisetsuzan, which reflects the contrast in the level of topographic irregularities. More specifically, peak-ratio in the lower frequency at Taisetsuzan seems to be elevated. According to the shown topography model in Figure 4.9, the scale of topographic irregularities at Taisetsuzan is larger, which may explain the peak-ratio in the lower frequency as longer wavelengths are more sensitive to these larger scale irregularities. In short, strong topographic irregularities at Taisetsuzan may invoke topographic scattering but weaker frequency dependency. Previously, we estimated the averaged frequency exponent value at Chokaisan to be 0.67 whereas the averaged frequency exponent value at Taisetsuzan Volcano is 0.03. This shows some indication that topographic effect may reduce frequency exponent estimate overall.

However, the contrast in topography between any two active volcanoes is still less significant compared to similar contrast between an active volcano and its surrounding regions, as we have already pointed out. In other words, we are aware that the previous examples given may not fully explain the behaviour of frequency exponent in a systematic way. Fortunately, we have results from using the Hi-net dataset to represent regions outside of active volcanoes (Chapter 3). Comparison of frequency exponents between JMA and Hi-net stations will offer a more relevant discourse with regard to topographic effect. This aspect will be examined further in the general discussions, in Chapter 5.

4.3.2 Interpreting the Contrast in Peak-Ratio Observations between Ground Surface and Borehole Stations

As clearly indicated in Figure 4.4, JMA ground surface stations display larger peak-ratios than JMA borehole stations. For the frequency bands of 0.5-1, 1-2, 2-4, and 4-8 Hz, the mean peak-ratios at JMA borehole stations are 0.30, 0.27, 0.26, and 0.34 respectively (Figure 4.4, Table 4.1). Correspondingly, the mean peak-ratios at JMA ground surface stations are 0.34, 0.40, 0.43, and 0.43, respectively (Figure 4.4, Table 4.1). This corresponds to an increase in peak-ratio of about 15%, 52%, 66%, and 25%, respectively, with reference to the JMA borehole stations averages.

We conducted the t-test to compare peak-ratio values at JMA ground surface stations and JMA borehole stations. Results show that the differences in peak-ratios are statistically significant at least at the 95% confidence level. In fact, apart from the 0.5-1 Hz frequency band, the t-tests return statistical significance at the 99.9% confidence level.

Larger peak-ratios at JMA ground surface stations compared to those at the borehole stations indicate stronger scattering intensity in the near surface. For example, such kind of strong scattering in the shallow parts of active volcanoes was suggested in Hirose et al. (2019), where strong scattering was indicated by the short mean free path of Rayleigh wave using passive ambient noise cross-correlation functions at Sakurajima Volcano. The effective depth of this method is fairly shallow as the source used mostly sample the shallow depths, making it useful for examining the shallow structure of active volcanoes. It has also been shown to be consistent with results from active shot experiments often applied at active volcanoes (e.g., at Asamayama Volcano, Yamamoto and Sato (2010)).

And so, to help us interpret the peak-ratio observation at JMA ground surface and borehole stations, we conduct an additional numerical simulation that includes a distinct shallow structure. We apply the same settings as Section 2.3.3. This includes the volcano topography model of Mt. Fuji based on the JIVSM model. We limit the stations to those at 2 km radius from the summit to maximise the observed effect of topography. For the

source, we similarly use vertically incident plane P wave of 1 km wavelength. There are two crucial differences to the previous simulations. The first is that we define a shallow low velocity zone (LVZ) with a thickness of 250 m. The LVZ has the same random medium parameters as the thick layer underneath. The P and S wave velocities in the LVZ are 0.75 km/s and 0.45 km/s respectively. These numbers were used so that waves can effectively trapped by the layer. The second crucial difference is that we extend station coverage down to 1 km deep at 100 m intervals. This allows us to investigate the depth dependency in peak-ratio as seen in the observation.

Figure 4.10 shows peak-ratios at selected stations against depth. As we can see, peak-ratio is stabilising to some lower values at depths below the LVZ (>0.25 km). Peak-ratio fluctuation is high for stations within the LVZ and on the ground surface, with the overall ratio being larger than those below the LVZ. In other words, the numerical simulation manages to reproduce the tendency for peak-ratio to decrease with increasing borehole depth.

To dissect this result further, we show histograms of peak-ratio below the LVZ, within the LVZ, and the ground surface (Figure 4.11). Accordingly, histograms are normalised as the probability function. Similarly, we can see that the distribution of peak-ratios at virtual stations below the LVZ is smaller than the distributions from the ground surface and within the LVZ. The mean peak-ratio value for stations below the LVZ is 0.23 with standard-deviation of 0.17. The mean for stations within the LVZ is 0.36 with standard-deviation of 0.16. Finally, the mean for stations on the ground surface is 0.37 with standard-deviation of 0.14. Once again, the peak-ratio from below the LVZ is much lower than those from the ground surface and within the LVZ. We conduct the t-test to examine these differences. Correspondingly, there is no statistical significance when comparing numerically simulated peak-ratios between values from the ground surface and within the LVZ. But crucially, comparing peak-ratios at stations below the LVZ to those at the ground surface and within the LVZ, both return differences statistically significant

at 99.9% confidence level.

Therefore, we can use the above numerical simulation results to interpret the previous observation where larger peak-ratios are found at JMA ground surface stations compared to those found at their borehole counterparts. More specifically, we can attribute this to the existence of a low velocity layer at shallow depths at volcanic edifices. Waves reflected by the surface topography may be trapped by such kind of layer. Hitherto, random medium parameters for the LVZ is the same as underlying medium. Having a stronger scattering regime in the LVZ could suppress the contribution of topography, hence some trade-off between topographic and random medium scatterings (Emoto et al., 2020). But nonetheless, the trapping of seismic wave can still prevail. As a result, scattering intensity at receivers installed within the layer or close to the ground surface might have been seemingly increased. Hence, the large peak-ratio estimates at JMA ground surface stations might have come from these trapped waves.

The current parameter settings of 250 m LVZ thickness, which is a quarter of the source wavelength (1 km) most efficiently trap the surface topography reflected waves. This does not mean that the LVZ needs to be of a specific thickness to trap the waves. Simulations using different parameter settings (hence different ratios of LVZ thickness and source wavelength) can also show contrasts between stations below the LVZ and those on the ground surface or within the LVZ. Figure 4.12a shows the normalised histograms where the thickness of the LVZ is doubled to 500 m (LVZ thickness one-half of the source wavelength). For this setting, the mean peak-ratio values for stations below the LVZ, within the LVZ, and on the ground surface are 0.22, 0.38, and 0.31, with standard-deviations of 0.14, 0.15, and 0.11, respectively. To incorporate a very thin low velocity layer in the simulation is more difficult because of limitation in the model grid space. So far we have been using a grid spacing of 50 m. And so with a source wavelength of 1 km, having a LVZ thickness one-eighth or one-sixteenth of the wavelength would translate to only a few grid-points defining the LVZ which is insufficient. But if we assume some

scaling relation, we can instead increase the source wavelength to 4 km while keeping the thickness of the LVZ the same as previous (250 m, thus LVZ thickness one-sixteenth of the source wavelength). Figure 4.12b shows the normalised histograms from using these simulation parameters. The mean peak-ratio values for stations below the LVZ, within the LVZ, and on the ground surface are 0.10, 0.22, and 0.26, with standard-deviations of 0.06, 0.14, and 0.16, respectively.

In both of the above simulations, stations below the LVZ still show considerably smaller peak-ratios, indicating a possibility of similar wave trappings near the ground surface (their histograms however clearly show that their peak-ratio distributions are more similar (Figure 4.12), perhaps indicating that the trapping is not as efficient). Interestingly, as the thickness of the LVZ gets larger with respect to the wavelength, we start to see larger peak-ratios at stations within the LVZ compared to stations on the ground surface (Figure 4.12a). Regardless, these numerical simulations show that simply by having a low velocity layer underneath the surface, we can demonstrate how larger peak-ratio can be found at the ground surface stations. Therefore, this suggests that there might be a shallow low velocity layer between JMA ground surface stations and JMA borehole stations. In reality, JMA borehole stations are at least 50-100 m deep. Thus, the thickness of the low velocity layer might be closer to such numbers in reality. Furthermore, if we assume a thickness of 50 m, it may effectively trap waves with a source wavelength of 200 m. Assuming a P wave velocity of 0.75 km/s which is the velocity used in the simulations, this means that a low velocity layer with a thickness of 50 m may effectively trap waves at a frequency of less than 4 Hz. Respectively, a thickness of 100 m may trap waves effectively at a frequency of less than 2 Hz. Accordingly, these frequency ranges (1-2, 2-4 Hz) show the biggest contrast in peak-ratio between JMA ground surface stations and borehole stations (Figure 4.4), which seems to back up this interpretation.

The existence of thin shallow low velocity layer is not uncommon at active volcanoes. It can be inferred from geological maps and their cross-sections such as that of Esan

Volcano (Miura et al., 2022) or Suwasenojima Volcano (Shimano et al., 2013). In these maps, formations right underneath the surface are often composed of lava bed, volcanic ash, and pyroclastic materials, and these young rocks, especially those that are unconsolidated, would correspond to low seismic velocities. The existence of the thin shallow low velocity layer can also be inferred from other evidence such as those from geophysical surveys using active seismic and refraction analyses. For example, from the refraction analysis of first P wave arrival time data, 2D P wave velocity structures along several profiles at the Sakurajima Volcano were generated (Miyamachi et al., 2013). They reveal very thin (∼100 m) shallow low velocity layers (∼1 km/s) made out of lava bed and unconsolidated volcaniclastic materials as well as tuff deposits. This low velocity surface layer overlies much thicker layers that include the basement and a deep layer with velocities of around 5 km/s. Additionally, analysis of first arrival times from an active seismic experiment using more than 400 temporary seismometers managed to delineate P wave velocity structure beneath Asamayama Volcano (Aoki et al., 2009). It indicates a shallow low velocity layer ($V_P < 2$ km/s) of varying thickness, from a few hundreds of metres to about 1 km. At Iwatesan Volcano, 3D P wave velocity structure was obtained via seismic tomography from an active source experiment (Tanaka et al., 2002). Shallow low velocity structure of less than $3 \sim 4$ km/s was revealed especially surrounding the summit area. This low velocity layer has a thickness of around 100 m to the West, but thickens to about 2 km to the East. Tanaka et al. (2002) suggested that the low velocity materials around the summit and the eastern flank of the Iwatesan Volcano are made out of young unconsolidated volcanic products. At Mount Fuji — whose topography we used in our numerical simulation model — 3D seismic velocity structures were obtained tomographically using both active and passive sources and a dense seismograph array (Nakamichi et al., 2007). They indicate low P wave velocity anomalies (∼3 km/s) underneath Mount Fuji at 0 km horizontal cross-section, with a strong negative perturbation compared to the initial 1D reference model. Nakamichi et al. (2007) suggested that these

low velocity structures correspond to volcanic mudflow and pyroclastic deposits.

4.4 Summary

We calculated the peak-ratio $\Re$ at the JMA volcanic seismometer network to measure the scattering strength at active volcanoes in Japan. We also directly measured the frequency dependent behaviour of peak-ratio at these JMA stations by computing the frequency exponent m. The results can be summarised as follows:

- The uncertainties in the peak-ratio computation were estimated to be less than 5% via the delete-1 Jack-knife test. Whereas, the fit of the line with regard to the frequency exponent computation were obtained by calculating the root-mean-square-error.

- Averaged peak-ratios at active volcanoes in Japan are predominantly large across all frequency bands. Seismic scattering and transverse component excitation at active volcanoes are strongly influenced by the the topographic effect. Thus scattering off the topographic irregularities might have inflated the peak-ratio estimates at the JMA stations.

- In contrast, averaged frequency exponents at active volcanoes in Japan are predominantly small. This demonstrates that frequency exponents at JMA stations might have been reduced due to topography.

- JMA stations can be categorised into ground surface stations and borehole stations. Peak-ratios at JMA ground surface stations are found to be larger than those at the borehole stations. With the help of additional numerical simulations, we can attribute this finding to a thin shallow low velocity layer that may trap topographically scattered waves which raises peak-ratio estimates at the ground surface stations.

Table 4.1 Peak-ratio $\Re$ and frequency exponent m mean plus-and-minus 95% confidence interval for all used JMA data, and after categorising JMA stations into either ground surface or borehole stations. Also given are the standard-deviation (S.D.) and the number of available stations (N).

	$\Re$			m		
		S.D.	N		S.D.	N
All data						
0.5-1 Hz	0.325 ± 0.020	0.12	134			
1-2 Hz	0.352 ± 0.021	0.13	140	0.200 ± 0.037	0.15	69
2-4 Hz	0.357 ± 0.023	0.13	136			
4-8 Hz	0.389 ± 0.022	0.12	109			
JMA ground surface						
0.5-1 Hz	0.342 ± 0.026	0.12	77			
1-2 Hz	0.403 ± 0.027	0.12	82	0.190 ± 0.051	0.16	38
2-4 Hz	0.425 ± 0.025	0.11	79			
4-8 Hz	0.428 ± 0.031	0.12	58			
JMA borehole						
0.5-1 Hz	0.298 ± 0.031	0.11	53			
1-2 Hz	0.266 ± 0.024	0.09	53	0.208 ± 0.055	0.14	29
2-4 Hz	0.256 ± 0.025	0.09	53			
4-8 Hz	0.343 ± 0.028	0.10	49			

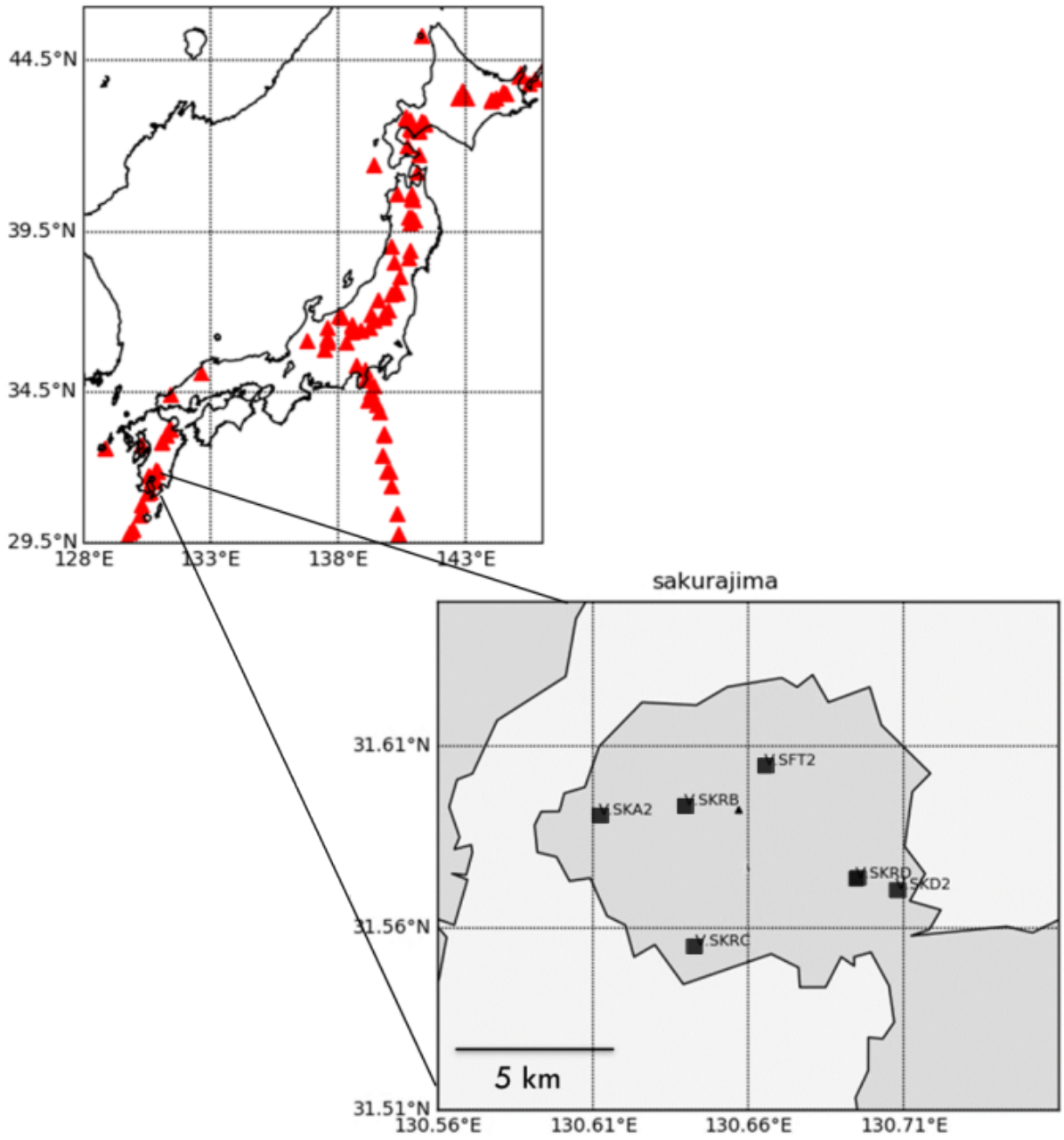

Figure 4.1 The distribution of active volcanic centres (red triangles) according to the National Catalogue of the Active Volcanoes in Japan (2013). Not all volcanoes are monitored by the JMA volcanic seismometer network but the extent of JMA stations does encompass the full length of the archipelago. The inset shows the JMA stations (black squares) at the Sakurajima Volcano of southern Kyushu.

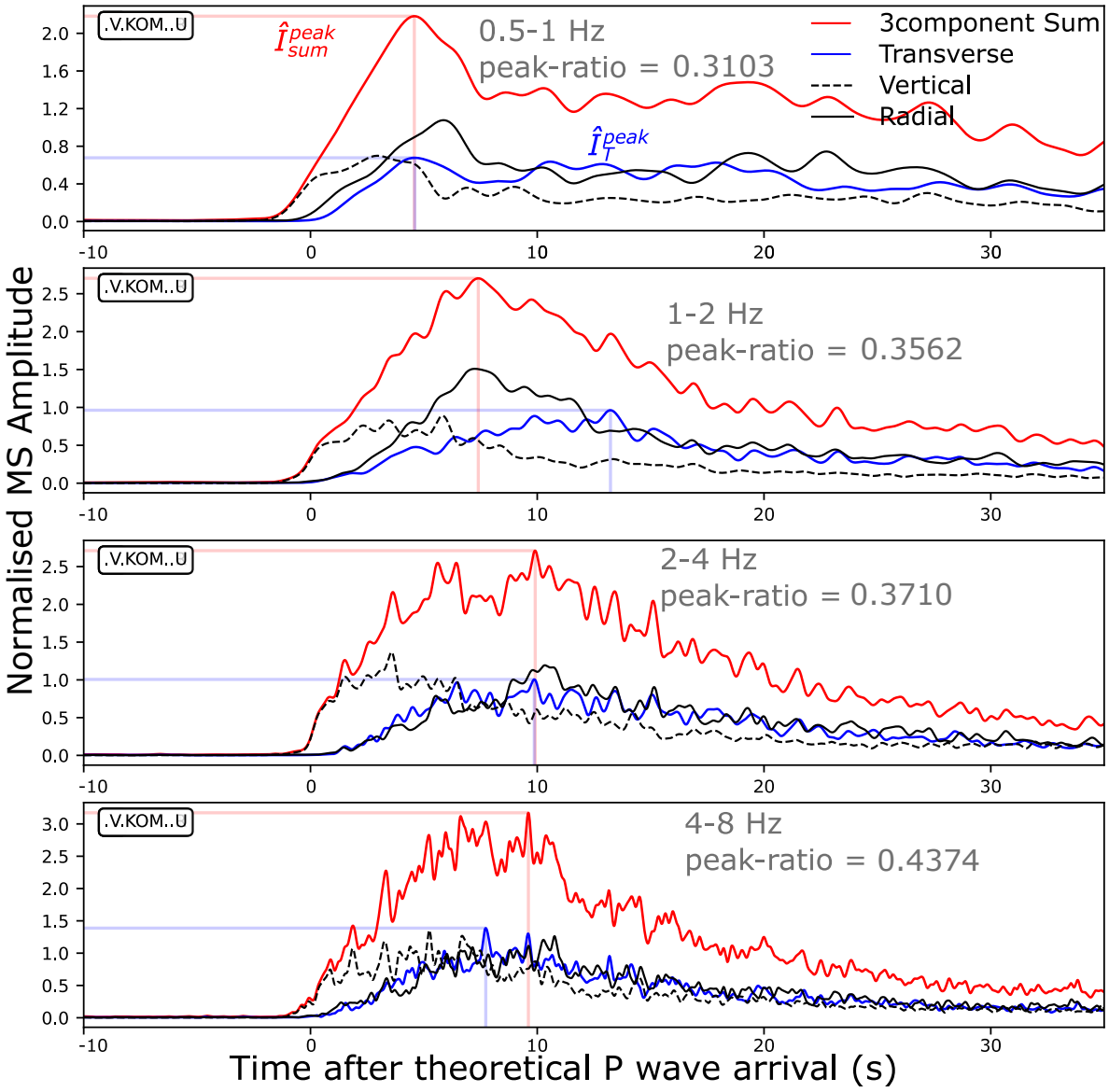

Figure 4.2 Mean squared (MS) envelope example for station KOMA which monitors the Hokkaido-Komagatake Volcano, computed at the four frequency bands of 0.5-1, 1-2, 2-4, and 4-8 Hz. Blue traces signify the transverse component envelopes, whilst red traces signify the three-component sum envelopes. Dashed-black and black lines are the vertical and radial component envelopes, respectively. The translucent lines mark the peaks of the transverse and the three-component sum envelopes, and they are denoted here as $\hat{I}^{peak}_{T}$ and $\hat{I}^{peak}_{sum}$, respectively. The peak-ratio $\Re$ is obtained by dividing the former over the latter (i.e., $\Re = \hat{I}^{peak}_{T} / \hat{I}^{peak}_{sum}$). Time is given relative to the theoretical P wave onset according to the ak135 model.

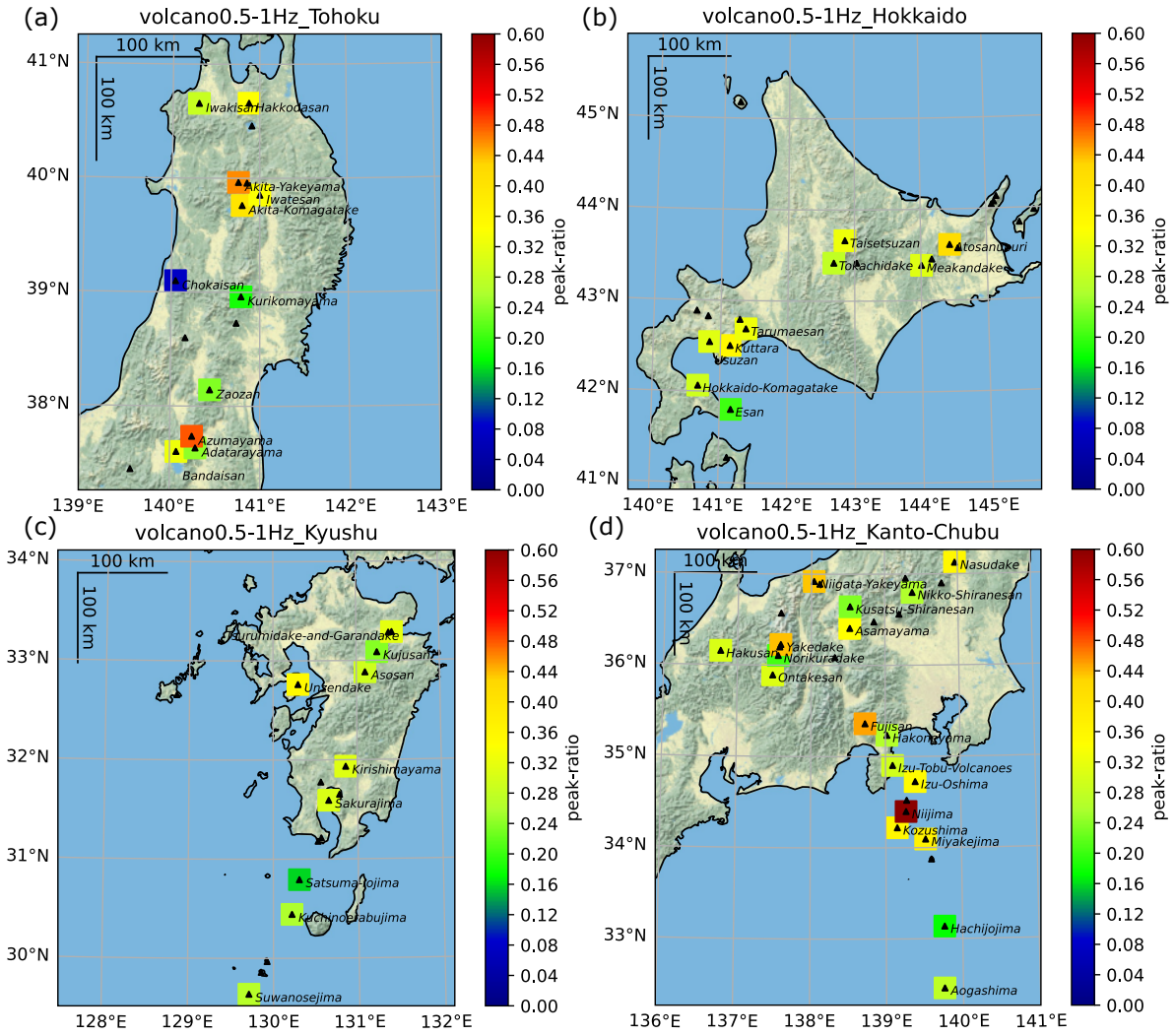

Figure 4.3 The distributions of peak-ratio $\Re$, calculated using the JMA volcanic seismometer network at the (a) Tohoku, (b) Hokkaido, (c) Kyushu, and (d) Kanto-Chubu regions. Peak-ratio values at each volcano are averaged to obtain the results. Shown are for the frequency band of 0.5-1 Hz. The same colour scale as the one we used for Hi-net is implemented.

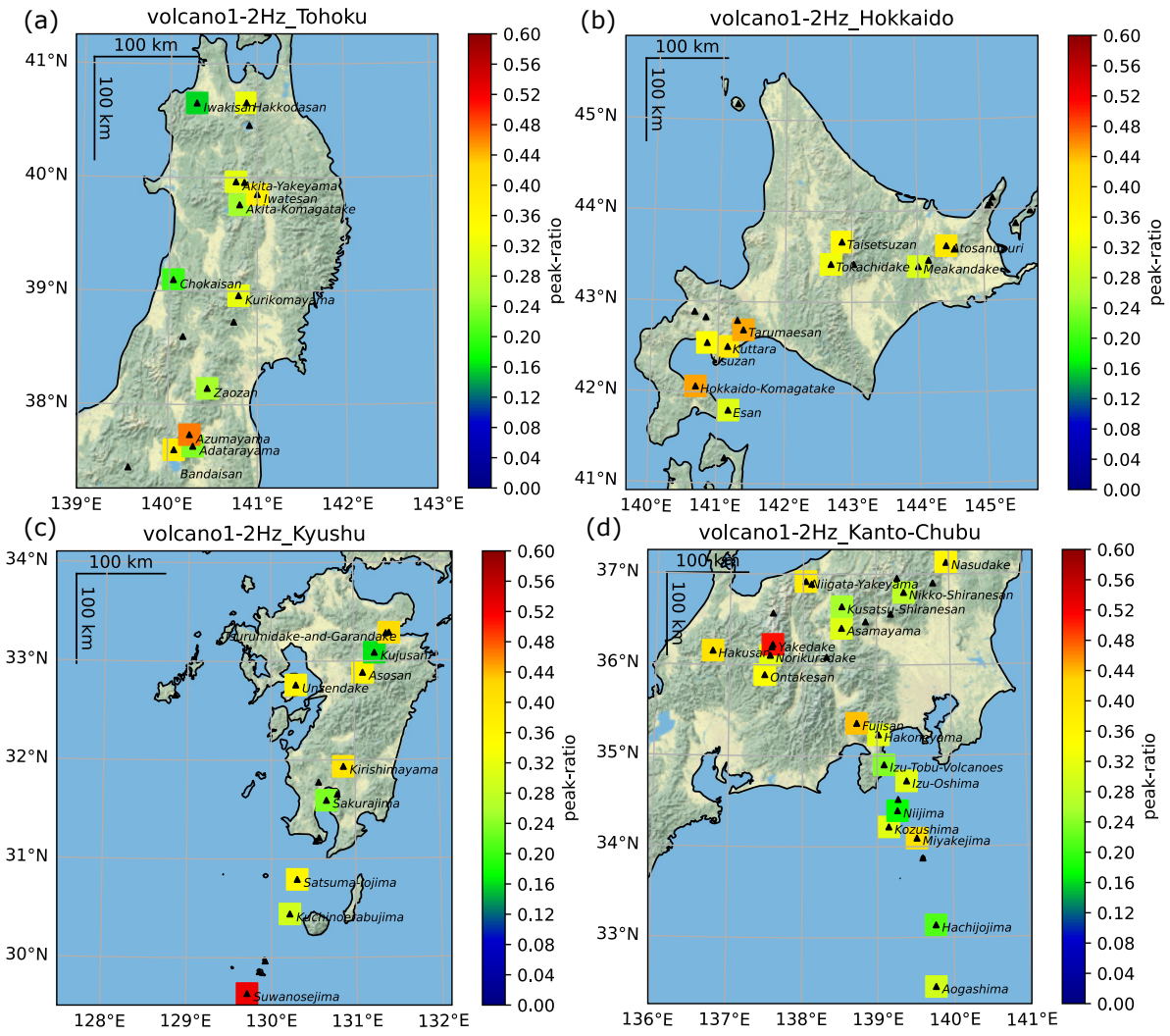

Figure 4.3 (*continued*) For the frequency band of 1-2 Hz.

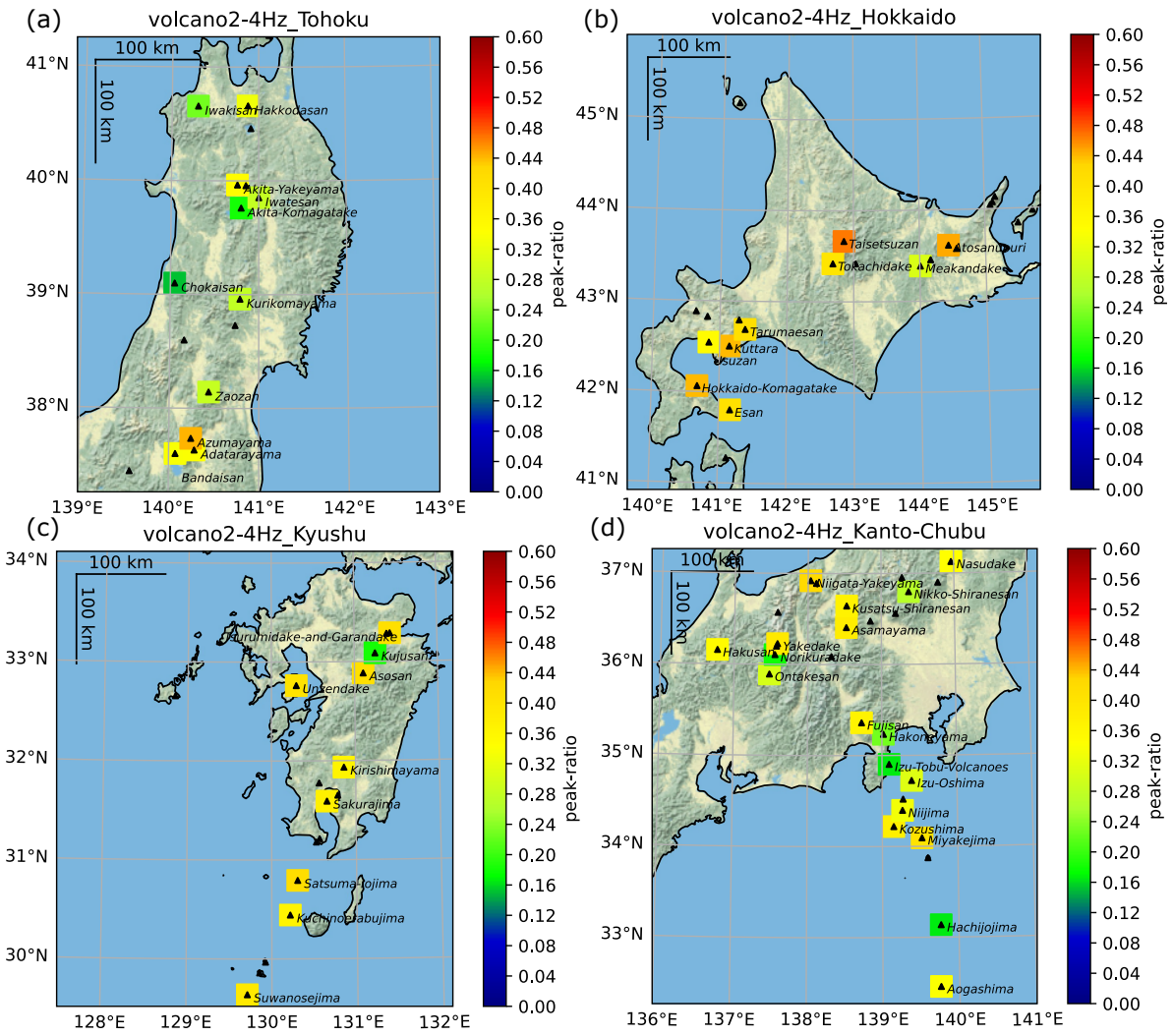

Figure 4.3 (*continued*) For the frequency band of 2-4 Hz.

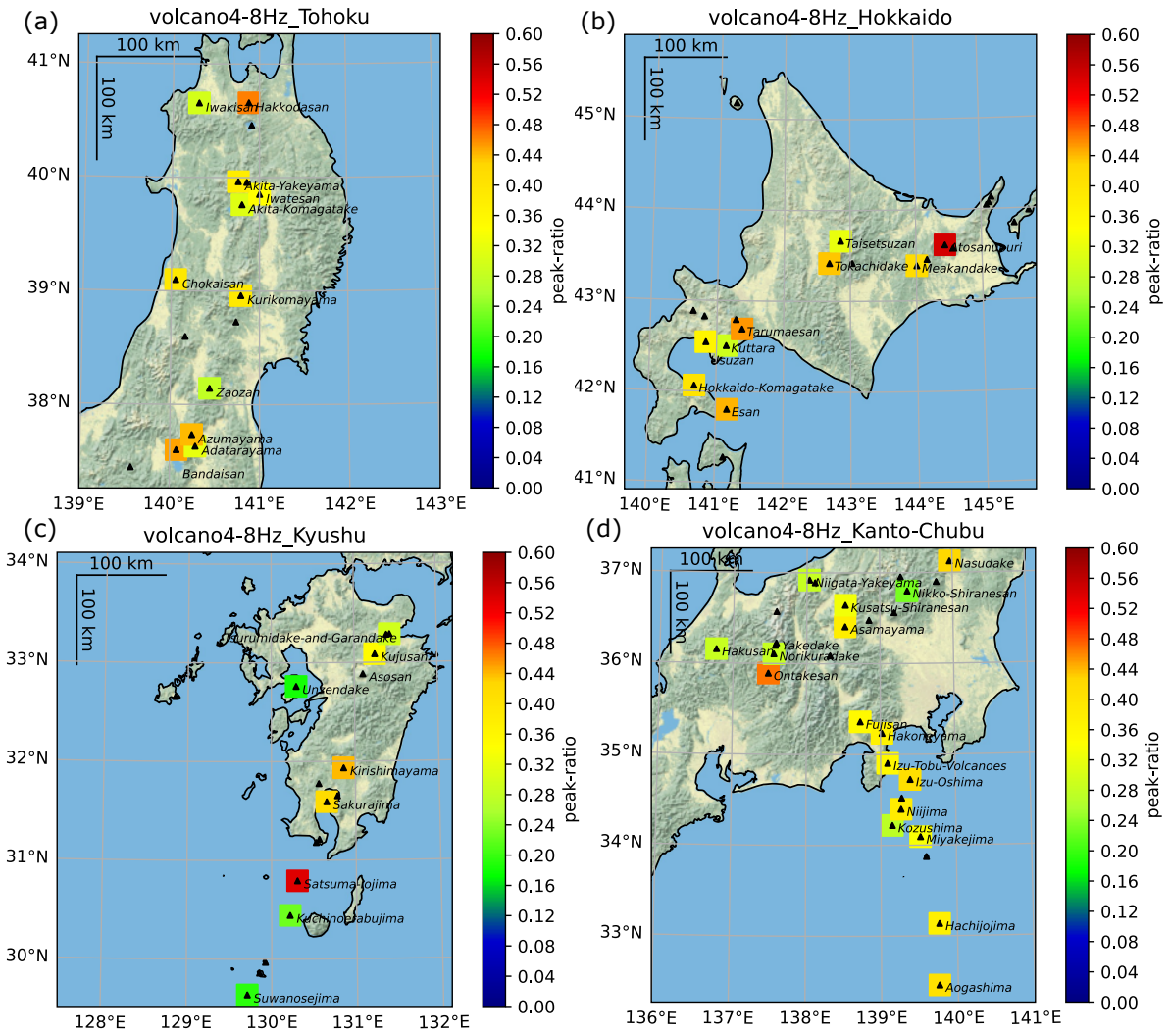

Figure 4.3 (*continued*) For the frequency band of 4-8 Hz.

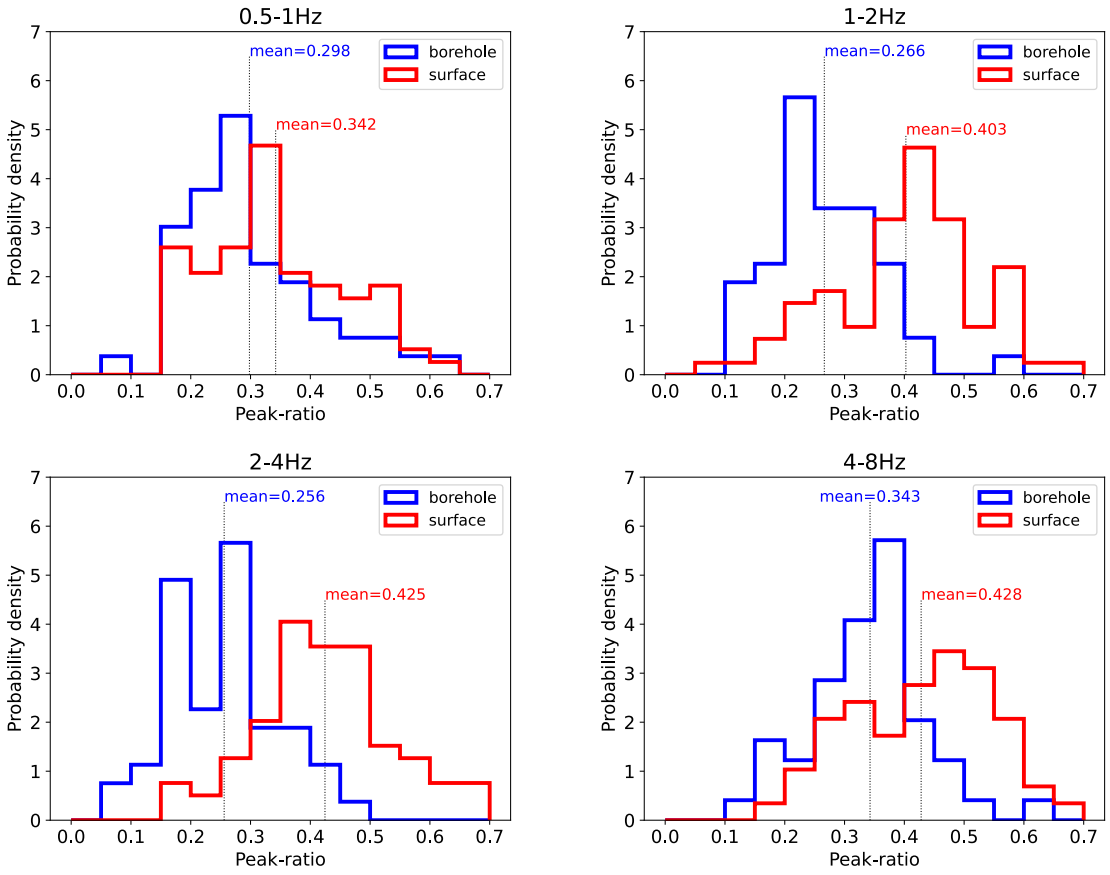

Figure 4.4 The probability density functions (normalised histograms) of peak-ratio $\Re$ for the frequency bands of 0.5-1, 1-2, 2-4, and 4-8 Hz. Blue histograms show the distributions of peak-ratios at JMA borehole stations. Red histograms show the distributions of peak-ratios at JMA ground surface stations. Peak-ratios at the ground surface stations are generally larger than those at their borehole counterparts.

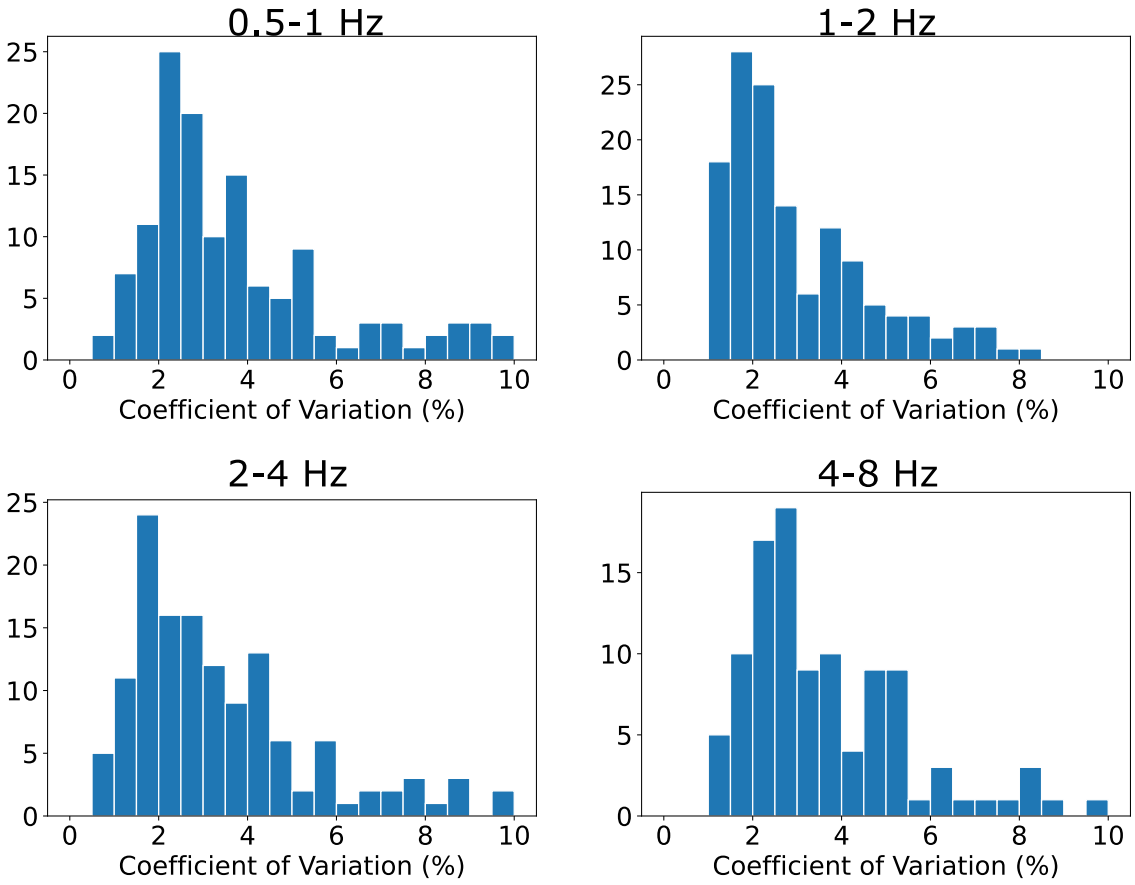

Figure 4.5 Histograms of coefficient of variations at JMA stations, representing the uncertainty in the peak-ratio computation at four frequency bands: 0.5-1, 1-2, 2-4, and 4-8 Hz. The typical error across all frequency bands is less than 5%.

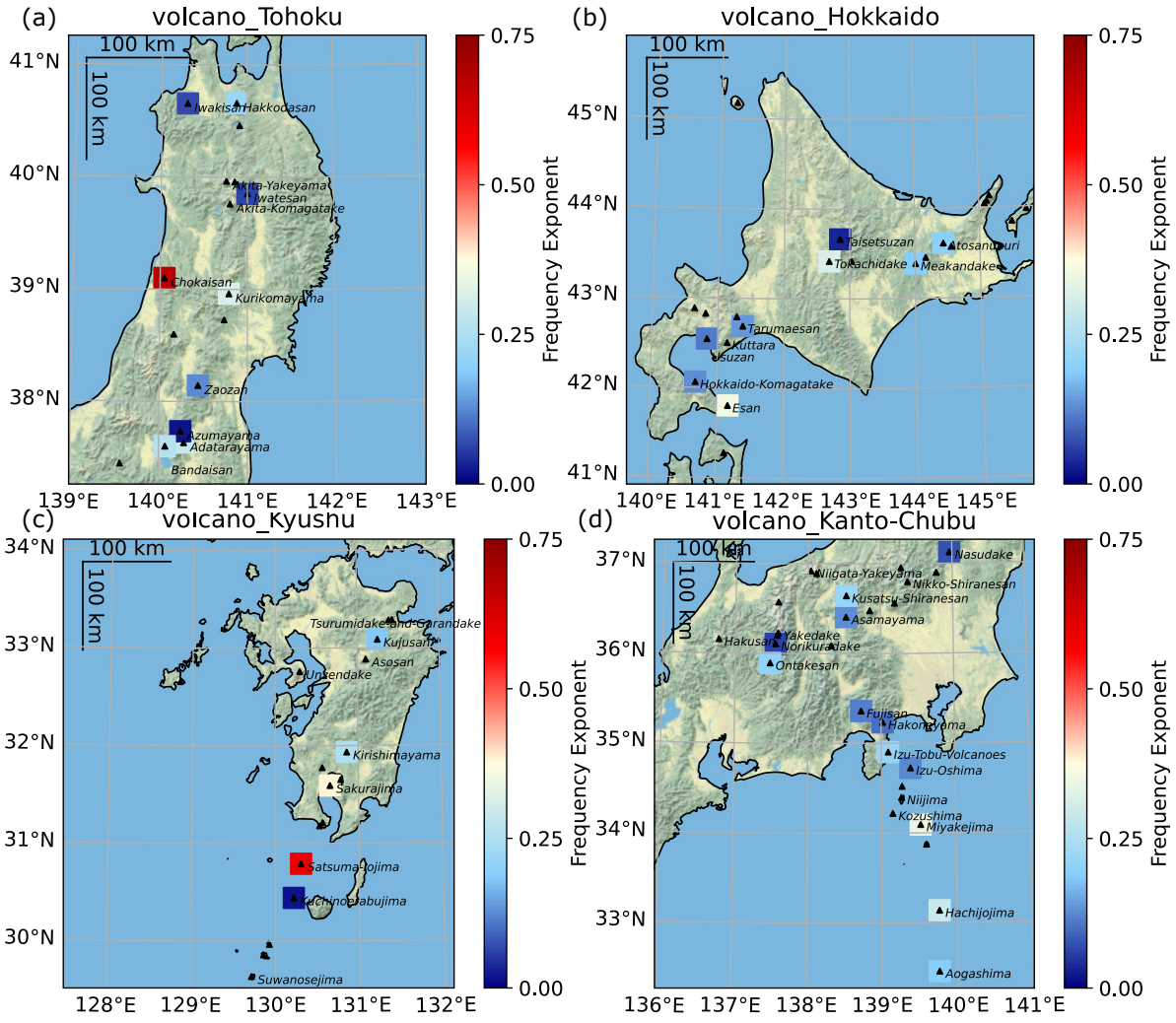

Figure 4.6 The distributions of frequency exponent m, calculated using the JMA volcanic seismometer network at the (a) Tohoku, (b) Hokkaido, (c) Kyushu, and (d) Kanto-Chubu regions. Frequency exponent values at each volcano are averaged to obtain the results. The same colour scale as the one we used for Hi-net is implemented.

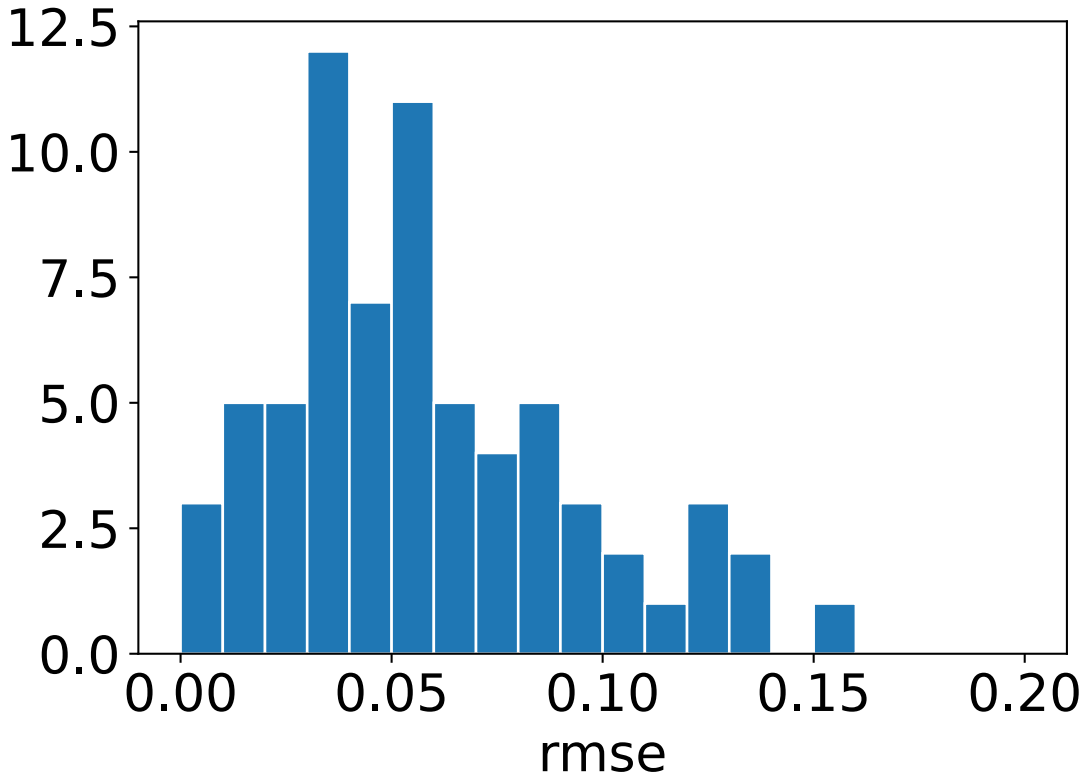

Figure 4.7 Histogram of root-mean-square-errors (rmse) which represents the error in the computation of frequency exponent m at JMA stations. The typical error is less than 0.09.

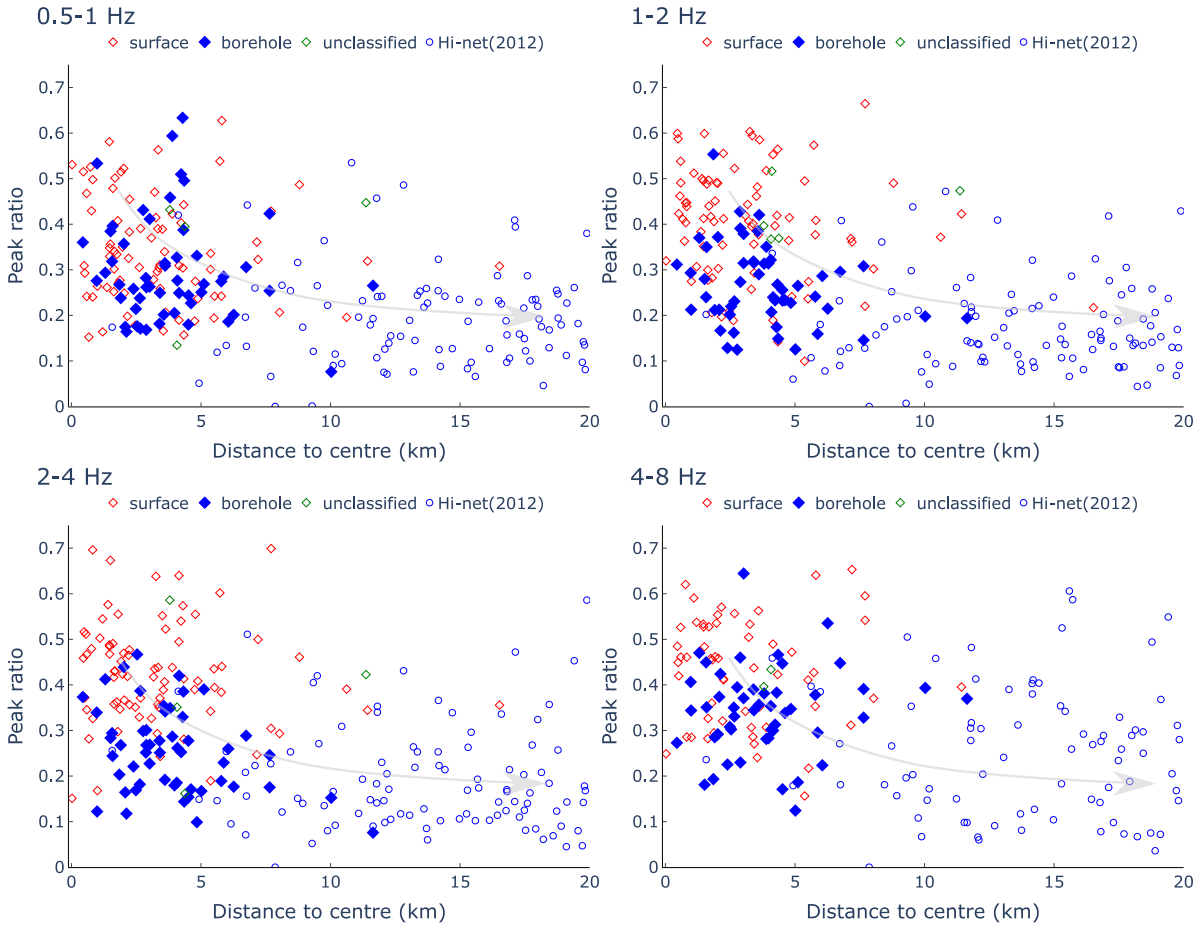

Figure 4.8 Peak-ratio $\Re$ according to stations' distances to the volcanic centre with respect to the National Catalogue of the Active Volcanoes in Japan (2013). JMA stations are categorised into ground surface and borehole stations. Stations in green are not classified in the JMA website. Also shown are peak-ratios at nearby Hi-net stations within 20 km from an active volcano from Nishimura (2012). Ostensibly, we see a drop in peak-ratio with respect to distance, and more specifically from the JMA stations to the surrounding Hi-net stations.

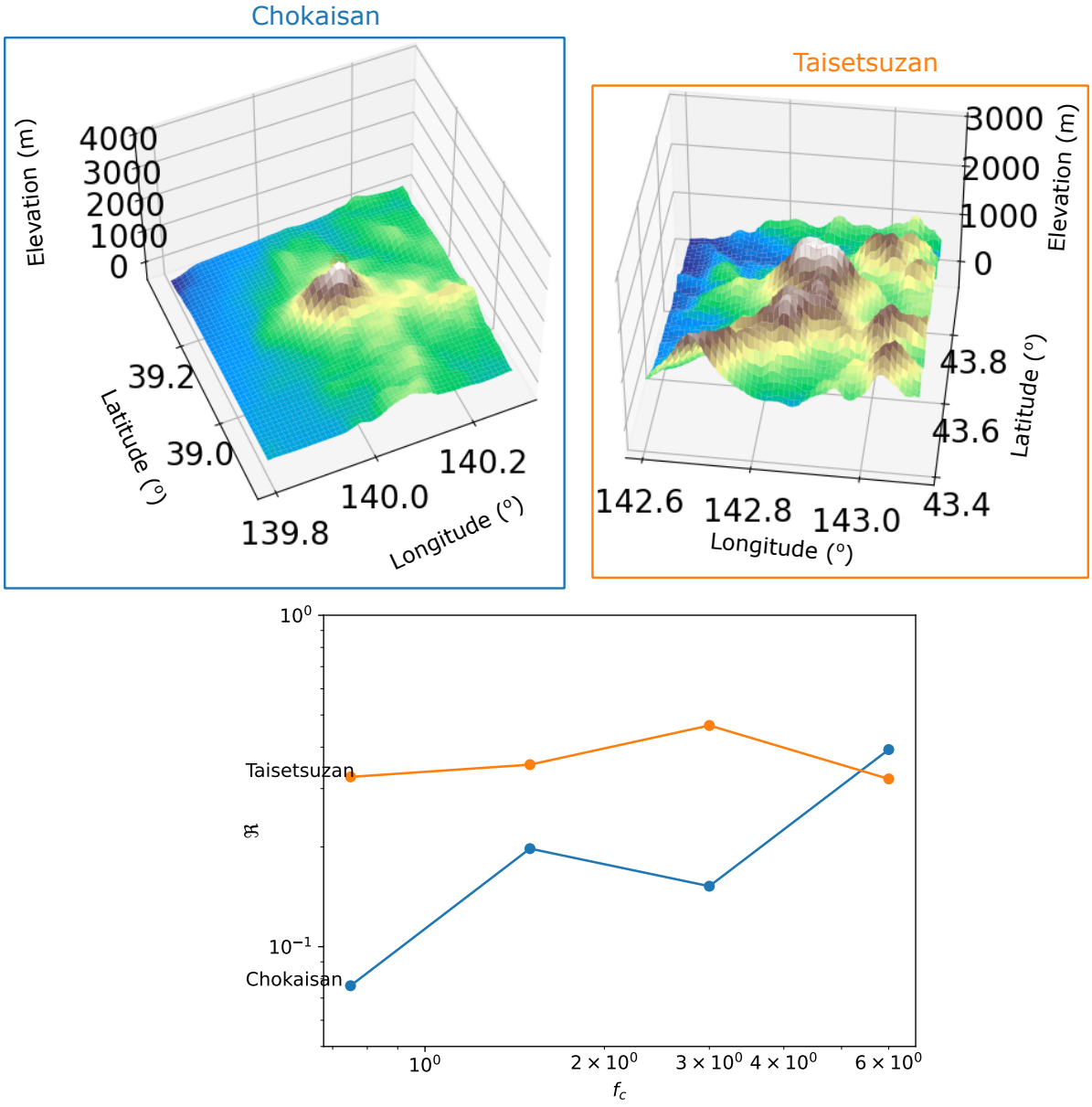

Figure 4.9 Averaged peak-ratio $\Re$ at Taisetsuzan and Chokaisan versus central frequency f_c signifying the frequency dependency of peak-ratio at these volcanoes. The insets show the 3D topography model of the two volcanoes according to the JIVSM ground surface model. The shown topography models cover the same area of 0.495^o latitude $\times 0.495^o$ longitude.

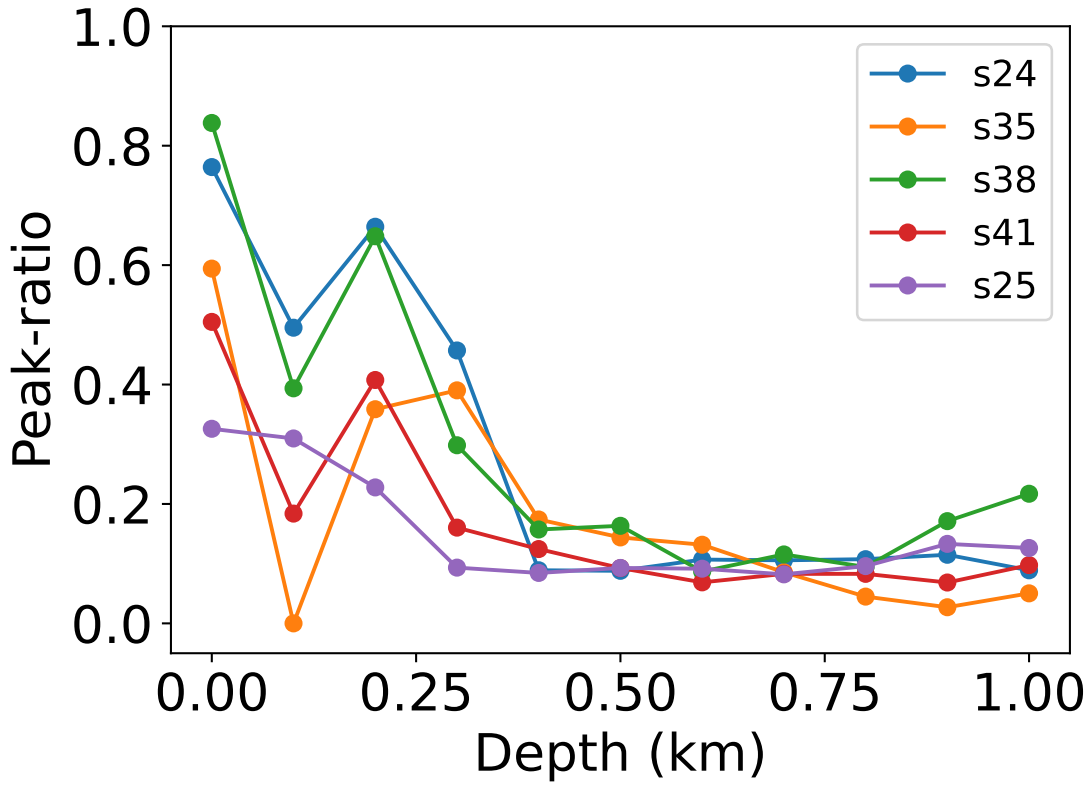

Figure 4.10 Peak-ratio $\Re$ versus depth at selected station locations distributed at 2 km radius around the summit. Different colours represent different station points on the 2 km radius while the dots represent stations at discrete depths beneath that location. The simulation model uses Mt. Fuji JIVSM topography model with a shallow low velocity zone of 250 m thickness.

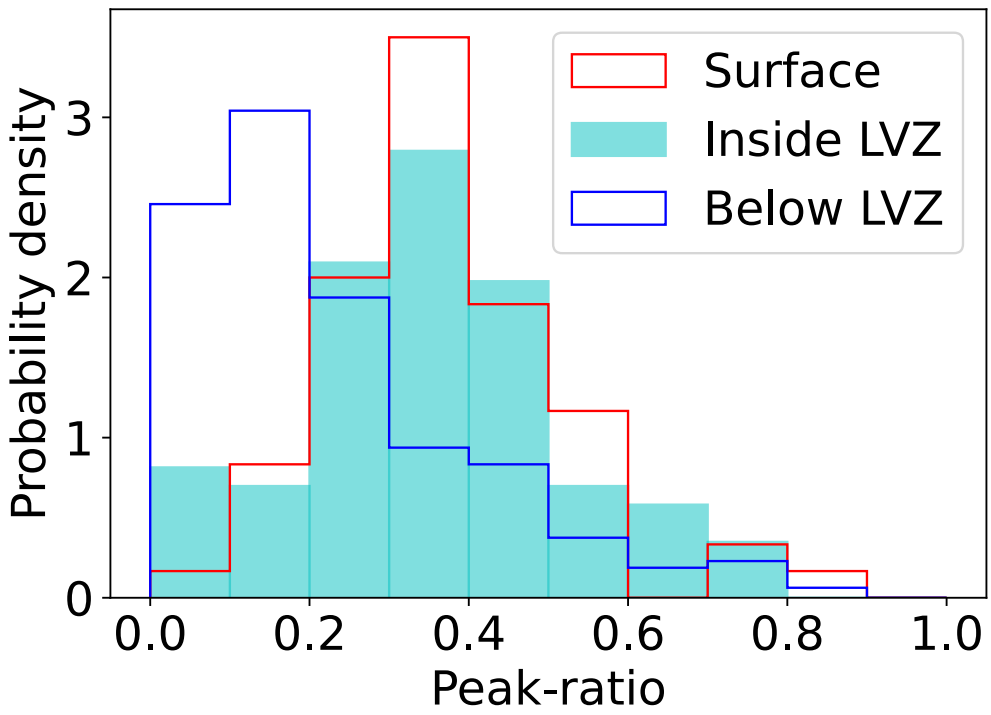

Figure 4.11 The probability density functions (normalised histograms) of peak-ratio $\Re$ obtained using numerically simulated data. The simulation model uses Mt. Fuji JIVSM topography model with a shallow low velocity zone (LVZ) of 250 m in thickness. Stations are distributed at 2 km radius around the summit, and extend from the ground level to the depth of 1 km at 100 m intervals. Blue step histogram shows the distribution of peak-ratios at stations below the LVZ. Red step histogram shows the distribution of peak-ratios at stations on the ground surface. Light blue histogram shows the distribution of peak-ratios at stations in the LVZ. Peak-ratios at stations below the LVZ are less than those on the ground surface and in the LVZ.

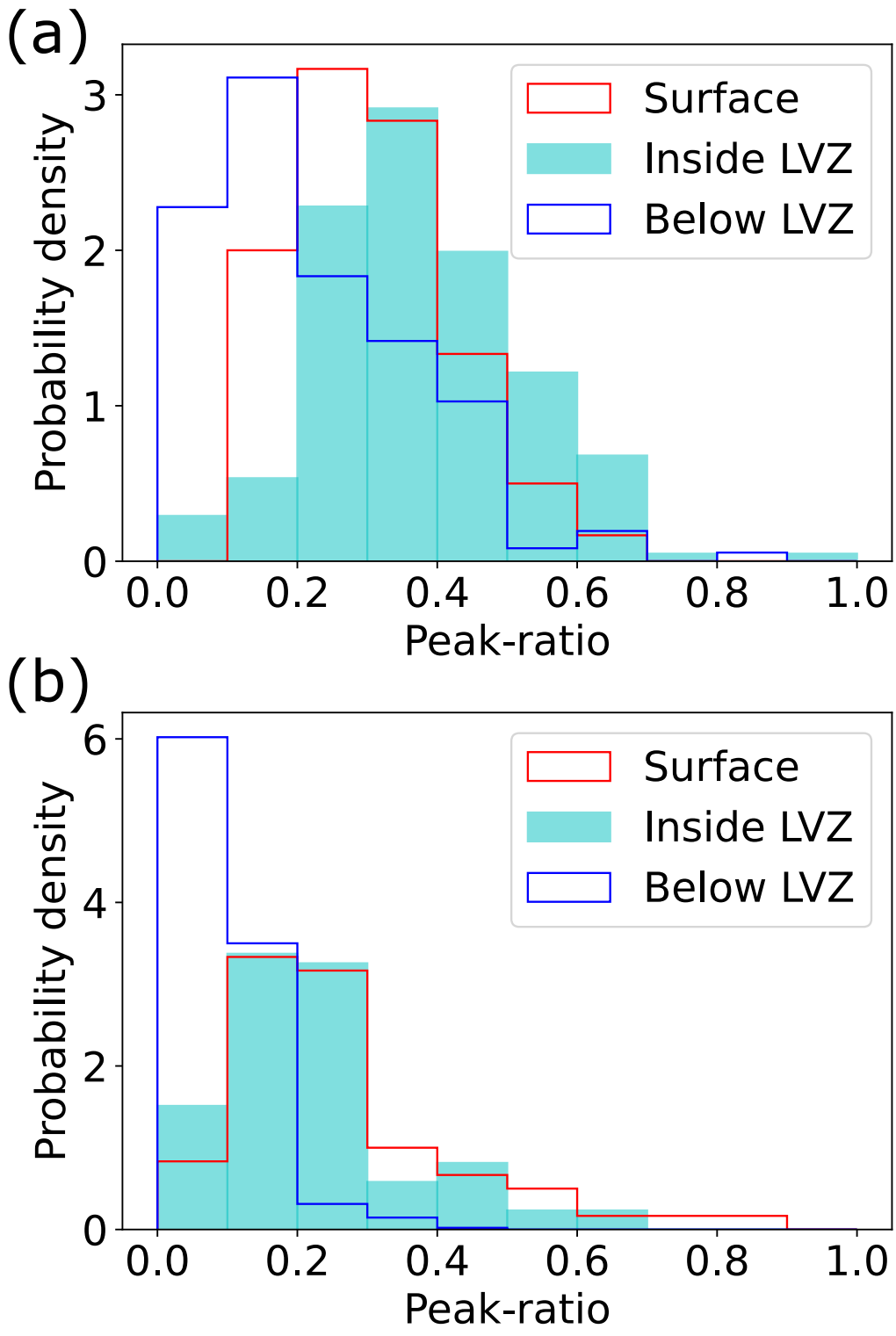

Figure 4.12 Same as Figure 4.11 but following parameters are used: (a) thickness of the low velocity zone (LVZ) equals to 500 m and a source wavelength of 1 km; (b) thickness of the LVZ equals to 250 m and a source wavelength of 4 km.

Chapter 5

Discussion

We have examined peak-ratio $\Re$ and its frequency dependency as measured by the frequency exponent m. We have done so for the ordinary crust of Japan, and active volcanoes in Japan. For the former, we made use of the densely distributed Hi-net stations, while for the latter, we made use of the volcanic seismometer network operated by JMA. We presented these cases in Chapters 3 and 4, respectively. These analyses were done while acknowledging the presence of free-surface and topographic effects on the peak-ratio and frequency exponent estimations. Such effects were identified and described via finite difference numerical simulations in Chapter 2.

We are bringing all of these aspects together in this general discussion chapter. We shall see how indeed the free-surface and topographic effects can be recognised using the real data as well. In Chapter 3, to mitigate these effects, we exclude some Hi-net stations from the analysis. By reintroducing these excluded data, we can see that the free-surface and topographic effects exist in the Hi-net dataset before the mitigation step, therefore, justifying our mitigation strategy.

We will continue our discussion with the comparisons of peak-ratios between Hi-net and JMA stations, followed by comparisons with respect to their frequency exponents accordingly. We recognise that topographic irregularities are stronger for the latter net-

work. Thus, such comparisons can highlight the existence of the topographic effect on peak-ratio and its frequency dependency in the real data.

Subsequently, we will touch on how topographic effect can potentially be separated from the medium heterogeneity contributions using numerical simulation. We shall also discuss our peak-ratio results in terms of random medium parameters, especially in the context of previously estimated parameters. Lastly, we will briefly discuss peak-ratio in relation to peak delay time.

5.1 Identifying the Free-Surface Effect in the Hi-net Dataset

In Chapter 2, we described the free-surface effect as the interference between the up-going incident phase and the down-going surface reflected phase. Such occurrence may inflate peak-ratio estimate for some specific depth and frequency band, and thus affecting the frequency exponent estimate, too. In this regard, according to our numerical simulation, peak-ratio at the lowest frequency band (0.5-1 Hz) is raised for stations around 2 km in depth, thus underestimating the frequency exponent estimate as a result (Figure 2.9). And for similar reasons, peak-ratio at the highest frequency band (4-8 Hz) is raised for stations around 250 m in depth, thus overestimating the frequency exponent estimate as a result (Figure 2.9).

The above examples are for the case of synthesised (simulated) data, but similar behaviour can be identified in the real data as well. A good example of this can be seen at Hi-net stations KAKH and KNHH (Figure 5.1). Due to their depths, these stations were excluded from our analysis in Chapter 3. Station KAKH from Ishinomaki in eastern Tohoku is installed at a depth of 207 m, where — based on the quarter-wavelength rule following the numerical simulation results — we expect wavelength of 828 m to be mostly affected by the free-surface effect. At this station, we observe that

peak-ratio at the highest frequency band (4-8 Hz) is raised as shown by Figure 5.1. As a result, the peak-ratio at the 4-8 Hz frequency band is breaking away from the apparent straight-line fit connecting the other three peak-ratios at the lower frequency bands, and thus, ostensibly overestimating the frequency exponent at KAKH. Conversely, station KNHH from the Kinki region is installed at a depth 2.03 km, where for similar reasons, peak-ratio at the lowest frequency band (0.5-1 Hz) is instead raised. Thus, ostensibly the frequency exponent at KNHH is underestimated.

For a more comprehensive analysis of the Hi-net data, we include Hi-net data from those at depths outside of the range used in Chapter 3. We examine frequency exponent under three different circumstances. A huge proportion of Hi-net stations are installed between 100-300 m in depth. Thus, we first classify Hi-net stations into two groups: those between 100-200 m which we shall call *Case A*, and those between 200-300 m which we shall call *Case B*. Because of its depth range, we can expect contamination of peak-ratio at the 4-8 Hz frequency band for Case B, following the numerical simulation and the example in Figure 5.1. Therefore, we define one final condition where we take Hi-net stations between 200-300 m depth but without including the 4-8 Hz frequency band in the subsequent analysis. We shall call this final case *Case C*.

We estimated the frequency exponent values as well as the root-mean-square-error for Case A, Case B, and Case C, separately, and show their 95% confidence intervals in Figure 5.2. The confidence interval of frequency exponent for Case B is markedly larger than those for Case A. Moreover, the confidence interval of the root-mean-square-error for Case B is also larger than Case A. We suggest that this is because for the depth range of Case B, the free-surface effect may overestimate frequency exponent by raising the peak-ratio at the 4-8 Hz band, which in turn would also worsen the residual fit (increase the root-mean-square-error), by deviating away from the trend implied by the other peak-ratio estimates at other frequency bands (e.g., Figures 2.9d, 5.1 top).

The removal of the contaminated peak-ratio at the 4-8 Hz band (i.e., Case C), resulted

in the lowering of the frequency exponent, and this new confidence interval overlaps with the interval for Case A. Moreover, using only the remaining three frequency bands, we reduce the root-mean-square-error. In other words, we significantly improve the fit of the frequency exponent line at stations between 200-300 m deep by not including the 4-8 Hz in the analysis as shown by the smaller error for Case C compared to Case B (Figure 5.2). This observation is in line with our understanding of the free-surface effect from the numerical simulation. In other words, we can see the same tendency in both real and synthesised data when it comes to the free-surface effect. That is, where the destructive interference between the up-going incident and the down-going surface reflected phases may increase peak-ratio estimate at the 4-8 Hz thus overestimating the frequency exponent at depths of around 250 m. Therefore, we attribute the original disparity between Case A and Case B to a more prominent free-surface effect at Hi-net stations in the 200-300 m depth range compared to those in the 100-200 m depth range. And thus, we showed that the free-surface effect can be identified in Hi-net data.

The amount of fluctuation in frequency exponent as a result of the free-surface effect is larger in the numerical simulation case compared to the real data observation. This is clear when we compare how much frequency exponent is overestimated in the numerical simulation result to the real data observation. Referring to Figure 5.2, frequency exponent at Hi-net stations between 200-300 m (Case B) is overestimated by about 0.1 due to the free-surface effect, assuming that the effect in Case A is minimal. On the other hand, in the numerical simulation, frequency exponents at similar depths are overestimated by almost 2 compared to values at very deep locations where such effect is non-existent (Figure 2.10). One explanation for this is that numerical simulation offers an ideal scenario. The main mechanism that creates the free-surface effect is the destructive interference between the up-going incident and the down-going surface reflected phases. In the ideal case, we can create this interference extremely effectively, with the perfectly flat free-surface and a vertically incident plane wave source. On the field, the ground

surface may not be perfectly flat, nor the source be vertically incident as an oblique incident angle can be expected. As such, even though the free-surface effect can be observed in the real data, its extent might be lessened compared to the idealised numerical scenario.

5.2 Identifying the Topographic Effect in the Hi-net Dataset

To perceive the presence of topographic effect in real data, we evaluate Hi-net stations with respect to their installation height or elevation. Unlike in Chapter 3 all stations are considered this time (i.e., here we are using the unmitigated dataset). We expect that higher stations would most likely be located on mountainous areas where there is a clear presence of topography. This view is corroborated by the fact that, in Chapter 3 — where we exclude stations that are too high or indeed too deep — there is a deficiency in station coverage in the Chubu region, which consists of high mountains. Therefore, any effect from topography would be more prevalent at these stations compared to those at lower elevations.

In that regard, we divide Hi-net stations into 11 bins according to their installation height. For each bin, we then compute the frequency exponent 95% confidence interval. We show the result in Figure 5.3. The most important feature of Figure 5.3 is that the frequency exponent is overall decreasing with increasing station elevation. We have established how presence of strong irregularities in topography may reduce the frequency dependency of scattering, in other words, frequency exponent estimate may be decreased (Chapter 2.3.3; 4.3.1). Therefore, Figure 5.3 shows that with increasing station elevation hence an increase in topographic effect, we see a decrease in frequency exponent as a consequence. Thus, the presence of topographic effect has been signifying in the Hi-net data.

Also note that the stations used in Chapter 3 are at 400 m in elevation or less. At this range, the trend in frequency exponent with respect to elevation is not so significant (Figure 5.3). Therefore, that suggests that topographic effect in our previous Hi-net analysis have been seemingly minimised.

We can interpret this observed trend as a result of topographical scattering. The topographic surface may act like additional 'scatterers' which would partition energies into the transverse seismogram as well. Our numerical simulation suggested that this occurrence seems to be more effective in the lower frequencies hence the decrease in frequency exponent (Chapter 2.3.3). However, this may depend on the characteristics of the topography themselves, in other words, it strongly depends on the size and shape of the mountain/volcano. In this regard, strong scattering contributions from a smooth topographic irregularity compared to the medium heterogeneity may significantly reduce scattering dependency on frequency at some volcanoes.

5.3 Comparisons of Peak-Ratios Between Hi-net and JMA Stations

We have inferred that the surface topography may deflect the incident wave which would partition more energy into the transverse component hence larger peak-ratio. We can observe this in the numerical simulation results (Figure 2.14). We can also see this tendency in Figure 4.8, where high peak-ratios can be found closer to the active volcanoes (summit) compared to the surrounding stations. In this section, we shall examine the topographic effect on peak-ratio in our real data analysis by comparing results obtained using Hi-net and JMA stations data.

Peak-ratio as a measure of scattering strength has been evaluated using the Hi-net data in Chapter 3. At the JMA stations, peak-ratio was similarly estimated in Chapter 4. Unlike the Hi-net stations, JMA stations are located on the volcanic edifices, in

other words, much closer to the active volcanoes. Thus, the presence of topography is much stronger at the JMA stations compared to Hi-net in general, and we can expect some repercussions to the estimated peak-ratio values there. Therefore, we expect peak-ratios at the JMA stations to be much affected by the topographic effect especially in comparison to those at the Hi-net stations, regardless of whether they are ground surface or borehole stations. For this reason, we use the results from all JMA stations from Chapter 4, and the mitigated Hi-net results from Chapter 3, in this comparison.

On a single isolated case, we can look at the MS envelopes in and around the Sakurajima volcano. Figure 5.4 shows two MS envelope examples for the frequency band of 2-4 Hz at this volcano. One example is from the JMA network while the other is from the Hi-net array. The JMA station is station SFT2, while the Hi-net station is station AIRH, which is located at 15 km from the summit and is also the closest Hi-net station to the Sakurajima volcano (SFT2 is less than 5 km from the summit in comparison). Computed peak-ratio values from the examples in Figure 5.4 are 0.294 and 0.217 for station SFT2 and AIRH, respectively. In other words, already we see a larger ratio at the JMA example compared to the nearby Hi-net example.

In fact, this tendency of having larger peak-ratios at JMA stations compared to Hi-net is the general observation in our results. We show histograms of peak-ratio values found at all JMA stations (Chapter 4) across the four frequency bands in Figure 5.5. Also shown are similar histograms of peak-ratio values at Hi-net stations as evaluated in Chapter 3. The histograms are normalised as the probability density functions. As we can see, the JMA histograms are to the right of the Hi-net histograms, indicating that the distributions of peak-ratio estimates at JMA stations contain higher proportions of large ratios compared to Hi-net and vice-versa.

Looking at the numbers more specifically, the average peak-ratio values at JMA stations across the frequency bands of 0.5-1, 1-2, 2-4, and 4-8 Hz are 0.33, 0.35, 0.36, and 0.39, respectively (Figure 5.5, Table 4.1). Compared to the averages at Hi-net stations of

0.15, 0.14, 0.17, and 0.23, respectively (Figure 5.5, Table 3.1 and 3.2), there is an increase in peak-ratio of 113%, 150%, 112%, and 70%, respectively. This implies that peak-ratios at active volcanoes (JMA stations) are about twice as large as the surrounding regions (Hi-net).

On the other hand, the standard-deviations at the JMA stations are very much comparable to those at Hi-net. Across the frequency bands of 0.5-1, 1-2, 2-4, and 4-8 Hz, the standard-deviations at the JMA stations are 0.12, 0.13, 0.13, and 0.12, respectively (Table 4.1), while the standard-deviations at the Hi-net stations are 0.10, 0.08, 0.10, and 0.13, respectively (Table 3.1 and 3.2). Considering the clear differences with regard to the means, this further indicates that peak-ratios at active volcanoes and those at the surrounding regions are distinctly distributed. To further verify the contrast, we perform the corresponding t-test. Results show that at all frequency bands, the differences in peak-ratio values between Hi-net and JMA stations are statistically significant at 99.9% confidence level.

In Chapter 3, we further categorise Hi-net stations into the active volcano group (Category ii in Section 3.3.1), as well as into the active volcano plus active fault group (Category iv in Section 3.3.1). These Hi-net stations would be located closer to the JMA stations. And so, we compare peak-ratios at JMA stations to these subclasses of Hi-net stations. The mean peak-ratio values at Hi-net Category ii group across the frequency bands of 0.5-1, 1-2, 2-4, and 4-8 Hz are 0.16, 0.17, 0.18, and 0.28, with standard-deviations of 0.06, 0.04, 0.09, and 0.12, respectively (Table 3.1). Whereas the mean peak-ratio values for Category iv group are 0.24, 0.17, 0.22, and 0.34 with standard-deviations of 0.10, 0.06, 0.09, and 0.12, respectively (Table 3.1). Comparison between JMA stations and Hi-net Category ii shows that on average, peak-ratio values at the former are larger by 100%, 106%, 100%, and 39% across the 0.5-1, 1-2, 2-4, and 4-8 Hz frequency bands, respectively. Similarly, comparison between JMA stations and Hi-net Category iv shows that on average, peak-ratio values at the former are larger by 33%, 106%, 64%, and 15%

across the four frequency bands respectively. Likewise, we perform the corresponding t-test to assess these differences in peak-ratio values across all frequency bands. The t-test results indicate that — apart from the case of JMA against Hi-net Category iv at the 4-8 Hz band, which returns a confidence level of 80% — all comparisons return a statistical significance with confidence levels of at least 99%, with most comparisons returning a 99.9% confidence level. Therefore, there is still a considerable contrast in peak-ratio at active volcanoes even compared to those at the immediate surrounding areas.

All of these results are aligned with our understanding of topographic effect on peak-ratio. We infer that the large ratios at JMA stations might have been driven by scatterings off the irregular surface topography. Especially compared to those at Hi-net stations where presences of topographic irregularities are clearly not as strong as at active volcanoes. Therefore, the combined analysis of peak-ratio at JMA and Hi-net stations offers another example of topographic effect on peak-ratio in the real data.

5.4 Comparisons of Frequency Exponents Between Hi-net and JMA Stations

In addition to increasing the peak-ratio estimate, topography may also affect the extent of peak-ratio frequency dependency, in other words, the estimation of frequency exponent. Numerical simulation results (Section 2.3.3), and examples of scattering frequency dependency at some selected volcanoes (Section 4.3.1), showed how increasing complexity in topographic irregularity may reduce the frequency exponent. We also saw this impact in Section 5.2 where frequency exponents from the entire Hi-net dataset may depend on station elevation and thus on proximity to topographically complex mountainous locations. In this section, we extend our real data analysis of topographic effect on frequency exponent by comparing results obtained for Hi-net and JMA stations.

The estimation of frequency exponents as direct measurements of scattering frequency

dependency was given in Chapter 3 for the Hi-net stations. For JMA stations located on the active volcanoes, frequency exponents were estimated in Chapter 4. Accordingly, topographic effect on frequency exponent is expected to be stronger at the JMA stations. Since we have identified that the overall impact of topography is to decrease the frequency exponent estimate, we can expect this to be reflected in the distributions of frequency exponents at the two networks.

Indeed, the normalised histogram of frequency exponent estimates at JMA stations shows a higher proportion of small m values compared to that for Hi-net and vice-versa (Figure 5.6). Looking at the numbers, the average frequency exponent value at the JMA network is 0.20 with a standard-deviation of 0.15 (Figure 5.6, Table 4.1), whereas the average for Hi-net is 0.33 with a standard-deviation of 0.23 (Figure 5.6, Table 3.1 and 3.2). This corresponds to a decrease in the frequency exponent by 40% relative to the Hi-net average. This also suggests that the distributions of frequency exponents at Hi-net and JMA stations are distinct from one another. The t-test result corroborates this proposition. It indicates that the difference in frequency exponent values between Hi-net and JMA stations are statistically significant at the 99.9% confidence level.

With regard to comparison to Hi-net stations in the immediate surroundings of active volcanoes, we compare the frequency exponents at JMA stations to those at Hi-net Category ii (within 20 km of an active volcano). The average frequency exponent at these Hi-net stations is 0.28 with a standard-deviation of 0.10 (Table 3.1). This equates to a decrease in frequency exponent from Hi-net Category ii to the JMA stations of 30% with respect to the Hi-net average. The corresponding t-test indicates that the difference in frequency exponent values between JMA stations and Hi-net Category ii stations is statistically significant at the confidence level of 98%.

The above real data observations support our understanding of the topographic effect. That albeit topography can inflate peak-ratio through the introduction of topographic scatterings, it reduces the overall frequency dependency. Our findings from using the

JMA stations where there is a strong topographic presence in a form of an active volcano, compared to similar findings at Hi-net stations where extreme topographic changes are less prominent, certainly gives some indications of such topographic effect.

5.5 Discussion on Random Medium Parameters in Japan

Following Equation 2.12, we can approximate ε^2/a from the peak-ratio. Estimating the absolute ε^2/a values from Hi-net stations' peak-ratios though is not as straightforward not least because some free-surface and topographic effects may still linger. However, we can look at how ε^2/a varies from non-active (weak heterogeneity) to active (strong heterogeneity) areas in Japan.

Taking our peak-ratio results from Table 3.1, we suppose stations from Category v (non-active group) and Category iv (active volcano plus active fault) belong to regions with relatively weak and strong heterogeneity, respectively. Assuming h of 25 km, for example, the average ε^2/a values across the four frequency bands for the weak heterogeneity are 0.0029, 0.0029, 0.0034, and 0.0047 km^{-1}, whereas the average ε^2/a values for the strong heterogeneity are 0.0052, 0.0037, 0.0049, and 0.0076 km^{-1}, respectively. This corresponds to percentage increases of 84%, 28%, 45%, and 62%, respectively.

On the other hand, from Table 1.1 we can estimate the range of ε^2/a from previously estimated parameters for weak and strong heterogeneous region globally. Taking the maximum of each parameter range, weak and strong heterogeneous regions imply ε^2/a values of 0.0004 and 0.004 km^{-1}, respectively. While taking the minimum of each parameter range returns ε^2/a values of 0.001 and 0.072 km^{-1}, for weak and strong heterogeneities respectively. The minimum ε^2/a ranges from taking the minimum of ε but the maximum of a are 4×10^{-6} and 3.6×10^{-4} km^{-1} for weak and strong heterogeneous regions, respectively. Correspondingly, the maximum ε^2/a ranges from taking the maximum ε but the minimum a are 0.1 and 0.8 km^{-1} for weak and strong heteroge-

neous regions, respectively. In other words, the increase in ε^2/a from weak to strong heterogeneous settings based on globally estimated parameters can be one to two order of magnitude larger. Similar order of magnitude increase can also be found in Kubanza et al. (2007) for stable continents and tectonically active regions. This seems to indicate that even though we see a considerable increase in ε^2/a from non-active to active areas with respect to Hi-net stations, the contrast is not as significant as can be perceived globally. In other words, it seems that even non-active areas in Japan are still relatively active compared to, for example, more stable continental crust.

5.6 The Significance of Shallow Structures in the Peak-Ratio Method

In Chapter 4, we found that peak-ratios at ground surface JMA stations are larger than those found at JMA borehole stations. We speculated that this observation might have been caused by shallow low velocity structures at active volcanoes, following additional numerical simulations. However, these JMA borehole and ground surface stations are not located at the same coordinate points.

Hence, we consider the V-net stations. Similar to JMA stations, these stations are distributed across numerous active volcanoes in Japan, and consist of borehole and ground surface stations. However, unlike JMA stations, V-net ground surface and borehole sensors are installed at the same coordinate points. We use data from the same set of earthquakes to examine these V-net stations (Figure 3.2). The downside to V-net is the availability of records. So to determine the peak-ratios, we stacked envelopes from at least two earthquake recordings per station instead of ten.

Figure 5.7 shows the comparison between V-net ground surface and borehole sensors with regard to peak-ratio. Overall, we can see that across all frequency bands, peak-ratios at the ground surface sensors are larger than those at the borehole sensors. This

shows that for two stations only separated in depth, larger peak-ratio can be found at the station on the ground surface rather than at the deeper borehole station. Thus, these V-net results corroborate the previous observation at JMA stations. Both JMA and V-net stations results clearly show considerable contrasts between ground surface and borehole stations' peak-ratios. This implies that shallow structures are rather significant in the estimation of peak-ratio.

5.7 Separation of Topography and Random Heterogeneity Contributions to Peak-Ratios and Their Frequency Dependency at Active Volcanoes

From our peak-ratio and frequency exponent analyses, we may infer that both topographic scattering, and scattering off the medium heterogeneities contribute to the transverse component excitation. We have shown that topography may increase peak-ratio observation at a station while decreasing its frequency exponent estimate. But even though the significance of topography is seemingly clear, we are still short of providing a robust correction for its effect. In other words, more work is still needed to be done to clarify how much the MS envelope is constructed by scatterings off the topography and medium heterogeneity specifically.

From our work thus far however, some workarounds might be possible. In Section 2.3.3, we carried out simulations of seismic wave propagation through a random heterogeneous medium using the topography model of Mt. Fuji. We showed that at stations near to the volcanic centre, on average the the flat-free surface model shows smaller peak-ratio compared to the topography model by -0.06, -0.14, -0.06, and -0.01 at 0.5-1, 1-2, 2-4, and 4-8 Hz, respectively (Figure 2.14). If we take the case at the far-away stations as reference, which show discrepancies of $+0.01$, -0.02, -0.04, and -0.04 on average in

terms of peak-ratio across the four frequency bands, respectively, there is a gap of 0.07, 0.12, 0.02, -0.03 increase in peak-ratio as a consequence of topography.

Assuming these numbers, we would roughly correct peak-ratio estimates at Mt. Fuji to 0.38, 0.32, 0.35, and 0.38 from roughly 0.45, 0.44, 0.37, 0.35 shown in Figure 4.3 for the four frequency bands, respectively. These numbers are still large compared to peak-ratio estimates at Hi-net stations (Tables 3.1, 3.2). Assuming that these values reflect the scatterings off the random medium heterogeneities and weak topographic effect at Hi-net, this implies that our results indicate presences of strong random medium heterogeneities at Mt. Fuji with large root-mean-square fractional velocity fluctuation ε and/or smaller correlation distance a.

An alternative way to the one described above for correcting peak-ratio is also conceivable. This particular approach is especially useful for when only the simulation with topography is available. In Figure 5.8 we present the histograms of estimated peak-ratio values from simulated data using topography, separated into the near-summit and far-away stations (Section 2.3.3). The average increase in peak-ratio from the far-away stations to the near-summit stations cases across the 0.5-1, 1-2, 2-4, 4-8 Hz frequency bands are 0.02, 0.06, 0.02, and -0.01, respectively. From Figure 4.8, we can obtain the averages at JMA (surface and borehole) stations, as well as those at the surrounding Hi-net stations. These may correspond to the near-summit and far-away stations in our simulated case, respectively. Assuming the above numbers as the contribution of the topographic effect, the corrected mean peak-ratio values at the (near) JMA stations become 0.31, 0.29, 0.34, and 0.40, across the four frequency bands, respectively, which are still larger than the mean at the surrounding Hi-net (0.19, 0.18, 0.19, and 0.25, respectively). This similarly suggests stronger random medium heterogeneities at active volcanoes.

With regard to the frequency exponent, the observed value at Mt. Fuji obtained from the JMA stations is 0.12 (Figure 4.6). Our simulation result indicated that for stations within 5 km of the Mt. Fuji summit, frequency exponent is underestimated

by about 0.2 with respect to a flat surface model (Figure 2.15). Therefore, if we take this rough correction, frequency exponent at Mt. Fuji corrected for topography becomes 0.32, which is closer to the frequency exponent mean at Hi-net stations under the active volcano category (Category ii, mean m of 0.28 in Table 3.1).

To illustrate the prospect of quantitative evaluation of random medium parameters especially κ using the peak-ratio method, we present here an example approach based on our numerical simulations and data analysis results so far. Previously, we estimated that frequency exponent at Mt. Fuji corrected for the topographic effect is 0.32. The challenge, however, is to convert this m value into κ. Hence, we estimated m values from three sets of simulations with a flat surface using κ values of 0.1, 0.4, and 0.8. m values are estimated using stations at 2 and 4 km radius from the model centre (i.e., near summit array). Their average frequency exponents and their standard-deviations for the κ values of 0.1, 0.4, and 0.8 are 1.04 ± 0.46, 0.67 ± 0.43, and 0.35 ± 0.48, respectively (Figure 5.9, black circles). We may approximate this using an exponential type function where:

$$m \approx 1.228 \, \mathrm{e}^{-1.559 \, \kappa} \, . \tag{5.1}$$

Therefore, with an estimated frequency exponent of 0.32, this puts the estimated κ value at Mt. Fuji at roughly 0.86 (Figure 5.9, green triangle).

Crucially, we have shown that fundamentally, real world setup (station locations, topography model) can be utilised to synthesise peak-ratio results from an ensemble of numerically simulated data. From these simulations, the extent of topographic effect at each station can be quantitatively examined. To achieve this, many random medium realisations need to be introduced which requires a significant number of simulations. We are yet to perform this feat considering that it took $1 \sim 2$ hr of computing time on the EIC-ERI cluster-type supercomputer for a single run of a simulation (i.e., it costs time and money). However, we have shown that such approach may worth the investment.

Currently, cross-volcano comparison is made complicated by the inability to separate topographic scatterings from scatterings off medium heterogeneity. Hence, mitigating the topographic effect across all volcanoes is not straightforward because of the unique shape and size of each volcano. With the help from numerical simulation, we can get some appraisals of topographic effect at each station at each volcano, which will most certainly help us conduct comparisons of scattering strengths at different active volcanoes that would reflect the medium heterogeneities at those volcanoes more conscientiously.

5.8 Analysis of Envelope Duration and Peak Delay Time

Theoretical envelope synthesis predicted a positive correlation between peak-ratio and envelope duration represented by the lag time (delay) from the onset and the maximum envelope amplitude (e.g., Sato (2006)). For the case of a vertically incident plane P wave through an infinite Gaussian type random medium, the peak delay in the horizontal/transverse component intensity spectral density (MS envelope) is scaled by the characteristic time t_M which increases in proportion to ε^2/a (Sato, 2006; Kubanza et al., 2007). We have established that peak-ratio is also proportional to ε^2/a as shown in Equation 2.12. Thus, a positive correlation between peak-ratio and peak delay time can be expected from the notion that both share a similar proportionality to ε^2/a. In addition, from their finite difference numerical simulations of wave propagation through von Karman type media, Takemura et al. (2015a) observed that scattering off the small-scale heterogeneities progressively accumulates with travel distance. As more energies are being partitioned into the transverse component with increasing travel distance, this would result in the broadening of the envelope, increasing the envelope duration, and delaying the peak in the transverse envelope, while at the same time, translates into larger peak-ratio.

And so, one would think of a positive correlation between peak-ratio and the peak

delay time of the transverse component seismogram envelope. We use the ak135 earth-model to measure the lag time between the expected direct P wave onset and the transverse component MS envelope peak amplitude time. Results, however, suggest that relationship between peak-ratio and peak delay time is complicated and not as straightforward as initially perceived.

Examination of transverse peak delay time at the JMA ground surface and borehole stations in the frequency band of 0.5-1 Hz, shows that transverse peak delay time at the ground surface stations on average is smaller (arrive earlier) than at the borehole stations by roughly 1.6 s (Figure 5.10). This is in contrast to the average increase in peak-ratio from borehole to ground surface stations at the same frequency band (Figure 4.4, Table 4.1). On the other hand, for higher frequency bands, transverse peak delay times increase from borehole stations to ground surface stations, on average by roughly 0.3, 1.0, and 0.7 s for 1-2, 2-4, and 4-8 Hz, respectively (Figure 5.10). Furthermore, there is no clear pattern between JMA stations and Hi-net stations transverse peak delay times (Figure 5.10). Peak delay time increases from (all) JMA to Hi-net by 3.4, and 1.0 s in the 0.5-1, and 1-2 Hz frequency bands, respectively, but decreases by 0.6 s in the 2-4 and 4-8 Hz frequency bands. This is despite the peak-ratio results consistently show larger peak-ratio estimates at JMA stations compared to Hi-net.

We may suspect that additional factors other than medium heterogeneity might have played a part in explaining this discrepancy in peak-ratio and peak delay time. It is possible that the excitation of transverse motion due to topography is one of them. Additionally, some P-to-S or body to surface wave conversions may have contributed to this discrepancy. The impact of surface waves is particularly under-represented in our simulations considering that we used vertically incident sources and a simple heterogeneous velocity structure. We have also shown the significance of shallow structures on peak-ratio estimation, but their impact on peak delay time is still unclear. Thus, the mechanisms behind these factors need to be examined more carefully. Furthermore, peak

delay time analysis can be further exacerbated by the selection of the envelope peak itself. Because of the fluctuating nature the seismogram envelopes, we may have several local peaks with similar amplitudes but a sufficient gap in lapse time. This would not change the estimation of peak-ratio, but it may introduce ambiguity in peak delay time. Further studies especially on the wave characteristics of distinct phases in both observed and simulated data may lead to the better understanding of peak-ratio and transverse component peak delay time. This could help us further our understanding of random heterogeneity from the transverse component seismogram.

5.9 Future Perspectives

We have shown and justified how free-surface and topographic effects can be mitigated when analysing peak-ratios and their frequency dependency using real dataset. Hence, we have shown how the qualitative examination of random medium heterogeneity can be carried out. However, more works are necessary to correct for these free-surface and topographic effects more quantitatively. By combining numerical simulation and real station observation at Mt. Fuji, we have shown a possible path towards the quantitative evaluation of random heterogeneity using the peak-ratio method.

From this study, we can identify several factors that may lead to a more accurate separation of topographic scatterings from scatterings off medium heterogeneities at seismic stations located on an active volcano. These are the use of precise topography model and real station configuration in the simulation, in addition to the use of an oblique incident source and a depth dependent velocity model. Our simulations so far have been utilising ideal arrangements of virtual arrays to the Mt. Fuji topography, mainly to bring down the cost of computing. To better appraise the contribution from scattering off the medium heterogeneity thus removing the topographic effect when analysing real volcanic stations, similar plots to Figure 5.9 can be produced using real station configuration at

various volcanoes. More specifically, to estimate the topographic effect at a particular volcano, we may compute the stations averages for simulations that contain real topography and a flat surface condition. The difference between the two simulation cases may represent a correction for the topographic effect more quantitatively. Similarly, real borehole station configuration (as well as the rough free-surface terrain/ground) can be used to better correct for the free-surface effect. Additionally, in reality we expect our sources to contain some oblique components. So to better represent this in the simulation, obliquely incoming sources should be considered, preferably in reference to the incident angles of the earthquakes to be analysed. The use of a layered velocity structure on top of using an obliquely incoming source can also better simulate surface wave conversions, thus allowing us to examine their effect. By improving upon the currently rather simple simulation settings, we might also finally resolve the observation of transverse peak delay time, through looking at the resulting waveform characteristics.

The catch to all of this is that a sufficient number of repeated simulations may be required, ideally, using different realisations of random medium heterogeneity to obtain the ensemble average. Simulations with numerous κ values are also necessary for the conversion between m and κ. But investing more on numerical simulations can help us towards the full quantitative estimation of random heterogeneity parameters especially κ, in which, our study have laid down the groundwork.

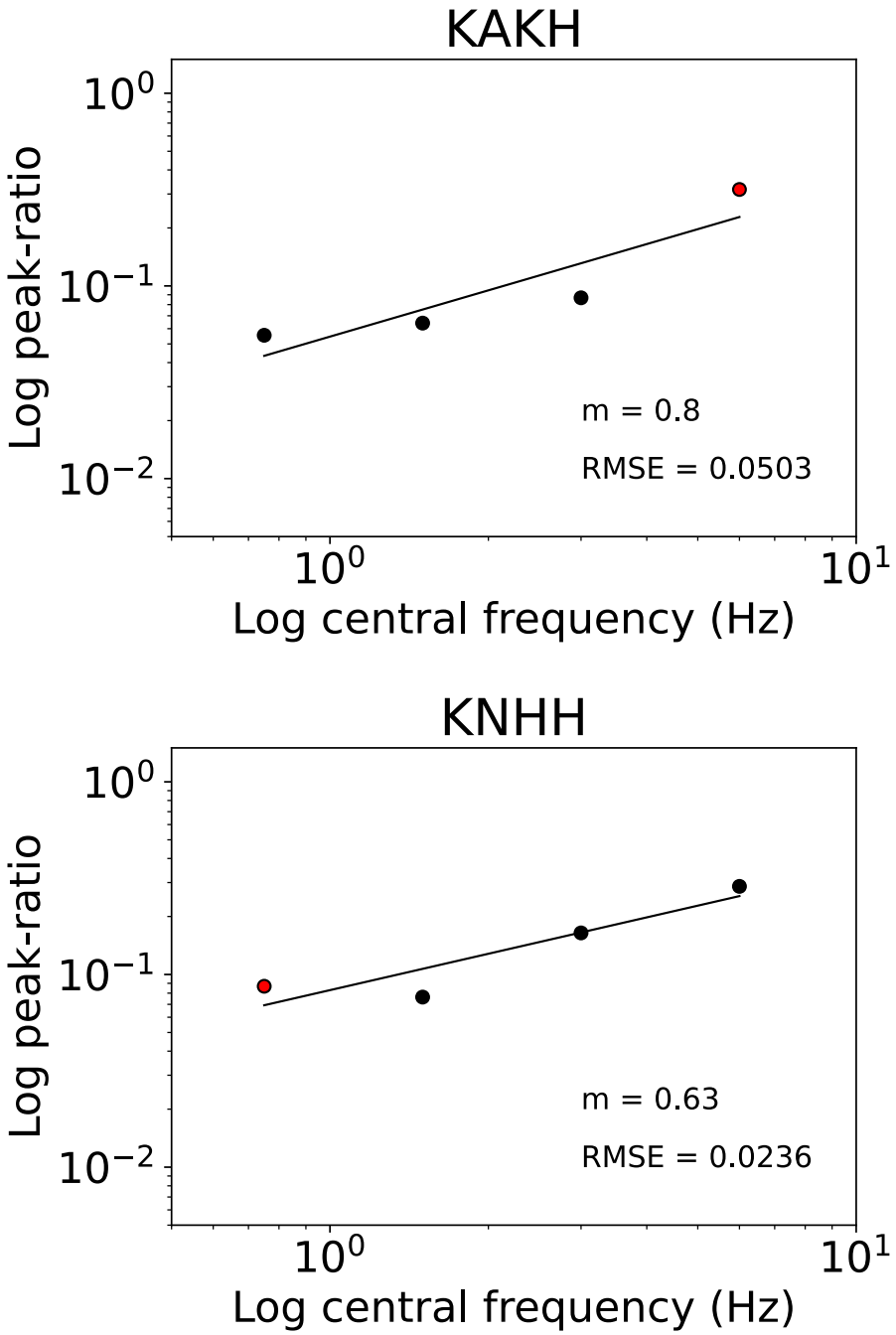

Figure 5.1 The free-surface effect in real data observation. Following the destructive interference between the up-going incident and the down-going surface reflected phases, peak-ratio $\Re$ at specific frequency band could be raised in relation to station depth. (*top*) Hi-net station KAKH from Ishinomaki in eastern Tohoku, with installation depth of 207 m. (*bottom*) Hi-net station KNHH from the Kinki region, with installation depth of 2.03 km. The inflated peak-ratio values are shown by the red symbols.

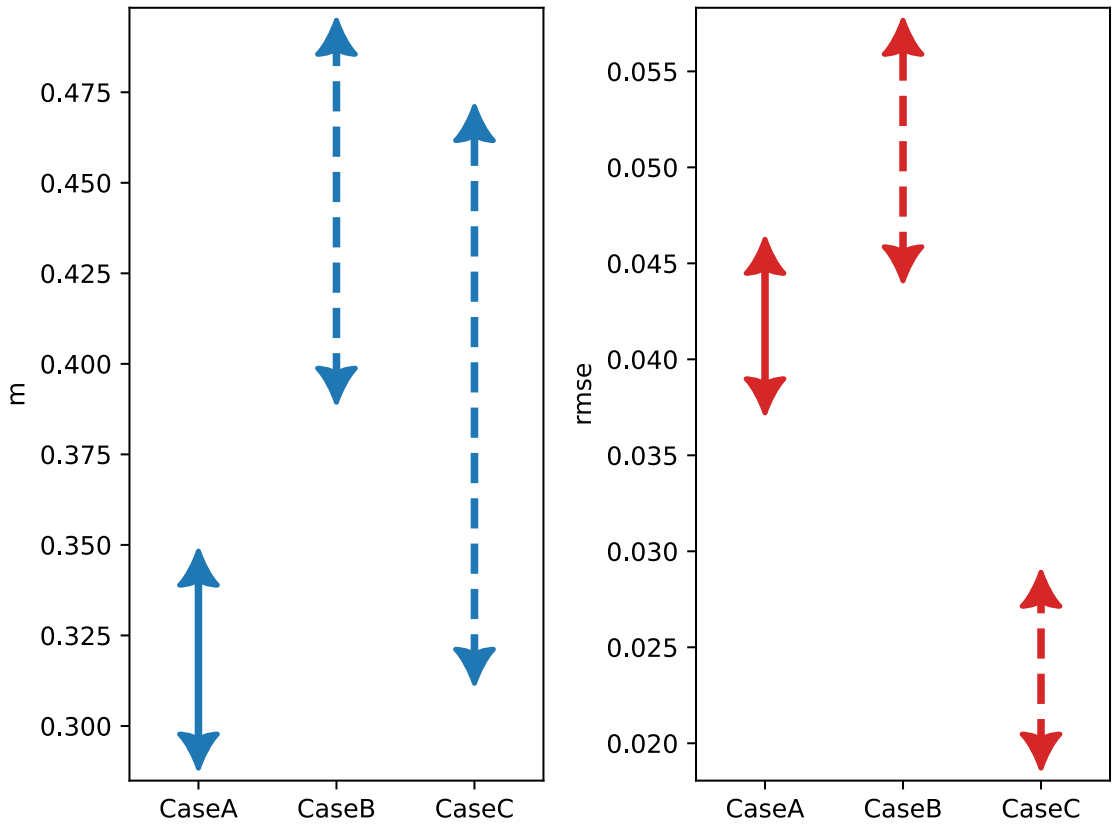

Figure 5.2 95% confidence intervals of estimated frequency exponent m (blue) and the corresponding root-mean-square-error (red) for three different cases. Case A: Hi-net stations at 100-200 m depth, using all four frequency bands (0.5-1, 1-2, 2-4, 4-8 Hz). Case B: Hi-net stations at 200-300 m depth, using all four frequency bands. Case C: Hi-net stations at 200-300 m depth, without using the 4-8 Hz band.

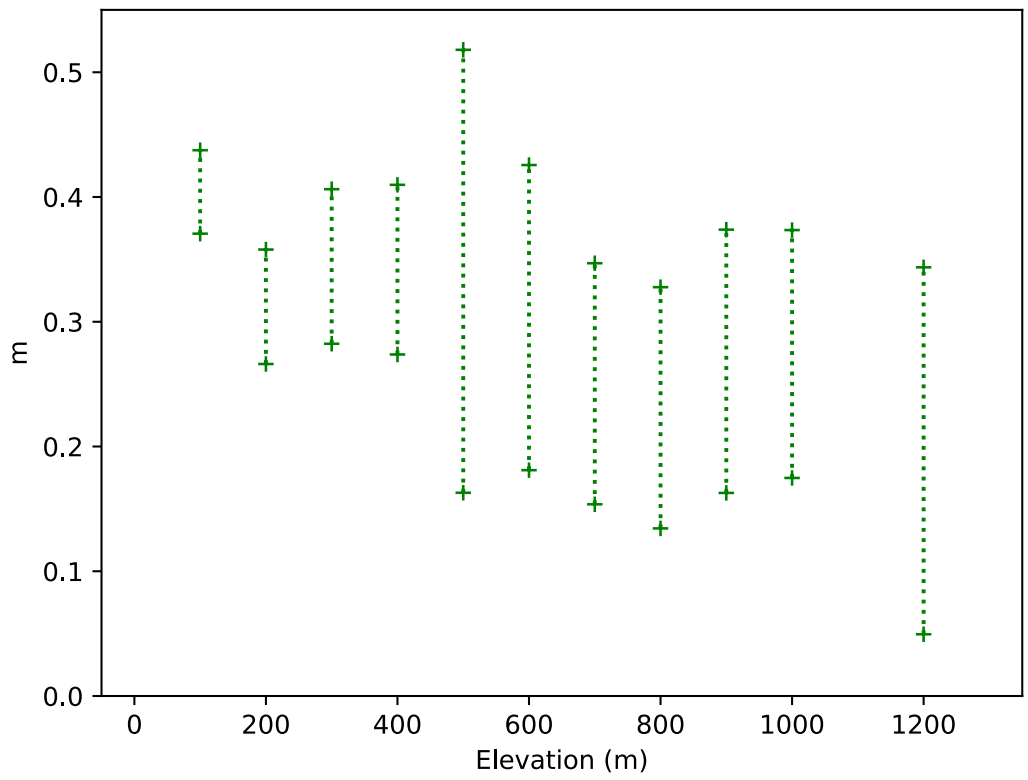

Figure 5.3 95% confidence intervals of frequency exponent m at Hi-net stations with respect to station elevation binned at every 100 metres.

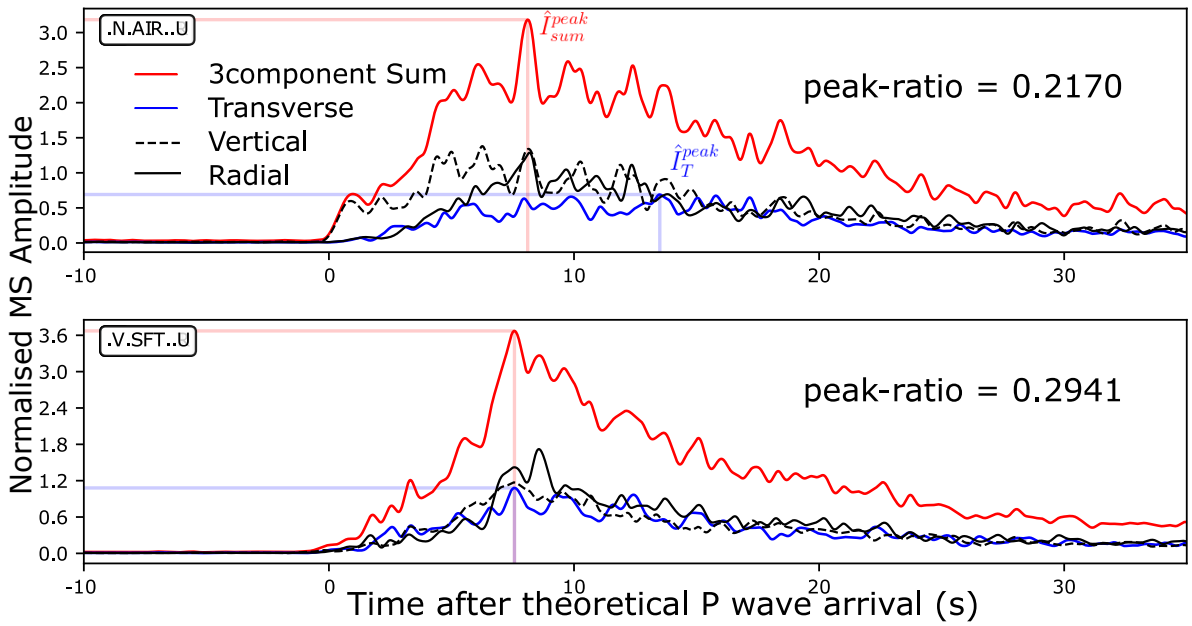

Figure 5.4 Example mean-squared (MS) seismogram envelopes from (*top*) station AIRH which is the closest Hi-net station to the Sakurajima Volcano, and (*bottom*) station SFT2 which is one of the JMA stations deployed on the Sakurajima Volcano. Blue traces represent the transverse component envelopes, while red traces represent the three-component sum envelopes. Dashed-black and black lines are the vertical and radial component envelopes, respectively. The translucent lines mark the peaks of the blue and red envelopes, denoted here as $\hat{I}_T^{peak}$ and $\hat{I}_{sum}^{peak}$. Peak-ratio is given by $\hat{I}_T^{peak}/\hat{I}_{sum}^{peak}$. Time is given with respect to the theoretical P wave arrival according to the ak135 model. The shown time-window excludes the direct S arrival. Examples are given for the frequency band of 2-4 Hz.

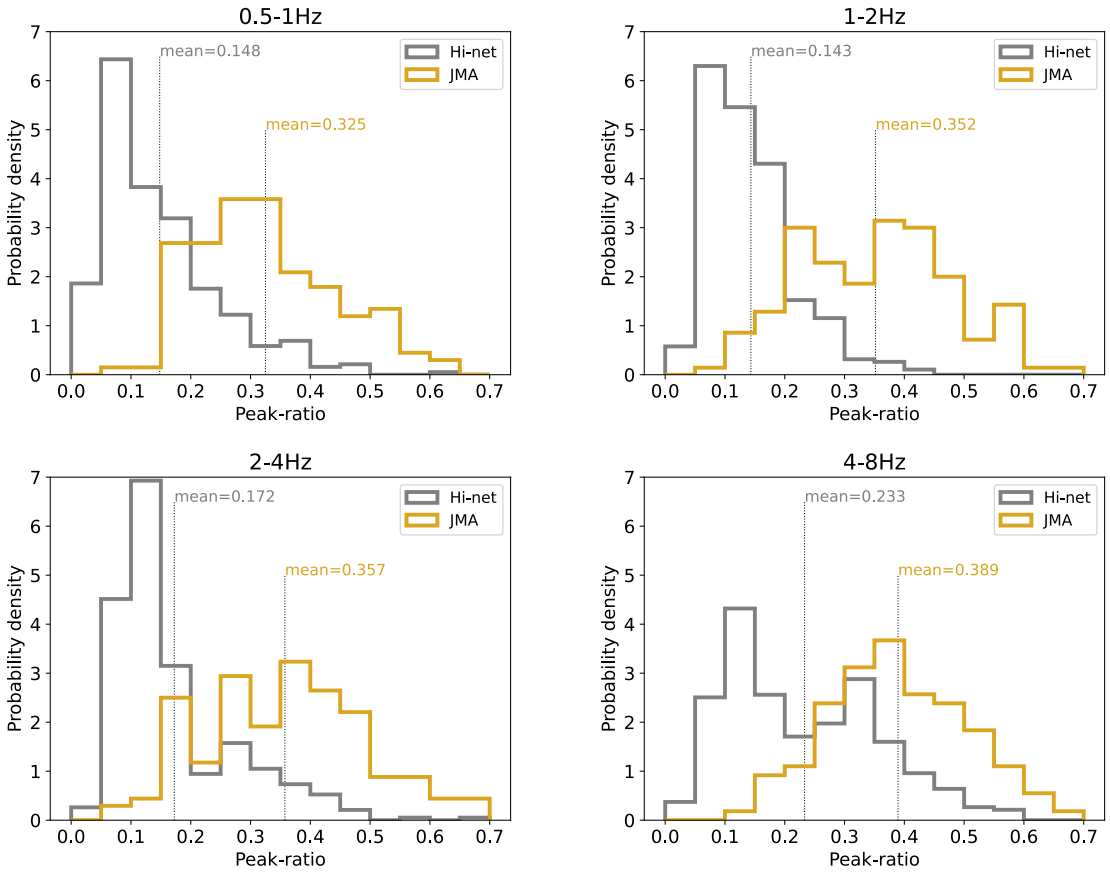

Figure 5.5 The probability density functions (normalised histograms) of peak-ratio $\Re$ for the frequency bands of 0.5-1, 1-2, 2-4, and 4-8 Hz. Grey histograms show the distributions of peak-ratio values for the Hi-net data (Chapter 3). Yellow histograms show the distributions of peak-ratio values for all JMA stations (Chapter 4). Peak-ratios at JMA stations are for the most part, larger than those at Hi-net stations.

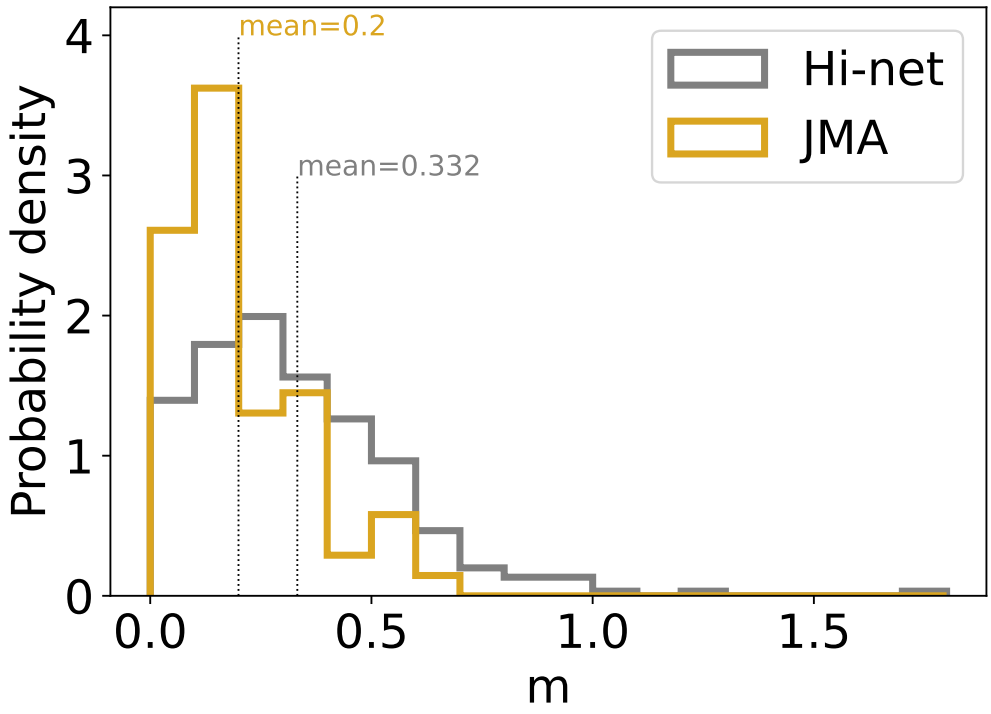

Figure 5.6 The probability density functions (normalised histograms) of frequency exponent m. Grey histogram shows the distribution of frequency exponents for the Hi-net data (Chapter 3). Yellow histogram shows the distribution of frequency exponents for all JMA stations (Chapter 4). Frequency exponents at JMA stations are, for the most part, smaller than those at Hi-net stations.

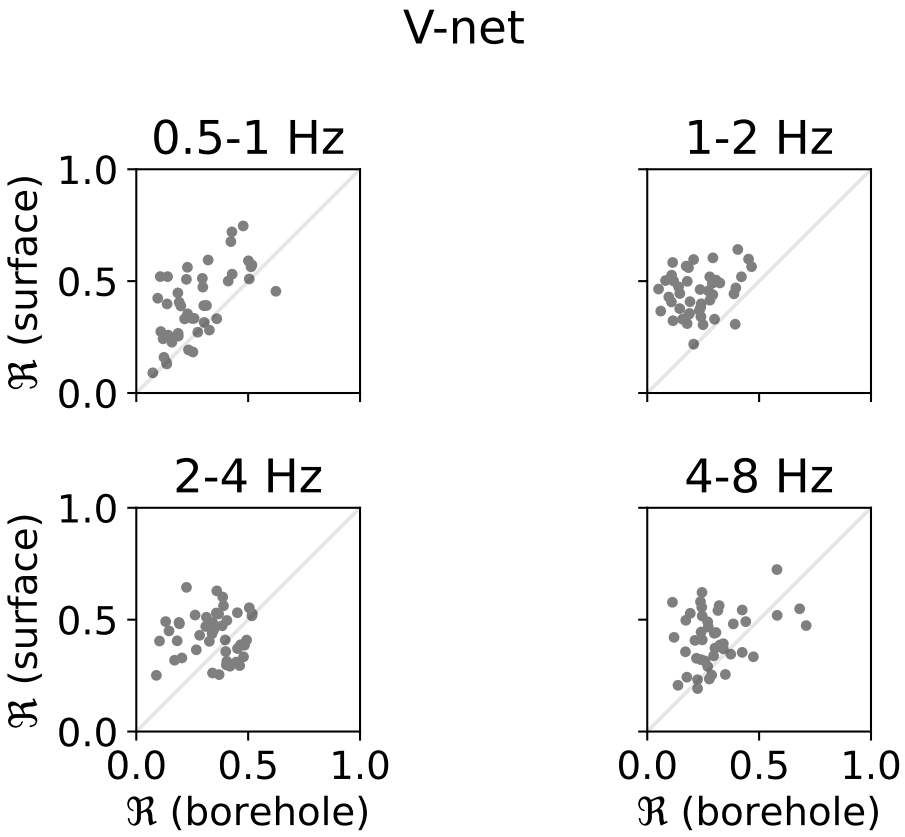

Figure 5.7 Comparisons of peak-ratio $\Re$ at V-net ground surface and borehole sensors across multiple frequency bands: 0.5-1, 1-2, 2-4, and 4-8 Hz. Peak-ratios at the ground surface sensors are larger than their borehole counterparts, corroborating our previous observation at the JMA stations.

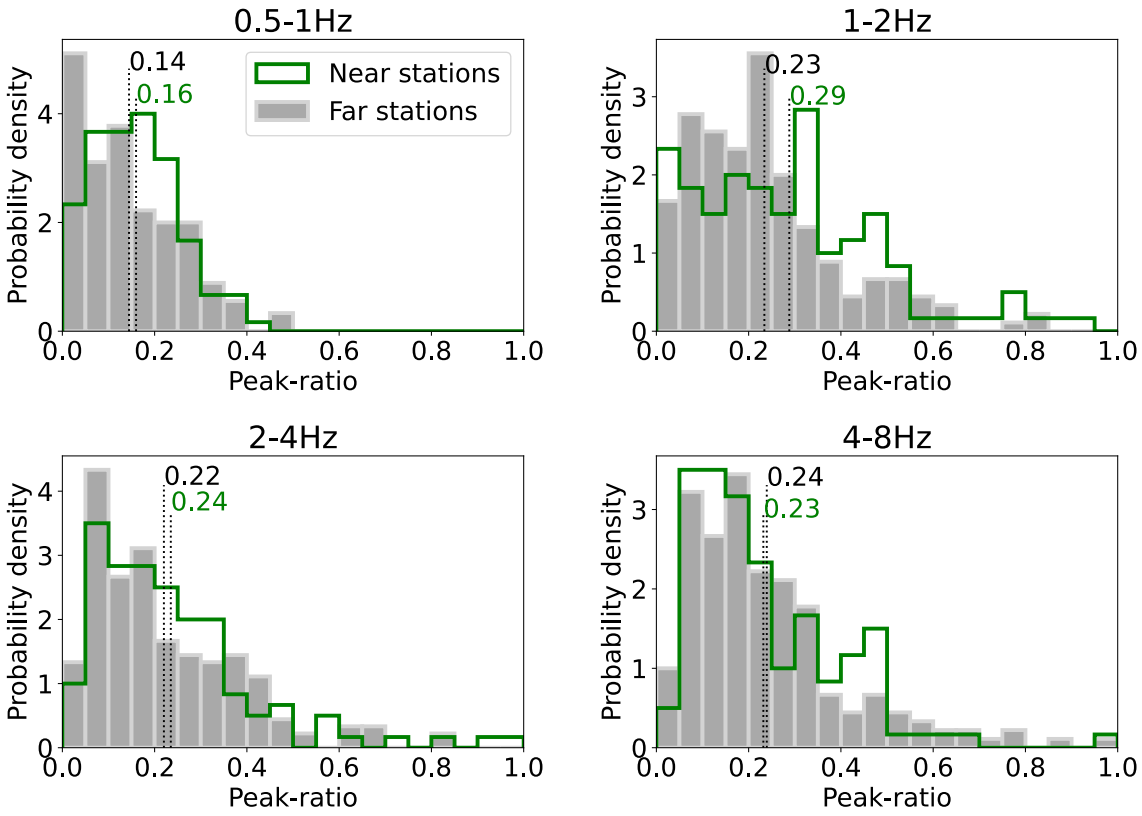

Figure 5.8 The probability density functions (normalised histograms) of peak-ratio $\Re$ obtained using simulated data with topography (Section 2.3.3). Green histograms show the distribution of peak-ratio at stations near to the summit. Grey histograms show the distribution of peak-ratio at the far-away stations. Dashed lines and the corresponding numbers indicate the average values of the distributions.

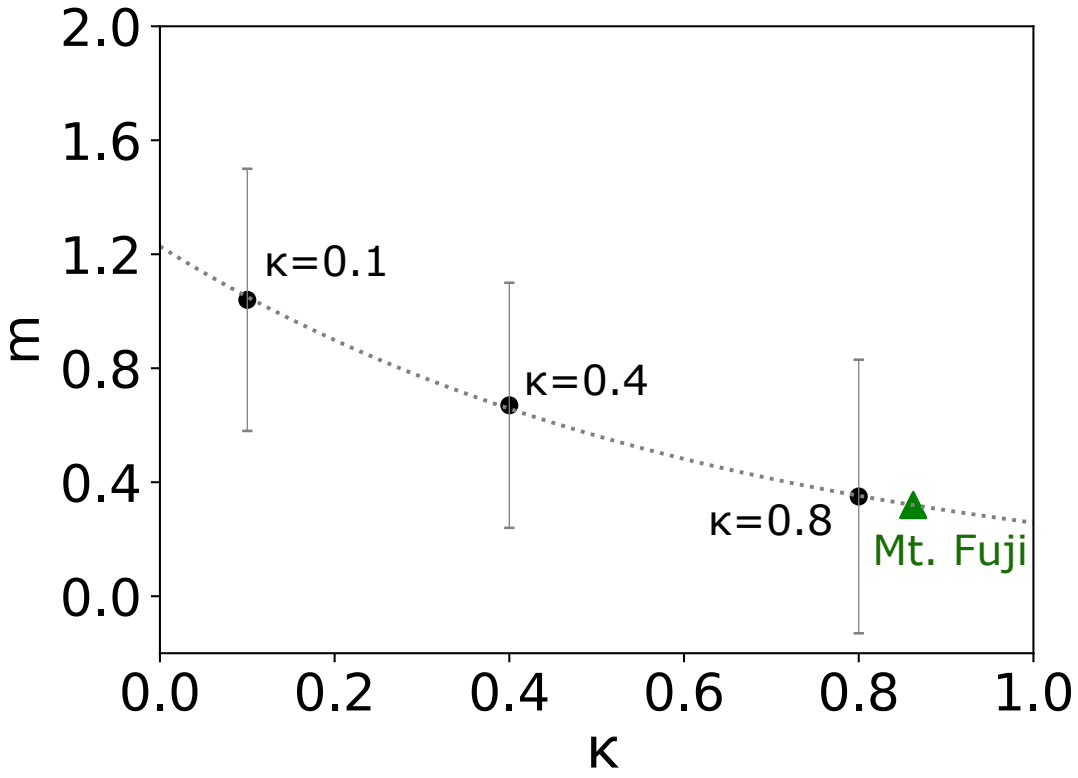

Figure 5.9 Frequency exponent m estimated from numerical simulations with a flat surface using stations at 2 and 4 km radius from the model centre. Using κ of 0.1, 0.4, and 0.8, we can fit an exponential type relation connecting m and κ. The topographically corrected observed m value at Mt. Fuji JMA stations is 0.32, which equates to a κ value of 0.86 (green triangle).

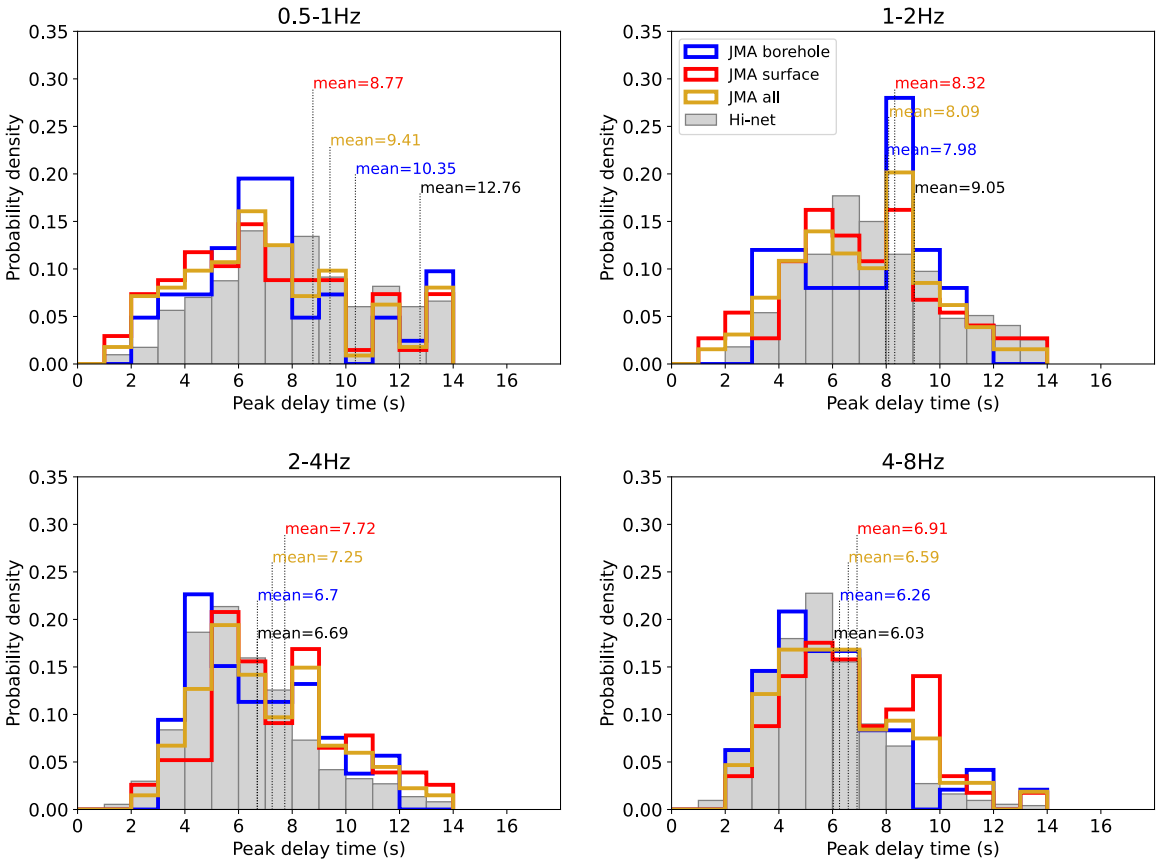

Figure 5.10 The probability density functions (normalised histograms) of transverse envelope peak delay time at four frequency bands: 0.5-1, 1-2, 2-4, 4-8 Hz. Yellow histograms show the distributions of transverse peak delay times when all JMA stations are considered. Red and blue histograms separate the transverse peak delay time distributions into JMA ground surface and borehole stations, respectively. Grey histograms show the distribution of transverse peak delay times at Hi-net stations. At 0.5-1 Hz, there are Hi-net data outside the range shown hence the larger mean than implied by the distribution.

Chapter 6

Conclusions

To characterise small-scale medium heterogeneities, we used the contribution of scattered P waves to the transverse component seismograms. This is done through the computation of peak-ratio $\Re$ and its frequency dependency measured by the frequency exponent m. The free-surface and topography can also affect the contribution of P wave energy in the transverse component. Therefore, we first examined the effects of free-surface and topography on peak-ratio and its frequency dependency by conducting numerical simulations of seismic wave propagation through random heterogeneous media. Subsequently, we tried to extend the applicability of the method to data recorded by stations in boreholes and at volcanic areas.

Through conducting numerical simulations of P wave propagations in random heterogeneous media, we have successfully identified the impacts of free-surface and topography on peak-ratio and frequency exponent. Mainly, these can be specified as follows:

1. The free-surface effect arises from the wave interference between incident and surface reflected phases. For a vertically incoming wave, the interference is destructive on the vertical component. This may increase the proportion of energy in the transverse component, hence inflating the peak-ratio. We found that this effect is especially strong at a specific depth of the quarter of the seismic wavelength. This

suggests that for borehole stations, evaluated peak-ratio can be raised depending on both installation depth and frequency. Specifically, at the depth of around 2 km, peak-ratio at the 0.5-1 Hz frequency band is inflated, while peak-ratio at the frequency band of 4-8 Hz is inflated at the depth of around 250 m. As a result, frequency exponents at borehole stations around 2 km depth can be underestimated, while frequency exponents are overestimated at borehole stations around 250 m depth.

2. Where a strong presence of topography is clear (e.g., near the summit of a volcano), transverse component signals can also be excited by scatterings off the topographic irregularities. Thus, both scattering off the medium heterogeneities and topography contribute to the peak-ratio. We found that this topographic effect may raise the peak-ratio estimate, especially in the lower frequencies of 1-2 Hz. Correspondingly, frequency exponent estimation is also well affected by topography. We found that the tendency is for frequency exponent estimates to be reduced by the topographic effect.

3. We propose mitigating the aforementioned free-surface and topographic effects by evaluating peak-ratio and frequency exponent at borehole stations of similar depths and elevation. This is because at those stations, the extent of the free-surface and topographic effects are much more comparable. Therefore, the results of such evaluation can be attributed to the small-scale heterogeneity of the random medium.

We analyse peak-ratio and its frequency dependency in Japan by evaluating data at Hi-net stations. We can confirm the existence of the free-surface and topographic effects in this dataset in relation to station elevations and borehole depths, thus justifying our mitigation strategy. So accordingly, we took a subset of Hi-net stations with a similar depth range of 100-200 m and a similar elevation range of $<$400 m, and estimate their peak-ratios and frequency exponents. The main observations are as follows:

1. After mitigating for the free-surface and topographic effects, peak-ratios range from 3.22×10^{-5} to 0.64 at the frequency band of 0.5-1 Hz, 1.73×10^{-6} to 0.72 at 1-2 Hz, 1.07×10^{-5} to 0.78 at 2-4 Hz, and 0.03 to 0.85 at 4-8 Hz. Their mean values are 0.15, 0.14, 0.17, and 0.23 across the four frequency bands, respectively. Most frequency exponent estimates fall between 0.01 and 0.80 with an average of 0.33.

2. Even after mitigating the free-surface and topographic effects, we see an east-west split in the peak-ratio values in Japan. This lateral variation therefore can be attributed to the contrasting medium heterogeneities in Japan. More specifically, we attributed this to heterogeneities related to geological activity and geological age. Large peak-ratios in Japan represent strong heterogeneities in young rocks at geologically active regions, and vice-versa. Thus, we attribute large peak-ratios in the East to the strong heterogeneities surrounding the volcanic front in Japan, and similarly we attribute the small peak-ratios in the West to the lack of active volcanoes in the area.

3. On the other hand, we found frequency exponent values associated with active volcanoes to be significantly small especially compared to those at sediments and plains. This suggests that sediments contain small-scale heterogeneities richer in short-wavelength components, whereas small-scale heterogeneities are poor in short-wavelength components near volcanoes.

To compliment the results from the Hi-net dataset, we estimated peak-ratios and their frequency dependency at JMA stations. Results from the JMA stations by themselves revealed interesting scattering mechanism at volcanic edifices. With JMA stations though, we obtained data containing strong topographic effect as these stations are located on active volcanoes. Therefore, cross-examination of peak-ratio and frequency exponent values at Hi-net and JMA stations revealed the topographic effect in real data observations. The specifics are as follows:

1. The ranges of peak-ratio values at JMA stations are from 0.08 to 0.63 at the frequency band of 0.5-1 Hz, 0.10 to 0.66 at 1-2 Hz, 0.08 to 0.70 at 2-4 Hz, and 0.12 to 0.65 at 4-8 Hz. While the mean values across the same frequency bands are 0.33, 0.35, 0.36, and 0.39, respectively.

2. We found that peak-ratios at JMA ground surface stations are significantly larger than those at JMA borehole stations. Across the 0.5-1, 1-2, 2-4, 4-8 frequency bands, the mean peak-ratio values at JMA borehole stations are 0.30, 0.27, 0.26, and 0.34, whereas the mean peak-ratio values at JMA ground surface stations are 0.34, 0.40, 0.43, and 0.43, respectively. Using additional numerical simulations, we found that the existence of a thin shallow low velocity layer commonly found at active volcanoes can trap topographically scattered waves in the near surface. We speculate that this is one possible explanation for the observed larger peak-ratios at the ground surface stations.

3. We found peak-ratios at JMA stations to be significantly larger than those at Hi-net stations, whereas frequency exponents at JMA stations are significantly smaller than those at Hi-net stations. Considering the clear topographic presence at JMA stations, we partially attribute this to the topographic effect. Although scattering contribution from intensified medium heterogeneity is likely present as well.

We have successfully identified the significance of free-surface and topography on P wave seismogram especially in relation to scattering contributions to the transverse component. By mitigating these effects, we can better infer small-scale medium heterogeneity as construed by the estimations of peak-ratio and frequency exponent. Henceforth, relative estimations of the parameters of random velocity heterogeneity have now become possible. Moreover, numerical simulations that include precise topographic model and real station configuration will enable us to correct for the free-surface and topographic effects, hence allowing for the quantitative estimation of random medium parameters, κ

value in particular. In this regard we attempted to estimate the κ value at Mt. Fuji, thus showing the possibility of similar analysis to be done for other volcanoes. The present study has laid down the groundwork for the quantitative estimation of the random velocity heterogeneities in the Earth using transverse-component P-wave seismograms.

Bibliography

Abramowitz, M. and Stegun, I. A. (1972). *Handbook of Mathematical Functions with Formulas, Graphs, and Mathematical Tables*. Wiley.

Akande, W. G., Siena, L. D., and Gan, Q. (2019). Three-dimensional kernel-based coda attenuation imaging of caldera structures controlling the 1982-84 Campi Flegrei unrest. *Journal of Volcanology and Geothermal Research*, 381:273–283. DOI: 10.1016/j.jvolgeores.2019.06.007.

Aki, K. (1969). Analysis of the seismic coda of local earthquakes as scattered waves. *Journal of Geophysical Research*, 74(2):615–631. DOI: 10.1029/jb074i002p00615.

Aki, K. (1973). Scattering of P waves under the Montana Lasa. *Journal of Geophysical Research*, 78(8):1334–1346. DOI: 10.1029/jb078i008p01334.

Aki, K. and Chouet, B. (1975). Origin of coda waves: Source, attenuation, and scattering effects. *Journal of Geophysical Research*, 80(23):3322–3342. DOI: 10.1029/jb080i023p03322.

Aki, K. and Richards, P. G. (1980). *Quantitative seismology: Theory and methods*, volume 2. Freeman.

Aoki, Y., Takeo, M., Aoyama, H., Fujimatsu, J., Matsumoto, S., Miyamachi, H., Nakamichi, H., Ohkura, T., Ohminato, T., Oikawa, J., and et al. (2009). P-wave velocity structure beneath Asama Volcano, Japan, inferred from active source seismic

experiment. *Journal of Volcanology and Geothermal Research*, 187(3–4):272–277. DOI: 10.1016/j.jvolgeores.2009.09.004.

Arfken, G. B., Weber, H. J., and Harris, F. E. (2013). *Mathematical methods for physicists a comprehensive guide*. Elsevier.

Bettinelli, P., Avouac, J.-P., Flouzat, M., Bollinger, L., Ramillien, G., Rajaure, S., and Sapkota, S. (2008). Seasonal variations of seismicity and geodetic strain in the Himalaya induced by surface hydrology. *Earth and Planetary Science Letters*, 266(3-4):332–344. DOI: 10.1016/j.epsl.2007.11.021.

Blanch, J. O., Robertsson, J. O., and Symes, W. W. (1995). Modeling of a constant Q: Methodology and algorithm for an efficient and optimally inexpensive viscoelastic technique. *GEOPHYSICS*, 60(1):176–184. DOI: 10.1190/1.1443744.

Brase, C. H. and Brase, C. P. (2013). *Understanding Basic Statistics. Ch. 10: Inferences About Differences*. Brooks/Cole Cengage Learning, 6th edition. ISBN: 978-1-111-82702-1.

Buehler, J. S., Mancinelli, N. J., and Shearer, P. M. (2018). S-to-Rayleigh wave scattering from the continental margin observed at USArray. *Geophysical Research Letters*, 45(10):4719–4724. DOI: 10.1029/2017gl076812.

Cafferky, S. and Schmandt, B. (2015). Teleseismic P wave spectra from USArray and implications for upper mantle attenuation and scattering. *Geochemistry, Geophysics, Geosystems*, 16(10):3343–3361. DOI: 10.1002/2015gc005993.

Calvet, M. and Margerin, L. (2013). Lapse-time dependence of Coda Q: Anisotropic multiple-scattering models and application to the Pyrenees. *Bulletin of the Seismological Society of America*, 103(3):1993–2010. DOI: 10.1785/0120120239.

Campbell, I. (2007). Chi-squared and Fisher-Irwin tests of two-by-two tables with small sample recommendations. *Statistics in Medicine*, 26(19):3661–3675.

Capon, J. (1974). Characterization of crust and upper mantle structure under LASA as a random medium. *Bulletin of the Seismological Society of America*, 64(1):235–266.

Carcione, J. M. and Tinivella, U. (2001). The seismic response to overpressure: a modelling study based on laboratory, well and seismic data. *Geophysical Prospecting*, 49(5):523–539. DOI: 10.1046/j.1365-2478.2001.00273.x.

Carcolé, E. and Sato, H. (2010). Spatial distribution of scattering loss and intrinsic absorption of short-period S waves in the lithosphere of Japan on the basis of the Multiple Lapse Time Window Analysis of Hi-net data. *Geophysical Journal International*, 180(1):268–290. DOI: 10.1111/j.1365-246x.2009.04394.x.

Cario, F. D. and de Souza, J. L. (2006). Crustal thickness beneath Rio de Janeiro, Brazil, from spectra of SH waves at station RDJ. *Geofisica Internacional*, 45(2):115–128.

Chamberlain, C. J., Hopp, C. J., Boese, C. M., Warren−Smith, E., Chambers, D., Chu, S. X., Michailos, K., and Townend, J. (2017). Eqcorrscan: Repeating and near repeating earthquake detection and analysis in Python. *Seismological Research Letters*, 89(1):173–181. DOI: 10.1785/0220170151.

Chevrot, S., Montagner, J. P., and Snieder, R. (1998). The spectrum of tomographic Earth models. *Geophysical Journal International*, 133(3):783–788. DOI: 10.1046/j.1365-246x.1998.00542.x.

Cormier, V. F. and Sanborn, C. J. (2019). Trade offs in parameters describing crustal heterogeneity and intrinsic attenuation from radiative transport modeling of high frequency regional seismograms. *Bulletin of the Seismological Society of America*, 109(1):312–321. DOI: 10.1785/0120180231.

da Silva, J. A., Poliannikov, O. V., Fehler, M., and Turpening, R. (2018). Modeling scattering and intrinsic attenuation of crosswell seismic data in the Michigan Basin. *GEOPHYSICS*, 83(3). DOI: 10.1190/geo2017-0448.1.

Das, A., Patel, V., and Ghosh, A. (2018). Ground motion selection considering seismicity of the area and response of the structure. *International Journal of Engineering Research and Technology*, V7(01). DOI: 10.17577/ijertv7is010108.

Del Pezzo, E., Giampiccolo, E., Tuvé, T., Di Grazia, G., Gresta, S., and Ibàñez, J. M. (2019). Study of the regional pattern of intrinsic and scattering seismic attenuation in eastern Sicily (Italy) from local earthquakes. *Geophysical Journal International*, 218(2):1456–1468. DOI: 10.1093/gji/ggz208.

Digital Active Fault Map of Japan (2002). University of Tokyo Press.

Dvorkin, J., Mavko, G., and Nur, A. (1999). Overpressure detection from compressional- and shear-wave data. *Geophysical Research Letters*, 26(22):3417–3420. DOI: 10.1029/1999gl008382.

Ekka, M. S., Vandana, Roy, P., and Mishra, O. (2020). Coda wave seismic structure beneath the Indian ocean region and its implications to seismotectonics and structural heterogeneity. *Journal of Asian Earth Sciences*, 188:104104. DOI: 10.1016/j.jseaes.2019.104104.

Emoto, K. (2018). *Synthesis of Seismic Wave Envelopes Based on the Markov Approximation*, page 127–142. Springer Singapore. ISBN: 978-981-10-2632-4. DOI: 10.1007/978-981-10-2633-1.

Emoto, K., Nishimura, T., Nakahara, H., Miura, S., Yamamoto, M., Sugimura, S., Ueda, T., Ishikawa, A., and Kimura, T. (2020). *Effect of complex topography on the wavefield recorded by DAS and buried fiber optic cable at Azuma volcano, Northeast*

Japan. EGU General Assembly 2020, Online, 4–8 May 2020, EGU2020-9825. DOI: https://doi.org/10.5194/egusphere-egu2020-9825.

Emoto, K., Saito, T., and Shiomi, K. (2017). Statistical parameters of random heterogeneity estimated by analysing coda waves based on finite difference method. *Geophysical Journal International*, 211(3):1575–1584. DOI: 10.1093/gji/ggx387.

Emoto, K., Sato, H., and Nishimura, T. (2010). Synthesis of vector wave envelopes on the free surface of a random medium for the vertical incidence of a plane wavelet based on the Markov approximation. *Journal of Geophysical Research*, 115(B8). DOI: 10.1029/2009jb006955.

Emoto, K., Sato, H., and Nishimura, T. (2012). Synthesis and applicable condition of vector wave envelopes in layered random elastic media with anisotropic autocorrelation function based on the markov approximation. *Geophysical Journal International*, 188(1):325–335. DOI: 10.1111/j.1365-246x.2011.05264.x.

Eulenfeld, T. and Wegler, U. (2016). Measurement of intrinsic and scattering attenuation of shear waves in two sedimentary basins and comparison to crystalline sites in Germany. *Geophysical Journal International*, 205(2):744–757. DOI: 10.1093/gji/ggw035.

Flatté, S. M. and Wu, R.-S. (1988). Small-scale structure in the lithosphere and asthenosphere deduced from arrival time and amplitude fluctuations at NORSAR. *Journal of Geophysical Research*, 93(B6):6601. DOI: 10.1029/jb093ib06p06601.

Frankel, A. and Clayton, R. W. (1986). Finite difference simulations of seismic scattering: Implications for the propagation of short-period seismic waves in the crust and models of crustal heterogeneity. *Journal of Geophysical Research*, 91(B6):6465. DOI: 10.1029/jb091ib06p06465.

Fujimoto, K. and Midorikawa, S. (2006). Relationship between average shear-wave velocity and site amplification inferred from strong motion records at nearby station

pairs. *Journal of JAEE Journal of Japan Association for Earthquake Engineering*, 6(1):11–22. DOI: 10.5610/jaee.6.11.

Gaebler, P., Eken, T., Bektaş, H. O., Eulenfeld, T., Wegler, U., and Taymaz, T. (2019). Imaging of shear wave attenuation along the central part of the North Anatolian Fault Zone, Turkey. *Journal of Seismology*, 23(4):913–927. DOI: 10.1007/s10950-019-09842-1.

Ganefianto, G., Nakahara, H., and Nishimura, T. (2021). Scattering strength at active volcanoes in Japan as inferred from the peak ratio analysis of teleseismic P waves. *Earth Planets and Space*, 73(207). DOI: 10.1186/s40623-021-01541-x.

Geldart, L. P. and Sheriff, R. E. (2004). *Problems in exploration seismology and their solutions*. SEG. DOI: http://dx.doi.org/10.1190/1.9781560801733. ISBN: 9781560801153.

Gusev, A. A. (1995). Vertical profile of turbidity and coda Q. *Geophysical Journal International*, 123(3):665–672. DOI: 10.1111/j.1365-246x.1995.tb06882.x.

Haney, M. M., Power, J., West, M., and Michaels, P. (2012). Causal instrument corrections for short-period and broadband seismometers. *Seismological Research Letters*, 83(5):834–845. DOI: 10.1785/0220120031.

Hansen, P. C. (1992). Analysis of discrete ill-posed problems by means of the L-curve. *SIAM Review*, 34(4):561–580. DOI: 10.1137/1034115.

Hartzell, S., Ramírez-Guzmán, L., Meremonte, M., and Leeds, A. (2016). Ground motion in the presence of complex topography II: Earthquake sources and 3D simulations. *Bulletin of the Seismological Society of America*, 107(1):344–358. DOI: 10.1785/0120160159.

Hasemi, A. and Horiuchi, S. (2010). Seismic reflector alignment along the volcanic front

in northeastern Honshu, Japan. *Journal of Geophysical Research*, 115(B7). DOI: 10.1029/2009jb006653.

Havskov, J. and Ottemöler, L. (2010). *Routine Data Processing in Earthquake Seismology - With Sample Data, Exercises and Software*. Springer.

Herman, G. T., Hurwitz, H., Lent, A., and Lung, H.-P. (1979). On the Bayesian approach to image reconstruction. *Information and Control*, 42:60–71.

Hirose, F., Miyaoka, K., Hayashimoto, N., Yamazaki, T., and Nakamura, M. (2011). Outline of the 2011 off the Pacific coast of Tohoku earthquake (Mw 9.0) —seismicity: foreshocks, mainshock, aftershocks, and induced activity—. *Earth, Planets and Space*, 63(7):513–518.

Hirose, T., Nakahara, H., and Nishimura, T. (2019). A passive estimation method of scattering and intrinsic absorption parameters from envelopes of seismic ambient noise cross-correlation functions. *Geophysical Research Letters*, 46(7):3634–3642. DOI: 10.1029/2018gl080553.

Hirose, T., Ueda, H., and Fujita, E. (2022). Scattering and intrinsic absorption parameters of Rayleigh waves at 18 active volcanoes in Japan inferred using seismic interferometry. *Bulletin of Volcanology*, 84(3). DOI: 10.1007/s00445-022-01536-w.

Holliger, K. (1996). Upper-crustal seismic velocity heterogeneity as derived from a variety of P-wave sonic logs. *Geophysical Journal International*, 125(3):813–829. DOI: 10.1111/j.1365-246x.1996.tb06025.x.

Horspool, N. A., Savage, M. K., and Bannister, S. (2006). Implications for intraplate volcanism and back-arc deformation in northwestern New Zealand, from joint inversion of receiver functions and surface waves. *Geophysical Journal International*, 166(3):1466–1483. DOI: 10.1111/j.1365-246x.2006.03016.x.

Hua, Y., Zhang, S., Li, M., Wu, T., Zou, C., and Liu, L. (2019). Magma system beneath Tengchong volcanic zone inferred from local earthquake seismic tomography. *Journal of Volcanology and Geothermal Research*, 377:1–16. DOI: 10.1016/j.jvolgeores.2019.04.002.

Imperatori, W. and Mai, P. (2015). The role of topography and lateral velocity heterogeneities on near-source scattering and ground-motion variability. *Geophysical Journal International*, 202(3):2163–2181. DOI: 10.1093/gji/ggv281.

Jankowski, K. R., Flannelly, K. J., and Flannelly, L. T. (2017). The t-test: An influential inferential tool in chaplaincy and other healthcare research. *Journal of Health Care Chaplaincy*, 24(1):30–39. DOI: 10.1080/08854726.2017.1335050.

Kanasewich, E. R. (1981). *Time Sequence Analysis in Geophysics*. Univ. of Alberta Pr., 3 edition.

Kästle, E. D., Rosenberg, C., Boschi, L., Bellahsen, N., Meier, T., and El-Sharkawy, A. (2020). Slab break-offs in the Alpine Subduction Zone. *International Journal of Earth Sciences*, 109(2):587–603. DOI: 10.1007/s00531-020-01821-z.

Kennett, B. L. N., Engdahl, E. R., and Buland, R. (1995). Constraints on seismic velocities in the earth from traveltimes. *Geophysical Journal International*, 122(1):108–124. DOI: 10.1111/j.1365-246x.1995.tb03540.x.

Kimura, J. and Yoshida, T. (1999). Mantle diapir-induced arc volcanism: The Ueno basalts, Nomugi-Toge and Hida volcanic suites, central Japan. *Island Arc*, 8(2):304–322. DOI: 10.1046/j.1440-1738.1999.00239.x.

Kitamura, K., Takahashi, M., Mizoguchi, K., Masuda, K., Ito, H., and Song, S.-R. (2010). Effects of pressure on pore characteristics and permeability of porous rocks as estimated from seismic wave velocities in cores from TCDP Hole-A. *Geophysical Journal International*, 182(3):1148–1160. DOI: 10.1111/j.1365-246x.2010.04694.x.

Kobayashi, M., Takemura, S., and Yoshimoto, K. (2015). Frequency and distance changes in the apparent P-wave radiation pattern: Effects of seismic wave scattering in the crust inferred from dense seismic observations and numerical simulations. *Geophysical Journal International*, 202(3):1895–1907. DOI: 10.1093/gji/ggv263.

Komatitsch, D. and Tromp, J. (1999). Introduction to the spectral element method for three-dimensional seismic wave propagation. *Geophysical Journal International*, 139(3):806–822. DOI: 10.1046/j.1365-246x.1999.00967.x.

Krischer, L., Megies, T., Barsch, R., Beyreuther, M., Lecocq, T., Caudron, C., and Wassermann, J. (2015). ObsPy: a bridge for seismology into the scientific Python ecosystem. *Computational Science & Discovery*, 8(1):014003. DOI: 10.1088/1749-4699/8/1/014003.

Kubanza, M., Nishimura, T., and Sato, H. (2007). Evaluation of strength of heterogeneity in the lithosphere from peak amplitude analyses of teleseismic short-period vector P waves. *Geophysical Journal International*, 171(1):390–398. DOI: 10.1111/j.1365-246x.2007.03544.x.

Kumagai, H., Londoño, J. M., Maeda, Y., Velez, C. M. L., and Lacson, R. (2018). Envelope widths of volcano-seismic events and seismic scattering characteristics beneath volcanoes. *Journal of Geophysical Research: Solid Earth*, 123(11):9764–9777. DOI: 10.1029/2018jb015557.

Kumagai, H., Saito, T., O'Brien, G., and Yamashina, T. (2011). Characterization of scattered seismic wavefields simulated in heterogeneous media with topography. *Journal of Geophysical Research*, 116(B3). DOI: 10.1029/2010jb007718.

Lay, T. and Wallace, T. C. (1995). *Modern global seismology*, volume 58. Acad. Press.

Levander, A. R. (1990). Seismic scattering near the earth's surface. *Pure and Applied Geophysics PAGEOPH*, 132(1-2):21–47. DOI: 10.1007/bf00874356.

Lowrie, W. (2007). *Fundamentals of geophysics*. Cambridge University Press.

Ma, X. and Huang, Z. (2020). Small-scale scattering heterogeneities beneath the northern Tien Shan from the teleseismic P wavefield. *Earth, Planets and Space*, 72(1). DOI: 10.1186/s40623-020-1136-1.

Maeda, S., Matsuzawa, T., Okada, T., Katao, H., Yoshida, T., Kosuga, M., and Otsubo, M. (2020). Spatiotemporal variations in the stress field in the northeasternmost part of the NE Japan arc: constraints from microearthquakes. *Earth, Planets and Space*, 72(117):1–7. DOI: 10.1186/s40623-020-01245-8.

Maeda, T., Furumura, T., Noguchi, S., Takemura, S., Sakai, S., Shinohara, M., Iwai, K., and Lee, S.-J. (2013). Seismic- and tsunami-wave propagation of the 2011 off the Pacific coast of Tohoku earthquake as inferred from the tsunami-coupled finite-difference simulation. *Bulletin of the Seismological Society of America*, 103(2B):1456–1472. DOI: 10.1785/0120120118.

Maeda, T., Furumura, T., and Obara, K. (2014). Scattering of teleseismic P-waves by the Japan trench: A significant effect of reverberation in the seawater column. *Earth and Planetary Science Letters*, 397:101–110. DOI: 10.1016/j.epsl.2014.04.037.

Maeda, T., Takemura, S., and Furumura, T. (2017). OpenSWPC: an open-source integrated parallel simulation code for modeling seismic wave propagation in 3D heterogeneous viscoelastic media. *Earth, Planets and Space*, 69(1). DOI: 10.1186/s40623-017-0687-2.

Mancinelli, N., Shearer, P., and Liu, Q. (2016). Constraints on the heterogeneity spectrum of Earth' s upper mantle. *Journal of Geophysical Research: Solid Earth*, 121(5):3703–3721. DOI: 10.1002/2015jb012641.

Margerin, L. (2011). *Scattering, Seismic Waves*, page 1210–1223. Encyclopedia of Solid Earth Geophysics. Springer.

Matsuoka, M. and Wakamatsu, K. (2008). Site amplification capability map based on the 7.5-arc-second Japan engineering geomorphologic classification map. *National Institute of Advanced Industrial Science and Technology, Intellectual property management, No.H20PRO-936*.

Meckel, T. A., Coffin, M. F., Mosher, S., Symonds, P., Bernardel, G., and Mann, P. (2003). Underthrusting at the Hjort trench, Australian-Pacific plate boundary: Incipient subduction? *Geochemistry, Geophysics, Geosystems*, 4(12). DOI: 10.1029/2002gc000498.

Megies, T., Beyreuther, M., Barsch, R., Krischer, L., and Wassermann, J. (2011). ObsPy – what can it do for data centers and observatories? *Annals of Geophysics*, 54(1):47–58. DOI: 10.4401/ag-4838.

Miura, D., Furukawa, R., and Arai, K. (2022). *Geological Map of Esan Volcano*. Geological Survey of Japan, AIST.

Miyamachi, H., Tomari, C., Yakiwara, H., Iguchi, M., Tameguri, T., Yamamoto, K., Ohkura, T., Ando, T., Onishi, K., Shimizu, H., and et al. (2013). Shallow velocity structure beneath the Aira Caldera and Sakurajima Volcano as inferred from refraction analysis of the seismic experiment in 2008. *Bull. Volcanol. Soc. Japan*, 58(1):227–237.

Murray, S. G. (2018). powerbox: A Python package for creating structured fields with isotropic power spectra. *Journal of Open Source Software*, 3(28):850. DOI: 10.21105/joss.00850.

Nakahara, H. (2013). Envelope inversion analysis for high-frequency seismic energy radiation from the 2011 mw 9.0 off the Pacific coast of Tohoku earthquake. *Bulletin of the Seismological Society of America*, 103(2B):1348–1359. DOI: 10.1785/0120120155.

Nakahara, H., Sato, H., Nishimura, T., and Fujiwara, H. (2011). Direct observation of rupture propagation during the 2011 off the Pacific coast of Tohoku earthquake (m

w 9.0) using a small seismic array. *Earth, Planets and Space*, 63(7):589–594. DOI: 10.5047/eps.2011.06.002.

Nakamichi, H., Watanabe, H., and Ohminato, T. (2007). Three-dimensional velocity structures of Mount Fuji and the South Fossa Magna, Central Japan. *Journal of Geophysical Research*, 112(B3). DOI: 10.1029/2005jb004161.

Nakamura, H., Oikawa, T., Geshi, N., and Matsumoto, A. (2014). Migration of a volcanic front inferred from K-Ar ages of late Miocene to Pliocene volcanic rocks in central Japan. *Island Arc*, 23(3):236–250. DOI: 10.1111/iar.12073.

Nakamura, T., Takenaka, H., Okamoto, T., and Kaneda, Y. (2012). FDM simulation of seismic-wave propagation for an aftershock of the 2009 Suruga Bay earthquake: Effects of ocean-bottom topography and seawater layer. *Bulletin of the Seismological Society of America*, 102(6):2420–2435. DOI: 10.1785/0120110356.

Nakata, N. and Beroza, G. C. (2015). Stochastic characterization of mesoscale seismic velocity heterogeneity in Long Beach, California. *Geophysical Journal International*, 203(3):2049–2054. DOI: 10.1093/gji/ggv421.

Nakata, N. and Shelly, D. R. (2018). Imaging a crustal low-velocity layer using reflected seismic waves from the 2014 earthquake swarm at Long Valley caldera, California: The magmatic system roof? *Geophysical Research Letters*, 45(8):3481–3488. DOI: 10.1029/2018gl077260.

National Catalogue of the Active Volcanoes in Japan (2013). Japan Meteorological Agency, fourth edition. `https://www.data.jma.go.jp/svd/vois/data/tokyo/STOCK/souran_eng/menu.htm`.

National Research Institute for Earth Science and Disaster Resilience (2019). *NIED Hi-net*. National Research Institute for Earth Science and Disaster Resilience. DOI: 10.17598/NIED.0003.

Nishida, K., Kawakatsu, H., and Obara, K. (2008). Three-dimensional crustal S wave velocity structure in Japan using microseismic data recorded by Hi-net tiltmeters. *Journal of Geophysical Research*, 113(B10). DOI: 10.1029/2007jb005395.

Nishimura, T. (2012). Heterogeneity of the Japanese islands as inferred from transverse component analyses of teleseismic P-waves observed at a seismic station network, Hi-net. *Earth, Planets and Space*, 64(11). DOI: 10.5047/eps.2012.10.001.

Obara, K. and Sato, H. (1995). Regional differences of random inhomogeneities around the volcanic front in the Kanto-Tokai area, Japan, revealed from the broadening of S wave seismogram envelopes. *Journal of Geophysical Research: Solid Earth*, 100(B2):2103–2121. DOI: 10.1029/94jb02644.

Obermann, A., Froment, B., Campillo, M., Larose, E., Planès, T., Valette, B., Chen, J. H., and Liu, Q. Y. (2014). Seismic noise correlations to image structural and mechanical changes associated with the Mw 7.9 2008 Wenchuan earthquake. *Journal of Geophysical Research: Solid Earth*, 119(4):3155–3168. DOI: 10.1002/2013jb010932.

Obermann, A., Planès, T., Hadziioannou, C., and Campillo, M. (2016). Lapse-time-dependent coda-wave depth sensitivity to local velocity perturbations in 3-D heterogeneous elastic media. *Geophysical Journal International*, 207(1):59–66. DOI: 10.1093/gji/ggw264.

Obermann, A., Planès, T., Larose, E., and Campillo, M. (2018). 4-D imaging of subsurface changes with coda waves: Numerical studies of 3-D combined sensitivity kernels and applications to the Mw 7.9, 2008 Wenchuan earthquake. *Pure and Applied Geophysics*, 176(3):1243–1254. DOI: 10.1007/s00024-018-2014-7.

Obermann, A., Planès, T., Larose, E., Sens-Schönfelder, C., and Campillo, M. (2013). Depth sensitivity of seismic coda waves to velocity perturbations in an elastic

heterogeneous medium. *Geophysical Journal International*, 194(1):372–382. DOI: 10.1093/gji/ggt043.

Ogiso, M. (2018). A method for mapping intrinsic attenuation factors and scattering coefficients of S waves in 3-D space and its application in southwestern Japan. *Geophysical Journal International*, 216(2):948–957. DOI: 10.1093/gji/ggy468.

Pacheco, C. and Snieder, R. (2005). Time-lapse travel time change of multiply scattered acoustic waves. *The Journal of the Acoustical Society of America*, 118(3):1300–1310. DOI: 10.1121/1.2000827.

Peter, D., Komatitsch, D., Luo, Y., Martin, R., Goff, N. L., Casarotti, E., Loher, P. L., Magnoni, F., Liu, Q., Blitz, C., Nissen-Meyer, T., Basini, P., and Tromp, J. (2011). Forward and adjoint simulations of seismic wave propagation on fully unstructured hexahedral meshes. *Geophysical Journal International*, 186(2):721–739. DOI: 10.1111/j.1365-246x.2011.05044.x.

Planès, T., Larose, E., Margerin, L., Rossetto, V., and Sens-Schönfelder, C. (2014). Decorrelation and phase-shift of coda waves induced by local changes: multiple scattering approach and numerical validation. *Waves in Random and Complex Media*, 24(2):99–125. DOI: 10.1080/17455030.2014.880821.

Prudencio, J., Aoki, Y., Takeo, M., Ibáñez, J., Pezzo, E., and Song, W. (2017a). Separation of scattering and intrinsic attenuation at Asama volcano (Japan): Evidence of high volcanic structural contrasts. *Journal of Volcanology and Geothermal Research*, 333-334:96–103. DOI: 10.1016/j.jvolgeores.2017.01.014.

Prudencio, J., Ibáñez, J. M., Pezzo, E. D., Martí, J., García-Yeguas, A., and Siena, L. D. (2015a). 3D attenuation tomography of the volcanic island of Tenerife (Canary islands). *Surveys in Geophysics*, 36(5):693–716. DOI: 10.1007/s10712-015-9333-3.

Prudencio, J., Manga, M., and Taira, T. (2018). Subsurface structure of Long Valley caldera imaged with seismic scattering and intrinsic attenuation. *Journal of Geophysical Research: Solid Earth*, 123(7):5987–5999. DOI: 10.1029/2017jb014986.

Prudencio, J., Pezzo, E. D., Ibáñez, J. M., Giampiccolo, E., and Patané, D. (2015b). Two-dimensional seismic attenuation images of Stromboli island using active data. *Geophysical Research Letters*, 42(6):1717–1724. DOI: 10.1002/2015gl063293.

Prudencio, J., Taira, T., Aoki, Y., Aoyama, H., and Onizawa, S. (2017b). Intrinsic and scattering attenuation images of Usu volcano, Japan. *Bulletin of Volcanology*, 79(4). DOI: 10.1007/s00445-017-1117-9.

Przybilla, J., Wegler, U., and Korn, M. (2009). Estimation of crustal scattering parameters with elastic radiative transfer theory. *Geophysical Journal International*, 178(2):1105–1111. DOI: 10.1111/j.1365-246x.2009.04204.x.

Ranjan, P., Konstantinou, K., and Andinisari, R. (2019). Spatial distribution of random velocity inhomogeneities in the southern Aegean from inversion of S wave peak delay times. *Journal of Geophysical Research: Solid Earth*, 124(10):10393–10412. DOI: 10.1029/2018jb017198.

Rawlinson, N., Kennett, B. L. N., and Heintz, M. (2006). Insights into the structure of the upper mantle beneath the Murray basin from 3D teleseismic tomography. *Australian Journal of Earth Sciences*, 53(4):595–604. DOI: 10.1080/08120090600686751.

Revenaugh, J. (2000). The relation of crustal scattering to seismicity in southern California. *Journal of Geophysical Research*, 105(B11):25403–25422.

Ripperger, J., Igel, H., and Wasserman, J. (2003). Seismic wave simulation in the presence of real volcano topography. *Journal of Volcanology and Geothermal Research*, 128(1-3):31–44. DOI: 10.1016/s0377-0273(03)00245-2.

Ritter, J. R. R. and Rothert, E. (2000). Variations of the lithospheric seismic scattering strength below the Massif Central, France and the Frankonian Jura, se Germany. *Tectonophysics*, 328(3-4):297–305. DOI: 10.1016/s0040-1951(00)00212-2.

Ritter, J. R. R., Shapiro, S. A., and Schechinger, B. (1998). Scattering parameters of the lithosphere below the Massif Central, France, from teleseismic wavefield records. *Geophysical Journal International*, 134(1):187–198. DOI: 10.1046/j.1365-246x.1998.00562.x.

Robertsson, J. O., Blanch, J. O., and Symes, W. W. (1994). Viscoelastic finite-difference modeling. *GEOPHYSICS*, 59(9):1444–1456. DOI: 10.1190/1.1443701.

Rost, S. and Thomas, C. (2002). Array seismology: Methods and applications. *Reviews of Geophysics*, 40(3). DOI:10.1029/2000rg000100.

Saito, T., Sato, H., and Ohtake, M. (2002). Envelope broadening of spherically outgoing waves in three-dimensional random media having power law spectra. *Journal of Geophysical Research*, 107(B5). DOI:10.1029/2001jb000264.

Saito, T., Sato, H., Ohtake, M., and Obara, K. (2005). Unified explanation of envelope broadening and maximum-amplitude decay of high-frequency seismograms based on the envelope simulation using the Markov approximation: Forearc side of the volcanic front in northeastern Honshu, Japan. *Journal of Geophysical Research*, 110(B1). DOI: 10.1029/2004jb003225.

Sanborn, C. J., Cormier, V. F., and Fitzpatrick, M. (2017). Combined effects of deterministic and statistical structure on high-frequency regional seismograms. *Geophysical Journal International*, 210(2):1143–1159. DOI: 10.1093/gji/ggx219.

Sánchez-Galvis, I. J., Serrano, J., Sierra, D. A., and Agudelo, W. (2021). Simulation of scattered seismic surface waves on mountainous onshore areas: Understand-

ing the "ground roll energy cone". *The Leading Edge*, 40(8):601–609. DOI: 10.1190/tle40080601.1.

Sato, H. (1977). Single isotropic scattering model including wave conversions simple theoretical model of the short period body wave propagation. *Journal of Physics of the Earth*, 25(2):163–176. DOI: 10.4294/jpe1952.25.163.

Sato, H. (1989). Broadening of seismogram envelopes in the randomly inhomogeneous lithosphere based on the parabolic approximation: southeastern Honshu, Japan. *Journal of Geophysical Research*, 94(B12):17735. DOI: 10.1029/jb094ib12p17735.

Sato, H. (2006). Synthesis of vector wave envelopes in three-dimensional random elastic media characterized by a Gaussian autocorrelation function based on the Markov approximation: Plane wave case. *Journal of Geophysical Research: Solid Earth*, 111(B6). DOI: 10.1029/2005jb004036.

Sato, H. (2011). Seismic waves in heterogeneous earth, scattering of. In Meyers, R. A., editor, *Extreme Environmental Events*, page 788–804. Springer. DOI: `https://doi.org/10.1007/978-1-4419-7695-6_42`.

Sato, H. (2019). Power spectra of random heterogeneities in the solid earth. *Solid Earth*, 10(1):275–292. DOI: 10.5194/se-10-275-2019.

Sato, H., Fehler, M. C., and Maeda, T. (2012). *Seismic Wave Propagation and Scattering in the Heterogeneous Earth Second Edition*. Springer Berlin.

Sato, H. and Korn, M. (2008). Chapter 3 synthesis of vector-wave envelopes in random elastic media on the basis of the Markov approximation. *Advances in Geophysics Earth Heterogeneity and Scattering Effects on Seismic Waves*, page 43–93. DOI: 10.1016/s0065-2687(08)00003-4.

Schardong, L., Ferreira, A. M., Berbellini, A., and Sturgeon, W. (2019). The anatomy of uppermost mantle shear-wave speed anomalies in the western U.S. from surface-wave amplification. *Earth and Planetary Science Letters*, 528:115822. DOI: 10.1016/j.epsl.2019.115822.

Schmandt, B., Jiang, C., and Farrell, J. (2019). Seismic perspectives from the western U.S. on magma reservoirs underlying large silicic calderas. *Journal of Volcanology and Geothermal Research*, 384:158–178. DOI: 10.1016/j.jvolgeores.2019.07.015.

Sens-Schönfelder, C. and Wegler, U. (2006). Radiative transfer theory for estimation of the seismic moment. *Geophysical Journal International*, 167(3):1363–1372. DOI: 10.1111/j.1365-246x.2006.03139.x.

Shearer, P. M. and Earle, P. S. (2004). The global short-period wavefield modelled with a Monte Carlo seismic phonon method. *Geophysical Journal International*, 158(3):1103–1117. DOI: 10.1111/j.1365-246x.2004.02378.x.

Shearer, P. M. and Earle, P. S. (2008). Chapter 6 observing and modeling elastic scattering in the deep earth. *Advances in Geophysics Earth Heterogeneity and Scattering Effects on Seismic Waves*, page 167–193. DOI: 10.1016/s0065-2687(08)00006-x.

Shiina, T., Katsumata, K., Yomogida, K., and Kato, A. (2021). Attenuation contrast in mantle wedge across the volcanic front of northeastern Japan that controls propagations of high-frequency S-wave later phases. *Earth, Planets and Space*, 73(1). DOI: 10.1186/s40623-021-01361-z.

Shimano, T., Geshi, N., and Kobayashi, T. (2013). *Geological Map of Suwasenojima Volcano*. Geological Survey of Japan, AIST.

Shiomi, K., Sato, H., and Ohtake, M. (1997). Broad-band power-law spectra of well-log data in Japan. *Geophysical Journal International*, 130(1):57–64. DOI: 10.1111/j.1365-246x.1997.tb00987.x.

Shito, A., Matsumoto, S., Ohkura, T., Shimizu, H., Sakai, S., Iio, Y., Takahashi, H., Yakiwara, H., Watanabe, T., Kosuga, M., Okada, T., Yoshimi, M., and Asano, Y. (2020). 3-D intrinsic and scattering seismic attenuation structures beneath Kyushu, Japan. *Journal of Geophysical Research: Solid Earth*, 125(8). DOI: 10.1029/2019jb018742.

Singh, C., Singh, A., Bharathi, V. S., Bansal, A., and Chadha, R. (2012). Frequency-dependent body wave attenuation characteristics in the Kumaun Himalaya. *Tectonophysics*, 524-525:37–42. DOI: 10.1016/j.tecto.2011.12.013.

Sirkova, I. and Mikhalev, M. (2006). Parabolic wave equation method applied to the tropospheric ducting propagation problem: A survey. *Electromagnetics*, 26(2):155–173. DOI: 10.1080/02726340500486484.

Smith, R. B., Jordan, M., Steinberger, B., Puskas, C. M., Farrell, J., Waite, G. P., Husen, S., Chang, W.-L., and O'Connell, R. (2009). Geodynamics of the Yellowstone hotspot and mantle plume: Seismic and GPS imaging, kinematics, and mantle flow. *Journal of Volcanology and Geothermal Research*, 188(1-3):26–56. DOI: 10.1016/j.jvolgeores.2009.08.020.

Snieder, R. and van Wijk, K. (2015). *A Guided tour of mathematical methods for the physical sciences*. Cambridge University Press, third edition.

Snoke, J. A. (2009). Traveltime tables for iasp91 and ak135. *Seismological Research Letters*, 80(2):260–262. DOI: 10.1785/gssrl.80.2.260.

Sreenivasiah, I., Ishimaru, A., and Hong, S. T. (1976). Two-frequency mutual coherence function and pulse propagation in a random medium: An analytic solution to the plane wave case. *Radio Science*, 11(10):775–778. DOI: 10.1029/rs011i010p00775.

Stern, R. J. and Dickinson, W. R. (2010). The Gulf of Mexico is a Jurassic backarc basin. *Geosphere*, 6(6):739–754. DOI: 10.1130/ges00585.1.

Suzaki, A. (2007). Study on vector-wave envelopes in von Karman-type random media. Master's thesis, Tohoku University, Sendai, Japan.

Takahashi, T., Sato, H., Nishimura, T., and Obara, K. (2009). Tomographic inversion of the peak delay times to reveal random velocity fluctuations in the lithosphere: method and application to northeastern Japan. *Geophysical Journal International*, 178(3):1437–1455. DOI: 10.1111/j.1365-246x.2009.04227.x.

Takemura, S., Emoto, K., and Yamaya, L. (2023). High-frequency S and S-coda waves at ocean-bottom seismometers. *Earth, Planets and Space*, 75(1). DOI: 10.1186/s40623-023-01778-8.

Takemura, S., Furumura, T., and Maeda, T. (2015a). Scattering of high-frequency seismic waves caused by irregular surface topography and small-scale velocity inhomogeneity. *Geophysical Journal International*, 201(1):459–474. DOI: 10.1093/gji/ggv038.

Takemura, S., Kobayashi, M., and Yoshimoto, K. (2017). High-frequency seismic wave propagation within the heterogeneous crust: effects of seismic scattering and intrinsic attenuation on ground motion modelling. *Geophysical Journal International*, 210(3):1806–1822. DOI: 10.1093/gji/ggx269.

Takemura, S., Yoshimoto, K., and Tonegawa, T. (2015b). Scattering of trapped P and S waves in the hydrated subducting crust of the Philippine Sea plate at shallow depths beneath the Kanto region, Japan. *Geophysical Journal International*, 203(3):2261–2276. DOI: 10.1093/gji/ggv423.

Takeuchi, N. (2016). Differential Monte Carlo method for computing seismogram envelopes and their partial derivatives. *Journal of Geophysical Research: Solid Earth*, 121(5):3428–3444. DOI: 10.1002/2015jb012661.

Tanaka, S., Hamaguchi, H., Nishimura, T., Yamawaki, T., Ueki, S., Nakamichi, H., Tsutsui, T., Miyamachi, H., Matsuwo, N., Oikawa, J., and et al. (2002). Three-dimensional

p-wave velocity structure of Iwate Volcano, Japan from active seismic survey. *Geophysical Research Letters*, 29(10).

Tanioka, Y. and Ruff, L. J. (1997). Source time functions. *Seismological Research Letters*, 68(3):386–400. DOI: 10.1785/gssrl.68.3.386.

Tian, D. (2020). HinetPy: A Python package to request and process seismic waveform data from Hi-net (version 0.6.7). *Zenodo*. `https://seisman.github.io/HinetPy/`. DOI: http://doi.org/10.5281/zenodo.3885779.

Ueno, T., Saito, T., Shiomi, K., and Haryu, Y. (2015). Monitoring the instrument response of the high-sensitivity seismograph network in Japan (Hi-net): effects of response changes on seismic interferometry analysis. *Earth, Planets and Space*, 67(1). DOI: 10.1186/s40623-015-0305-0.

Wakamatsu, K., Kubo, S., Matsuoka, M., Hasegawa, K., and Sugiura, M. (2005). Japan Engineering Geomorphologic Classification Map. *University of Tokyo Press*.

Wakamatsu, K. and Matsuoka, M. (2013). Nationwide 7.5-arc-second Japan engineering geomorphologic classification map and vs30 zoning. *Journal of Disaster Research*, 8(5):904–911. DOI: 10.20965/jdr.2013.p0904.

Wang, W. and Shearer, P. M. (2017). Using direct and coda wave envelopes to resolve the scattering and intrinsic attenuation structure of Southern California. *Journal of Geophysical Research: Solid Earth*, 122(9):7236–7251. DOI: 10.1002/2016jb013810.

Weaver, R. L., Hadziioannou, C., Larose, E., and Campillo, M. (2011). On the precision of noise correlation interferometry. *Geophysical Journal International*, 185(3):1384–1392. DOI: 10.1111/j.1365-246x.2011.05015.x.

Wegler, U., Korn, M., and Przybilla, J. (2006). Modeling full seismogram envelopes

using radiative transfer theory with Born scattering coefficients. *Pure and Applied Geophysics*, 163(2-3):503–531. DOI: 10.1007/s00024-005-0027-5.

Wei, W. and Fu, L. (2014). Monte Carlo simulation of stress-associated scattering attenuation from laboratory ultrasonic measurements. *Bulletin of the Seismological Society of America*, 104(2):931–943. DOI: 10.1785/0120130082.

Wu, R.-S., Xu, Z., and Li, X.-P. (1994). Heterogeneity spectrum and scale-anisotropy in the upper crust revealed by the German continental deep-drilling (KTB) holes. *Geophysical Research Letters*, 21(10):911–914. DOI: 10.1029/94gl00772.

Xu, X., Hofmann, R., Batzle, M., and Tshering, T. (2006). Influence of pore pressure on velocity in low-porosity sandstone: Implications for time-lapse feasibility and pore-pressure study. *Geophysical Prospecting*, 54(5):565–573. DOI: 10.1111/j.1365-2478.2006.00569.x.

Yamamoto, M. and Sato, H. (2010). Multiple scattering and mode conversion revealed by an active seismic experiment at Asama volcano, Japan. *Journal of Geophysical Research*, 115(B7). DOI: 10.1029/2009jb007109.

Yamanaka, H. and Yamada, N. (2006). Estimation of 3D S-wave velocity model of the Kanto basin, Japan, using Rayleigh wave phase velocity. *Bulletin of Earthquake Research Institute*, 81:295–301.

Yoshimoto, K. (2000). Monte Carlo simulation of seismogram envelopes in scattering media. *Journal of Geophysical Research: Solid Earth*, 105(B3):6153–6161. DOI: 10.1029/1999jb900437.

Yoshimoto, K., Sato, H., and Ohtake, M. (1993). Frequency-dependent attenuation of P and S waves in the Kanto area, Japan, based on the coda-normalization method. *Geophysical Journal International*, 114(1):165–174. DOI: 10.1111/j.1365-246x.1993.tb01476.x.

Yoshimoto, K., Sato, H., and Ohtake, M. (1997). Short-wavelength crustal heterogeneities in the Nikko area, Central Japan, revealed from the three-component seismogram envelope analysis. *Physics of the Earth and Planetary Interiors*, 104(1-3):63–73. DOI: 10.1016/s0031-9201(97)00062-9.

Zeng, Y. (2017). Modeling of high-frequency seismic-wave scattering and propagation using radiative transfer theory. *Bulletin of the Seismological Society of America*, 107(6):2948–2962. DOI: 10.1785/0120160241.

Zieger, T. R. R., Sens-Schönfelder, C. R. R., Ritter, J. R. R., Lühr, B.-G. R. R., and Dahm, T. R. R. (2016). P wave scattering and the distribution of heterogeneity around Etna volcano. *Annals of Geophysics*, page 1–13. DOI: 10.4401/ag-7085.